Particle Rate Studies and Technical Design Development for the P2 Silicon Pixel Tracking Detector

Dissertation

zur Erlangung des Grades
„Doktor der Naturwissenschaften“
am Fachbereich Physik, Mathematik und Informatik der
Johannes Gutenberg-Universität in Mainz

vorgelegt von
Marco Zimmermann
geboren in Lörrach

Mainz, den 27. Mai 2019

Jeder dumme Junge kann einen Käfer zertreten. Aber alle Professoren der Welt können keinen herstellen.

(Arthur Schopenhauer)

Abstract

The P2 Experiment intends to determine the weak mixing angle $\sin^2\theta_w$ at low momentum transfer Q^2 by measuring the parity violating asymmetry in elastic electron-proton scattering. The targeted relative uncertainty on $\sin^2\theta_w$ is 0.15 %. The experiment is at the same time a precision test of the Standard Model of particle physics and a search for New Physics at the intensity frontier. It will be carried out at the Mainz Energy Recovery Superconducting Accelerator (MESA), which will provide a 150 µA beam of alternatingly polarized 150 MeV electrons with excellent beam stability. While the parity violating asymmetry will be measured with integrating Cherenkov detectors, the tracking detector is developed to determine the four momentum transfer Q^2 of the electrons in the liquid hydrogen target, and to reconstruct individual electron tracks for systematic studies. The novel technology of High Voltage Monolithic Active Pixel Sensors (HV-MAPS) will be used in order to minimize the material budget and thus reduce multiple scattering. One main difficulty for the tracking detector design is the demand to minimize the material of the infrastructure needed for mechanical support, powering, readout and cooling of the sensors. Moreover, the rate of about 0.1 THz of electrons being scattered into the acceptance of the tracking detector is challenging for the data acquisition system and the radiation hardness of all used components.

This work presents feasibility studies on the tracking detector of the P2 experiment. In the first part, the signal and background particle rates as well as the overall radiation load are estimated based on a detailed GEANT4 Monte Carlo simulation. Photons represent the most abundant background type. The detection probability of photons is therefore further investigated in experimental tests.

In the second part of this work, the technical design of a tracker module is worked out. The full tracking detector will consist of eight identical modules, each containing around 630 sensors of dimensions 2 cm × 2 cm that are arranged in two planes. A thermo-mechanical detector prototype has been constructed based on this design, demonstrating its feasibility. In this prototype, a flexprint with heatable copper traces is implemented as a mock-up of the actual sensors mounted on polyimide foil. The sensor cooling concept based on gaseous helium was integrated into the mechanical design and investigated in computational fluid dynamics simulations. The assembled prototype will allow to compare these simulations to experimental cooling tests.

Zusammenfassung

Das P2 Experiment beabsichtigt, den elektroschwachen Mischungswinkel bei niedrigem Viererimpulsübertrag Q^2 mit einer Genauigkeit von 0.15 % zu bestimmen. Hierzu soll die paritätsverletzende Asymmetrie in elastischer Elektron-Proton-Streuung gemessen werden. Das Experiment ist ein Präzisionstest des Standardmodells der Teilchenphysik. Es wird dabei der Ansatz verfolgt, mit Hilfe sehr hoher Teilchenraten mögliche Hinweise für sogenannte Neue Physik zu finden. Das Experiment wird am Mainz Energy Recovery Superconducting Accelerator (MESA) stattfinden, der einen zeitlich abwechselnd polarisierten Elektronenstrahl bei 150 µA Intensität und 150 MeV Energie mit hervorragender Stabilität bereitstellen wird. Die paritätsverletzende Asymmetrie wird mit integrierenden Cherenkov-Detektoren gemessen. Zudem wird ein Spurdetektor entwickelt, der für die Messung des Viererimpulsübertrages der Elektronen im Flüssigwasserstofftarget vorgesehen ist. Die Rekonstruktion einzelner Elektronentrajektorien wird zudem auch für systematische Untersuchungen verwendet. Um das Material im Detektor und somit Vielfachstreuung zu minimieren, werden neuartige High Voltage Monolithic Active Pixel Sensoren (HV-MAPS) verwendet. Eine der größten Herausforderungen bei der Entwicklung des Spurdetektors stellt die weitgehende Minimierung des Materials für die Infrastruktur, die für die mechanische Fixierung, die Stromzufuhr, die Auslese und die Kühlung der Sensoren benötigt wird, dar. Zudem ist die Rate von 0.1 THz an gestreuten Elektronen innerhalb der Akzeptanz des Detektors anspruchsvoll für das Auslesesystem und die Strahlenhärte aller verwendeten Komponenten.

In dieser Arbeit werden Machbarkeitsstudien zum Spurdetektor für das P2 Experiment vorgestellt. Im ersten Teil werden die erwarteten Signal- und Untergrundraten sowie die gesamte Strahlenbelastung auf der Basis einer detaillierten GEANT4 Monte Carlo Simulation abgeschätzt. Photonen stellen hierbei den häufigsten Untergrundtyp dar. Die Detektionswahrscheinlichkeit von Photonen wurde daher zudem in experimentellen Versuchen untersucht.

Die Entwicklung der technischen Ausführung eines Detektormodules stellt den zweiten Schwerpunkt dieser Arbeit dar. Der komplette Spurdetektor wird aus acht identischen Modulen bestehen, wovon jedes etwa 630 Sensoren mit einer Fläche von 2 cm × 2 cm beinhaltet, die auf zwei Ebenen angeordnet sind. Die Umsetzbarkeit des technischen Konzeptes wurde durch die Konstruktion eines thermo-mechanischen Prototypen gezeigt. Auf diesem Prototyp werden die Sensoren durch heizbare Kupferbahnen auf Polyimidfolie imitiert. Das Kühlkonzept für den P2 Spurdetektor sieht vor, die Sensoren mit gasförmigem Helium zu kühlen. Dieses Konzept wurde mit numerischen Strömungssimulationen untersucht und in das vorgestellte technische Konzept eingearbeitet. Der zusammengebaute Prototyp wird es daher ermöglichen, die Kühlungssimulationen mit experimentellen Tests zu vergleichen.

Contents

Part I.

Introduction

1 Introduction

Over the past century, huge progress has been achieved in our understanding of the universe. Our experimental knowledge is today best described by the Standard Model of Particle Physics (SM). The predictions of the SM agree to the observations of numerous particle physics experiments at a remarkably high level of precision. It is today clear that the SM as a theory of nature is at least an excellent approximation down to a distance scale of 1×10^{-16} cm. With the discovery of the Higgs Boson, announced in 2012 by the ATLAS[1] and CMS[2] experiments [1, 2], both placed at the Large Hadron Collider (LHC), all elementary particles included in the SM have been directly or indirectly observed in experiments. All properties of the Higgs boson predicted by the SM so far agree with the measured properties of the detected particle.

Although the SM succeeds to describe almost all phenomena observed with ordinary matter, several observations expose that the SM is an incomplete description of the universe. For example, it does not explain the abundance of dark matter and dark energy, which together make up about 95% of the universe [3]. The composition of dark matter remains a mystery and thus motivates plenty of ongoing and planned particle physics experiments. Furthermore, another example of observed phenomena which are not described within the SM is the evidence of neutrino oscillations obtained in various experiments [4–6]. It shows that neutrinos have a finite mass, although being considered massless in the SM. Finally, the SM does not explain the matter-antimatter asymmetry in the universe and it does not include gravity. As a consequence, there is a quest for Physics beyond the SM, so-called *New Physics*, in order to solve these and some further observed discrepancies.

There are several experiments planned or already running that search for New Physics.

[1] **A** **T**oroidal **L**HC **A**pparatu**S**

[2] Compact **M**uon Solenoid

With two colliding proton beams at 14 TeV, the LHC today provides the highest center of mass energy of all present particle accelerators. Consequently, the experiments placed at the LHC can look for new phenomena emerging at the TeV scale which were not detectable with past experiments at lower energies. However, the energy frontier is not the only possible way to find New Physics. The presence of Physics beyond the SM, which is supposed to manifest itself mainly at energies at or above the TeV scale, is expected to cause tiny deviations from the predictions of the SM even at lower energy scales, so that very precise experiments might be able to detect these anomalies. The detection of such small discrepancies usually requires very high statistics and therefore very many particle interactions. Such precision experiments therefore feature very high beam intensities. This way to search for New Physics is therefore often designated as the intensity frontier. In addition, another promising approach to gain further insight to the composition of the universe is represented by cosmic particle physics experiments.

The MESA[3] beam facility [7–9] which is currently under construction in Mainz will offer perfect conditions for precision tests of the SM using an intense electron beam. It will offer an energy recovery mode in which a windowless gas target is used so that it is possible to reuse the energy of electrons that did not interact considerably in the target. The gas target and a spectrometer detector system are the main parts of the MAGIX experiment [10, 11]. The MAGIX experiment will offer a high luminosity and and excellent resolution. It will enable a wide physics program in hadron and nuclear physics, including for example the search for dark photons or measurements on the magnetic radius of the proton.

The P2 experiment [12–14] is the second high precision experiment which will be placed at MESA. For this experiment, an electron beam with alternating polarization is extracted and directed on a liquid hydrogen target. The setup gives the possibility to measure the parity violating asymmetry in elastic electron-proton scattering with high precision. The measurement can be used to determine the weak mixing angle, a fundamental parameter in the Standard Model. Extensions of the SM predict slightly different values of this parameter, so that the P2 experiment tests these kinds of theory models. In addition, the setup can be used to measure parity violating asymmetries with different target materials, promising to provide further insights on nucleon density distributions [15].

This thesis presents investigations on the tracking detector for the P2 experiment. The main purpose of the tracking detector which will be installed in the P2 detector is the reconstruction of the electron momentum transfer inside the liquid hydrogen target. The tracking of individual electron trajectories will also help to detect systematic deviations of operational parameters as for example the beam position. The

[3] **M**ainz **E**nergy **R**ecovery **S**uperconducting **A**ccelerator

work on the tracking detector presented here focuses on background estimation studies based on Monte Carlo simulations and the development of the technical design.

The structure of this text is as follows: In the introductory part, the role of the weak mixing angle in the Standard Model of particle physics is discussed as theoretical background in chapter 2, before the basic concept of the P2 experiment and its tracking detector are described in chapter 3. The second part focuses on simulation studies concerning the tracking detector. The simulation setup is presented in chapter 4, followed by studies on the signal and background rates in chapter 5. Photons are the most abundant background type, which is why their detection was further tested experimentally, as described in chapter 6. The third part is dedicated to the actual construction of the tracking detector modules. The technical design presented in chapter 7. The tracking detector will be built with active pixel sensors, which need to be cooled. The feasibility of the cooling concept based on gaseous helium is investigated in computational fluid dynamics simulations which are discussed in chapter 8. In order to test the practicability of the technical design and its detector components, a thermo-mechanical prototype is constructed. These developments are presented in chapter 9. The thesis then finishes with conclusions and an outlook in chapter 10.

2 The Weak Mixing Angle θ_W in the Standard Model of Particle Physics

Elementary particle physics addresses the question of what the universe is made of. The most fundamental constituents of matter in the universe do not have any substructure and are therefore called elementary particles. Which types of elementary particles exist and how they interact is presently best described by the Standard Model of Particle Physics (SM). The following section will introduce the basic building blocks of this theory. The subsequent sections address the theory aspects which are most relevant for the P2 experiment, in particular the weak mixing angle θ_w as a fundamental parameter in the electroweak theory and its measurement via electron-proton scattering. The contents of this section are based on the references given within the text.

2.1. Introduction to the Standard Model

The Standard Model of Particle Physics was developed over the past century as a striking interplay between experiment and theory. Unexpected experimental observations like the photo-effect [16, 17] or P- and CP-violation [18, 19] were explained by evolving theoretical models, and the predictions of those models were subsequently confirmed by even more sophisticated experiments, such as the recent discovery of the Higgs boson at the Large Hadron Collider (LHC) [1, 2].

The elementary particles included in the SM are depicted schematically in figure 2.1. Since the SM is a quantum field theory, elementary particles can be categorized according to their quantum numbers. The first group of elementary particles are the matter particles, which form the matter in the universe. They all have spin 1/2. Since this is a half-integer spin, they belong to the group of *fermions*. Important features of fermions are that they follow the Pauli exclusion principle and obey Fermi-Dirac

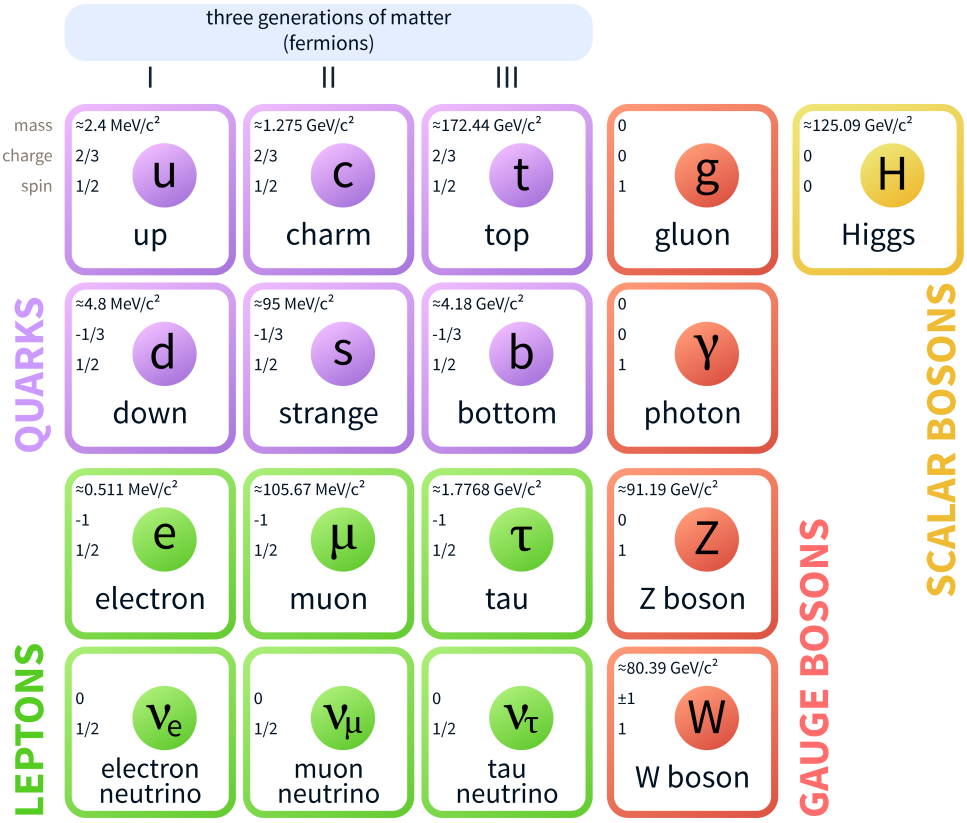

Figure 2.1.: *Particles in the Standard Model of Particle Physics. Based on figure taken from Ref. [20].*

statistics. Note that for each massive matter particle shown in figure 2.1, there is a corresponding anti-particle which has opposite charges while all other properties are identical. The elementary fermions are further subdivided into *leptons* and *quarks* according to their electric charges and color charges. Leptons do not carry color charge. They come in three different generations, or lepton *flavors*, differing only in the particle masses. For each generation, there is a lepton with integer electric charge (electron, muon and tau lepton) and the corresponding uncharged neutrino. As mentioned before, the SM neutrinos are considered to be massless, however, experimental evidence for finite neutrino masses was found already more than 20 years ago [4]. Quarks are fermions that carry both color charge and electric charge. Similar to the leptons, there are three different generations with different quark masses and two quarks per generation with different electric charge. The particle masses and their quantum numbers spin and electric charge are also given in figure 2.1.

The three fundamental forces between the matter particles are themselves implemented in the SM by the exchange of particles. The exchanged particles have integer spin and are therefore *bosons*. The strong force is mediated by massless gluons. Glu-

ons couple to all color charged particles and have a color charge themselves. That means that quarks participate in the strong interaction while leptons do not. Gluons and quarks always form color neutral bound states. The strong force is therefore only relevant at short distances $\leq O(10^{-15}\text{m})$, at which it is about two orders of magnitude stronger than the electromagnetic force. For the electromagnetic force, the photon serves as the exchange particle. Since the photon is massless and has no charge, the range of the force is infinite, but its strength decreases with the distance squared. The third fundamental interaction in the SM, the weak force, has three different exchange particles, namely the neutral Z-boson and the charged $W^{\pm}$-bosons. In contrast to photons and gluons, the exchange bosons of the weak force have masses at the 100 GeV scale. Therefore, the weak force only takes place at subatomic distances. Its field strength at given distances is typically several orders of magnitudes less than that of the electromagnetic or strong interaction. Nevertheless, it plays an important role since many processes can not be mediated by gluons or photons. One example is the muon decay to an electron and two neutrinos.

The Higgs boson is the only elementary particle with zero spin, which makes it a scalar boson. In order to incorporate particle masses to the SM, especially the massive weak exchange bosons, the Higgs mechanism [21–26] was developed in the 1960's. In this formalism, particle masses are generated by the interaction with a Higgs field penetrating all of space. This field comes with an additional particle, the Higgs boson. The experimental confirmation of this theory took several decades and was obtained only recently with the detection of the Higgs boson at LHC [1, 2].

There is much evidence that the three generations of matter make up the visible matter in the universe and that there is no fourth one [27]. The masses of the matter particles and the Higgs boson mass are empiric parameters, meaning that these ten parameters are not predicted by the theory but are free parameters. This also holds true for the three coupling constants of the fundamental forces in the SM. In total, there are nineteen free parameters in the SM (if neutrinos are massless), however, different sets of independent free parameters are possible so that their choice is arbitrary. The inclusion of massive neutrinos requires to add another seven free parameters to the SM.

The forces in the SM can not only change a particle's momentum, as it would be in classical mechanics, but also alter other properties and therefore yield different final state particles. However, in addition to energy and momentum conservation, there are several conserved quantities which must be the same for the particle system in the initial and in the final state. One quantity that is always conserved is the total electric charge Q of the system. According to Noether's theorem [28], a conserved quantity is linked to a symmetry of the underlying physics. In the case of charge conservation, this symmetry is given by the global gauge invariance of the electromagnetic field.

The SM is a gauge theory and therefore its Lagrangian has to be invariant even under local gauge transformations, which will be discussed further in sections 2.2 and 2.4.

The weak isospin I_3 is another conserved quantum number. For fermions, it depends on the chirality (see section 2.3) of the fermion. Leptons with negative chirality and (in the same way) anti-fermions with positive chirality can be grouped into weak isospin doublets φ_L with $I_3 = \pm\frac{1}{2}$ in the following way:

$$I_3 \begin{matrix} +\frac{1}{2} \\ -\frac{1}{2} \end{matrix} \quad \begin{pmatrix} \nu_e \\ e \end{pmatrix}, \begin{pmatrix} \nu_\mu \\ \mu \end{pmatrix}, \begin{pmatrix} \nu_\tau \\ \tau \end{pmatrix} \quad . \tag{2.1}$$

Quarks can also be grouped into isospin doublets, however, it has to be considered that the quark mass eigenstates q are not the eigenstates q' of the weak isospin operator, but related by the Cabibbo-Kobayashi-Maskawa matrix V_{CKM} [29, 30]:

$$\begin{pmatrix} d' \\ s' \\ b' \end{pmatrix} = \begin{pmatrix} V_{ud} & V_{us} & V_{ub} \\ V_{cd} & V_{cs} & V_{cb} \\ V_{td} & V_{ts} & V_{tb} \end{pmatrix} \cdot \begin{pmatrix} d \\ s \\ b \end{pmatrix} \tag{2.2}$$

The weak isospin quark doublets φ_L then read

$$I_3 \begin{matrix} +\frac{1}{2} \\ -\frac{1}{2} \end{matrix} \quad \begin{pmatrix} u \\ d' \end{pmatrix}, \begin{pmatrix} c \\ s' \end{pmatrix}, \begin{pmatrix} t \\ b' \end{pmatrix} \quad . \tag{2.3}$$

All fermion isospin doublets behave in the same way under the weak force. Fermions with positive chirality and anti-fermions with negative chirality are weak isospin singlets $I_3 = 0$. They do not interact weakly, which also means that there are no neutrinos with positive chirality or anti-neutrinos with negative chirality present in the SM since they would not interact at all.

Further conserved quantities are the lepton flavor and quark flavor numbers. As seen before, there are three different lepton flavors (electron, muon, tau lepton) and six different quark flavors (up, down, charm, strange, top, bottom). The number of particles of each flavor is strictly conserved under the strong and under the electromagnetic force. Lepton flavor violation has so far only be found experimentally in neutrino oscillations, which are not part of the SM. The search for lepton flavor violation in the massive sector is therefore ongoing research. The quark flavor is not conserved in the weak interaction. The reason for that are the different mass and weak isospin eigenstates for the quarks, as seen in equation 2.2. The elements of the CKM-matrix correspond to the additional coupling factor between quarks of the flavors given in the indices, so for example V_{ud} gives the coupling $u \leftrightarrow d$ in the weak interaction.

2.2. Quantum electrodynamics (QED)

Quantum electrodynamics (QED) is the theory describing the interaction of relativistic charged particles via the electromagnetic force. The elementary matter particles are fermions, while the photon is a massless boson. Therefore, we search for a theory that describes spin-$\frac{1}{2}$-particles which interact by the exchange of a massless spin-1-particle. Any quantum field theory can be described in the Lagrangian formalism. In this section, the Lagrangian of QED is constructed starting with the Lagrangian for free fermions and then demanding local gauge invariance. This procedure serves as a template for the construction of the electroweak Lagrangian in section 2.4, which will then lead to the definition of the weak mixing angle θ_w. Both sections aim to give only a short outline on the mathematical formulation of the electroweak part of the SM in order to introduce all quantities necessary to understand the motivation and measurement principle of the P2 experiment. A more detailed description and derivation of all the formulas given in the following sections in this chapter can be found in several particle physics textbooks, as for example Ref.s [31–34], which were used as input for this text. There one can also find the definition of several quantities which are used in the following and considered to be known like the Dirac spinor ψ or the gamma matrices γ^μ.

The Dirac equation is the relativistic wave equation of a fundamental fermion with mass m:

$$\left(i\,\gamma^\mu\partial_\mu - m\right)\psi = 0. \tag{2.4}$$

The corresponding Lagrangian for free fermion fields reads

$$\mathcal{L} = i\overline{\psi}\gamma^\mu\partial_\mu\psi - m\overline{\psi}\psi. \tag{2.5}$$

It can be shown quite easily that the Dirac equation in 2.4 is obtained from this Lagrangian by applying the Euler-Lagrange equation to $\overline{\psi}$. Since QED is a gauge theory and its symmetry group is U(1), the QED Lagrangian and the derived wave equation are demanded to be invariant under local phase transitions of the fermion fields

$$\psi \rightarrow \psi' = e^{-iq\theta(x)}\psi \tag{2.6}$$

with $\theta(x)$ a space-time dependent phase factor and q the electric charge. However, the free Lagrangian in 2.5 is not invariant under such phase transitions, but transforms like

$$\mathcal{L} \rightarrow \mathcal{L}' = \mathcal{L} + \left(q\overline{\psi}\gamma^\mu\psi\right)\partial_\mu\theta(x). \tag{2.7}$$

Local gauge invariance can be achieved by adding some additional vector field A_μ to

the Lagrangian, if this field transforms as

$$A_\mu \rightarrow A'_\mu = A_\mu + \partial_\mu \theta(x). \tag{2.8}$$

With this new field A_μ, the locally gauge invariant Lagrangian becomes

$$\mathcal{L} = i\overline{\psi}\gamma^\mu \partial_\mu \psi - m\overline{\psi}\psi - \left(q\overline{\psi}\gamma^\mu \psi\right) A_\mu = i\overline{\psi}\gamma^\mu \mathcal{D}_\mu \psi - m\overline{\psi}\psi \tag{2.9}$$

with $\mathcal{D}_\mu = \partial_\mu + iqA_\mu$ the covariant derivative. Consequently, all what was needed to ensure local gauge invariance was to replace ∂_μ by the covariant derivative $\mathcal{D}_\mu$. However, the Lagrangian in equation 2.9 is still not the complete QED Lagrangian since it does not include any term for a free particle that must be connected to the newly introduced field A_μ. The only candidate for such a particle in QED is the photon, which is a boson. The Lagrange density for a spin-1 particle with mass m is given by the Proca Lagrangian

$$\mathcal{L} = -\frac{1}{4}F^{\mu\nu}F_{\mu\nu} + \frac{1}{2}m^2 A^\nu A_\nu \tag{2.10}$$

with the field tensor $F^{\mu\nu} = (\partial^\mu A^\nu - \partial^\nu A^\mu)$. The first term fulfills local gauge invariance under U(1) symmetry, however, the mass term does not. Nevertheless, since the photon is massless, this term vanishes and the complete gauge invariant QED Lagrange density results in

$$\mathcal{L}_{\text{QED}} = i\overline{\psi}\gamma^\mu \mathcal{D}_\mu \psi - m\overline{\psi}\psi - \frac{1}{4}F^{\mu\nu}F_{\mu\nu} \tag{2.11}$$

and describes fermions in an electromagnetic field.

2.3. Helicity and Chirality

The electromagnetic field couples to all particles proportionally to their electric charge. In order to describe processes involving the weak force, however, the concepts of helicity and chirality need to be introduced first.

The helicity h of a particle is defined as the projection of its spin on its three-momentum vector $\mathbf{p}$ (with the notation $\mathbf{p} \equiv |\vec{p}|$):

$$h \equiv \frac{\mathbf{S} \cdot \mathbf{p}}{p} \tag{2.12}$$

with the spin vector $\mathbf{S}$. In Dirac space, the helicity operator acting on a Dirac spinor

becomes

$$\hat{h} = \frac{1}{2p}\begin{pmatrix} \boldsymbol{\sigma}\cdot\hat{\mathbf{p}} & 0 \\ 0 & \boldsymbol{\sigma}\cdot\hat{\mathbf{p}} \end{pmatrix} \tag{2.13}$$

with the three Pauli matrices $\boldsymbol{\sigma}$ and the momentum operator $\hat{\mathbf{p}} = -i\boldsymbol{\nabla}$. For a spin-half-particle, the eigenvalues of the helicity operator are $\pm\frac{1}{2}$. Hence, there are two possible helicity states for a fundamental fermion, positive and negative helicity. With the helicity projection operators

$$\mathcal{P}_{\pm} = \frac{\mathbb{1}_4 \pm \hat{h}}{2}, \tag{2.14}$$

any Dirac spinor ψ can be written as the sum of its helicity eigenstates

$$\psi = \mathcal{P}_+\,\psi + \mathcal{P}_-\,\psi \equiv \psi_+ + \psi_-. \tag{2.15}$$

In contrast to the spin operator S_z (with some externally defined z-axis), the helicity operator commutes with the free particle Dirac Hamiltonian, meaning that helicity is a conserved quantity along the motion of a particle. More over, it is a conserved quantity within the interaction of particles, which makes it an important concept in particle physics. Nevertheless, it is not Lorentz-invariant for massive particles, as one can always find a Lorentz-transformation for them which flips the direction of the particle, but leaves the spin direction unchanged.

Chirality instead is a Lorentz-invariant concept. It is a purely quantum mechanical phenomenon and hence does not have any simple physical interpretation. The chirality operator is given by the matix

$$\gamma^5 = i\gamma^0\gamma^1\gamma^2\gamma^3 = \begin{pmatrix} 0 & \mathbb{1}_2 \\ \mathbb{1}_2 & 0 \end{pmatrix}. \qquad \text{(Dirac-Pauli representation)} \tag{2.16}$$

The eigenvalues of the chirality operator are ± 1. Particles with negative chirality are often labeled as *left-handed*, particles with positive chirality as *right-handed*[1]. For massive particles, the representing Dirac spinor always has a left-chiral and a right-chiral component and is therefore no eigenvector of the chirality operator by itself. It is indeed possible to decompose the Dirac spinor into its chiral components using the chiral projection operators

$$\mathcal{P}_R = \frac{1}{2}\left(1+\gamma^5\right) \quad \text{and} \quad \mathcal{P}_L = \frac{1}{2}\left(1-\gamma^5\right) \tag{2.17}$$

[1] Unfortunately, the terms left- and right-handed are sometimes also used for particles with negative and positive helicity, respectively. In this chapter, the handedness of a particle always refers to its chirality state if not explicitly stated otherwise.

such that

$$\psi = \mathcal{P}_L\,\psi + \mathcal{P}_R\,\psi \equiv \psi_L + \psi_R. \tag{2.18}$$

Unlike the helicity of a particle, chirality is not conserved in time. This is on the first glance surprising since it was shown already in section 2.1 that changing the chirality of a particle also changes its weak isospin, which is a conserved quantity. The solution for this puzzle is the continuous interaction of massive particles with the Higgs field that breaks the isospin symmetry.

Although helicity and chirality are different concepts, the eigenstates are the same for massless fermions. The right-chiral component of the Dirac spinor vanishes so that massless fermions are always purely left-handed and have negative helicity. In the same way, massless anti-fermions are always purely right-handed and have positive helicity. For massive fermions, helicity and chirality are different, but not completely independent of each other. For example, taking a spin-half fermion with positive helicity, it can be shown that its Dirac spinor ψ_+ expressed in terms of its chiral components ψ_R and ψ_L gives

$$\psi_+ \propto \left(\frac{1+\kappa}{2}\right)\psi_R + \left(\frac{1-\kappa}{2}\right)\psi_L \quad \text{with} \quad \kappa = \frac{p}{E+m}\,. \tag{2.19}$$

The probability to find such a particle in a left-handed state is therefore proportional to $(1-\kappa)^2$ and vanishes in the limit $E \gg m$.

The weak force distinguishes between left-handed and right-handed particles, as described in the following sections. In order to test this chiral structure of the SM experimentally, the helicity of particles needs to be manipulated. It is not possible to prepare massive particles in a defined chirality state because it is not conserved in time. Nevertheless, by knowing the energy and momentum of a particle in a defined helicity state, the probability for it to be in a particular chirality state can be evaluated.

2.4. Electroweak Theory at Tree Level

The electroweak theory describes the electromagnetic and the weak force in a unified way as the electroweak force. It was formulated in the 1960's by Glashow, Salam and Weinberg [35–37] and is therefore often referred to as the GSW model.

The underlying gauge symmetry group of the GSW model is $U(1)_Y \times SU(2)_L$. The subscript Y refers to the weak hypercharge, which is the generator of the $U(1)_Y$ group.

It can be related to the electric charge (operator) Q and the third weak isospin (operator) component I_3 via the Gell-Mann-Nishijima formula

$$Y = 2Q - 2I_3. \tag{2.20}$$

The subscript L for the $SU(2)_L$ group indicates that only left-handed fermions couple to weak isospin currents. In order to describe the chiral structure of the weak force, it is helpful to use equation 2.18 and to write the Lagrange density decomposed to the chiral components of the Dirac spinor. The Lagrangian for free fermion fields in equation 2.5 then becomes

$$\mathcal{L} = \overline{\psi}_L \left(i\gamma^\mu \partial_\mu - m \right) \psi_L + \overline{\psi}_R \left(i\gamma^\mu \partial_\mu - m \right) \psi_R. \tag{2.21}$$

Left-handed particles can be written as isospin doublets φ_L, as it was shown in equations 2.1 and 2.3. In order to fulfill the demand of local gauge invariance, the Lagrange density needs to be invariant under local SU(2) phase transformations of the left-handed doublets, which read

$$\varphi_L \rightarrow \varphi'_L = \exp\left[i \frac{g}{2} \boldsymbol{\sigma} \cdot \boldsymbol{\alpha}(x) \right] \varphi_L. \tag{2.22}$$

The three Pauli matrices $\boldsymbol{\sigma}$ are the generators of the SU(2) group, multiplied by some new coupling constant g, and $\boldsymbol{\alpha}(x)$ is a three-dimensional function specifying the space-time dependent local phase. In order to make the Lagrangian in equation 2.21 gauge invariant, new vector fields must be introduced analogous to the previously discussed electromagnetic case. However, in contrast to QED, this time three vector fields $W_1^\mu, W_2^\mu, W_3^\mu$ need to be introduced. The derivative for the terms involving left-chiral fields must then be replaced by the covariant derivative:

$$\partial^\mu \rightarrow D_L^\mu = \partial^\mu + i \frac{g}{2} \boldsymbol{\sigma} \cdot \mathbf{W}^\mu. \tag{2.23}$$

In addition, local gauge invariance must also hold for $U(1)_Y$ phase transitions of both the left-chiral weak isospin doublets φ_L and the right-chiral weak isospin singlets φ_R:

$$\varphi_L \rightarrow \varphi'_L = \exp\left(i \frac{g'}{2} Y \, \beta(x) \right) \varphi_L \tag{2.24}$$

$$\varphi_R \rightarrow \varphi'_R = \exp\left(i \frac{g'}{2} Y \, \beta(x) \right) \varphi_R \tag{2.25}$$

with another space-time dependent phase factor $\beta(x)$ and a new coupling constant g'. Gauge invariance under $U(1)_Y$ transformations therefore requires the introduction

of one more vector field B^μ. The complete covariant derivatives ensuring local gauge invariance under $U(1)_Y \times SU(2)_L$ symmetry then become

$$\partial^\mu \rightarrow D_R^\mu = \partial^\mu + i\frac{g'}{2} Y B^\mu \tag{2.26}$$

for the right-handed field terms and

$$\partial^\mu \rightarrow D_L^\mu = \partial^\mu + i\frac{g}{2}\boldsymbol{\sigma} \cdot \mathbf{W}^\mu + i\frac{g'}{2} Y B^\mu \tag{2.27}$$

for the left-handed field terms. Inserting these covariant derivatives into the Lagrangian in equation 2.21 and adding terms for the self-interactions and kinematic energy of the newly introduced fields results in

$$\mathcal{L} = \overline{\varphi}_L \left(i\gamma^\mu \mathcal{D}_\mu^L - m \right) \varphi_L + \overline{\psi}_R \left(i\gamma^\mu \mathcal{D}_\mu^R - m \right) \psi_R - \frac{1}{4}\mathbf{W}_{\mu\nu}\mathbf{W}^{\mu\nu} - \frac{1}{4} B_{\mu\nu} B^{\mu\nu} \tag{2.28}$$

with the field tensors

$$W_{\mu\nu}^i = \partial_\mu W_\nu^i - \partial_\nu W_\mu^i - g\epsilon_{ijk} W_\mu^j W_\nu^k \tag{2.29}$$

$$B_{\mu\nu} = \partial_\mu B_\nu - \partial_\nu B_\mu. \tag{2.30}$$

However, it turns out that this Lagrangian is only gauge invariant for the case of $m = 0$ for all fermion fields. In addition, it does not account for any mass of the gauge bosons in the weak interaction. This contradiction to the experimental observations is in the SM resolved by adding the Higgs mechanism. For the further discussion of the theory aspects with regard to the P2 experiment, the mass problem is not of particular relevance and therefore omitted here. The Lagrangian in equation 2.28 includes the fermion coupling terms which are necessary for the further discussion and the introduction of the weak mixing angle.

2.4.1. The Weak Mixing Angle θ_{w}

The easiest way to assign the four fields with the observed gauge bosons is to identify the fields $\mathbf{W}^\mu$ with the W^+-, W^-- and Z-boson fields and the field B^μ with the photon field. It can however be seen quite easily that this assignment is not realized in nature. First, it would imply that the Z-boson only couples to left-handed particles, which is in contradiction to experimental observations. In addition, the photon does not couple to the neutrinos, but the B^μ field does according to the Lagrangian above. Hence, the observable fields must be mixtures of the $\mathbf{W}^\mu$ fields and the B^μ field. The actual composition of the physical fields can be derived in a formal way from the Higgs mechanism. Having said that, the field mixtures can also be motivated by the

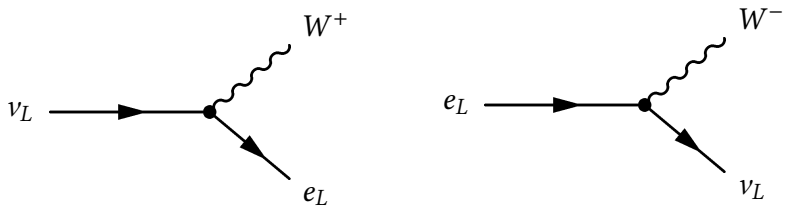

Figure 2.2.: *Feynman graphs for the transitions in the electron weak isospin doublet via the weak charged current interaction. Time axis from left to right.*

experimentally observed couplings of the gauge bosons. These couplings must be reproduced by the electroweak theory.

For example, one can consider the transitions in the electron weak isospin doublet, which are realized by interactions with the $W^{\pm}$ bosons, as shown in figure 2.2. In the weak isospin space, the isospin is increased or lowered by the action of the raising operator σ^+ or the lowering operator σ^-, respectively. The action of the $\sigma^{\pm}$ operator can be associated with the absorption of a $W^{\pm}$-boson or with the emission of a $W^{\mp}$-boson. The two operators can be written in terms of the Pauli matrices $\boldsymbol{\sigma}$

$$\sigma^+ = \tfrac{1}{2}\left(\sigma_1 + i\sigma_2\right) , \quad \sigma^- = \tfrac{1}{2}\left(\sigma_1 - i\sigma_2\right) . \tag{2.31}$$

Considering the Dirac probability current j^μ, the weak currents $j_i^\mu = \frac{g}{2}\overline{\varphi}_L \gamma^\mu \sigma_i \varphi_L$ in the first term of the Lagrangian in equation 2.28 can be written

$$\mathbf{j}^\mu \cdot \mathbf{W}_\mu = j_1^\mu W_\mu^1 + j_2^\mu W_\mu^2 + j_3^\mu W_\mu^3 = j_+^\mu W_\mu^+ + j_-^\mu W_\mu^- + j_3^\mu W_\mu^3 \tag{2.32}$$

with the weak charged currents $j_\pm^\mu = \frac{1}{\sqrt{2}}\left(j_1^\mu \pm i j_2^\mu\right)$ and the identification of the physical W-bosons as the linear combinations

$$W_\mu^\pm = \frac{1}{\sqrt{2}}\left(W_\mu^1 \mp i W_\mu^2\right) . \tag{2.33}$$

The current j_+^μ corresponds to the absorption of a W^+- or the emission of a W^--boson (see figure 2.2) and can then be evaluated for any fermion doublet. For the electron doublet φ_L as an example, the probability current is

$$j_+^\mu = \frac{g}{\sqrt{2}}\overline{\varphi}_L \gamma^\mu \sigma_+ \varphi_L = \frac{g}{\sqrt{2}}\overline{\nu}_L \gamma^\mu e_L , \tag{2.34}$$

and similarly it can be derived that

$$j_-^\mu = \frac{g}{\sqrt{2}}\overline{\varphi}_L \gamma^\mu \sigma_- \varphi_L = \frac{g}{\sqrt{2}}\overline{e}_L \gamma^\mu \nu_L \tag{2.35}$$

for the absorption of a W^-- or the emission of a W^+-boson. Here, ν_L and e_L denote the dirac spinors for a left-handed electron-neutrino and a left-handed electron, respectively.

Since the $W^\pm$ boson fields are composed of the fields W_1^μ and W_2^μ, the photon field A^μ and the Z-boson field Z^μ must be composed of the fields W_3^μ and B^μ. Without any further assumption, A^μ can therefore be parametrized as $A^\mu = \alpha W_3^\mu + \beta B^\mu$ with $\alpha, \beta \in \mathbb{C}$. The current of a photon coupling to a neutrino can be calculated with the covariant derivative in equation 2.27 entering the Lagrange density in equation 2.28:

$$j_{\text{em}}^\mu = \overline{\nu}_L \left(\alpha \frac{g}{2} \gamma^\mu \sigma_3 - \beta \frac{g'}{2} \gamma^\mu \right) \nu_L = \frac{1}{2} \overline{\nu}_L \gamma^\mu \left(\alpha g - \beta g' \right) \nu_L \text{ with } \sigma_3 \cdot \nu_L = \nu_L \tag{2.36}$$

This current has to equal zero so the terms in the brackets need to cancel out. With the additional normalization condition $\alpha^2 + \beta^2 = 1$, this leads to the result

$$\beta = \frac{g}{\sqrt{g^2 + g'^2}}. \tag{2.37}$$

Seeing that α and β turn out as real parameters, the *weak mixing angle* θ_w is introduced such that $\alpha = \sin\theta_w$ and $\beta = \cos\theta_w$. Consequently, θ_w can be defined via the relations

$$\cos\theta_w = \frac{g}{\sqrt{g^2 + g'^2}} \tag{2.38}$$

$$\sin\theta_w = \frac{g'}{\sqrt{g^2 + g'^2}}. \tag{2.39}$$

The weak mixing angle is a key parameter in the electroweak theory and so in the SM since it quantifies the mixing of the neutral fields of the $U(1)_Y$ and $SU(2)_L$ symmetries. The linear combinations of the photon and the Z-boson thus are

$$A_\mu = +B_\mu \cos\theta_w + W_\mu^3 \sin\theta_w \tag{2.40}$$

$$Z_\mu = -B_\mu \sin\theta_w + W_\mu^3 \cos\theta_w. \tag{2.41}$$

Next to the vanishing coupling of the photon to neutrinos, the electroweak theory also needs to reproduce the coupling of the photon to the electron as it is predicted by QED. It must be the same both for left- and right-handed electrons, since QED does not distinguish them. The current for the electromagnetic interaction can anyway be written in terms of the chiral components of the electron, e_L and e_R. It then becomes (see the QED Lagrange densitiy in equation 2.11)

$$j_{\text{em}}^\mu = \overline{e} \left(q\gamma^\mu \right) e = \overline{e}_L \left(q\gamma^\mu \right) e_L + \overline{e}_R \left(q\gamma^\mu \right) e_R \tag{2.42}$$

with the electric charge of the electron $q = -e$. Calculating the same quantity by using the electroweak Lagrange density in equation 2.28 and by inserting the photon field composition in equation 2.40 yields

$$j^{\mu}_{\text{em}} = \overline{e}_L \left(-\frac{g}{2} \sin\theta_w \, \gamma^{\mu} - \frac{g'}{2} \cos\theta_w \, \gamma^{\mu} \right) e_L - \overline{e}_R \left(g' \cos\theta_w \, \gamma^{\mu} \right) e_R. \tag{2.43}$$

Hence, the electromagnetic and the two electroweak couplings are related by the weak mixing angle:

$$e = g \sin\theta_w = g' \cos\theta_w. \tag{2.44}$$

These relations between the weak mixing angle and the coupling constants are equivalent to a relation of the weak mixing angle to the masses of the weak gauge bosons, as it can be derived from the Higgs mechanism. With the mass m_W of the $W^{\pm}$-bosons and m_Z as the mass of the Z-boson, the weak mixing angle θ_w can be related to them via

$$\sin^2\theta_w = 1 - \left(\frac{m_W}{m_Z} \right)^2. \tag{2.45}$$

The masses of the gauge bosons can be measured quite precisely, so that this relation allows for the most precise determination of $\sin^2\theta_w$. The current best value for the so-defined weak mixing angle is $\sin^2\theta_w = 0.2223(21)$ [38].

It is very important to notice that the discussions and relations of the weak mixing angle derived in this section are only valid at tree-level, meaning that they do not consider higher order (loop) corrections. A precise test of the SM is certainly only possible factoring in these corrections, which means that the theory needs to be renormalized. The necessity of renormalization and the consequences for a consistent and handy definition of the weak mixing angle are outlined in section 2.5.

2.4.2. The Neutral Weak Current and Weak Charges

The mixture of the electroweak fields is one of the key features of the electroweak theory. Whereas the $W^{\pm}$-bosons exclusively couple to left-handed particles, the Z-boson couples to both left- and right handed particles, but not with equal strength. The relative coupling strengths are determined by the weak mixing angle. According to the Lagrangian in equation 2.28 and the Z-field-mixture in equation 2.41, the fermion neutral weak current is at tree-level given by

$$j^{\mu}_{Z} = \overline{\varphi}_L \, \gamma^{\mu} \left(-\frac{g'}{2} Y \sin\theta_w + \frac{g}{2} \sigma^3 \cos\theta_w \right) \varphi_L - \overline{\psi}_R \, \gamma^{\mu} \left(\frac{g'}{2} Y \sin\theta_w \right) \psi_R. \tag{2.46}$$

The operator $\sigma^3/2$ can be identified as the weak isospin operator I_3. The term for the left-handed isospin doublets φ_L can be written component-wise, so that for any particular fermion and its chiral states u_L and u_R, the current for the interaction with the Z-boson becomes

$$j_Z^\mu = \overline{u}_L \gamma^\mu \left(-\frac{g'}{2} Y \sin\theta_w + I_3 \, g \cos\theta_w \right) u_L - \overline{u}_R \gamma^\mu \left(\frac{g'}{2} Y \sin\theta_w \right) u_R. \tag{2.47}$$

The weak hypercharge operator Y can be replaced according to equation 2.20 by the charge operator Q and the weak isospin operator I_3. In addition, the coupling constant g' can be replaced using $g' = g \tan\theta_w$, see equation 2.44, and hence

$$j_Z^\mu = \overline{u}_L \gamma^\mu \left(-g \frac{\sin^2\theta_w}{\cos\theta_w} \left(Q - I_3 \right) + g \cos\theta_w \, I_3 \right) u_L - \overline{u}_R \gamma^\mu \left(g \frac{\sin^2\theta_w}{\cos\theta_w} Q \right) u_R \, . \tag{2.48}$$

The operators can be evaluated and give the eigenvalues Q^f and I_3^f for the corresponding fermion f. In addition, a coupling constant to the physical Z-boson can be defined by

$$g_Z = \frac{g}{\cos\theta_w}, \tag{2.49}$$

so that the neutral weak current can finally be written as

$$j_Z^\mu = g_Z \, \overline{u}_L \left(I_3^f - Q^f \sin^2\theta_w \right) \gamma^\mu \, u_L + g_Z \, \overline{u}_R \left(-Q^f \sin^2\theta_w \right) \gamma^\mu \, u_R. \tag{2.50}$$

The couplings of the chiral states are therefore identified as

$$c_L = I_3^f - Q^f \sin^2\theta_w \;\text{ and }\; c_R = -Q^f \sin^2\theta_w \tag{2.51}$$

as illustrated in figure 2.3.

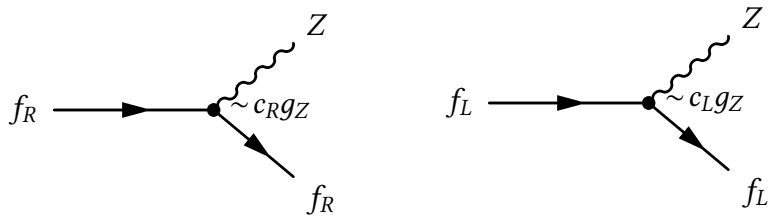

Figure 2.3.: *The Z-boson interaction vertex for the chiral states of a fermion f.*

Alternatively, the neutral weak current can equally be expressed in terms of its vector

and axial-vector couplings, so that for any fermion and its Dirac spinor u one gets

$$j_Z^\mu = \tfrac{1}{2}\, g_Z\, \overline{u}\, \gamma^\mu \left(c_V + c_A\, \gamma^5\right) u, \tag{2.52}$$

where the couplings c_V and c_A can be identified as

$$c_V = c_L + c_R = I_3^f - 2Q^f \sin^2\theta_w \;\text{ and }\; c_A = c_L - c_R = I_3^f \tag{2.53}$$

by comparing equations 2.17, 2.50 and 2.52. The fact that both the vector and axial-vector couplings of the weak neutral current are nonzero directly shows that it violates parity. Table 2.1 lists the charges and the corresponding couplings to the Z-boson for the fundamental fermions in the Standard Model.

Fermion	Charge	Isospin	Couplings			
			left-chiral	right-chiral	vector	axial
	Q	I_3	c_L	c_R	c_V	c_A
$\nu_e,\ \nu_\mu,\ \nu_\tau$	0	$+\frac{1}{2}$	$+\frac{1}{2}$	0	$+\frac{1}{2}$	$+\frac{1}{2}$
$e^-, \mu^-,\ \tau^-$	-1	$-\frac{1}{2}$	$-\frac{1}{2} + \sin^2\theta_w$	$\sin^2\theta_w$	$-\frac{1}{2} + 2\sin^2\theta_w$	$-\frac{1}{2}$
$u,\ c,\ t$	$+\frac{2}{3}$	$+\frac{1}{2}$	$+\frac{1}{2} - \frac{2}{3}\sin^2\theta_w$	$-\frac{2}{3}\sin^2\theta_w$	$+\frac{1}{2} - \frac{4}{3}\sin^2\theta_w$	$+\frac{1}{2}$
$d,\ s,\ b$	$-\frac{1}{3}$	$-\frac{1}{2}$	$-\frac{1}{2} + \frac{1}{3}\sin^2\theta_w$	$+\frac{1}{3}\sin^2\theta_w$	$-\frac{1}{2} + \frac{2}{3}\sin^2\theta_w$	$-\frac{1}{2}$

Table 2.1.: *The fermion electroweak charges and the respective couplings to the Z-boson.*

The vector couplings of the neutral weak current, as given in table 2.1, can be interpreted as a weak charge of the respective fermion, analogous to the electric charge for the electromagnetic current. It is conventional to add another normalization factor to the definition of the weak charge, so that the weak charge of fermion f is given by

$$Q_W^f = 2c_V^f. \tag{2.54}$$

The weak charge of nucleons is then at leading order simply given by the sum of the constituent quark weak charges. The weak charge of the proton at tree level hence is:

$$\begin{aligned} Q_W(p) &= \sum_q Q_W^q = 2Q_W^u + Q_W^d = 2\left(1 - \frac{8}{3}\sin^2\theta_w\right) + \left(-1 + \frac{2}{3}\sin^2\theta_w\right) \\ &= 1 - 4\sin^2\theta_w. \end{aligned} \tag{2.55}$$

The neutron weak charge can be calculated in the same way and yields $Q_W(n) = 1$.

With the observed weak mixing angle $\sin^2\theta_w \sim 0.22$, the proton weak charge emerges to be highly suppressed. The neutral weak current explicitly prefers neutrons to protons, while the electromagnetic current does the opposite. The weak charge of the proton is therefore particularly sensitive to $\sin^2\theta_w$.

2.5. The Scale-dependance of $\sin^2\theta_W$

The discussions in the preceeding sections so far considered processes invoking a minimum number of vertices necessary for a particular interaction, so-called tree level processes. These processes are in fact accompanied by various additional possibilities to manifest an interaction with more vertices, so called higher-order processes. The quest for theory predictions on the sub-percent precision level makes it essential to take into account corrections due to these higher order processes.

One example for the realization of additional vertices is a fermion that emits a virtual particle and then absorbs it again, as shown in figure 2.4. Such a process can be added to any interaction involving massive fermions. The virtual particles in the loop can violate energy conservation so that corrections need to account for the entire energy range. In some cases, this leads to diverging integrals. The procedure to treat these infinities and to specify effective parameter relations at a given energy scale is called renormalization. The bare parameters appearing in the tree-level electroweak theory and their relations to measurable quantities do not exactly represent what can be observed in nature, but need to be replaced by renormalized quantities [39]. The predictive power of the electroweak theory in perturbative calculations is hence only possible because it is a renormalizable theory [40–43].

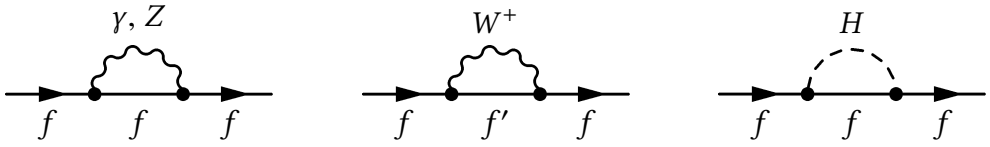

Figure 2.4.: *First order loop corrections to the fermion propagation.*

Parameters that need to be renormalized in the Standard Model are masses, couplings and mixing angles. The weak mixing angle $\sin^2\theta_w$ is directly affected by higher order corrections, as it can be motivated by the diagrams shown in figure 2.5. Various particle loops can be added to the Z propagation and also Z-γ-transitions are possible. The exact value of the renormalized weak mixing angle depends on the renormalization scheme chosen. Several definitions of renormalized weak mixing angles can be found in the literature, as discussed e.g. in [44, 45]. The on-shell renormalization

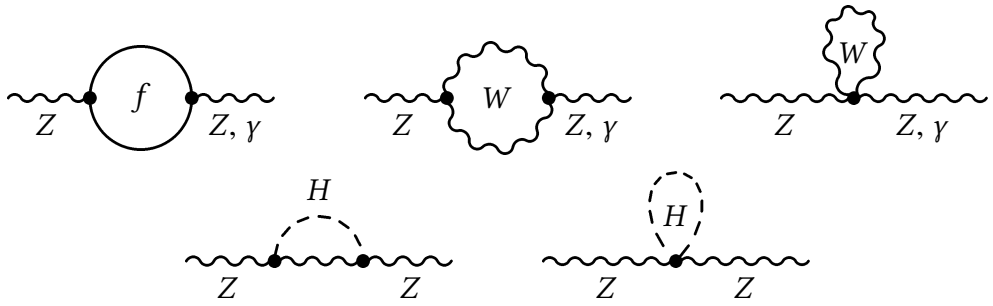

Figure 2.5.: *Z-γ transitions and first order loop-corrections to the Z propagation.*

scheme fixes the weak mixing angle $\sin^2\theta_w^{\text{on-shell}}$ to the gauge boson mass relationship given in equation 2.45 for all orders in perturbation theory. The advantage of this definition is the direct relation to physical observables. However, it induces radiative corrections of $O(\alpha m_t^2/m_W^2)$ to neutral current amplitudes [45], which is unfavorable because of the large top quark mass m_t. For measurements at the Large Electron-Positron Collider (LEP), an effective weak mixing angle was defined in terms of the ratio of the leptonic vector and axial-vector coupling strengths at the Z pole, g_V^l and g_A^l, so that [46]

$$\sin^2\theta_w^{\text{LEP}} = \frac{1}{4}\left(1 - \frac{g_V^l}{g_A^l}\right) . \tag{2.56}$$

Unfortunately, this definition still requires additional radiative corrections for non-Z-pole applications, which become non-negligible for high precision asymmetry measurements.

In the modified minimal subtraction ($\overline{\text{MS}}$) renormalization scheme [47–51], the divergent parts arising in (higher order) loop calculations and an additional constant are absorbed into counterterms. This renormalization scheme is computationally convenient and the relations of renormalized $\overline{\text{MS}}$ parameters are equal to the corresponding ones of bare parameters. Due to the absorption of radiative corrections, the weak mixing angle in the $\overline{\text{MS}}$ scheme, $\sin^2\theta_w(\mu)_{\overline{\text{MS}}}$, now depends on an arbitrary sliding mass scale $\mu \equiv \mu_{\overline{\text{MS}}}$. The LEP definition of the weak mixing angle in equation 2.56 and $\sin^2\theta_w(m_Z)_{\overline{\text{MS}}}$ are numerically related by [52]

$$\sin^2\theta_w^{\text{LEP}} - \sin^2\theta_w(m_Z)_{\overline{\text{MS}}} = 2.8 \times 10^{-4}. \tag{2.57}$$

The choice of a particular renormalization scheme allows to compare measurement results of the weak mixing angle at different energies with the theory prediction of the scale dependence. The absolute scale of the weak mixing angle remains a free

parameter in the SM and needs to be determined experimentally for one particular energy, which is usually chosen as the Z-boson mass. The most precise measurements of $\sin^2\theta_w(m_Z)_{\overline{\text{MS}}}$ were obtained at the Stanford Linear Accelerator Center (SLAC) and at the LEP, for which an averaged value of [53] [2]

$$\sin^2\theta_w(m_Z)_{\overline{\text{MS}}} = 0.231\,25(16) \tag{2.58}$$

is obtained.

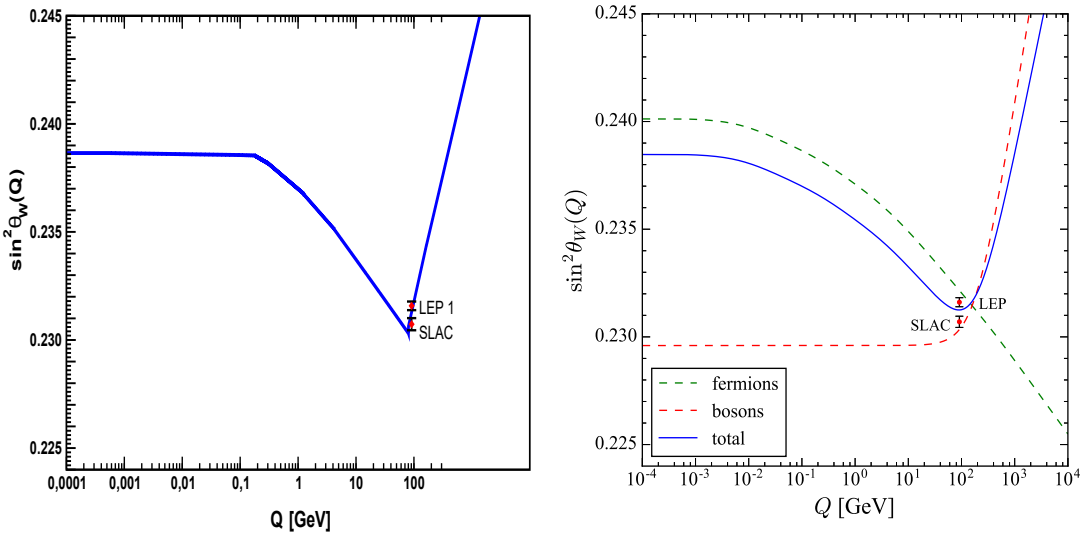

(a) *Scale dependence of the weak mixing angle in the $\overline{MS}$ scheme [54]. Picture modified from Ref. [55].*

(b) *Effective weak mixing angle at one loop level with fermion and boson contributions. Calculated according to Ref. [56].*

Figure 2.6.: *Scale dependence of the weak mixing angle $\sin^2\theta_w$ normalized to the experimental Z-pole average (see eq. 2.58) obtained from the measurements at LEP and SLAC [53].*

The scale dependence of the weak mixing angle in the $\overline{\text{MS}}$ scheme is shown in figure 2.6a. The minimum of the curve corresponds to the W-boson mass. As one can see, there are unphysical discontinuities of the slope at the W-boson mass and also at the fermion masses. This problem is often avoided defining a more physical running effective weak mixing angle, as for example done in Ref. [56], by

$$\sin^2\theta_w(Q^2) = \kappa(Q^2)\sin^2\theta_w(m_Z)_{\overline{\text{MS}}}. \tag{2.59}$$

Radiative corrections mainly due to γ-Z-mixing (see fig. 2.5), WW box diagrams

[2] The results in reference [53] are given for $\sin^2\theta_w^{\text{LEP}}$, but can be translated using equation 2.57

and photonic vertex and box diagrams, are incorporated into the scale dependent quantity $\kappa(Q^2)$. Figure 2.6b shows the result of a one-loop calculation performed in Ref. [56], in which the fermion and boson loop contributions were calculated seperately, such that $\kappa(Q^2) = \kappa_f(Q^2) + \kappa_b(Q^2)$ with the subscripts f and b for fermions and bosons, respectively.

The fermion loops effectively lead to a *screening* of the weak charge, and with more fermions contributing at higher energies, this leads to a reduction of the weak mixing angle with rising energy. The shift of $\sin^2\theta_w$ from $Q = 0$ to $Q = m_Z$ is about 3% [56]. However, since boson loops lead to *anti-screening* of the weak charge and therefore to the contrary effect on $\sin^2\theta_w(Q^2)$, the running effective weak mixing angle quickly increases for energies higher than the W-boson mass.

The running of the weak mixing angle is experimentally poorly measured and might be affected by New Physics beyond the Standard Model. The P2 experiment is one experiment in a broad measurement program that will test the electroweak theory by determining the weak mixing angle experimentally very precisely at various energies. The measurement method exploited by the P2 experiment is parity violating electron scattering (PVES).

2.6. Parity Violation in Electron-Proton Scattering

The scattering of electrons on nucleons is a powerful method in order to test the nuclear structure and has been exploited by various past measurements in Mainz and elsewhere. While the measurement principle is well known for many decades, technological progress nowadays allows to perform measurements with unprecedented precision at which higher order processes become relevant. In particular, using polarized electron beams, very small parity violating asymmetries become accessible and the V-A-structure of the weak force can be probed. This section discusses main principles employed to measure the weak mixing angle by scattering polarized electrons on a proton target, while the experimental challenges will be discussed later in this thesis.

2.6.1. Cross Sections and Kinematics

Elastic electron-proton scattering is dominated by the electromagnetic interaction. The parity violating effects induced by the weak interaction when using polarized electrons are tiny and can be neglected for the discussion of the scattering kinematics in this section. The differential cross section for a relativistic spin-half particle with

energy E scattering elastically on a static, spinless and point-like particle is given by the Mott cross section

$$\left(\frac{\mathrm{d}\sigma}{\mathrm{d}\Omega}\right)_{\mathrm{Mott}} = \frac{\alpha^2}{4E^2 \sin^4 \frac{\theta}{2}} \cos^2 \frac{\theta}{2}, \tag{2.60}$$

where θ denotes the scattering angle in the laboratory frame and α is the finestructure constant. The Mott cross section corresponds to the well-known Rutherford formula with an additional angular factor due to the electron spin. In order to describe the electron-proton scattering properly, the proton recoil and its spin need to be taken into account. With E' being the electron energy after scattering, the elastic scattering cross section including these two effects becomes

$$\left(\frac{\mathrm{d}\sigma}{\mathrm{d}\Omega}\right) = \left(\frac{\mathrm{d}\sigma}{\mathrm{d}\Omega}\right)_{\mathrm{Mott}} \frac{E}{E'} \left(1 + 2\tau \tan^2 \frac{\theta}{2}\right) \tag{2.61}$$

with the Lorentz-invariant factor

$$\tau = -4\frac{q^2}{m_p^2}\,, \tag{2.62}$$

depending on the four-momentum transfer q and the proton mass m_p. The additional factor relating the initial and the final electron energy describes the effect of the proton recoil, while the additional angular term is due to the spin-spin-interaction. The electron energy after scattering is related to the incoming electron beam energy by

$$E' = \frac{m_p\, E}{m_p + E\,(1 - \cos\theta)}\,, \tag{2.63}$$

where the electron mass was neglected with respect to the proton mass. One of the main goals of the P2 tracking detector is the determination of the (average) four-momentum transfer $Q^2 = -q^2$. From energy and momentum conservation and using the energy relation in 2.63, it follows directly that

$$Q^2 = 4EE' \sin^2 \frac{\theta}{2} = \frac{2m_p E^2\,(1 - \cos\theta)}{m_p + E\,(1 - \cos\theta)}\,, \tag{2.64}$$

and therefore Q^2 only depends on the incident electron energy and the scattering angle θ.

The above cross section still neglegts the finite size of the proton. This can be accounted for by introducing structure functions $G_E^{\gamma,p}(Q^2)$ and $G_M^{\gamma,p}(Q^2)$, which are further discussed in the following section. Inserting these two structure functions yields

the general Rosenbluth formula

$$\left(\frac{\mathrm{d}\sigma}{\mathrm{d}\Omega}\right)_{\text{Rosenbluth}} = \left(\frac{\mathrm{d}\sigma}{\mathrm{d}\Omega}\right)_{\text{Mott}} \frac{E}{E'} \left(\frac{(G_E^{\gamma,p})^2 + \tau\,(G_M^{\gamma,p})^2}{1+\tau} + 2\tau (G_M^{\gamma,p})^2 \tan^2\frac{\theta}{2} \right). \quad (2.65)$$

It can be seen that for low momentum transfer, $Q^2 \ll m_p^2$ and hence $\tau \to 0$, the term in brackets reduces to the electric charge form factor squared.

2.6.2. Proton Form Factors

The correct description of elastic electron-proton scattering requires to account for the finite proton size. Since it is not possible to model the dynamics of valence quarks, gluons and sea quarks inside the proton in QCD theory with sufficient accuracy, the proton is described by so-called form factors that are determined in scattering experiments. Experimentalists usually prefer using the Sachs electric and magnetic form factors included in the Rosenbluth formula (eq. 2.65), $G_E^{\gamma,p}(Q^2)$ and $G_M^{\gamma,p}(Q^2)$. They describe the electric charge distribution and the distribution of the magnetic moment of the proton, respectively. For the low-Q^2 limit, where the time-like component of Q^2 is relatively small and $Q^2 \approx \mathbf{q}^2$, the Sachs form factors can be interpreted approximately as the Fourier transforms of the charge and magnetic moment distributions of the proton [34]

$$G_E^{\gamma}(Q^2) \approx G_E^{\gamma}(\mathbf{q}^2) = \int e^{i\mathbf{q}\cdot\mathbf{r}} \rho(\mathbf{r})\,\mathrm{d}^3\,\mathbf{r} \quad (2.66)$$

$$G_M^{\gamma}(Q^2) \approx G_M^{\gamma}(\mathbf{q}^2) = \int e^{i\mathbf{q}\cdot\mathbf{r}} \mu(\mathbf{r})\,\mathrm{d}^3\,\mathbf{r} \quad (2.67)$$

The electromagnetic proton form factors are normalized such that in the static limit one gets $G_E^{\gamma,p}(0) = 1$ and $G_M^{\gamma,p}(0) = 2.79$, equal to the observed anomalous magnetic moment of the proton.

The Sachs electromagnetic form factors are relevant for the electromagnetic interaction mediated by the photon, dominating the electron-proton scattering cross section. In order to quantify this process, both the photon-electron coupling vertex and the photon-nucleon vertex need to be calculated. The coupling of the photon and the electron is described by the current given in equation 2.42. The nucleon vertex is more complicated, but can be written with the help of the Pauli and Dirac form factors for the photon exchange, $F_1^{\gamma}(Q^2)$ and $F_2^{\gamma}(Q^2)$, as [57]

$$j^{\mu}_{\text{em}} = \overline{\psi} \left(F_1^{\gamma}(Q^2)\,\gamma^{\mu} + F_2^{\gamma}(Q^2)\,\frac{i\sigma^{\mu\nu}q_{\nu}}{2m_p} \right) \psi, \quad (2.68)$$

with $\sigma^{\mu\nu} = i\left[\gamma^\mu, \gamma^\nu\right]$. The two electromagnetic form factors can be written in terms of the contributing quark flavors weighted by their electric charges, so that one gets

$$F_{1,2}^{\gamma} = \frac{2}{3} F_{1,2}^{u} - \frac{1}{3} F_{1,2}^{d} - \frac{1}{3} F_{1,2}^{s} \,. \tag{2.69}$$

Contributions of heavier quarks can be neglected [58]. In addition, the Pauli and Dirac form factors are related to the Sachs electric and magnetic form factors by the linear combinations

$$G_E^{\gamma} = F_1^{\gamma} - \tau F_2^{\gamma} \tag{2.70}$$
$$G_M^{\gamma} = F_1^{\gamma} + F_2^{\gamma}. \tag{2.71}$$

Experiments examining parity violating effects in electron-nucleon scattering aim to reveal the parity violating effects induced by the neutral weak current and hence neutral weak form factors have to be considered in addition. The neutral weak electron vertex was given in equation 2.52. In contrast to the photon exchange, the exchange of a Z-boson does not conserve parity, which is why another axial form factor $G_A^Z(Q^2)$ is needed in addition to the Dirac and Pauli Form factors $F_{1,2}^Z(Q^2)$ to describe the weak neutral proton vertex in elastic scattering. The nucleon neutral weak current then reads: [57]

$$j_Z^{\mu} = \overline{\psi} \left(F_1^Z(Q^2)\, \gamma^{\mu} + F_2^Z(Q^2)\, \frac{i\sigma^{\mu\nu} q_{\nu}}{2m_p} + G_A^Z(Q^2)\, \gamma^{\mu}\gamma_5 \right) \psi. \tag{2.72}$$

Again, the weak form factors can be decomposed into contributions by the individual quarks, but this time weighted by their weak charges, reading

$$F_{1,2}^Z = \left(1 - \frac{8}{3}\sin^2\theta_w\right) F_{1,2}^u + \left(-1 + \frac{4}{3}\sin^2\theta_w\right)\left(F_{1,2}^d + F_{1,2}^s\right) \,. \tag{2.73}$$

Note that the in the same way as for the electromagnetic form factors, the weak Sachs form factors $G_{E,M}^Z(Q^2)$ are defined as linear combinations of the Dirac and Pauli form factors analogous to equations 2.70 and 2.71.

2.6.3. The Parity Violating Asymmetry A_{PV}

The elastic scattering of electrons with protons can either be mediated by the exchange of a photon or the exchange of a Z-boson, as shown in the leading-order feynman graphs in figure 2.7. The total scattering cross section is dominated by

the electromagnetic interaction. Nevertheless, the proton weak charge and the weak mixing angle θ_w can be determined by quantifying the parity violating effects caused by the neutral weak current interaction.

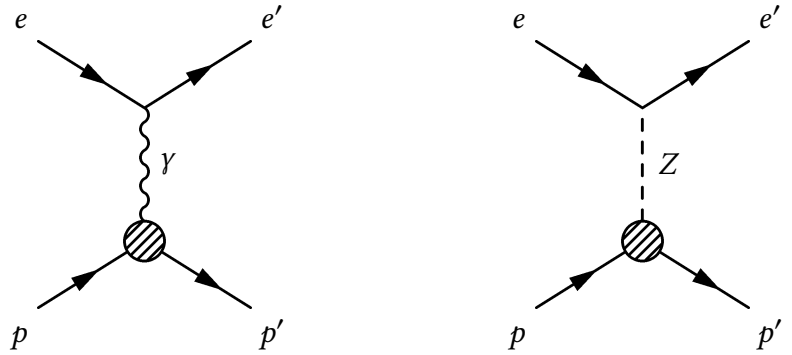

Figure 2.7.: *Leading order Feynman diagrams for elastic electron-proton scattering. The 'blob' at the proton vertex illustrates the finite size of the proton entering the cross sections in the form of structure functions.*

For low Q^2, the scattering process can be described in terms of effective electron-quark couplings. In such an effective theory, the parity violating neutral current term in the Lagrangian reads [55, 59]

$$\mathcal{L}_{eq}^{PV} = -\frac{G_F}{\sqrt{2}} \sum_q \left[\bar{e}\,\gamma_\mu\gamma_5\, e \cdot C_{1q}\, \bar{q}\,\gamma^\mu\, q \;+\; \bar{e}\,\gamma_\mu\, e \cdot C_{2q}\, \bar{q}\,\gamma^\mu\gamma_5\, q \right] \tag{2.74}$$

with the Fermi constant G_F. The first term with the electron axial-vector current coupling to the quark vector current has the helicity dependence in the electron vertex, which is the main parity violating contribution for PVES experiments. The quark vector couplings C_{1q} can be calculated as the product of the corresponding vector and axial-vector couplings given in table 2.1, while again an additional normalization factor of two was absorbed into the couplings. For the up- and down-quark, the effective quark vector couplings are

$$\begin{aligned} C_{1u} &= 2\, c_A^e c_V^u = -\frac{1}{2} + \frac{4}{3}\sin^2\theta_w \\ C_{1d} &= 2\, c_A^e c_V^d = +\frac{1}{2} - \frac{2}{3}\sin^2\theta_w. \end{aligned} \tag{2.75}$$

In this notation, the proton weak charge is by definition given as

$$Q_W(p) = -2(2C_{1u} + C_{1d}). \tag{2.76}$$

In order to quantify parity violation in polarized electron-proton scattering, one de-

fines the parity violating electroweak asymmetry

$$A_{PV} = \frac{\sigma_R - \sigma_L}{\sigma_R + \sigma_L}, \tag{2.77}$$

where $\sigma_L(\sigma_R)$ is the cross section for left-handed (right-handed) electrons in terms of helicity. The parity violating neutral weak current Lagrange terms in equation 2.74 give rise to interference with the parity conserving contributions. However, it is straightforward to see that many terms cancel out at leading order. The only difference in the matrix elements $\mathcal{M}_{L(R)} = \mathcal{M}_\gamma + \mathcal{M}_{L(R),Z}$ for left-handed (right-handed) electrons is that the matrix element $\mathcal{M}_Z^{PV}$ of the above Lagrangian switches sign, so that:

$$\mathcal{M}_L - \mathcal{M}_R = 2\mathcal{M}_Z^{PV}. \tag{2.78}$$

Taking this relation when inserting the squared matrix elements into the above defined asymmetry and approximating the term in the denominator using $|\mathcal{M}_\gamma|^2 \gg |\mathcal{M}_Z|^2$, the parity violating asymmetry becomes

$$A_{PV} \approx \frac{2\,\Re\left[\mathcal{M}_\gamma \mathcal{M}_Z^{PV}\right]}{\left|\mathcal{M}_\gamma\right|^2}. \tag{2.79}$$

Calculating the matrix elements in the laboratory frame with the proton at rest, one gets for the leading order parity violating asymmetry

$$A_{PV} = -\frac{G_F Q^2}{4\sqrt{2}\pi\alpha}\left(Q_W(p) - F(Q^2)\right) \equiv A_0\,\left(Q_W(p) - F(Q^2)\right). \tag{2.80}$$

The normalization is such that the hadronic structure function $F(Q^2)$ vanishes at zero momentum transfer, but has to be taken into account for non-zero momentum transfer.

Following the explanations in Ref. [13], the structure function can be written as the sum of three contributing terms

$$F(Q^2) \equiv F^{\mathrm{EM}}(Q^2) + F^{\mathrm{A}}(Q^2) + F^{\mathrm{S}}(Q^2). \tag{2.81}$$

The first term describes the contribution of the electric and magnetic form factors of the proton and the neutron:

$$F^{\mathrm{EM}}(Q^2) \equiv \frac{\epsilon\, G_E^{\gamma,p} G_E^{\gamma,n} + \tau\, G_M^{\gamma,p} G_M^{\gamma,n}}{\epsilon\,(G_E^{\gamma,p})^2 + \tau\,(G_M^{\gamma,p})^2}. \tag{2.82}$$

The second term includes the axial form factors for the neutral weak current interaction and can be written as

$$F^{\mathrm{A}}(Q^2) \equiv \frac{(1-4\sin^2\theta_w)\sqrt{1-\epsilon^2}\,\sqrt{\tau(1-\tau)}\,G_M^{\gamma,p}\,G_A^{Z,p}}{\epsilon\,(G_E^{\gamma,p})^2+\tau\,(G_M^{\gamma,p})^2}. \tag{2.83}$$

Finally, the last term contains the contributions of the strange electric and magnetic form factors $G^s_{E,M}$, but also the isospinbreaking form factors $G^{u,d}_{E,M}$:

$$F^{\mathrm{S}}(Q^2) \equiv \frac{\epsilon\,G_E^{\gamma,p}G_E^s+\tau\,G_M^{\gamma,p}G_M^s}{\epsilon\,(G_E^{\gamma,p})^2+\tau\,(G_M^{\gamma,p})^2}+\frac{\epsilon\,G_E^{\gamma,p}G_E^{u,d}+\tau\,G_M^{\gamma,p}G_M^{u,d}}{\epsilon\,(G_E^{\gamma,p})^2+\tau\,(G_M^{\gamma,p})^2}. \tag{2.84}$$

The kinematic factor τ was already defined in 2.62, while ϵ is defined as

$$\epsilon \equiv \left[1+2\,(1+\tau)\tan^2\left(\frac{\theta}{2}\right)\right]^{-1} \tag{2.85}$$

with θ being the electron scattering angle.

The choice of the average Q^2 of electron scattering on a nucleon is crucial for any PVES experiment. It decides which contribution to A_{PV} dominates and therefore to which contribution the experiment is mainly sensitive. As shown in equation 2.64, the momentum transfer is defined by the incident electron energy and the scattering angle.

Figure 2.8 shows the contributions to A_{PV} depending on the electron scattering angle for an electron incident energy of $E = 155\,\mathrm{MeV}$, the beam energy chosen for the P2 experiment. It can be seen that the contribution of the proton weak charge dominates for lower scattering angles, corresponding to lower values of Q^2. However, the overall parity violating asymmetry decreases with decreasing scattering angle, making the measurement more challenging. The central scattering angle of the P2 experiment is 35°, which yields $A_{PV} = -67.34\,\mathrm{ppb}$. It is the result of analyses optimizing the expected precision of the weak mixing angle determination (see Ref. [13, 14]), which are outline in section 3.4.3.

Since the proton weak charge is at tree level directly related to the weak mixing angle by $Q_W(p) = 1-4\sin^2\theta_w$, the determination of the asymmetry is a direct measurement of the weak mixing angle on the condition that the proton structure function $F(Q^2)$ is sufficiently well known. In addition, since the weak charge of the proton is small, it is straightforward to deduce by error propagation that the relative precision measuring the weak mixing angle is about ten times higher than the relative precision of the determination of A_{PV} and $Q_W(p)$.

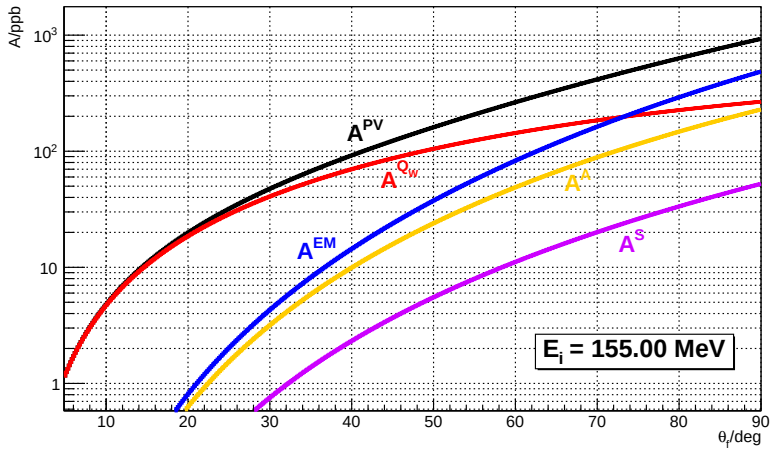

Figure 2.8.: *Dependence of A_{PV} on the electron scattering angle, here denoted as θ_f, for an electron incident energy of $E_i = 155\,\mathrm{MeV}$. Plotted are the absolute values of the asymmetry and the contributions by the proton's weak charge and the nucleon form factors to A_{PV}. Picture taken from [13].*

The P2 experiment as a high precision scattering experiment is sensitive to phenomena triggered by higher order processes. In section 2.5, it was shown that the inclusion of such corrections manifests in the running of the weak mixing angle. In order to obtain theory predictions with higher precision than the experiment, such corrections also need to be taken into account when relating the proton's weak charge to the weak mixing angle and to the parity violating asymmetry [13]:

$$A_{PV} = A_0 \left[Q_W^{\text{1-loop}}(p) - F(Q^2) + \Delta_\Box(Q^2) - \Delta_\Box(0) \right] \tag{2.86}$$

and

$$Q_W^{\text{1-loop}}(p) = (\rho_{nc} + \Delta_e)\left(1 - 4\sin^2\theta_w(\mu)_{\overline{\text{MS}}} + \Delta_e^{'}\right) + \Delta_\Box(0). \tag{2.87}$$

Here, Δ_e and $\Delta_e^{'}$ are due to contributions to the electron vertex, ρ_{nc} is a renormalization factor for the neutral and charged current strengths. These corrections are known to high precision at the one-loop-level [60]. However, two-loop corrections need to be considered for the P2 experiment additionally. The term $\Delta_\Box$ describes contributions due to processes indicated by so-called box graphs. These Feynman diagrams are shown in figure 2.9.

The calculation of these corrections is part of ongoing research. Further theory challenges for a complete NNLO description include the calculation of initial two-photon radiation. A brief status report on these developments is e.g. given in Ref. [13].

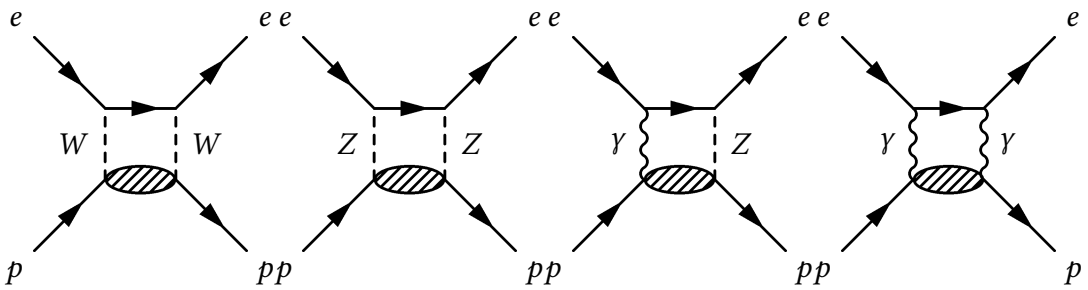

Figure 2.9.: *Box graphs for electron-proton scattering. The diagrams show the WW-, the ZZ-, the γZ- and the $\gamma\gamma$-exchange (from left to right). The shaded blobs indicate possible excited intermediate proton states.*

3 The P2 Experiment

The forthcoming P2 experimental facility is dedicated to measuring parity violating asymmetries in electron-proton scattering with unprecedented precision. These precise asymmetry measurements will enable a wide physics program searching for New Physics beyond the Standard Model at the intensity frontier. In particular, they allow to determine the weak mixing angle at low momentum transfer. The P2 detector is currently under development and will be placed at the upcoming Mainz Energy-Recovering Superconducting Accelerator (MESA). The conceptual design and the main challenges for this experiment will be shortly presented here, while a more detailed description of the planned facility being developed by the P2 collaboration and its physics program was recently published in Ref. [13].

3.1. Physics Motivation

The measurement of parity violating asymmetries in electron scattering experiments is a well-established experimental method in order to precisely measure SM parameters. Many necessary techniques for such kind of experiments were developed already 20 to 30 years ago [61–63]. However, it is nowadays possible to perform similar experiments with much higher precision, which allows for an accurate experimental determination for example of the proton weak charge. The Qweak collaboration recently published its result on the weak charge of the proton [64]

$$Q_W^p = 0.0719(45)\,, \tag{3.1}$$

which was obtained by measuring a parity violating asymmetry of

$$A_{PV} = -226.5(93)\,\text{ppb} \tag{3.2}$$

for polarized electrons scattered on protons. The weak charge of the proton is suppressed in the SM and therefore a perfect place to search for New Physics that might induce tiny changes on electroweak SM parameters. The P2 experiment will add another measurement of the proton weak charge with improved precision and therefore check the result obtained in the Qweak experiment.

Parity violating electron scattering precision experiments are also a perfect tool in order to study the running of the weak mixing angle. Several proposed complementary experiments will allow to accurately test the running of the weak mixing angle predicted in the SM. The P2 experiment intends to measure the weak mixing angle at lower momentum transfer and to improve the precision by another factor of three compared to the Qweak experiment. The MOLLER experiment [65] at Jefferson Lab aims to measure the weak mixing angle using Møller scattering and by that improve the according previous measurement of the SLAC E158 experiment [66] by a factor of five. The SOLID experiment [67] will measure the parity violating asymmetry in deep inelastic scattering of an 11 GeV electron beam. It will allow to obtain an accurate measure of the weak mixing angle at intermediate momentum transfer. Figure 3.1 shows the predicted running of the weak mixing angle in the Standard Model together with the values obtained in past experiments and with the anticipated sensitivities of future experiments. The combination of the results obtained in the discussed upcoming weak polarized electron scattering experiments will put stringent constraints on New Physics models.

3.1.1. Sensitivity to Physics Beyond the Standard Model

The parity violating asymmetry in electron-proton scattering and the weak mixing angle $\sin^2\theta_w$ might be influenced by New Physics beyond the Standard Model. In the previous chapter, the influence of loop diagrams (see figure 2.5) on the self-energies of the electroweak gauge bosons and the resulting energy dependence of the weak mixing angle in the Standard Model were discussed. The presence of new particles and corresponding additional loop contributions could lead to an observable shift of $\sin^2\theta_w$. The sensitivity of parity violating electron scattering experiments to New Physics beyond the Standard Model is reviewed e.g. in Ref.s [44] and [68], some ideas are reported in the following.

Possible New Physics manifesting at an energy scale $\Lambda \gg Q^2$ might still be observable in the P2 experiment as it could induce tiny deviations from the SM expectations also at the electroweak scale. The sensitivity of precision experiments like P2 can be analyzed in an effective Lagrangian approach. Here, new contact interaction terms interfering with the SM amplitudes are considered. The effective Lagrangian can be realized by various New Physics scenarios, such as composite fermions, leptoquarks, and heavy Z' bosons, among others [44]. The effective theory approach allows to

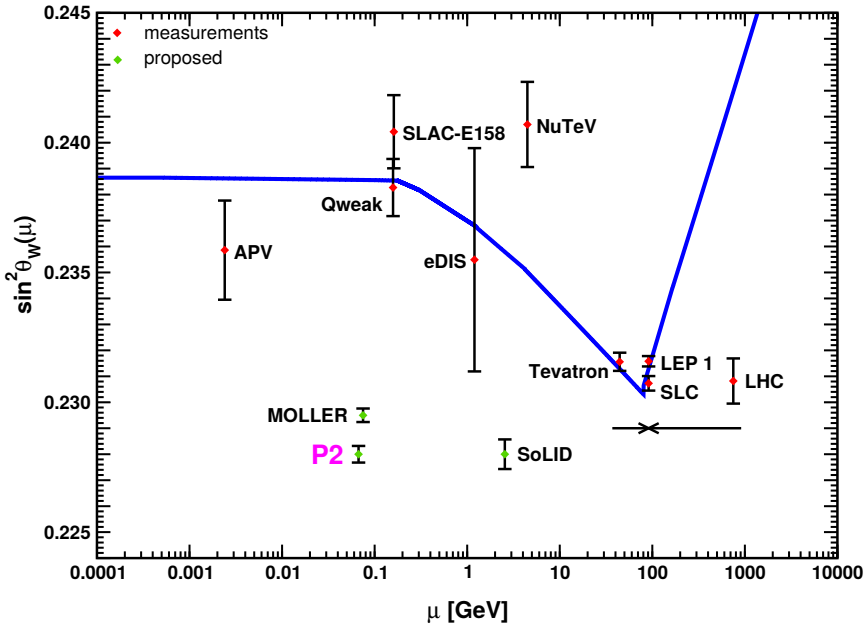

Figure 3.1.: *Scale dependence of the weak mixing angle in the $\overline{MS}$ renormalization scheme compared with past and forthcoming measurements. The points for the proposed experiments are put to arbitrary vertical positions, but their error bars represent their predicted precision. Picture updated from Ref. [13] with the published Qweak result.*

establish the expected reach to the New Physics scale Λ for different experiments after choosing a common convention for the coupling scale g of the new interactions. The bounds on scenarios with different coupling strength can then be obtained by rescaling. Precision parity-violation experiments are sensitive to New Physics on the multi-teraelectronvolt scale [44, 68] and therefore competitive to direct searches at collider experiments.

The possibility of a new light vector boson Z_d in the mass range $10\,\text{MeV} \leq m_{Z_d} \leq 10\,\text{GeV}$ has recently been discussed as the so-called dark Z scenario [69–72]. Due to the relatively light new degrees of freedom, it cannot be absorbed into contact interactions. The presence of the Z_d boson is explained by a new spontaneously broken $U(1)_d$ gauge symmetry that may be related to dark matter. The couplings of any new light particle to SM particles must be very small because otherwise it would have been observed in high-energy experiments. The presence of the Z_d would lead to a modified running of the weak mixing angle $\sin^2\theta_w$ at low energies. Parity violation experiments at low Q^2 will therefore provide strong bounds on such models.

Shifts of the electron and proton weak charges can also be obtained in the scope of supersymmetry (SUSY) scenarios. It is therefore possible to deduce complemen-

tary information on the possible realization of SUSY scenarios from the analysis of precision electroweak measurements [73].

3.2. Measurement Principle

In the P2 experiment a parity violating asymmetry will be measured in elastic electron-proton scattering. The measurement principle is schematically shown in figure 3.2. A beam of longitudinally polarized electrons with an energy of $E_{in} = 155\,\text{MeV}$ is directed on a liquid hydrogen target. The P2 spectrometer will select those electrons which are scattered on protons within the angular range between 25° to 45°, and they will be detected with an azimuthally symmetric Cherenkov detector system. The predominant number of beam electrons interact solely with hydrogen electrons within the target and are therefore scattered at low angles, under a few degree or less. These electrons will be dumped.

The main challenge for the P2 experiment is to measure the extremely small parity violating asymmetry with high precision. As one can see in figure 2.8, the parity violating asymmetry for electrons within the selected scattering angle range is between about 30 ppb and 100 ppb. It is therefore considerably smaller compared to the Qweak experiment. Finally, achieving a precision on the one percent level requires high statistics and a good control of any systematic uncertainties.

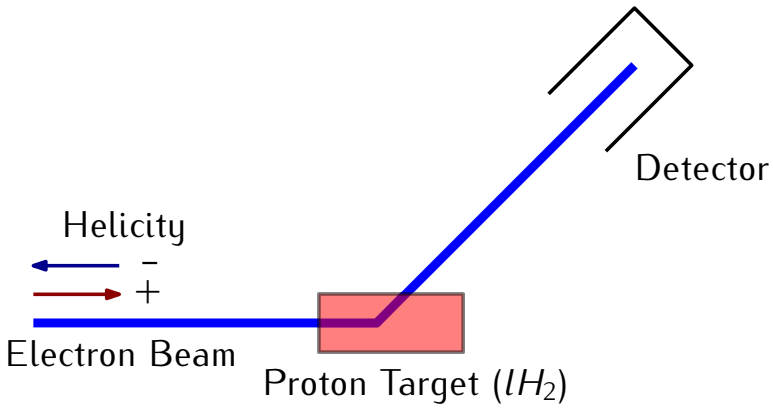

Figure 3.2.: *Sketch of the measurement principle to be used in the P2 Experiment. The rate in the Cherenkov Detector will be measured for each helicity state.*

In order to collect a maximum achievable number of scattered electrons in the integrating Cherenkov detectors, a high beam current of $I_{\text{beam}} = 150\,\mu\text{A}$ is used. In addition, the liquid hydrogen target is chosen to have a length of $L = 600\,\text{mm}$, which results in an instantaneous luminosity around $\mathcal{L} = 2.38 \times 10^{39}\,\text{cm}^{-2}\,\text{s}^{-1}$. The expected

rate of detected electrons is in the order of 0.1 THz which makes it necessary to do an integrating measurement of the event rate. The high rate and the resulting radiation dose has to be taken into account carefully when developing detector components. The P2 experiment will be the first experiment to use the upcoming MESA accelerator described in the following section. The runtime schedule will allow the experiment to make use of a running time of about 11 000 h. Despite this effort, the precision of the P2 experiment will anyway be dominated by the statistical uncertainty, as it will be discussed later in section 3.4.3.

An important requirement for the P2 experiment is the control of any helicity correlated uncertainties, which particularly concerns the electron beam. This challenge is one of the reasons for the development of the MESA accelerator. MESA will allow to switch the beam polarization at a rate of around 1 kHz. By integrating the number of electrons detected in the Cherenkov detectors for each helicity cycle, the parity violating asymmetry A_{PV} as defined in equation 2.77 can be measured. The high helicity reversal rate helps to suppress any systematic effects occurring on larger timescales. The measurement of A_{PV} makes it possible to finally extract the weak mixing angle. At leading order, combining equations 2.55 and 2.80 yields

$$A_{PV} = \frac{\sigma_R - \sigma_L}{\sigma_R + \sigma_L} = -\frac{G_F Q^2}{4\sqrt{2}\pi\alpha}\left[Q_w(p) - F(Q^2)\right] = -\frac{G_F Q^2}{4\sqrt{2}\pi\alpha}\left[\left(1 - 4\sin^2\theta_w\right) - F(Q^2)\right]. \tag{3.3}$$

The suppression of the weak charge of the proton in the SM makes it very sensitive for a measurement of the weak mixing angle, as it can be understood quite easily using Gaussian error propagation. Any determination of the weak charge of the proton leads to an about ten times more precise determination of the weak mixing angle:

$$\frac{\Delta \sin^2\theta_w}{\sin^2\theta_w} = \frac{1 - 4\sin^2\theta_w}{4\sin^2\theta_w} \cdot \frac{\Delta Q_w(p)}{Q_w(p)} \approx 0.09 \cdot \frac{\Delta Q_w(p)}{Q_w(p)} \text{ for } \sin^2\theta_w \approx 0.23. \tag{3.4}$$

Note that that higher order corrections need to be considered in the evaluation of the actual experimental data and will modify the relation given in equation 3.3 as it was already outlined in section 2.6.3.

The measurement of the parity violating asymmetry A_{PV} with unprecedented precision requires the development of a dedicated experimental facility. The demand for extensive availability and for a very precise control of any beam fluctuations represents one of the motivations to build the new accelerator facility MESA, which is summarized in the following section. The P2 detector system consisting of the spectrometer setup and the tracking detector are described afterwards.

3.3. The MESA Accelerator

The Mainz Energy-Recovery Superconducting Accelerator (MESA) is currently being developed and built in Mainz. It will mainly be placed in a new experimental hall, for which civil construction has started and will presumably be completed by 2020. The development and construction of the new MESA accelerator facility profits from the experience of successfully operating the Mainzer Mikroton (MAMI) beam facility at the Institute for Nuclear Physics in Mainz for more than 25 years [74–76]. The P2 experiment puts demanding stability constraints on beam parameters like intensity and position, which can not be fulfilled by the existing MAMI accelerator. However, many of the concepts proven to be working at MAMI are adopted and advanced for the MESA design.

The MESA accelerator features an energy recovering linac (ERL) operation mode, which is developed in conjunction with the gaseous target of the MAGIX experiment [10, 11]. In this operation mode, unpolarized electrons are accelerated and then pass the gas target. Those electrons which traverse the target without any considerable deflection are directed back to the first accelerator module. Instead of being accelerated again, their trajectory length is chosen such that they arrive at a phase in time at the superconducting radio frequency (SRF) acceleration modules that will lead to a deceleration. In this way, the energy of the electrons is transferred to the SRF module and therefore reused. This allows for a beam current of up to 10 mA, which would not be feasible with conventional techniques due to an unaffordable power demand. For the P2 experiment, a beam of polarized electrons is needed, which will be extracted from the accelerator, directed to the experiment and afterwards stopped in a beam dump. This section aims to shortly summarize the MESA parameters and components which are important for the P2 experiment. More details on MESA can be found e.g. in Ref.s [7–9, 13]. The main accelerator layout and the placement of its components and the connected experiments in the experimental hall are shown in figure 3.3.

The electron production for MESA is based on photo-electron emission from semiconductors. The electrons will be emitted from a 100 keV GaAs photo-cathode that is illuminated with laser light. For P2, a beam of 155 µA with at least 85 % spin-polarization is needed. The electron spin polarization is controlled by the polarization of the laser light with a Pockels cell and needs to be flipped at a rate of about 1 kHz. The source developed and used for MAMI [77, 78] is well capable of providing this polarization level and beam intensity. A copy of the design can therefore also be used for MESA.

The electrons produced in the source are injected into the Mesa Low-Energy Beam Apparatus (MELBA), which is a spin manipulation system. An α-magnet directs

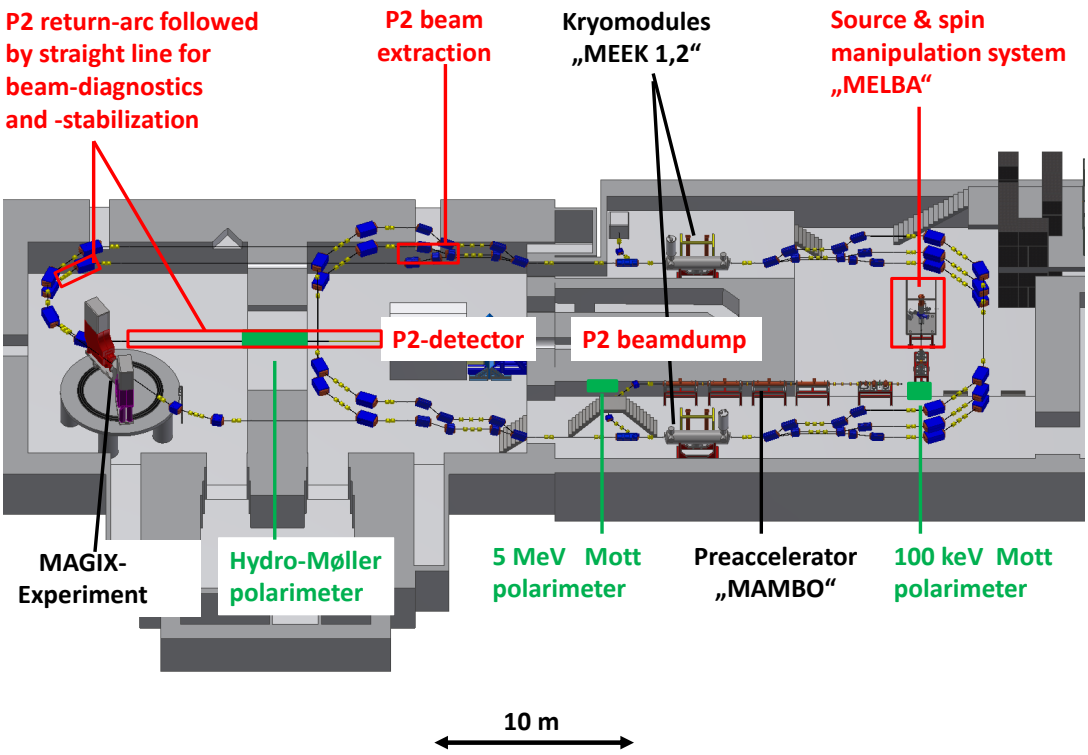

Figure 3.3.: *View of the MESA accelerator with indicated areas of specific importance for P2. Electron optical components are labeled in black, beam and spin control in red and polarimeters in green [13].*

the beam to the beam bunching and collimation system, before it reaches the pre-accelerator MAMBO (MilliAmpereBooster) [79, 80], which is a room temperature linac that will accelerate the electrons to an energy of 5 MeV. The main acceleration is achieved by recirculating the electron beam three times through two superconducting radio frequency acceleration modules (SRF cryomodules), which are labeled MEEK (Mesa Elbe-Enhanced-Kryomodule). There are two 9-cell TESLA/XFEL-type cavities per cryomodule [81]. The cavities are operated at a frequency of 1300 MHz and provide an energy gain of 12.5 MeV each, resulting in 50 MeV acceleration per turn. After that, the beam has reached its final energy of 155 MeV and is extracted via magnets. It is directed to the P2 experiment through a straight beam line in front of the experiment to be used for beam diagnostics and stabilization.

One of the key requirements for the P2 experiment is a very precise knowledge of the beam spin polarization. In order to achieve a total systematic error on the polarization value of around 0.5 %, a dedicated polarimetry concept was worked out [82]. It consists of three independent polarization measurements.

A double scattering Mott polarimeter (DSP) [83, 84] operating at the source energy of 100 keV is reached by switching off the α-magnet behind the source. The second polarization measurement is done with a single scattering Mott polarimeter which operates at 5 MeV and is placed behind the pre-accelerator. Both types of polarimeters determine the beam polarization by measuring an asymmetry of Mott scattering on a thin target. This measurement requires a precise knowledge of the effective analyzing power of the target with finite thickness due to multiple scattering. For the single scattering Mott polarimeter, a calibration is necessary which extrapolates from asymmetry measurements on a series of targets with different thicknesses. The achievable precision of this procedure is restricted by background contributions, the uncertainty on the extrapolation and theoretical uncertainties on the target analyzing power. The single scattering Mott polarimeter used for MESA will follow the design of the 3.5 MeV Mott polarimeter used at MAMI [85] and is expected to provide an accuracy better than 1 %. A double scattering Mott polarimeters uses Mott scattering on two identical thin targets in order to evaluate the analyzing power of the target within the setup and therefore reduces the associated uncertainties. The precision is mainly limited by the control of instrumental asymmetries during this internal calibration. Once the thin target is calibrated, the beam polarization is determined by single scattering. Both Mott polarimeters represent invasive devices, but allow for fast polarization measurements. The measurement with the double Mott polarimeter must be done at beam currents at the order of a few nA, while the dynamic range of the single Mott polarimeter is larger. It allows for measurements near the P2 beam intensity and is therefore used to check that the beam polarization did not change compared to the DSP measurement.

The third polarization measurement will be performed at the final beam energy with a Hydro-Møller polarimeter [86, 87] located in front of the P2 experiment and offers the possibility of an online measurement. The beam polarization is determined with an asymmetry measurement while scattering the electron beam on atomic hydrogen. The hydrogen atoms are enclosed radially by the wall of a storage cell, which is covered with a superfluid film of helium. In that way, the hydrogen atoms are cooled down to about 0.3 K by wall collisions, but adsorption and recombination are suppressed. The necessary polarization of the hydrogen atoms is provided by an 8 T solenoid magnet. The cryogenic environment for the Hydro-Møller experiment and its operation in a high intensity electron beam are very challenging. The design of a refrigerator has been developed and is currently under construction. The scattered electrons must be separated from the electron beam to be detected on a segmented detector. In a conceptual design, this is achieved by a focusing quadrupole magnet centered on the beam axis followed by a dipole chicane. Further investigations on this subject are ongoing. According to first studies, it seems possible to achieve a total systematic error around 0.5 % on the beam polarization measurement integrated over the full running period [13].

A precise knowledge of any helicity correlated fluctuation of the beam position, angle, energy and intensity is crucial for the P2 experiment to be able to correct for false asymmetries. The main uncertainties contributing to the achievable precision of the P2 experiment will be discussed later in section 3.4.3. The uncertainty on the false asymmetry contribution due to beam instabilities must satisfy $\Delta A^{\text{false}} \leq 0.1\,\text{ppb}$. In order to achieve this goal, improvements compared to the fluctuations measured at MAMI of one order of magnitude or more need to be achieved concerning beam intensity, angle and position. The energy stability of MAMI would be sufficient for MESA, but still needs to be taken special care of to ensure a comparable value for MESA. However, these precision goals are considered to be feasible with an optimized design and elaborate beam control system. The beam control system planned for MESA will include beam cavity monitors both for beam current monitors and beam position monitors. A digital readout and control system is currently being tested at MAMI.

3.4. The P2 Detector Design

The P2 detector consists of three major parts: The high power liquid hydrogen target, the solenoid spectrometer to measure the asymmetry of the scattered electrons and the tracking system which will be used to reconstruct the momentum transfer in the target. Since the work presented in this thesis concerns simulation studies and design development for the tracking system, a short summary of the target and spectrometer design will be followed by a more detailed description of the tracking system in the following section.

3.4.1. High Power Liquid Hydrogen Target

A closed recirculating cryogenic liquid hydrogen ($l\text{H}_2$) target loop is currently being developed for the P2 experiment. The target cell is planned to have a length of 60 cm. This target length still allows electrons scattered over the whole target length and within the polar angle range 25° to 45° to be directed to the detector for the asymmetry measurement. The target geometry within the beam has to provide azimuthal symmetry and the material in the path of the electrons after scattering must be minimized. The target cell geometry that is currently investigated for the P2 experiment is cylindrical and has a hemispherical window at the downstream end. This design is based on the target design for the G0 experiment [88, 89]. It will be further validated and optimized with extensive Computational Fluid Dynamics (CFD) studies. The cell design features an internal conical flow diverter consisting of 75 µm thin aluminum

foil. The cell wall thickness is supposed to be 250 µm, which is sufficient for a self-supporting structure. A rendering of the current target cell design can be seen in figure 3.4a. The target diameter in this figure is 10 cm, while the final diameter still needs to be evaluated, but likely it will be in the range between 10 cm and 15 cm. The target cell will be mounted on a movable table with motion control system.

The operation of the liquid hydrogen target requires additional components that will be placed outside of the beam. The main components of the hydrogen target loop next to the target cell are the $l\mathrm{H}_2$ centrifugal pump, the heat exchanger (HX) and the high power heater (HPH). All these components will be placed inside one vacuum chamber, but only the target cell will be within the P2 solenoid (see section 3.4.2). A rendering of the P2 target loop design including the mounting table is shown in figure 3.4b.

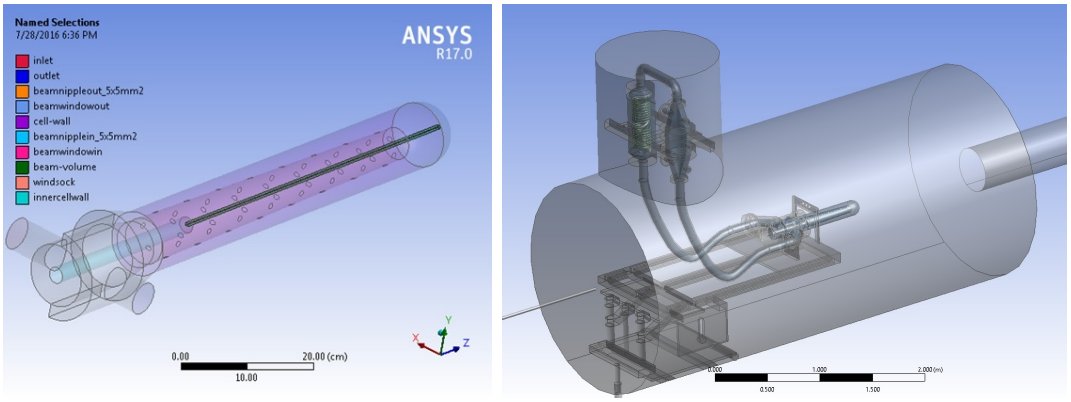

(a) *G0 type cell design for P2* (b) *Configuration of the P2 target loop*

Figure 3.4.: *Current design for the P2 high power liquid hydrogen target setup. Both pictures taken from [13].*

The heat deposit of the electron beam in the target is expected to be 3135 W. The total heat load including other effects like viscous heating will be around 4 kW and needs to be cooled using liquid helium. The heat load is about 50 % more than for the target of the QWeak experiment, which is currently the highest power $l\mathrm{H}_2$ target in the world. The liquid helium cooling power must be supplied by the MESA refrigerator and has to supply cooling to the hydrogen target loop through the heat exchanger. The heat exchanger is also used to liquefy the hydrogen in the beginning. The P2 target loop will be operated with constant heat load, which means that the heat load is kept constant independent from the beam. This is achieved by the high power heater, which is integrated to a feedback-loop with temperature sensors placed in the target fluid.

The desired precision of the P2 experiment puts constraints both on target density

reduction and on density fluctuations. Density reduction occurs if the target fluid heats up and therefore decreases its density. The design goal for the P2 target is less than 2 % density reduction. Density fluctuations are a time dependent noise effect caused by an imbalanced heat load due to the electron beam. The P2 target must satisfy less than 10 ppm density fluctuations over the time period of one electron helicity reversal [13]. This goal represents a noise reduction of a factor five compared to the Qweak target. A control system will be integrated into the target design in order to ensure safe operation and control. In addition, it is currently evaluated whether larger target density fluctuations might be detectable for the tracking system during operation of the experiment.

3.4.2. P2 Spectrometer Setup

The P2 spectrometer is the main part of the P2 detector setup. It is designated to measure the number large angle electron scatterings in the target for each helicity period. The main challenge here is the development of a suitable detector geometry to separate the signal of large angle scattered electrons from various background processes that need to be suppressed. Møller scattered electrons and bremsstrahlung photons from the target are the most prominent ones. The separation of these processes is achieved by a solenoid magnet and a lead shielding system. Cherenkov light producing fused silica bars are chosen as detector technology primarily because of a very low detector response to photons and excellent radiation hardness. The development of the P2 spectrometer geometry and the choice of detector components includes detector simulations, material studies and prototype tests in beam test experiments.

The concept of the detector geometry chosen for the P2 spectrometer is illustrated schematically in figure 3.5. Note that this schematic is not to scale. Only the parts which are essential for the understanding of the detector geometry are shown, while for example the tracking system (see section 3.5) is omitted. The plotted electron tracks are only for illustrative purposes and originate from an arbitrary point in the target.

Electrons traversing a magnetic field travel on helix shaped trajectories. The spectrometer geometry is optimized such that the electrons scattered in the target within the signal angle range between 25° and 45° are focused onto the Cherenkov detectors. Most electrons scattered under larger angles will hit the inner wall of the magnet, while those being scattered under lower angles will mainly hit the Møller shield. Photons produced in the target cannot hit the Cherenkov detectors directly on a straight track. The geometric concept of this shielding is illustrated in figure 3.5 by the line of sight which is defined by the beginning of the target and the barrel shield.

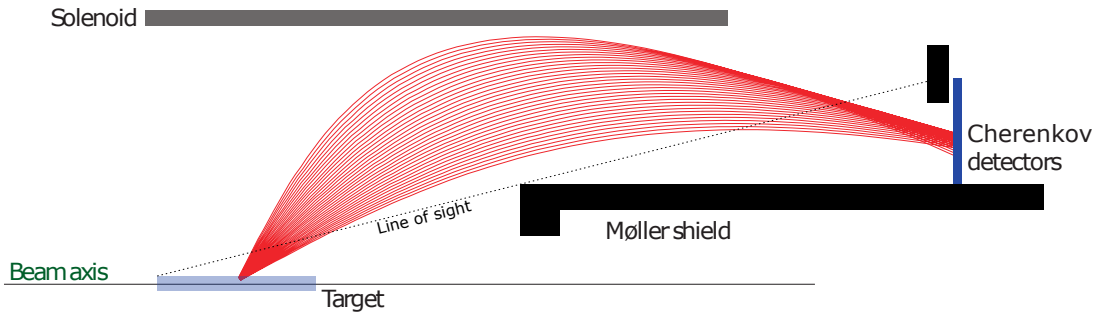

Figure 3.5.: *Schematic projection view of the P2 spectrometer geometry (not to scale). Electron tracks (in red) are for illustration and do not represent physical tracks. Modified from Ref. [13].*

The magnetic field for the P2 experiment will be provided by a superconducting solenoid. The current detector geometry is based on a magnetic field along the beam axis of $B_z = 0.6\,\mathrm{T}$. The field strength and geometry of the magnet are adopted from the magnet used for the FOPI [90] experiment. Figure 3.6 shows a CAD rendering of the complete P2 detector setup. The liquid hydrogen target being placed within the solenoid magnet needs to be operated in a vacuum chamber (also referred to as scattering chamber). However, it is not possible to operate the whole experiment in vacuum since the tracking detector needs to be operated in a helium atmosphere for cooling reasons. Although the layout of the tracking detector in this figure is simplified, it illustrates that several tracking detector modules are placed between the Møller shield and the inner magnet wall. The tracking detector geometry will be discussed in section 3.5. The placement of the tracking detector in any case requires a large gas window that separates helium and vacuum environments and withstands the pressure difference. In addition, the material of the gas window needs to be minimized to prevent additional scattering. For the P2 detector, a Kevlar® window will be developed. It is inspired by the NA48 detector, where a 0.9 mm thin Kevlar® window was used in a similar geometry with 2.3 m outer diameter [91]. A Kevlar® window of 1 mm thickness corresponds to about 0.3 % of a radiation length. The gaseous helium over a length of 2 m at atmospheric pressure in comparison only contributes with about 0.04 % of a radiation length.

Electrons passing the target without considerable scattering traverse the magnet approximately in beam direction and are further focused by the solenoid magnetic field. The vacuum in the scattering chamber extends across the inner circular opening in the Møller lead shield to the P2 beam dump. The shield will be held by a steel support system. The outer lateral surface of the lead cylinder is enhanced by a pattern of triangular profiles, which serves to suppress the reflection of photons on the surface.

The Cherenkov detector consists of 82 wedged fused silica (SiO_2) bars, wrapped in a highly reflective aluminum foil, that are arranged in a circular pattern. They provide

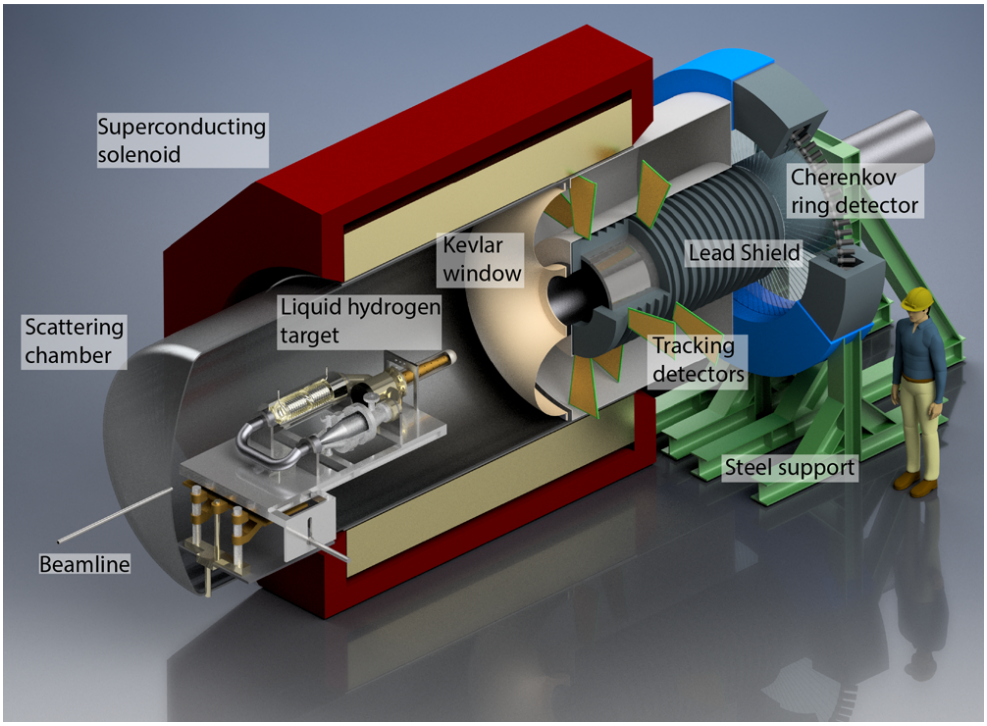

Figure 3.6.: *CAD drawing of the P2 experimental setup [13].*

nearly full azimuthal coverage. A photomultiplier tube (PMT) is attached to each bar at the outer end. The SiO_2 bars span over the radial range from 45 cm to 110 cm, but only the inner part of 45 cm length is used as active detector area. The PMTs and the outer 20 cm of the silica bars, which serve as light guides to the PMTs, are covered by an additional 10 cm thick lead shielding. The fused silica material is not only the Cherenkov medium, but at the same time also an effective light-guide. The geometry is optimized both for production and transmission of photons. In particular, light collection is improved by choosing a design that increases the likeliness of total internal reflection. Since the spectral distribution of the photons produced in the Cherenkov medium is enhanced for small wavelengths in the UV-region, both the bar material and the PMTs are selected to be working well with UV light.

The average rate of scattered electrons hitting the Cherenkov detector is expected to be around 20 MHz/cm^2. This high rate leads to an estimated total radiation dose of 80 Mrad over the whole running period and hence requires a radiation hard design for all components. It was shown that synthetic fused silica features an excellent radiation hardness.

Even though the detector geometry was optimized such that photons from the target can not hit the Cherenkov detectors directly, detector simulations have shown that the signal electron rate is dominated by photon background, which is more than one

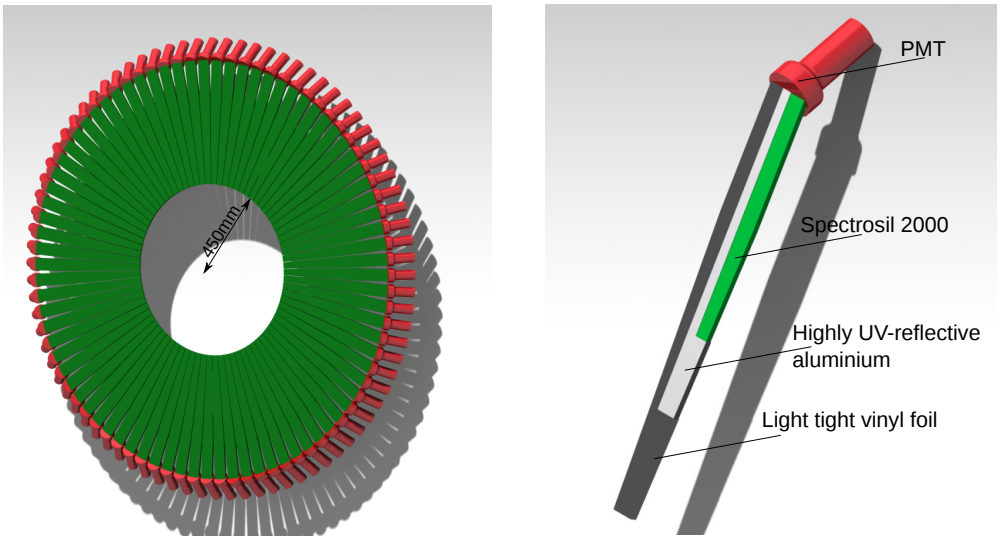

(a) *Rendering of the Cherenkov detector geometry, consisting of 82 fused silica bars arranged as one detector ring.*

(b) *Rendering of one Cherenkov detector element, consisting of the fused silica bar with optical outlet, PMT, UV reflective wrapping and light tight vinyl.*

Figure 3.7.: *Current design for the integrating Cherenkov detector elements and their arrangement. Both pictures taken from [13].*

order of magnitude higher than the signal. The photon rate therefore needs to be drastically reduced by the detector response, and the response needs to be well understood. Studies including simulations and beam test experiments have shown that the Cherenkov detectors suppress the photon background very successfully. Considering the rate of photo-electrons emitted at the PMT cathode, divided into the particle type producing this signal, the signal of scattered electrons is now more than two orders of magnitudes enhanced compared to the photon background [13, 14]. Photons hitting the Cherenkov detector need to convert to an electron-positron pair first in order to produce Cherenkov light. In addition, the produced electron or positron need to have an energy above the Cherenkov threshold of about 0.7 MeV. Since photons in the P2 experiment are mainly produced by Bremsstrahlung, most of them have very low energies.

The high rate of electrons makes it impossible to detect single electrons via the Cherenkov effect. Instead, the quartz glass PMTs are operated in a charge integrating mode. This operation mode is also referred to as current mode, since the individual pulses overlap to a continuous current, making counting statistics and any cuts based on pulse shapes impossible. For the current mode operation at low gain, the PMT must support high cathode currents and have a good linearity. The Cherenkov detector system is additionally designed to support a tracking mode operation at lower

beam current and therefore reduced particle rates ($\gtrsim$ 100 reduction factor). In this mode, tracks that are reconstructed with the tracking detector will be matched to a signal on the Cherenkov detector. This measurement serves as a systematic study in order to ensure the proper operation of all detector components. For this operation mode, the PMTs must provide fast charge collection at high gain.

The readout electronics for the integrating detectors are based on the design for the QWeak experiment. The current signal at the anode of the PMT is converted to a voltage with a trans-impedance preamplifier. This voltage signal is then further filtered and digitized with an Analog-to-Digital Converter (ADC). The ADC is located away from the detector with a shielding wall in between which implies that a cable driver is necessary for the signal transmission. An external clock synchronized to the helicity reversal will be used to control the ADC. The voltage difference of the electron signal within one helicity cycle which is attributed to the parity violating asymmetry A_{PV} is much smaller than the expected RMS signal width dominated by shot noise at the PMT anode and also smaller than the bit resolution of the ADC. In order to resolve the tiny voltage difference, the voltage signal will be sampled by the ADC many times within one helicity cycle. The voltage is then evaluated as the mean of the sampled distribution. This oversampling procedure allows to detect very small differences, given that the RMS width is much larger than the ADC resolution; this is necessary in order to exceed the digitization error.

The signal of the integrating detector is normalized to the MESA beam current monitor signal in order to get rid of any drifts and fluctuations of the beam current. The readout chain for both detectors is therefore kept identical. The usage of a fast helicity reversal rate of about 1 kHz ensures that this time scale is much shorter than any random drifts of beam current or noise level that might cause false asymmetries. In addition, helicity quartets (+−−+ and −++−) with a pseudo-random initial state are used as helicity patterns, thus removing linear and quadratic drifts.

3.4.3. Estimation of Relevant Uncertainties

The development of an experiment requires a careful analysis of its achievable accuracy and precision. All possible systematic uncertainties which might influence the result of the experiment should be investigated and quantified before its operation. Otherwise, unforeseen or underestimated sources of uncertainties might lead to less meaningful results. Such an analysis was performed for the P2 experiment in Ref. [14] and is also summarized in Ref. [13]. The method and results are very shortly summarized here.

The easiest approach in order to calculate the achievable uncertainty $\Delta \sin^2\theta_w$ would be an analytical calculation based on Gaussian error propagation for each source of

uncertainty. However, this approach is not possible since the parameter relations involve integrals which need to be solved numerically. Consequently, the analysis is done with the Monte Carlo method by generating randomized pseudo-experiments. All sources of uncertainty are assumed to be independent from each other, so that all parameters are kept constant while the parameter of interest is randomly varied within its expected uncertainty according to a Gaussian probability density function around its expectation value. For each pseudo-experiment, the weak mixing angle $\sin^2\theta_w$ is calculated, so that the uncertainty $\Delta \sin^2\theta_w$ can be derived from the obtained distribution. The dominating uncertainty contributions considered in this analysis include the statistical uncertainty, any false asymmetries A^{false}, the beam polarization P, the nucleon form factors (see sections 2.6.2 and 2.6.3 for definitions) and the theoretical uncertainty $\Delta_\square$ on the contribution of so-called box-graphs (see figure 2.9). The nucleon form factors were parametrized for this analysis.

For the beam energy E_{beam}, the central electron scattering angle $\bar{\theta}_f$ and the angular detector acceptance $\delta\theta_f$, an additional analysis was performed in which the expectation value of these three parameters were varied separately in order to scan for their optimal values with respect to the total uncertainty on the weak mixing angle. Figure 3.8 shows the result for a scan of the central scattering angle. This analysis revealed the optimal values for the beam energy $E_{\text{beam}} = 155\,\text{MeV}$, the central electron scattering angle $\bar{\theta}_f = 35^\circ$ and the angular detector acceptance $\delta\theta_f = 20^\circ$, which are the basis for the detector geometry as presented in the previous section. The total uncertainty is clearly dominated by the statistical uncertainty.

As a result of this analysis, the expected, uncorrected (meaning that it includes all systematic effects that need to be corrected for) parity violating asymmetry for signal events is obtained to be $A_{PV}^{\text{sig}} = (-39.94 \pm 0.56)\,\text{ppb}$. This result is valid for a running period of 10 000 h. The corresponding relative uncertainty on the weak mixing angle measurement for signal events is obtained to be 0.14 %. A full GEANT4 [92–94] simulation allows to investigate the influence of detector effects and background events on the measurable parity violating asymmetry. The GEANT4 simulation of the P2 detector is explained in detail in Ref.s [13, 14]. In addition, the simulation used to simulate the tracking system is based on this simulation and will be discussed in the following chapter. The expected uncorrected parity violating asymmetry incorporating effects induced by the detector geometry is reduced to $(-24.03 \pm 0.57)\,\text{ppb}$. In this case, the uncertainty was already scaled to the scheduled running time of 11 000 h. The largest contribution on the reduction is observed to be caused by electrons with lower scattering angles hitting the Cherenkov detector, but also electrons scattering off the target entry and exit windows as well as the realistic treatment of beam-target interactions have an influence. Finally, the relative precision of the P2

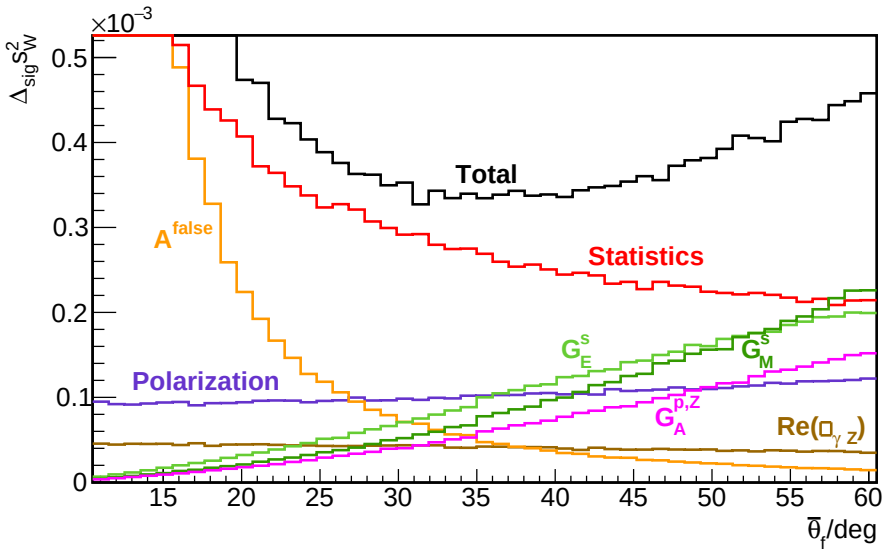

Figure 3.8.: *Dependence of* $\Delta s^2_W \equiv \Delta \sin^2\theta_w$ *on the central scattering angle* $\bar{\theta}_f$ *for* $E_{beam} = 155\,\text{MeV}$ *and* $\delta\theta_f = 20°$ *with the most dominant error contributions [13, 14]. The statistical uncertainty is calculated for a running period of* 10 000 h.

experiment regarding the measurement of the weak mixing angle is derived to be

$$\left.\frac{\Delta \sin^2\theta_w}{\sin^2\theta_w}\right|_{\text{exp}} = 0.15\,\%. \tag{3.5}$$

This relative precision value corresponds to the error bars plotted for the P2 experiment in figure 3.1.

3.5. The P2 Silicon Pixel Tracking Detector

The analysis and interpretation of the asymmetry measured with the integrating Cherenkov detectors requires advanced knowledge on the distribution of the electron momentum transfer Q^2 in the liquid hydrogen target. A tracking detector (also referred to as "tracker") based on silicon pixel sensors will be installed in the P2 detector for this task. The reconstruction of full electron tracks with the tracking detector will give further insights into the kinematics of electrons hitting the Cherenkov detectors. In particular, the scattering angle and energy must be reconstructed for a representative set of these particles. After successful operation of the P2 experiment, the value for the average momentum transfer $\langle Q^2 \rangle$ reconstructed with the tracking detector will finally fix the position of the P2 data point on the X-axis in a plot like

that shown in figure 3.1. In addition, the reconstruction of individual electron tracks with pixel sensors allows further studies of backgrounds or systematic effects that turn out to be position or momentum dependent.

The tracking detector will on the one hand be operated at reduced rates, for which the Cherenkov detectors will be operated in a single electron mode (see section 3.4.2), so that coincident hits can be matched. This mode of operation requires that at least all electrons collected on one fused silica bar are principally accessible for the tracking detector. In addition, the material in the active region of the tracking detector must be reduced as much as possible in order to suppress multiple scattering. On the other hand, it is investigated whether the tracking detector can also be operated at full beam rate. In order to achieve that, the silicon pixel sensors themselves as well as any infrastructure inside the solenoid that is needed for the sensor powering and readout must be sufficiently radiation hard. Given that suitable components can be found, the tracking detector will need to be operated in a gated mode. This means that data is only taken for a small fraction of time in order to keep the readout data rates manageable. The option to keep the tracking detector installed even at full beam rate would require to reduce any material even for mechanics outside the active tracker area. As an alternative, the tracking detector could be taken out of the experiment when running at full rate. However, this option then requires to develop a sophisticated technical design for the removal and insertion of the tracking detector.

This section aims to give an overview of the tracking detector concept, including its geometry, the sensor technology and the track reconstruction. The research conducted for this thesis, which includes Monte Carlo simulations of signal and background rates, investigations on the photon response of the pixel sensors, development of the tracker module technical design, development and simulation of the cooling system as well as the implementation of a thermo-mechanical prototype of one tracker module, will be covered in detail in the subsequent chapters.

3.5.1. Concept and Geometry

The tracking detector system is developed to reconstruct momentum and scattering angle of a representative set of signal electrons with the best achievable resolution. Both the sensor technology and the detector geometry must be optimized with the objective of reducing any systematic uncertainties. The momentum of electrons scattered in the target is limited by the beam energy of $E_{\text{in}} = 155\,\text{MeV}$. At such low momentum, multiple Coulomb scattering in the detector material is the dominant uncertainty contribution to the tracking resolution.

Electrons traversing matter are scattered many times consecutively under low angles from the material nuclei, resulting in one effective scattering angle. The projected scattering angle θ_0 for an electron scattering on some material with radiation length X_0 and thickness x can be approximated as being Gaussian distributed. The mean projected scattering angle vanishes, while the expected scattering width is then given by [55, 95, 96]

$$\theta_0^{\text{rms}} \equiv \frac{1}{\sqrt{2}}\theta_{\text{space}}^{\text{rms}} = \frac{13.6\,\text{MeV}}{\beta c\, p}\sqrt{\frac{x}{X_0}}\left[1 + 0.038\ln\left(\frac{x}{X_0}\right)\right] \sim \frac{1}{p}\sqrt{\frac{x}{X_0}}\,. \tag{3.6}$$

Here, p is the momentum of the track and βc the velocity. The formula does not account for non-Gaussian tails. For the P2 experiment, the reduction of any detector material is crucial not only because of multiple scattering, but also due to the fact that the interaction of electrons with any material other than the target protons might induce false asymmetries.

The spatial uncertainty of the track measurement points contributes additionally to the momentum and angle reconstruction resolution. A highly granular detector system for fast and precise position measurements with a low material budget can be achieved either using silicon pixel sensors or gaseous detectors. While traditional gaseous detector systems were usually limited to timing resolutions at the order of microseconds, timing resolutions better than 10 ns and at the same time spatial resolutions of less than 70 µm were already realized some time ago with Micro Mesh Gas Detectors (Micromegas) at a low material budget below 0.35 % of a radiation length [97]. There is also large progress made regarding the rate capability of this technology, however, the single particle detection is limited to particle rates of $O(10\,\text{MHz/cm}^2)$[98]. In addition, the readout of large area gas detectors with high granularity is a huge effort due to the large amount of analog channels. High particle rates can be detected reliably with novel silicon pixel sensor technologies; the P2 experiment intends to use High Voltage Monolithic Active Pixel Sensors (HV-MAPS) [99–103]. More details on this pixel sensor technology will be given in the next section.

The HV-MAPS made of silicon are 50 µm thin with only little additional aluminum material needed for signal traces. For the P2 tracking detector, they will be assembled on polyimide flexprint strips containing aluminum traces. The material budget at the active tracker area is in that way minimized to around 0.1 % of a radiation length. The pixel sensors are active electronics which implies that they consume electric power and hence produce heat. The exact heat load depends on particular chip operation parameters and is not finally known yet, but it will be in the range of 100 mW cm^{-2} to 400 mW cm^{-2}. As mentioned before, the tracking detector modules will be placed in a helium atmosphere for cooling reasons. Furthermore, additional

cooling by forced convection will be necessary. A detailed description on the mechanical design and research on the cooling requirements for the tracking detector modules will be presented later in this thesis.

The reconstruction of the electron momentum relies on measuring the curvature of the trajectory in the magnetic field. Consequently, the tracking detector system needs to be placed within the solenoid magnet. Unfortunately, the geometry of the P2 spectrometer does not allow for a geometric shielding of the tracker against photons produced in the target. It is therefore essential to use a sensor technology which ensures a low detection probability for photons. The detector response of HV-MAPS to photons was investigated for different photon energies, as it will be discussed later. In addition, the good timing resolution of these sensors helps to suppress electron track misidentification because of randomly distributed background contributions. This is of particular importance when operating the tracking system at full beam current.

An electron trajectory in a solenoid magnetic field can be reconstructed reliably by measuring its position on four tracking planes. The optimal distance between the planes depends on whether the reconstruction resolution is dominated by multiple scattering or by the positional measurement. With multiple scattering as the limiting factor, a wide drift region between two tracking planes improves the transverse momentum reconstruction. In particular, the relative momentum resolution is proportional to the scattering angle θ^{MS} divided by the track deflection angle Ω (defined in the plane perpendicular to the magnetic field, see figure 3.9) between two position measurements [104]:

$$\frac{\sigma_p}{p} \sim \frac{\theta^{\mathrm{MS}}}{\Omega} \tag{3.7}$$

A large deflection angle Ω between at least two tracking planes is therefore essential for an excellent momentum reconstruction. The placement of two tracking planes close to each other in turn facilitates the track finding. The geometry chosen for the P2 tracking detector hence consists of two tracking plane pairs. The two plane pairs allow for a direction measurement at two points along the trajectory. The optimal plane pair distance is around 1 cm to 2 cm, which roughly corresponds to the typical spatial distance of two trajectories within the time resolution of the pixel sensors, evaluated at full beam current. The distance in the built P2 tracking detector will be slightly larger than 2 cm due to mechanical constraints.

Ideally, the first position and direction measurement is done as close to the scattering vertex as possible. Unfortunately, it is not possible to build the tracking detector directly around the target because the overwhelming bremsstrahlung photon background would make any electron track finding impossible. In addition, using

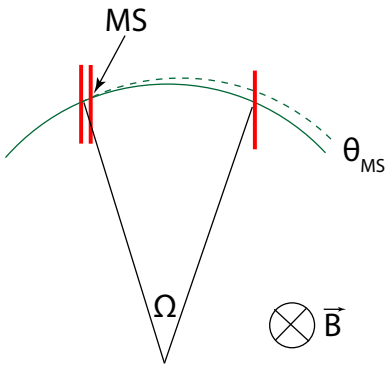

Figure 3.9.: *Projection of a charged particle track in a magnetic field deflected at the sensor plane due to multiple scattering. The relative uncertainty on the curvature measurement is reduced for larger deflection angle Ω.*

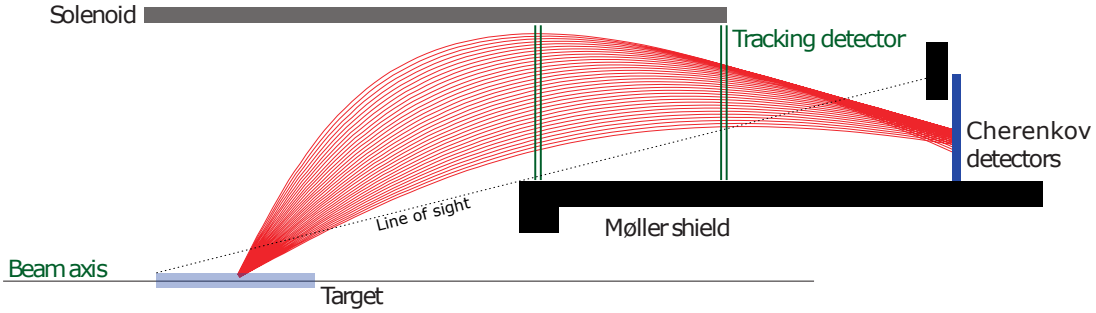

Figure 3.10.: *Schematic projection view of the P2 tracker geometry (not to scale). Two double tracker planes are placed within the solenoid and separated by a wide drift region. Electron tracks (in red) are for illustration and do not represent physical tracks. Modified from [13].*

identical detector modules for the two plane pairs facilitates their development. The optimal placement was subject to intensive Monte Carlo simulation studies, finding that placing one tracker plane pair at the beginning of the Møller barrel shield and the other one at the end of the magnet will allow for a robust track reconstruction. The placement of the tracker planes is sketched in figure 3.10.

A very simplified track reconstruction algorithm which neglects all second order effects can be constructed quite easily. Such a simplified algorithm is presented in the following in order to further illustrate the functionality of the tracker geometry described above. First, a constant homogeneous magnetic field along the beam axis is assumed and hence a helix shaped electron trajectory with its origin near the beam axis is supposed. Using a coordinate system with the z-axis along the beam axis, each of the four tracking planes $i = 1 \ldots 4$ provides a measurement of x_i and y_i coordinates at fixed z_i-coordinate. The xy-projection of a helix trajectory in a magnetic field along

the z-axis is a circle whose radius R is defined by the transverse momentum p_T of the electron track:

$$p_T = e \cdot B_z \cdot R. \tag{3.8}$$

This relation is obtained by equating Lorentz force and centripetal force. The simple model can be demonstrated by reconstructing an arbitrarily chosen signal electron trajectory from the Monte Carlo detector simulation. In order to show the limitations of this simple track reconstruction, an electron trajectory is reconstructed both for the realistic simulation and in addition for an idealized simulation. The following changes are applied in the idealized simulation with respect to the realistic one:

- A constant magnetic field along the beam axis is used instead of a realistic field map
- Any secondary scattering in the target occurring after the large angle electron-proton scattering is suppressed
- Multiple scattering in detector material is turned off.

The fit of a circle in the xy-plane to the projection of the positional measurements in the tracker planes is illustrated in figure 3.11. The coordinate system center is placed at the center of the solenoid. The data coordinates represent the exact intersection of the electron trajectory with the tracker plane since the finite granularity of the pixel sensors is not considered. For this illustrative reconstruction example, a simple least-squares fit was applied that does not consider any uncertainties on the fitted data points. Any error propagation is omitted here. Note that for the fit to the data points of the realistic simulation, an additional point at the origin was fitted. This is motivated by the constraint that the trajectory originates from the target placed on the beam axis, but it is only an approximation due to the target diameter of 15 cm. Nonetheless, it improves the reconstruction result because the additional constraint with a long flight path and the large lever arm for the curvature measurement to the first tracking plane help to reduce uncertainties induced by multiple scattering in the tracking planes. The target constraint is not used for the fit of the idealized event as any sources of uncertainty are switched off in this proof of concept.

Along a helix shaped trajectory in a constant magnetic field, the polar angle θ for the track direction in a local coordinate system with $\mathbf{e_z} \| \mathbf{B}$ is conserved. At the scattering vertex, this angle corresponds to the scattering angle, supposing an electron direction along the beam axis before the scattering event. Therefore, the scattering angle can be reconstructed by determining θ at any arbitrary point along the track. As the distance of two tracking planes of one pair is quite small, the electron trajectory between the two planes can be linearized. The track direction at this point is then given directly by the connection vector between the hit positions on the two tracking

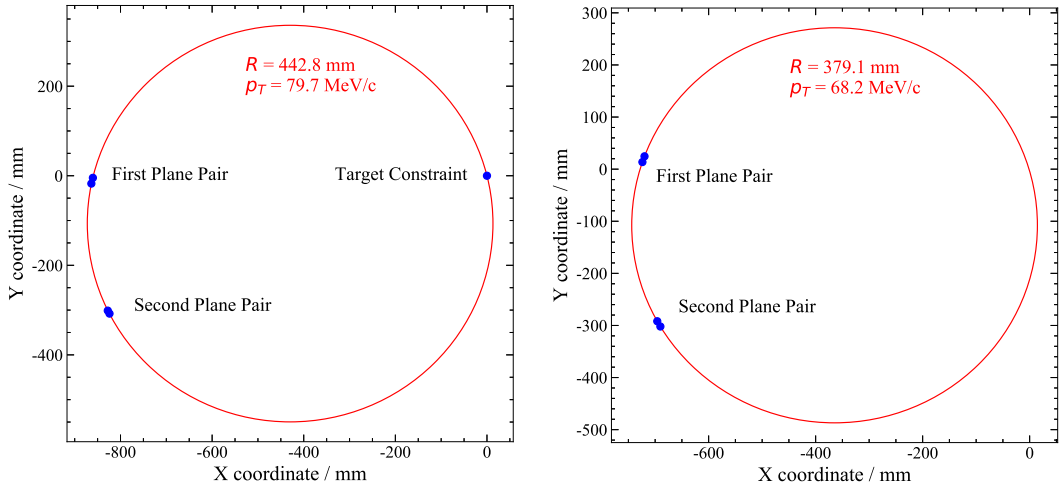

(a) *Realistic simulation event.* (b) *Idealized simulation event.*

Figure 3.11.: *Illustration of least-squares circle fit on projection of two exemplary tracker hits from simulation. The fit is illustrated both for a realistic simulation event and for an idealized simulation, see explanations in the text.*

planes. The scattering angle thus corresponds to the polar angle θ of this direction vector in spherical coordinates.

Table 3.1 summarizes the results obtained with the simplified reconstruction algorithm. Comparing the reconstructed parameter with the Monte Carlo truth information shows that both momentum and scattering angle are well reconstructed in the idealized case. The slight deviation in the reconstruction of the transverse momentum might be attributed to the finite precision of track propagation in a magnetic field in the detector simulation. At the same time, it can be noticed that the results differ notably for the realistically simulated electron track. While the reconstruction of the transverse momentum is acceptable, the deviation in the reconstruction of the scattering angle is too large in order to precisely determine the momentum transfer Q^2 in the target, which is the main task for the tracking detector. The most likely reason for the bad reconstruction is additional scattering in the hydrogen target, which can easily distort the angle under which the track leaves the target. The tracking detector system has no insight to the interactions taking place within the target, but is limited to reconstructing the direction and momentum of the electron when it leaves the target. The difference in the scattering angle reconstruction leads to the observed discrepancy in the determination of the total track momentum.

In addition, the θ angle is only conserved on a perfect helix track. However, the magnetic field in the P2 detector will not be perfectly uniform along the z-axis so that tracks will not be perfectly helix shaped. The expected field map for the P2

	Realistic Event	Idealized Event
Fit Data Coordinates $[x,y,z]$	[0,0,0] [−860.3, −4.7, 1079.9] [−863.6, −17.5, 1099.9] [−827.8, −301.2, 1639.9] [−824.0, −307.9, 1659.9]	 [−719.9, 24.6, 1079.9] [−723.8, 13.6, 1099.9] [−696.0, −291.9, 1639.9] [−690.2, −302.0, 1659.9]
p_T simulated / MeV	80.98	68.19
$\|\mathbf{p}\|$ simulated / MeV	137.82	135.08
θ simulated / °	35.99	30.32
p_T reconstructed / MeV	79.70	68.24
$\|\mathbf{p}\|$ reconstructed / MeV	144.34	135.17
θ reconstructed/°	33.52	30.32

Table 3.1.: *Reconstruction results for one realistic and one idealized sample event. Both the simplified reconstruction method and the idealized simulation setup are described in the text.*

solenoid which is based on the field map determined by the FOPI [90] collaboration and which is implemented to the P2 detector simulation is shown in figure 3.12.

As a summary, the tracking detector geometry is appropriate for track reconstruction, but more involved algorithms for reconstruction need to be developed that take care of uncertainties attributed to effects as additional interactions in the target, multiple scattering in detector material or the inhomogeneous magnetic field. The development of sophisticated track finding and reconstruction algorithms is not part of this thesis, but some results on the achievable Q^2 reconstruction performance will be summarized in section 3.5.4.

Unfortunately, building a tracking detector that is able to reconstruct all possible signal particle trajectories is not affordable because the area to cover would be too large. However, the P2 detector system is azimuthally symmetric so that covering slices of space in azimuthal direction to first order selects a representative set of particles. Investigations on the azimuthal coverage and the rotation angle of the downstream tracker modules relative to the front ones will be presented in section 4.2.1. The current design foresees each tracker module to cover around 15° in azimuthal direction. Four modules with this coverage will be arranged in a circle, so that up-down and left-right asymmetries can be tested. The optimal rotation angle is found to be around 17° for the tracking detector plane positions along the z-axis as depicted in figure 3.10.

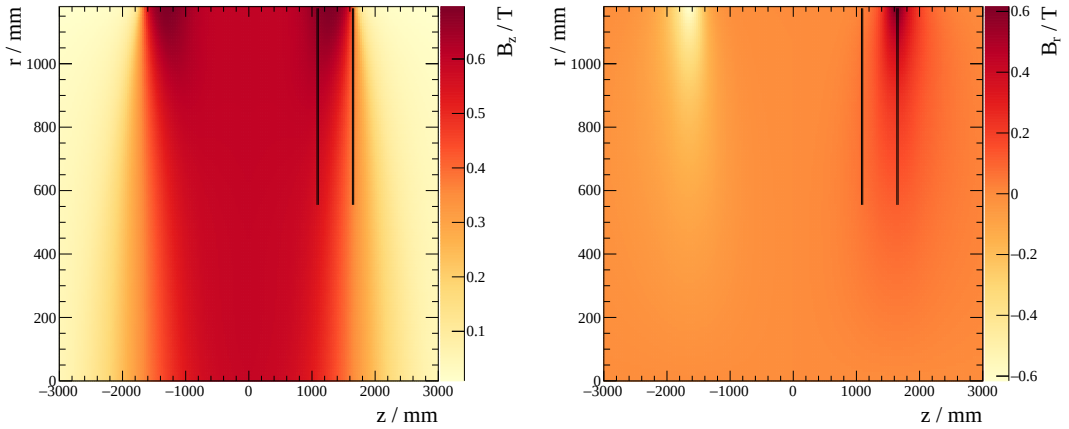

(a) *z-component of the magnetic field* (b) *r-component of the magnetic field*

Figure 3.12.: *FOPI [90] magnetic fieldmap assumed to be appropriate for the P2 detector. Courtesy of Y. Leiffels (FOPI collaboration). The placement of the tracker planes is shown for illustration. The ϕ-component of the magnetic field is considered to be zero.*

3.5.2. Silicon Pixel Sensors

Silicon pixel sensors are the most common detector technology used for high rate tracking applications like the P2 tracking detector. There are plenty of different silicon pixel sensor types used in particle physics which all specialize on particular requirements like material budget, detection efficiency, high rate capability or radiation hardness. Nevertheless, the fundamental functional principle is always the same and known as a p-n-junction-diode which is for some sensors operated with an additional reverse bias voltage.

Semiconductor materials like silicon are characterized by a relatively low energetic difference between the electrons in the valence band and the free electrons in the conduction band. This energy difference, usually referred to as band-gap, is at the order of electronvolts for most semiconductor materials and gives rise to electrons jumping from the valence to the conduction band due to thermal excitation, leaving a "hole" in the covalent bond. The random generation of electron-hole pairs is reversed again by recombination of pairs. The concentration of free electrons and holes as charge carriers can be artificially enhanced by so-called doping. In this process, silicon atoms in the lattice are replaced by donor atoms with either five (n-doped) or three (p-doped) valence electrons (compared to four valence electrons in a silicon atom), which results in one additional weakly bound electron or an artificial hole in the atom bond, respectively. Putting together differently doped volumes, the difference in the charge carrier concentration is compensated by electrons and

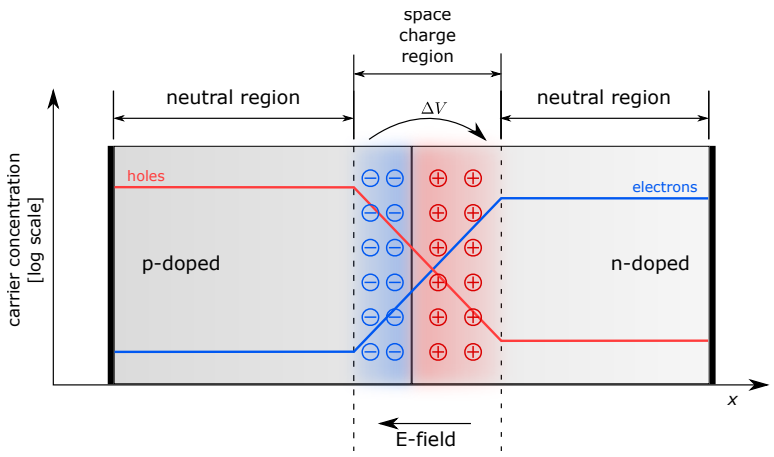

Figure 3.13.: *Schematic representation of the p-n-junction region. Both charge carrier concentration and space charges are shown. Figure taken from Ref. [105].*

holes which diffuse to the neighboring volume and then recombine. As a result, a region without free charge carriers, also referred to as depletion zone, develops at the transition region between the doped volumes. Note that this region is now however electrically charged, as it is indicated by the alternative label “space charge region”. The process is stopped by the emerging electric field preventing further diffusion of charge carriers. The p-n-junction region is depicted schematically in figure 3.13.

Operating the p-n-junction region in reverse bias voltage implies applying an external voltage between the two doping volumes with the plus pole connected to the n-doped volume and the minus pole to the p-doped volume. The reverse external voltage increases the width of the depletion zone as the charge carriers are pushed away from the transition region. This is beneficial as the depleted area acts as the sensitive volume of a silicon pixel sensor. Charged particles traversing the sensor material deposit energy due to ionization, photons might eventually deposit energy by absorption. In both cases, electron-hole pairs are created in the sensor volume. As there are no free charge carriers in the depletion zone, pairs created in this region usually do not recombine, but the electrons and holes drift in the electric field to the anode and cathode, respectively. The charge collected at the anode and/or cathode is taken as the signal indicating the detection of a particle. Electron-hole pairs created in non-depleted detector material most likely recombine and do not produce a signal, but some of them can cause a slow signal contribution due to diffusion.

The functional principle of particle detection in silicon pixel sensors as described above allows to vary and optimize many design, production and operation parameters so that different sensor types vary for example in their thickness, pixel size (corresponding to the size of the electrodes), the external voltage or the substrate resistivity. In addition to the particular sensor configuration, there are two differ-

ent main concepts concerning the realization of the sensor readout. Standard pixel sensors currently used in particle physics are so-called hybrid pixel sensors, which means that they consist of separate chips for detection and readout. The two chips are connected by one bump-bond per pixel to transfer the analog signal. This concept is outlined in figure 3.14a. The main disadvantage of the hybrid pixel technology is the additional material attributed to the bump-bond and the readout chip.

Monolithic pixel sensors integrate both sensor matrix and readout in one piece of silicon. The P2 tracking detector will be built using High Voltage Monolithic Active Pixel Sensors (HV-MAPS), which combine high-voltage CMOS (complementary metal-oxide-semiconductor) technology with standard low-voltage CMOS transistors to implement complex internal electronics for the readout. The sensor taken for P2 uses a P-substrate process; the CMOS logic is then embedded in deep N-wells. The PMOS (p-type metal-oxide semiconductor) transistors are placed directly in the N-well, while the NMOS (n-type metal-oxide semiconductor) transistors are in P-wells which are placed inside the deep N-well. The concept is shown in figure 3.14b. An external high voltage of 60 V to 90 V is used as reverse bias voltage, allowing for fast charge collection via electron drift. The depletion zone width at these voltages is at the order of 10 µm. The remaining non-depleted P-substrate is not needed so that these sensors can be thinned down from the back to 50 µm.

The sensors which will be used for the P2 tracking detector are primarily developed for the Mu3e experiment [107]. Several prototypes of this type of sensors - known as the MuPix chips [108, 109] - have been built and tested. The newest prototype is the MuPix8 sensor [110], which is the first large area prototype with a size of 1 cm × 2 cm. The final sensor is supposed to have a size of 2 cm × 2 cm with a pixel size of $(80\,\mu m)^2$. Any test measurements presented in this thesis were performed with the MuPix7 prototype sensor [111, 112]. This prototype sensor has a smaller active area of 3.8 mm × 4.1 mm and consists of a pixel matrix with 32 × 40 pixels of size 103 µm × 80 µm. It is the first prototype sensor that contains all components required for the readout scheme of the final sensor. The electronics implemented in each pixel include a signal amplifier and a line driver. Four high voltage pixels are depicted in figure 3.15. Further processing steps such as signal discrimination, digitization or timestamp generation are done in the sensor periphery at the bottom of the sensor.

The MuPix sensors have been tested extensively in several beam test measurements (see the references given for detailed results). The detection efficiency for charged particles was measured to be above 99 % with background noise rate below 1 Hz per pixel. The efficiency was also tested for high electron rates at MAMI. An area of about $0.2\,mm^2$ was illuminated on the MuPix7 sensor with 800 MeV electrons at a rate around $10\,MHz/mm^2$, leading to only a slight decrease of the efficiency which can be explained by the deadtime for every pixel of around 1 µs. The timing resolution

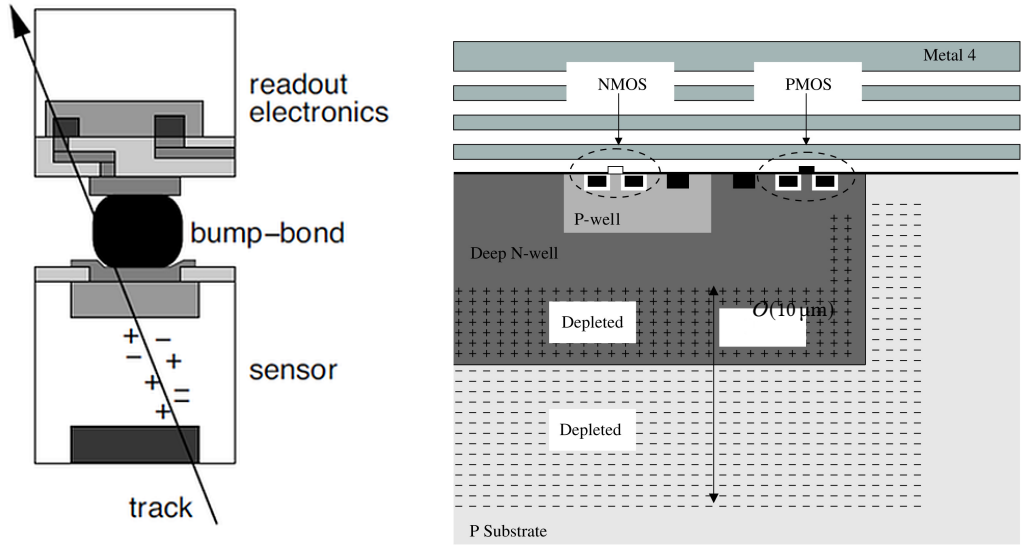

(a) *Hybrid pixel concept. One bump-bond per pixel connects sensor and readout chip. Picture taken from [106].*

(b) *HV-MAPS pixel concept. Complex pixel electronics is placed directly inside the diode cathode of the sensor. Picture taken from [99] with modified annotation.*

Figure 3.14.: *Hybrid pixel sensor and monolithic pixel sensor in comparison. The integration of readout electronics into the sensor chip reduces the material budget and makes the complex bump-bonding process redundant.*

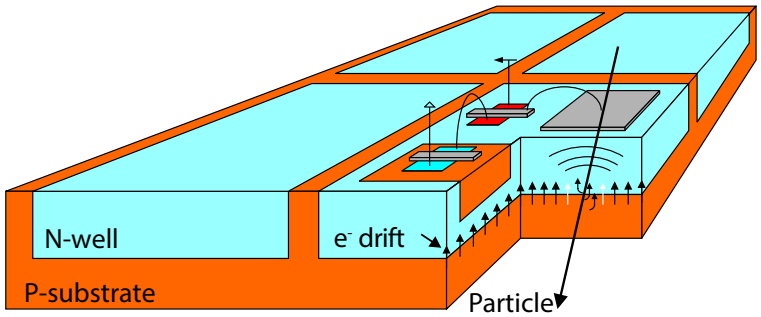

Figure 3.15.: *Four high voltage pixels with electronic readout circuitry embedded in N-well. Picture taken from Ref. [99] with modified annotation.*

of the MuPix7 was determined to be below 15 ns. Due to the high rates and long running time of the P2 experiment, radiation hard sensors are required. The MuPix7 sensor was found to feature an excellent radiation hardness in a dedicated irradiation study [113].

3.5.3. Readout

The data rate generated in the sensors while running the experiment at full beam rate with the tracker modules put in place would be excess of 1 Tbit/s, as it will be shown in section 5.2. Such a high data rate is more than any affordable readout system can possibly manage. In case that track reconstruction at full beam rate is actually aimed for, it would require to operate the pixel sensors in a gated mode. The sensors would then collect data only for short time slices and be inactive for the remaining time. Again, for the reconstruction of Q^2 in the target or for any systematic studies, a representative subset of particles is perfectly sufficient, as the reconstruction uncertainties will anyway be dominated by systematic uncertainties. For the operation of the experiment in a tracking mode, where the Cherenkov detectors are detecting single electrons which can be matched to reconstructed tracks, the beam rate is not determined yet, but it will be reduced such that continuous data taking becomes possible.

The MuPix HV-MAPS include a state-machine collecting and serializing the hits. Each sensor will then send triggerless, fully digital and zero suppressed hit data, in particular column and row positions of the hit and the timestamp generated on the sensor, via a Low Voltage Differential Signaling (LVDS) link at a rate of 1.25 Gbit/s. The further processing of the data is foreseen to be controlled using Field Programmable Gate Arrays (FPGAs) on front-end boards. These boards are placed outside the P2 detector volume in order to avoid radiation damage. As the sensor chips are not capable of driving the signal over such long distances, either LVDS repeaters or radiation hard optical links need to be implemented on the tracker modules.

The data streams of several nearby sensors of a tracker plane pair will arrive at one front-end board. After synchronizing the data, the rate can be reduced by finding hit pairs being compatible with particle tracks traversing a tracker plane pair and by rejecting the hits for which no matching hit is found. In particular, this approach is efficiently rejecting photons that get absorbed in a sensor and thus create only one hit. The data containing hits with one or more matched hit is afterwards transferred to computers on which the sophisticated track finding and reconstruction algorithms will be executed.

3.5.4. Reconstruction Performance

The track reconstruction has to be done in two steps, namely track finding and track fitting. Track finding in the P2 experiment is a very challenging task since the high occupancy allows for numerous possibilities to combine hits on all four tracker planes to one trajectory. Instead of analyzing all those possible combinations and check for physical electron trajectories originating from the target, a less computational power intensive algorithm was developed [114]. This track finding algorithm tries to find a track by following it backwards, starting with hit pairs on the tracker plane pair farther away from the target at the end of the magnet. This starting point is chosen as the occupancy at this plane pair is lower compared to the front plane pair. The algorithm then aims to match further hits on the front plane pair which are compatible to a helix trajectory originating from the target. However, explicit extrapolation based on two hits on the back plane pair is not possible since three measurement points are necessary for a momentum estimate. The two measurements on the plane pair are very close to each other so that using the extended target as the third point does not define sufficient constraints for a proper momentum estimate. The main challenge hence is defining a region of interest (ROI) for each of the two front tracking planes in which possible matching hits are searched for. Using rather large ROI is inefficient due to the overwhelming combinatorial background while using smaller ROI might increase the possibility of missing the correct hits. The main feature of the mentioned algorithm labeled "parametrization based tracking" is the pre-calculation of search windows based on Monte Carlo simulation. The possible hit combinations within the determined regions of interest are then accepted or rejected as track candidates based on the χ^2 of a track fit. It was shown that this algorithm is capable of providing a signal-to-background ratio better than 10 and an efficiency around 85 % even at full beam rate [114]. Further analyses are ongoing evaluating possible biases in the reconstructed Q^2 distribution due to inefficiencies or misidentifications of the track finding algorithm.

The second step in the reconstruction chain is track fitting. The full fit must take into account the inhomogeneous magnetic field and multiple scattering in detector material. The fit developed for the P2 tracking detector [115] makes use of the General Broken Lines track fitting method [116]. A rough seed track is needed for this fitting method. It is constructed in a similar way as the method described in section 3.5.1. The propagation of the track in the inhomogeneous magnetic field between the tracker planes and to the target is implemented using an adaptive Runge-Kutta-Nyström method [117–120]. This track fitting framework takes into account multiple scattering in the tracking planes, which implies that not only momentum and polar angle θ of the helix trajectory are determined, but also shifts in the measurement planes and the projected angle of multiple scattering for each of the tracker planes are fitted. The momentum and θ angle are reliably reconstructed considering their

values on the very front tracking plane. Figure 3.16 shows the residuals for the reconstructed values of these two parameters evaluated with Monte Carlo simulations. It can be seen that the momentum resolution is around 2 MeV and the polar angle resolution is around 3 mrad.

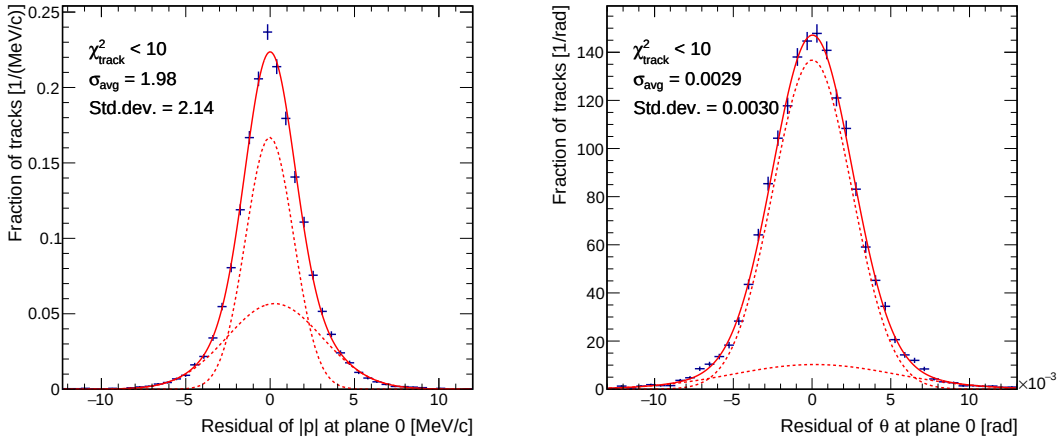

(a) *Absolute momentum* (b) *Polar angle*

Figure 3.16.: *Reconstructed minus simulated parameters of simulated electron tracks determined at the first tracking plane with a requirement on the track fit* $\chi^2 \leq 10$. *The fit to the residual distribution is the sum of two Gaussians, the resolution* σ *is the area-weighted mean. The given standard deviation is calculated from the histogram. Figures taken from [13].*

The extrapolation of the trajectory from the first tracker plane back to its vertex induces additional uncertainties. Scattering is possible both in the Kevlar® window and in the target itself, the latter one represents the dominant contribution. While scattering uncertainties mainly affect the reconstruction of the scattering angle, the total momentum $|\mathbf{p}|$ is altered by additional energy loss in the target. Consequently, taking the momentum and angle reconstructed on the first tracking plane, as shown in figure 3.16, and inserting them into equation 2.64 for the Q^2 determination might lead to substantial deviations from the true momentum loss Q^2 actually occurring in the target. The treatment of energy loss and scattering processes in the extended target hence is the main challenge in order to achieve an unbiased estimate of Q^2. This is particularly difficult as the energy loss and the detector acceptance feature non-Gaussian distributions. The same issue appears when considering corrections due to initial state radiation when an electron emits a photon before scattering. All these processes occurring in the target will need to be modeled with the help of a Monte Carlo simulation. The simulation must be tuned such that it agrees with control distributions observed in data. Above all, the parameter distributions of reconstructed

tracks that can be extrapolated back to the target envelope must be reproduced. The development of such algorithms is ongoing. Figure 3.17 shows the residuals for a current version of the Q^2 reconstruction algorithm. It can be seen that the statistical precision is sufficient even with only a few reconstructed tracks. The observed resolution per track is $3 \times 10^{-4}\,\mathrm{GeV}^2$, which corresponds to around 4 %. The overall uncertainty will hence be determined by systematic effects. The uncertainty on the applied multiple Coulomb scattering models describing the target interactions are currently presumed to be the largest contribution.

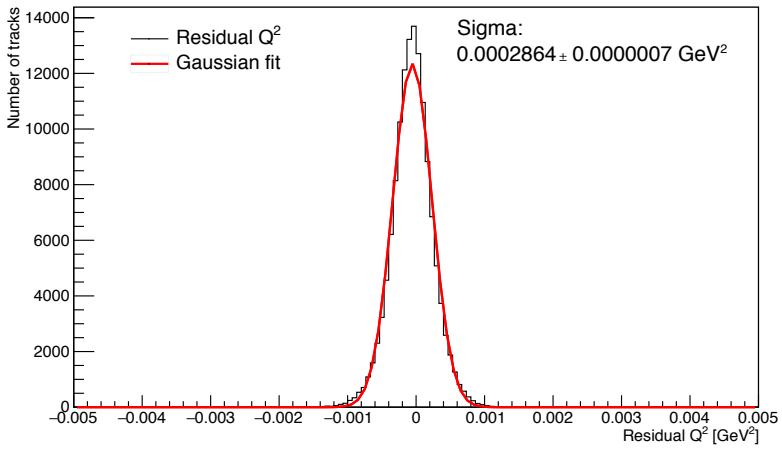

Figure 3.17.: *Reconstructed minus simulated momentum transfer Q^2 for simulated electron tracks. Figure taken from [13].*

The reconstruction of electron tracks with the P2 tracking detector requires a proper sensor alignment. The tracking detector will be built with the premise to achieve the best possible mechanical alignment. However, mechanical detector alignment is expected to be limited to $O(100\,\mu\mathrm{m})$ precision. The results can be improved to micrometer precision with several iterations of track based alignment, a technique that is used in several particle physics experiments. Shifts in the positioning of single sensors or complete detector modules can be identified using tracks recorded at very low beam rate, preferably originating from a small-sized target for easier locating of the track vertex. The track based alignment for the P2 tracking detector will make use of alignment software developed for the Mu3e experiment [121] based on the Millepede II framework [122, 123].

Part II.

Simulation and Background Studies

4 Detector Simulation

The feasibility of the P2 experiment in general and the tracking detector in particular are studied with a GEANT4 [92–94] based detector simulation. The simulation allows to consider both individual particle tracks and accumulated particle distributions on different detector parts. The possibility to evaluate the physics results for various different detector configurations makes the simulation an important tool for the optimization of the detector geometry. With the GEANT4 framework, the outcome of an experiment is predicted based on the Monte Carlo method. A given number of initial incoming particles, in the case of the P2 experiment electrons of 155 MeV, are simulated consecutively. Every particle is followed along its track and subject to randomized interactions based on the corresponding cross sections. Several physical processes lead to the creation of new particles, which are then simulated with the same approach as the initial particle. Every particle is simulated until it is absorbed, leaves the defined detector volume or is artificially killed. The Monte Carlo approach leads to a large amount of simulated particles and an even higher number of calculated and randomized physical processes and is therefore computationally intensive.

The generation of meaningful simulation results requires a sufficient statistical sample of simulated particles. At the same time, the simulation run time to produce the results must be kept reasonable. The time to simulate a given number of initial particles is mainly determined by the complexity of both the implemented detector geometry and the models used to simulate particular physical processes. Different physical models for the same process are available within the GEANT4 framework. They vary in their complexity, thus providing more accuracy for the cost of more computations. The implementation of a detector simulation for a particular experiment requires considerations on which physical processes are most relevant for the outcome of the experiment and therefore need to be modeled most accurately. The

interpretation of the simulation results needs awareness for this intrinsic model dependence.

The P2 detector simulation was originally written by Dominik Becker and used for the development of the P2 spectrometer geometry and extended sensitivity studies, which were outlined in the previous chapter. These efforts are described in detail in Ref. [14] and are also summarized in Ref. [13]. The original version of the P2 simulation was adapted to the specific requirements of analyses concerning the tracking detector as a part of this thesis. The main changes and their motivation are recapitulated in this chapter. In addition, the main experiment specific features of the P2 simulation itself are summarized.

4.1. Physics Models

The choice of suitable physics models is crucial in order to obtain meaningful simulation results. The GEANT4 framework is the standard tool used for the detector simulation of basically any particle physics experiment, but also for other applications for example in medical science. A variety of standard physics list constructors is therefore available, each of them matching specific use cases. The choice of a suitable list of physics processes is mainly determined by the energy range of the experiment. The beam energy in the P2 experiment is 155 MeV so that processes in the energy range far above the proton mass are not relevant. However, for the correct representation of hadronic background and for radiation load analyses, electro-nuclear and hadronic processes need to be considered.

As the physics lists provided by the GEANT4 collaboration are regularly validated both technically and physically, it is recommended to make use of them. The P2 tracking detector simulation was hence reconfigured to use the `QGSP_BIC_HP_EMZ` physics list. It is slightly adapted in order to remove events interfering with the custom signal event generator described later in this chapter. This physics list uses a quark gluon string model for high energy interactions of hadrons. However, the energies where such physics processes happen are much higher than those appearing in the P2 experiment so that this model will actually never be applied. Protons, neutrons and pions at lower energies are simulated using a binary cascade model [124], which is recommended to be used for energies below 200 MeV [125]. In addition, a high precision neutron model is used for neutrons below 20 MeV. It was observed that the inclusion of this more precise low energy neutron transport model has a notable influence on the neutron background observed in the simulation. The chosen physics list includes the electromagnetic physics of the `G4EmStandardPhysics_option4` package, which applies the most accurate electromagnetic models available.

4.1.1. Single and Multiple Scattering Models

Multiple Scattering in detector material is the dominant contribution to the resolution of reconstructed momentum and scattering angle. It is therefore crucial to correctly model this process in the simulation, otherwise any reconstruction study could possibly be biased. The scattering models available in GEANT4 were therefore compared in a test simulation to investigate whether changes in this sector with regard to the default physics list configuration are necessary.

For the passage of particles through dense materials, numerous interactions with atoms take place. Single scattering models are available which take into account each of these interactions. However, simulating each individual interaction quickly becomes very computationally intensive, thus making the simulation intolerably slow. Several multiple scattering models are available within the GEANT4 framework in order to solve this problem [126]. Instead of simulating each individual scattering interaction, these models parametrize the scattering process based on the incident particle and its energy as well as the scatter material and its thickness. These models are expected to model the scattering process quite accurately for dense materials [127], while they might easily fail for materials with lower density.

The available scattering models were tested considering the passage of 155 MeV electrons through 50 µm silicon and through 1 m helium. Both are materials that contribute to the multiple scattering interactions appearing within the P2 detector. As a single scattering model, the default single scattering model `G4CoulombScattering` was tested. For multiple scattering, the models `G4UrbanMscModel`, `G4GoudsmitSaundersonMscModel` and `G4WentzelVIModel` were tested. The `GoudsmitSaunderson` model was updated from version 10.1 to 10.2 of GEANT4 so that both models are considered for this analysis. This model was again updated for version 10.4, but this newest version was not considered. For each model and material configuration, 100000 electrons were directed orthogonally on the scatter volume and the angle θ_{space} between the ingoing and the outgoing electron direction after traversing the material was investigated. No limits to the internal GEANT4 step length calculation were applied. Other electromagnetic processes such as ionization and bremsstrahlung were simulated simultaneously using the respective default models.

Figure 4.1 shows the resulting normalized angular distributions. The graph labeled as Highland formula gives the normalized distribution described by the scattering width based on equation 3.6 and was added for comparison. The underlying scattering widths are calculated to be 0.782 mrad for 1 m helium and 1.446 mrad for 50 µm silicon. This formula only models the central 98 % of the projected scattering angles and assumes them to be Gaussian distributed. The GEANT4 scattering models additionally take into account non-Gaussian larger angle scatterings and are therefore not expected to perfectly match this distribution. Beside that, the space angle θ_{space}

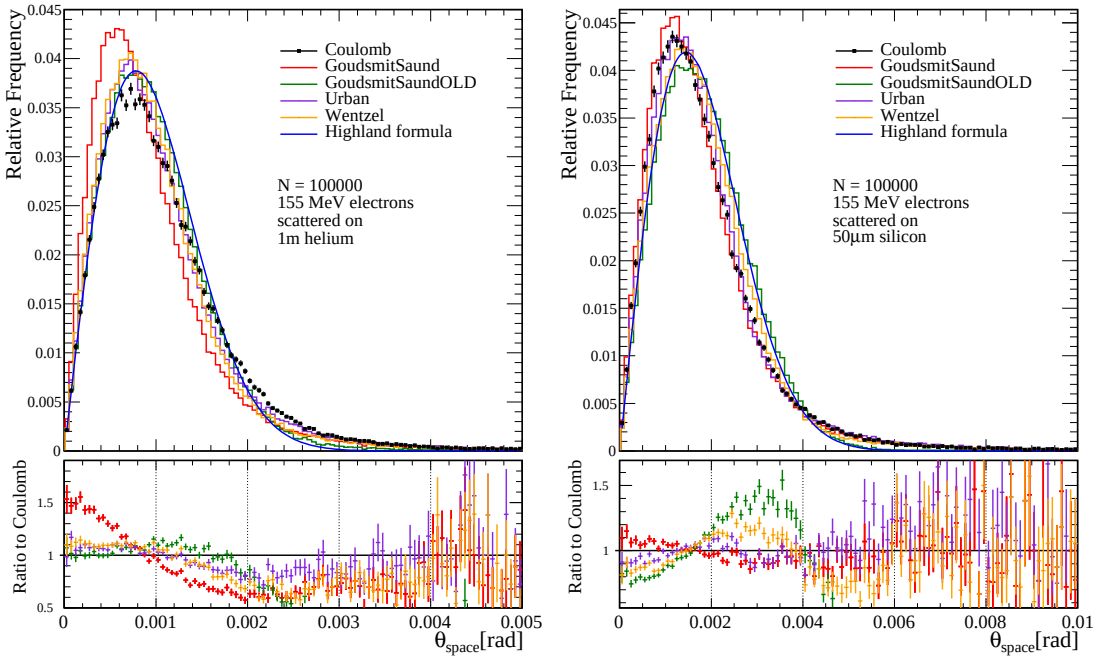

(a) 1 m *Helium* (b) 50 µm *Silicon*

Figure 4.1.: *Test of* GEANT4 *multiple scattering models for* 155 MeV *electrons scattered on helium and silicon. The curves show the normalized space angle distributions. The prediction of the Highland formula is shown for comparison. The ratio of the multiple scattering models to the single Coulomb scattering model is shown in the bottom. More details on the simulation configuration are given in the text.*

considered here is not Gaussian distributed as it includes an additional geometrical factor $\sin\theta$. The ratio plots at the bottom of figure 4.1 show the ratios of the multiple scattering models to the single scattering model for better visualization of the differences in the distributions.

The comparison of the different multiple scattering models shows that most of the models agree with each other quite well. However, considerable differences can be observed for particular models and material configurations. The old (GEANT4 version $\leq$ 10.1) GoudsmitSaunderson model fits best to the Highland curve both for helium and silicon, but hardly produces any larger scattering angles. It is therefore not recommendable to use this model if larger angle scatterings are relevant, as it is the case in the P2 experiment. The new implementation [128] of this theory model [129] shows good agreement with the single scattering model [130, 131] as well as with the Urban [132] and Wentzel [130, 133] multiple scattering models for the scattering of electrons in silicon.

However, larger deviations of these models appear for the scattering in helium. The angle distribution obtained with the new GoudsmitSaunderson implementation is clearly shifted to lower angles compared to the other models and the prediction by the Highland formula. All multiple scattering models seem to generate less large angle scatterings than the single scattering model. Nevertheless, the Urban and Wentzel multiple scattering model still show fairly good agreement with the single scattering model.

As a summary, both the Wentzel and the Urban multiple scattering model produce adequate results in helium and silicon. The newer implementation of the Goudsmit-Saunderson model works well in silicon. These models should potentially be further evaluated experimentally with a particle beam.

4.1.2. Signal Generation and Event Normalization

The P2 spectrometer is designed such that it selects electrons which leave the target under a scattering angle in the range of 25° to 45°. It is expected to scatter one electron into the signal angle and energy range for about 10 000 simulated beam electrons. Note that electrons which scatter on many electrons and/or protons in the target under low angles and by that leave the target under an accumulated effective large scattering angle are considered as background. This distinction is of course only possible with Monte Carlo events. The low probability of signal events makes it hard to simulate a sufficient number of them in order to get statistically meaningful results. It is therefore necessary to bias the simulation and generate more signal events relative to background events as there are in reality. For that purpose, a tailored signal generator was developed and implemented to the P2 detector simulation by Dominik Becker [14]. Although it would be possible to bias the simulation with tools implemented into the GEANT4 framework, the implementation of a custom signal generator will allow to consider more complex processes such as initial state radiation in the future. The signal event generator is simulating exclusively large angle scatterings, while all other energy loss and low angle scattering processes in the target are further modeled with standard GEANT4 libraries. The artificial enhancement of signal events is balanced by weighting events corresponding to their cross section in any analysis of simulation results, thus ensuring the correct representation of signal counts.

The signal generator is implemented such that large angle scattering events are induced at random positions along electron trajectories through the target. A reference length parameter l_{ref} is introduced which defines the average track length between two generated large angle scattering vertices. Technically, the simulation is done in three steps. First, only the interaction of the beam with the target is simulated. The trajectories of the electrons along the target are tracked and vertex positions for the

large angle scatterings are sampled. Only electrons with an energy above 20 MeV are considered for vertex generation, as the signal generator is implemented in order to enhance the abundance of rare events while large angle scatterings become rather likely at low energies. In addition, electrons with lower energies will not reach the integrating detectors. The sampled vertex positions and the corresponding track states, defined by energy and direction of the electron, are logged to a ROOT [134] file, while the particle itself and all secondary particles are further simulated unaffectedly until they leave some volume defined around the target. The positions and track states where the particles leave this volume are again logged and the simulation is stopped. The signal and background events are then simulated in further independent simulation runs based on these saved initial states. This approach has the advantage that any change in the setup that does not affect the target interactions can be simulated without simulating the target again. The background simulation simply continues the particle tracks as they were stopped when leaving the defined volume around the target without any changes of parameters, so that the simulation of these events in two steps is only a technical feature without any physical implications.

In a signal production run, an electron track is started at each previously generated initial vertex. The scattering angle θ and the azimuthal angle ϕ of the electron track are randomized according to flat probability density functions within a defined angular range. For the simulation results presented within this thesis, the angular ranges were chosen to be $\theta \in 10°$ to $90°$ and $\phi \in 0°$ to $360°$. Note that this θ-range is larger than the angular range selected by the P2 spectrometer which means that not all events generated with the signal generator represent signal events as defined beforehand, but are labeled as signal events within this section. In addition to the electron track, a proton track is initiated at the same vertex position with an initial four momentum that corresponds to the proton recoil caused by the associated electron track.

The main part of the signal generator is the weighting of the generated signal events. Both signal and background events in the P2 simulation are normalized such that the results can be interpreted as event rates. The event weight is therefore defined as the ratio of the particle flux expected in real data divided by the corresponding number of simulated particles. The event weights hence have dimension s^{-1}. The beam current of 150 µA in the P2 experiment corresponds to an incoming flux of beam particles $\Phi = 9.36 \times 10^{14}\,\mathrm{s}^{-1}$. In the case of background events, the event weight is therefore simply given as

$$w_{\mathrm{bkg}} = \frac{\Phi}{N} \tag{4.1}$$

with N being the number of simulated beam electrons.

The events produced by the signal generator are weighted according their cross sec-

tion. In the real experiment, the probability $\frac{\mathrm{d}p}{\mathrm{d}\Omega}$ for an electron to be scattered within an infinitesimal trajectory segment $\mathrm{d}l$ in the target to a given direction can be calculated to be

$$\frac{\mathrm{d}p}{\mathrm{d}\Omega} = \eta \cdot \mathrm{d}l \cdot \frac{\mathrm{d}\sigma}{\mathrm{d}\Omega} \tag{4.2}$$

with the target particle density η. The differential cross section $\frac{\mathrm{d}\sigma}{\mathrm{d}\Omega}$ is calculated based on the Rosenbluth formula given in equation 2.65. It can be seen from this formula that the energy of the incoming electron E at the interaction vertex and the scattering angle θ determine the probability of the scattering event. As the energy dependence of the cross section will enter the weight of each signal event, the signal generator relies on the correct simulation of energy loss processes within the target. In the simulation, the infinitesimal trajectory segment $\mathrm{d}l$ is approximated by a step length Δl. The step length is limited to a maximum of 1 mm within the target. The probability to create a signal vertex within a simulation step in the target is given by the ratio $\Delta l / l_{\mathrm{ref}}$. For each simulation step, the probability $p_{\mathrm{sim}}(\Omega)$ for an electron to be scattered to a given direction is then given by

$$\frac{\mathrm{d}p_{\mathrm{sim}}}{\mathrm{d}\Omega} = \frac{\Delta l}{l_{\mathrm{ref}}} \cdot \frac{\mathrm{d}\rho}{\mathrm{d}\Omega} = \frac{\Delta l}{l_{\mathrm{ref}}} \cdot \frac{1}{\sin\theta \, \Delta\theta \, \Delta\phi} \, . \tag{4.3}$$

In this case, ρ is the probability to pick a particular set of $(\theta,\ \phi)$ values. As flat probability densities are used, it is given as the reciprocal of the angle ranges within which the angles were randomly picked. With the approximation $\mathrm{d}l \ \rightarrow \ \Delta l$, the weight of each signal event generated as described above is given by the ratio of the two preceding scatter probabilities multiplied by the background weight for the overall normalization:

$$w_{\mathrm{sig}} = w_{\mathrm{bkg}} \cdot \frac{p}{p_{\mathrm{sim}}} = \frac{\Phi}{N} \left(\eta \cdot l_{\mathrm{ref}} \cdot \Delta\phi \, \Delta\theta \cdot \sin\theta \cdot \frac{\mathrm{d}\sigma}{\mathrm{d}\Omega} \right) \, . \tag{4.4}$$

Any analysis following the detector simulation must take into account the weight associated to each event, as the pure event count does not have any physical meaning for a biased simulation.

As the signal generator described as above adds additional signal events to the outcome of the simulation with only the GEANT4 physics models applied, large angle scatterings might be considered twice and therefore overestimated. It is therefore crucial to suppress the occurrence of scattering events in the background simulation if they fall into the scattering angle and energy range covered by the signal generator. More details on how this suppression is achieved in the P2 tracking detector simulation will be given in the following section.

A signal generator taking into account initial state radiation is available as a prototype version and further developed by the P2 theory group. The radiation of a photon has an influence on the momentum transfer Q^2 in the target and hence needs to be considered for such analyses. However, this new signal generator was not used for any of the results presented in this thesis.

4.1.3. Combination of Signal and Background Scattering Models

The simulations performed for this thesis were done using version 10.2 of GEANT4. In this software version, the default multiple scattering configuration of the chosen "option 4" for the electromagnetic physics list is to use the Urban multiple scattering model up to a particle energy of 100 MeV[1]. At energies above this value, the Wentzel model is used combined with the single Coulomb scattering model. The combination works such that a limit angle between the two models is computed dynamically based on the kinematics and material [128]. As mentioned in section 4.1.2, the simulation is done in three consecutive simulation runs. First, the target interactions are simulated. After that, signal and background are simulated in two additional runs based on the vertex positions and particle states generated in the first run. For these two runs, the original configuration of the "option 4" electromagnetic physics list is used without any additional changes.

When simulating the target interactions, and generating vertices for the custom signal generator, scattering angles in the range covered by the signal generator must not appear in a single scattering event. Nonetheless, a large scattering angle due to the accumulation of many small scattering angles in multiple scatterings is an additional background that needs to be considered. Single scattering events are hardly distinguishable from the parametrized multiple scatterings within the Urban multiple scattering model. In the unadapted version of the simulation, the Urban model was replaced by a modified version of the old GoudsmitSaunderson implementation, which allowed to remove particles interfering with the signal generator. Unfortunately, this model was shown previously to systematically underestimate larger scattering angles. It was therefore decided to use other scattering models and therefore to rewrite the removal of large angle scatterings for the simulation used in tracking detector analyses.

Single scattering events can easily be identified in the case that the Wentzel model is used in combination with the single scattering model. Here, every event in which the single scattering model is invoked is interpreted as a single scattering event,

[1] From version 10.4 of GEANT4, the default configuration is to use the again updated implementation of the GoudsmitSaunderson model in this energy range

for which the scattering angle can easily be recorded. The physics list is therefore changed such that the Urban model is used only up to 10 MeV kinetic energy, which is outside the application range of the signal generator. The combination of the Wentzel multiple scattering and the single Coulomb scattering model is then used down to this energy. It is possible to assign an upper limit for the dynamically calculated limit angle between these two models[2]. Larger angles are then always simulated by the single scattering model independent of the kinematics. The upper limit is therefore set to 10°, which is in the default simulation parameter configuration the low angle limit of the signal generator. The default single Coulomb scattering model is replaced by a slightly modified custom model, which is implemented as a class derived from the original scattering model. The only difference to its base class is that it additionally checks the scattering angle after the calculation of the scattering process. In case that a scattering angle above the limit appeared for a beam electron within the liquid hydrogen target volume, the corresponding electron track is killed at the scattering vertex. This procedure ensures that the scatterings treated by the signal generator are not added twice to the simulation.

The correct operation of the custom signal generator and the removal of scattering events interfering with it were tested by comparing kinematic distributions of the removed electrons with those of the generated ones. Figure 4.2 shows the results for the angular distribution of the scattered electrons and for their kinetic energy before the scattering. It can be seen that in both cases, the kinematics of the generated electrons agree very well with those of the removed ones. The distributions are normalized to the foreseen beam current of the P2 experiment by weighting the corresponding events in the way described in section 4.1.2. The good agreement of the distributions hence not only shows the signal generator and the removal of interfering events to be working properly, but also proves the correct normalization of the generated signal events relative to the background processes.

4.2. Detector Geometry

The detector simulation as used for the development of the P2 spectrometer geometry and for asymmetry analyses uses an interface based on the Standard Triangulation Language (STL) in order to import the detector geometry. This approach is useful for such analyses as it allows to investigate different geometries in every detail without any changes in the simulation code. However, the description of the geometry with triangulated surfaces increases the simulation runtime significantly. In addition, for most analyses concerning the tracking detector, many geometry details are irrelevant. It was therefore decided to implement a slightly simplified detector geometry

[2] This is achieved using the `SetMscThetaLimit()` method of the static `G4EmParameters` class

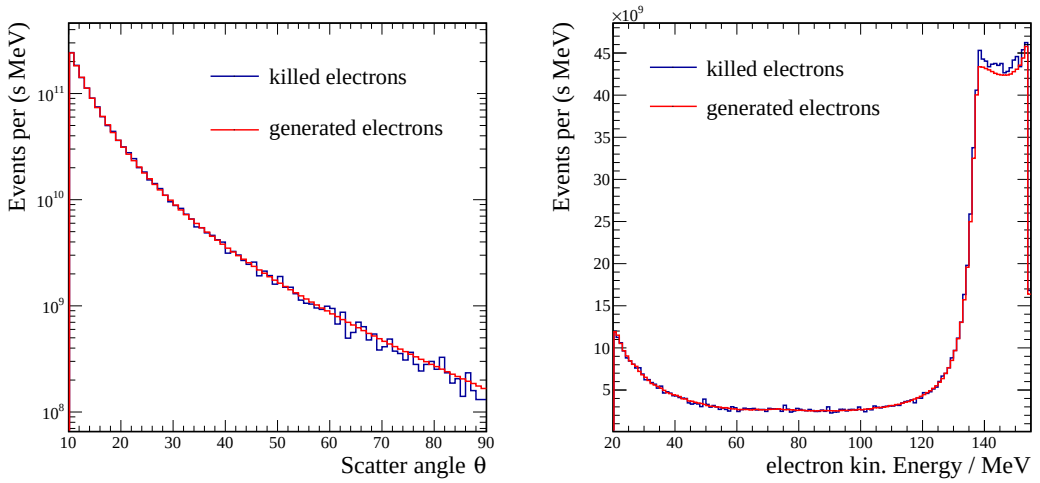

(a) *scattering angle (logarithmic y-scale)* (b) *Kinetic energy before scattering*

Figure 4.2.: *Kinematic distributions of electrons produced by the signal generator for large angle scattering compared to electrons removed from the background simulation. The distributions are normalized independently to the P2 beam flux.*

which is completely modeled with shapes that are natively supported by GEANT4. The main simplifications are documented in the following. The detector geometry as implemented in the simulation together with some signal events is shown in figure 4.3. The simplifications applied to the detector geometry can easily be identified by comparing this figure to the CAD rendering of the actual detector design shown in figure 3.6.

The detector elements of the Integrating Cherenkov Detector (ICD) and the lead shielding protecting the photomultipliers are greatly simplified in the tracking detector simulation. The individual fused silica bars are replaced by one quartz volume with perfect azimuthal coverage. For analyses within the scope of this thesis, the only interesting information is whether a particular simulated electron trajectory will cross the volume of the ICD or not. The detector is therefore implemented to perfectly detect electrons but not any other particles.

The target is currently installed with a diameter of 15 cm. As mentioned earlier, the target diameter for the final experiment is not yet fixed. The most relevant features of the target shape shown in figure 3.4a are reproduced in the simulation. The internal flow diverter however is omitted. No mechanical attachment of the target and no cooling pipes are considered so far. The electron beam entering the target is usually simulated to point along the z-axis, but any extended beam profile could be investigated with little additional effort.

The magnetic field in the simulation makes use of the FOPI field map. The field

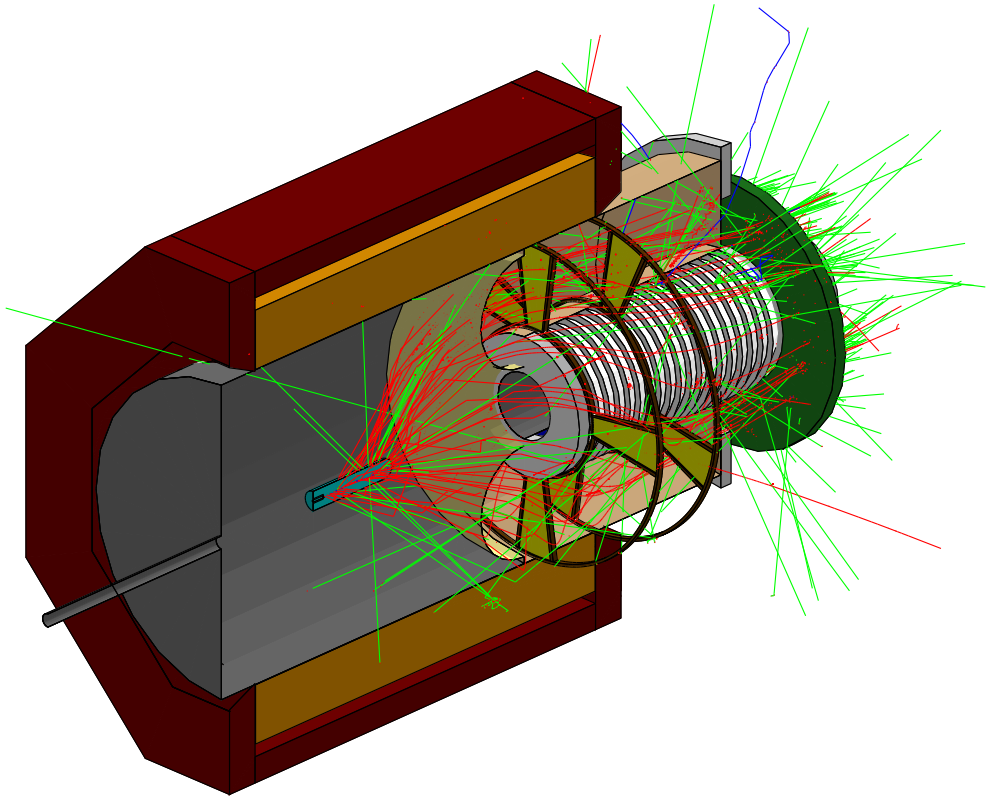

Figure 4.3.: *Visualization of the detector geometry implemented to the tracking detector simulation. Some parts are cut in the xz-plane for visualization. The tracking planes are colored in yellow, the integrating detector in dark green. Trajectories (red = electrons, green = photons, blue = positrons) are shown for 50 signal events with electrons generated in the target using random scattering angles* $\theta \in [25^\circ, 45^\circ]$.

map gives a field value every 1.5 cm and is interpolated in between. The magnetic field is set to zero outside the field map range. The FOPI field map and its extent can be seen in figure 3.12. There is also the possibility to run the simulation with a constant magnetic field along the z-axis with given field strength. This simplification is useful in order to investigate the influence of the inhomogeneous magnetic field in reconstruction studies, but not further considered here.

4.2.1. Tracking Detector Geometry

The most important simplification of the detector geometry concerns the tracking detector modules. The actual mechanical assembly of such a tracker module will be presented later in this thesis and is quite complex. Moreover, many details of this assembly are not expected to add anything essential to the simulation results. The active detector area of each module is currently modeled as one continuous volume instead of individual sensor chips. Particular sensors can be considered by segmenting the active area during analysis. The active area has the shape of an azimuthal slice of a disc-like geometry, see figure 4.3. In this area, the detector material is silicon with 50 µm thickness, followed by 100 µm of Kapton® polyimide and 20 µm aluminum. Only part of the silicon thickness is implemented to be sensitive, which means that a hit is recorded for every particle traversing the sensitive section of the silicon volume. The same holds true for particles being created or absorbed within this area. The sensitive section is centered in the silicon volume and has a thickness of 15 µm. Regarding the real HV-MAPS sensors, it was described earlier in section 3.5.2 that the active material is mainly limited to the depletion zone with a thickness of $O(10\,\mu\text{m})$. The setup in the simulation intends to account for this internal structure. In addition, the mechanical mounting for each tracker module is implemented as a 20 mm thick plastic frame surrounding the active area.

As described in section 3.5.1, the tracker modules are placed at the beginning of the barrel shield and the end of the magnet, respectively. These positions are chosen in order to ensure a robust track reconstruction while taking into account the geometric constraints in the P2 detector. Only slices of space in azimuthal direction are covered with pixel sensors as covering the full area is not affordable. To first order, the smaller covered area reduces the number of reconstructable tracks by the ratio of the area covered, but selects a representative set of particles. However, the track loss will be larger compared to this purely geometric ratio as signal electrons might hit the front tracker planes and the Cherenkov detector, but miss the downstream tracker plane pair due to its limited azimuthal coverage. The effect was analyzed by running the simulation several times with different values of azimuthal coverage $\Delta\varphi$ of each tracker module. The downstream tracker modules were rotated by $\phi_{\text{rot}} = -16.85^\circ$ relative to the front ones. In this simulation run, the front tracker plane pair was

still placed 10 cm farther away from the target compared to the described geometry as the optimization of plane positions was done later than this particular analysis. Figure 4.4a shows the resulting relative hit count on all tracker planes relative to the first one. As the electrons were not required to hit the Cherenkov detector in this analysis, a constant fraction of electrons is lost because they hit the barrel shield or the magnet. Nonetheless, it can be seen that the hit loss increases for lower values of $\Delta\varphi$. The additional relative hit loss due to the limited azimuthal coverage must be kept reasonably low as it might bias the set of selected particles. Figure 4.4b shows the normalized distribution of the difference $\Delta\phi$ evaluating the hit positions on the second and third tracker plane of electrons traversing both planes and hitting the Cherenkov detector. For this analysis, a coverage of $\Delta\varphi = 15°$ and a rotation $\phi_{\text{rot}} = 17°$ were used. The shape of the distribution can be explained by the Landau-distributed energy loss in the target, which leads to the long tail of larger absolute values of $\Delta\phi$.

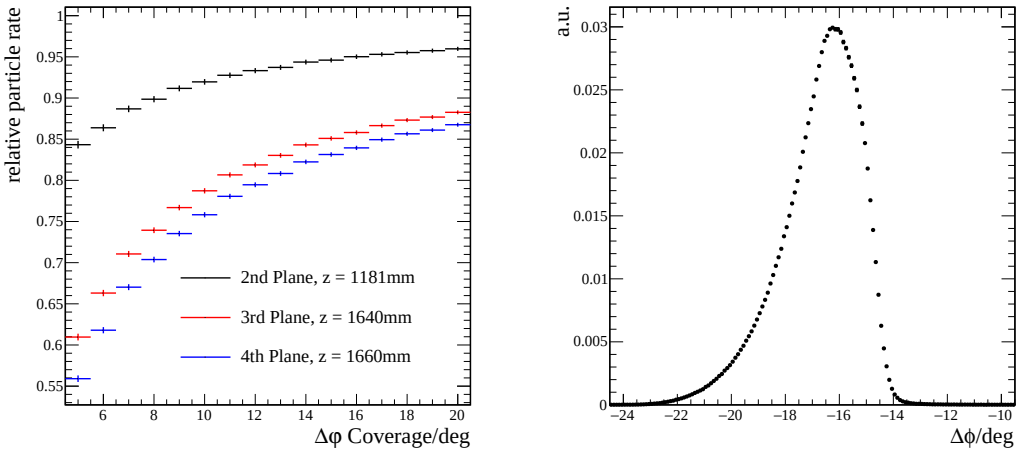

(a) *Particle rate on downstream tracker planes relative to the front one for different azimuthal coverages.*

(b) *Difference in azimuthal angle for hits on second and third tracker plane.*

Figure 4.4.: *Simulation analyses investigating the required azimuthal coverage of tracking modules and the rotation of the downstream tracker modules relative to the front ones.*

The azimuthal coverage must be adjusted additionally such that all electrons that hit one particular fused silica bar can be reconstructed since this is needed for the operation of the experiment in the single electron detection mode. Figure 4.5 shows the result of such an analysis done by a colleague in our working group. It can be seen that almost all particles hitting one fused silica bar are covered by the front tracker module covering $\Delta\varphi = 15°$.

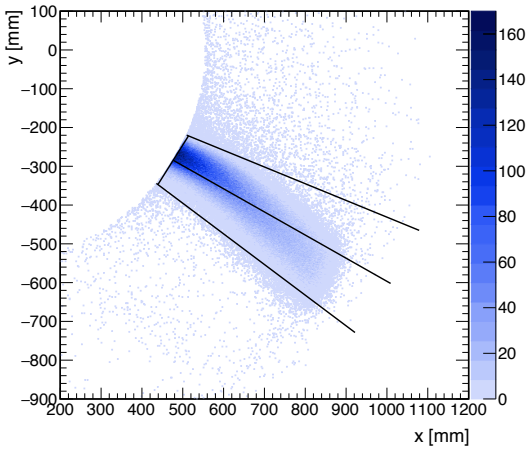

Figure 4.5.: *Position of electrons which hit one particular fused silica bar evaluated at the front tracker plane. The area covered by the tracker module is depicted additionally. Figure taken from [13].*

4.3. Data Selection

The main advantage of a simulation using the Monte Carlo approach is that in principle any parameter and the trajectories of all particles appearing in the detector are perfectly known. However, only very little of this information is really interesting and therefore relevant for analysis. Filtering the information available in the simulation can be done effectively in two steps: First, it has to be defined which particle trajectories are considered at all. Second, the variables that are stored for each of these trajectories are determined. For simplicity, the same set of parameters is stored for each trajectory that is selected. The simulation results for every run are stored in a single ROOT file, replacing the text file based output of the original simulation version. This approach is considered to be most effective for analysis, as it makes it very easy to match and link data from different particle trajectories and detector parts.

Relevant information on the trajectories is stored for all particles that traverse one of the sensitive detectors in the simulation setup, namely the tracking planes or the integrating detector (only electrons). Photons that do not hit any detector are not saved. Electrons and positrons without hits are not considered if their initial kinetic energy is below 10 MeV. All remaining particles are recorded if they travel more than 5 mm in the simulation volume outside the target.

Three categories of parameters are recorded. The first category concerns event specific information, such as the event weight, the scattering angle generated by the

signal generator or the total number of trajectories in the event. The second category includes all the information that is stored on the particle trajectories. Both the vertex position and the momentum are recorded. Every particle in a particular event has a unique identification number and another integer value defining its type. In addition, the production process number and the particle number and type of the mother particle are stored. An extra truth value is written to file that is true for electrons that hit the integrating detector. The third category contains the information on the hits recorded by the tracking planes. Every particle traversing the silicon volume creates a hit since no minimum energy deposit is required. However, the total energy deposit and the non ionizing energy deposit are stored so that cuts are possible on the analysis level. For each hit in a particular tracker plane, the plane number, the hit position and the momentum of the corresponding particle are stored as well as its type and identification number. This makes it possible to link hits in the silicon sensors with the corresponding particle trajectory and its properties.

The simulation can be tuned with several input parameters. In particular, the tracker modules can be placed at different positions in the detector and the parameters for the signal generator can be changed. Table 4.1 gives the default configuration of the simulation which was used for the results presented in the following chapters, if not explicitly stated otherwise.

Parameter	Value	Description
z_1	1080 mm	front plane z-position of the upstream tracker modules
z_2	1640 mm	front plane z-position of the downstream tracker modules
Δz	23 mm	Distance of tracker planes within one tracker module
R_{min}	555 mm	Min. radial coordinate covered by the tracker modules
R_{max}	1175 mm	Max. radial coordinate covered by the tracker modules
$\Delta\varphi$	15°	Azimuthal coverage of each tracker module
ϕ_{rot}	−17°	Rotation of the downstream tracker modules
d_{Si}	50 µm	Silicon material thickness in active tracker area
δ_{Si}	15 µm	Sensitive silicon thickness centered within the silicon volume
d_{Kapton}	100 µm	Kapton® material thickness in active tracker area
d_{Al}	20 µm	Aluminum material thickness in active tracker area
N_{sim}	1×10^8	Number of simulated beam electrons
l_{ref}	600 mm	Reference length parameter of the signal generator
$\theta_{\text{ep, min}}$	10°	Min. scattering angle generated by the signal generator
$\theta_{\text{ep, max}}$	90°	Max. scattering angle generated by the signal generator
$\phi_{\text{ep, min}}$	0°	Min. ϕ angle of tracks generated by the signal generator
$\phi_{\text{ep, max}}$	360°	Max. ϕ angle of tracks generated by the signal generator
$E_{\text{kin, min}}$	20 MeV	Lower kinetic energy limit for the signal generator

Table 4.1.: *Default simulation parameters*

5 Signal and Background Studies

The detector simulation is used for extensive studies on the signal and background rate distributions that are expected on the tracker planes. The rate capability is one of the major requirements for which the tracking detector must be designed. It has implications on the operation of the pixel sensors and their readout, but also on the mechanical design in terms of radiation hardness. Evidently, a good estimate of the instantaneous particle rates and of the accumulated amount of particles over the operation time of the experiment is crucial for the development of the tracking detector. The studies presented in this chapter are followed by currently ongoing more detailed track finding [114] and reconstruction [115] studies which are not part of this thesis.

5.1. Instantaneous Particle Rates

The P2 experimental facility is developed for New Physics searches at the intensity frontier. It is in the nature of such kind of experiments that the associated particle rate environment represents very challenging working conditions for any detector system. It was mentioned already that the Cherenkov detector system will therefore be operated in an integrating mode for most of the experiment time, meaning that only the accumulated current of arriving electrons will be assessed. In contrast, the tracking detector system has to reconstruct individual electron tracks, but does not require to detect the full set of electrons.

The hit rates on the four tracking planes per area categorized into different types of particles are shown in figure 5.1, depending on the radial coordinate R in cylindrical coordinates. The radial range of the x-axes in this figure corresponds to the space between the barrel lead shield and the solenoid magnet, see figures 3.6 and 4.3. As

the area covered by each individual bin depends on its position in R, the bin contents were weighted correspondingly. This plot considers all particles traversing, being created or absorbed within the active silicon area of the tracker planes in the detector simulation, without any cuts on the energy deposit in the active volume. The accumulated particle rates per plane are given in table 5.1. As each detector plane is made up of four modules with 15° azimuthal coverage each, and the particle rates are expected to be equally distributed in azimuthal direction, every module is expected to be exposed to one fourth of the particle rates given in this table.

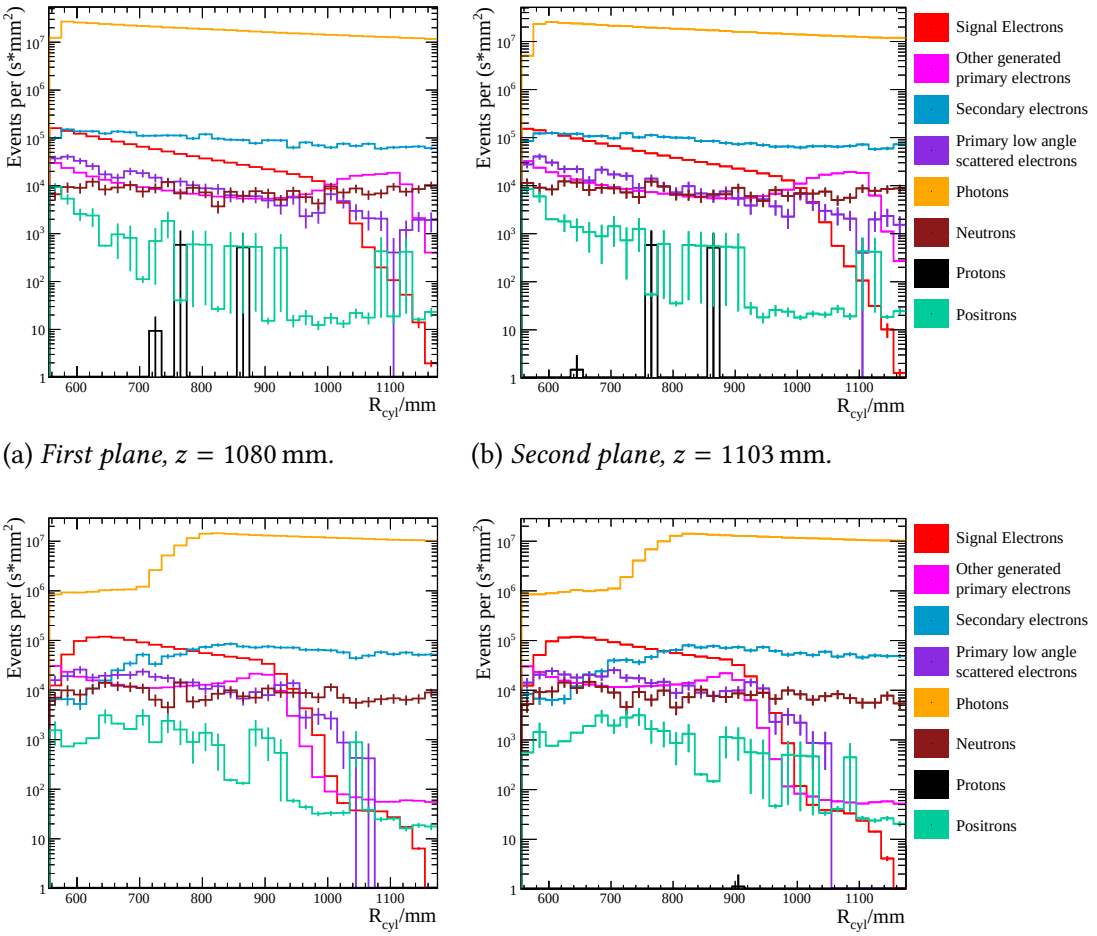

(a) *First plane,* $z = 1080\,\text{mm}$. (b) *Second plane,* $z = 1103\,\text{mm}$.

(c) *Third plane,* $z = 1640\,\text{mm}$. (d) *Fourth plane,* $z = 1663\,\text{mm}$.

Figure 5.1.: *Hit rate distributions on the four tracking planes for full beam current. The bin contents are normalized according to the covered area. Every particle moving within the active silicon volume inside of the planes is counted, irrespective of its energy deposit.*

In any real particle physics experiment, the particle rate measured by a detector is composed of two factors, namely the number of particles actually traversing the sen-

Particle Type	First Plane Rate [s^{-1}]	Second Plane Rate [s^{-1}]	Third Plane Rate [s^{-1}]	Fourth Plane Rate [s^{-1}]
Signal electrons	$1.894(2) \times 10^{10}$	$1.916(2) \times 10^{10}$	$1.958(2) \times 10^{10}$	$1.959(2) \times 10^{10}$
Other generated primary electrons	$5.735(5) \times 10^{9}$	$5.742(5) \times 10^{9}$	$4.606(5) \times 10^{9}$	$4.533(5) \times 10^{9}$
Secondary electrons	$5.02(7) \times 10^{10}$	$4.69(7) \times 10^{10}$	$3.00(6) \times 10^{10}$	$2.80(6) \times 10^{10}$
Primary low angle scattered electrons	$5.0(3) \times 10^{9}$	$4.9(3) \times 10^{9}$	$4.9(3) \times 10^{9}$	$4.9(3) \times 10^{9}$
Photons	$9.43(1) \times 10^{12}$	$9.17(1) \times 10^{12}$	$5.262(7) \times 10^{12}$	$5.097(7) \times 10^{12}$
Neutrons	$4.4(2) \times 10^{9}$	$4.3(2) \times 10^{9}$	$4.7(2) \times 10^{9}$	$4.5(2) \times 10^{9}$
Protons	$2(2) \times 10^{7}$	$2(2) \times 10^{7}$	$7.1(9) \times 10^{4}$	$6(2) \times 10^{4}$
Positrons	$4.0(5) \times 10^{8}$	$4.1(5) \times 10^{8}$	$4.1(5) \times 10^{8}$	$4.6(5) \times 10^{8}$

Table 5.1.: *Accumulated particle rates on the four tracker planes for full beam current. The uncertainties given represent statistical errors and do not contain any systematic effects.*

sor and the detection efficiency for different types of particles. The detection efficiency of the silicon pixel sensors used for the P2 experiment can be treated to be close to 100 % for charged particles with energies in the keV range or above. The plots in figure 5.1 however show that the raw particle rates are dominated by photons. Photons interact in the pixel sensors mainly via photoelectric effect and Compton scattering, depending on their energy. In each case, some energy is transferred to secondary electrons, which are then possibly detected. The amount of photons that will contribute to the background hit rate can therefore be estimated by the secondary electron rate. Only secondary electrons that reach the 15 µm active silicon layer centered in the 50 µm silicon plane are counted. As they might move back and forth between the active layer and the passive one, it must be taken care that only one hit per plane and secondary electron is counted. Although most of the secondary electrons are attributable to photons and are "created" within the tracker plane itself, they can also originate from other detector parts. It can be seen in figure 5.1 by comparing the photon and secondary electron rate distributions that the photon background contribution is largely reduced due to the low photon detection probability. Additionally, it is in fact much more unlikely that a photon creates a hit on two neighboring tracking planes, and even impossible if it is absorbed via photoelectric effect on the first plane. More detailed studies on the photon background are

given in section 5.1.2 within this chapter. As the amount of background created by the large number of photons is specifically relevant for the operation of the tracking detector system, experimental tests of the photon detection efficiency were done and are presented in the next chapter.

The rate contribution of primary electrons, defined as electrons originating from the particle beam, is further divided into three categories: signal electrons, other generated primary electrons and low angle scattered electrons. The first two categories are electrons generated by the custom event generator described in section 4.1.2. Signal electrons are defined as electrons from the event generator that hit the integrating Cherenkov detector. Note that they are allowed to have a scattering angle outside the nominal signal angle range of the P2 experiment, $\theta \in [25^\circ, 45^\circ]$. As the tracking detector has primarily the aim to reconstruct the average momentum transfer of all electrons that are integrated in the Cherenkov detectors, and since these detectors cannot distinguish between different electrons anyway, all electrons that contribute to the measured parity violating asymmetry are considered as signal for the tracker system. The second category represents the remaining electrons originating from the event generator, which do not reach the Cherenkov detector. Low angle scattered electrons are all electrons originating from the electron beam that are modeled exclusively with GEANT4 scattering models. As scattering events interfering with the event generator are removed from the simulation (see section 4.1.3), no single scattering event with scattering angle above 10° can appear for this electron category. These electrons can however leave the target with larger effective scattering angles due to the accumulation of many low angle scattering events, so that they can hit the tracker planes and even the Cherenkov detectors. Further discussion is needed on whether it might therefore be reasonable to count those electrons in this category, that hit the Cherenkov detectors, as additional signal electrons for the tracking detector or whether they have to be considered as irreducible background.

The signal electron rate quickly decreases for larger radii. This effect can be observed on all four tracker planes. The signal rate drop starts at $R \approx 1\,\mathrm{m}$ for the planes on the front tracker modules and already at $R \approx 0.9\,\mathrm{m}$ for the downstream planes. Electrons at larger radii are likely to hit either the magnet or the barrel shield due to the geometry of the P2 spectrometer. The highest signal electron rates can be observed near the barrel shield at lower radii. It has to be considered that for the construction of the real tracking detector, more space will be needed for mechanics than the 2 cm circular frame implemented in the detector simulation. The shape of the signal rate distribution shows that this is probably not problematic for mechanical mountings at the outer end of the tracker modules near the magnet walls. However, any infrastructure next to the barrel shield should be hidden within the triangular surface structure of the barrel shield if this is mechanically achievable. Otherwise it would be necessary to further optimize the spectrometer geometry such that the particle loss due to these mechanical mountings is minimized. The rate of electrons

from the signal generator that do not reach the Cherenkov detector and the rate of low angle scattered electrons are similar. Both rate contributions are rather flat on the front tracker planes, but drop with the signal electron rate on the rear ones.

The rate distributions on the tracker planes show that the particle rate caused by secondary electrons exceeds the signal electrons on the complete first two tracker planes and for most of the area on the rear two detector planes. Although this background contribution can be effectively suppressed by combining hits on the tracker plane pairs, the amount of combinatorial background induced by this high background particle rate makes the P2 tracking detector a very challenging environment for track finding. Only on pixel sensors at lower radii on the downstream detector planes, a signal-to-background ratio larger than one is observable in the hit rates. These sensors are hidden by the barrel shield for photons being produced within the target, so that photons traversing this region must be produced or scattered in other detector parts. The lower photon background on the downstream detector planes motivates that the track finding algorithm developed for the P2 tracking detector starts by building pairs of coincident hits close in space on the two downstream detector planes. It then matches hits on the front detector planes which are compatible with electron tracks originating from the target. With this approach, being summarized in section 3.5.4, a signal electron track finding efficiency of 85 % can be reached at full beam current with a signal-to-background ratio of 10 at the same time [114].

Neutrons represent another background contribution. The rate is rather equally distributed over the tracker area and one order of magnitude less than the signal rate. This background contribution is therefore not the most relevant one for the challenge of track finding, but the impact regarding the radiation load needs to be considered more carefully. Results on that will be given in section 5.3. Protons and positrons are the remaining particle types which appear in the P2 experiment, but their contribution to the background rates is negligible.

In the following sections, more detailed studies on the individual rate contributions of the different particle types are presented. As in general the hit distributions are very similar for the two planes of each plane pair, it is sufficient to consider only the first and the third plane for most of these analyses.

5.1.1. Primary Electrons

Reconstructing tracks of primary electrons being scattered in the liquid hydrogen target is the main task the tracking detector system is built for. It aims to determine the average momentum transfer in the target for all electrons that contribute to the parity violating asymmetry. For this task, it is vital to carefully analyze the track parameter distributions of electrons which are accessible to the Cherenkov detector and

compare them to the subset of electrons which can be reconstructed by the tracking detector.

Although the P2 detector is designed in order to direct electrons with scattering angles within 25° to 45° to the integrating detectors, one has to keep in mind that such a selection of particles by the detector geometry cannot work perfectly. It is therefore possible both that electrons outside the nominal signal angle range hit the integrating Cherenkov detectors (ICD) and that electrons within the angle range do not. In addition, electrons hitting the ICD can be reconstructable for the tracker system, meaning that they hit every tracker plane, or not. Most of the integrated electrons do not pass the tracking detector at all due to its limited coverage of the transverse plane. In addition, a limited number of electrons will hit some but not all tracker planes.

Tracker plane hits	All Rate [s^{-1}]	$\theta \in [25°, 45°]$ Rate [s^{-1}]	Hitting ICD Rate [s^{-1}]
no condition	1.323×10^{12}	1.374×10^{11}	1.180×10^{11}
first plane	2.467×10^{10}	1.634×10^{10}	1.894×10^{10}
second plane	2.490×10^{10}	1.634×10^{10}	1.916×10^{10}
third plane	2.419×10^{10}	1.583×10^{10}	1.958×10^{10}
fourth plane	2.413×10^{10}	1.575×10^{10}	1.959×10^{10}
no plane	1.293×10^{12}	1.182×10^{11}	9.604×10^{10}
exactly one arbitrary plane	2.386×10^{9}	1.466×10^{9}	1.301×10^{9}
exactly two arbitrary planes	6.319×10^{9}	3.302×10^{9}	2.476×10^{9}
exactly three arbitrary planes	2.212×10^{9}	1.368×10^{9}	1.608×10^{9}
first two planes	2.306×10^{10}	1.529×10^{10}	1.795×10^{10}
first three planes	1.957×10^{10}	1.343×10^{10}	1.686×10^{10}
all planes	1.906×10^{10}	1.302×10^{10}	1.655×10^{10}

Table 5.2.: *Tracker plane hit count rates of electron scattering events induced by the event generator. Electrons are scattered in the scattering angle θ range 25° to 45° and for $E_{kin} \geq 20\,\mathrm{MeV}$. The event rates are normalized to full beam current.*

Table 5.2 summarizes the expected counts of primary electrons based on their hit count and scattering angle. Note that the total number of integrated electrons from the event generator exceeds the corresponding number given in Ref. [13] by around 15 %. The difference is probably attributable to the simplified geometry of the Cherenkov detector implemented in the version of the detector simulation (see section 4.2) that is used for tracking detector studies.

The hit count rates given in table 5.2 show that about one sixth of all electrons reach-

ing the integrating detector hit the first tracker plane, which corresponds to the geometrical coverage. Around 87 % of these electrons hit all four tracking planes. This number can be considered as the highest achievable reconstruction efficiency of the tracking detector.

The number of electrons scattered within the nominal signal angle range is higher than the number of integrated electrons. However, the tracking detector covers more integrated electrons than electrons in the signal angle range. This difference occurs due to additional scattering within the target. The generated scattering angle can differ from the angle under which the track leaves the target. In conclusion, it can be seen that the criterion of an electron track to hit the integrating detectors is more useful as a categorization for tracker efficiency studies than the initial scattering angle.

The accuracy of the Q^2 reconstruction that can be achieved with the tracking detector depends on the representability of the selected and reconstructed set of electrons. It is therefore necessary to compare the kinematic distributions of particles that hit the Cherenkov detectors with those that can be reconstructed. Figure 5.2 shows this comparison for the kinetic energy and scattering angle distributions.

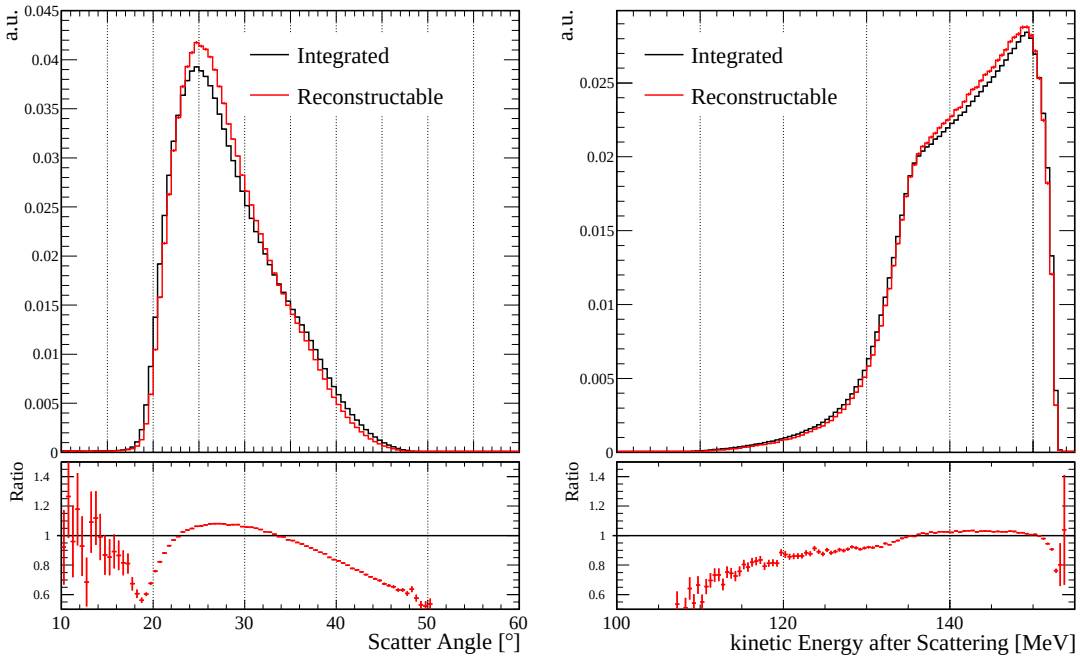

(a) *scattering angle* (b) *Kinetic energy*

Figure 5.2.: *Normalized scattering angle and kinetic energy distributions for integrated and reconstructable scattered electrons.*

The compared kinematic distributions are similar, but some differences can be observed. Considering the scattering angle distributions, higher scattering angles above 35° are underrepresented in the set of reconstructable electrons. Large scattering angles are correlated to lower electron kinetic energies. The lack of reconstructed electrons with lower energies visible in the kinetic energy comparison is therefore consistent with the angular distributions. The fact that those kind of electrons are reconstructable less often can be explained by the limited azimuthal coverage of the downstream tracker modules which are rotated with respect to the front ones. Electrons with lower energies bend more in the magnetic field and therefore miss the downstream plane pair more often after hitting the upstream one compared to electrons with energies closer to the initial beam energy. The effect is also visible by the long tail to larger absolute values of $\Delta\phi$, shown in figure 4.4b.

The quick drop in the rate of reconstructable electrons for low scattering angles near 20° is rather surprising. An explanation for this effect is that the coverage of the tracker planes is not perfect in radial direction, either. Electrons with such low scattering angles can hit the ICD only if they are scattered rather at the beginning of the target, otherwise they would hit the barrel lead shield. Their trajectories are therefore close to the barrel shield at the z-position of the upstream plane pair. Some electrons cross the 2 cm circular frame implemented in the simulation as some mechanical mounting of the tracker plane pairs. It was pointed out already earlier in this chapter that an active area starting at lowest possible radial coordinate R very close to the barrel shield would be very beneficial regarding the achievable track reconstruction efficiency.

5.1.2. Photons and Secondary Electrons

Photons are the particles with the highest abundance on the P2 tracking planes. A good understanding of this background is therefore crucial for an adequate estimation of the overall background. This section concentrates on studying the origin, properties and detection mechanisms of the photons arriving on the tracking planes according to the detector simulation, whereas experimental tests on their detection efficiency will be presented later in chapter 6.

The high intensity electron beam penetrating through the hydrogen target produces a tremendous number of bremsstrahlung photons. It was one of the primal concerns in the design of the P2 spectrometer that the Cherenkov detectors are shielded against direct photon tracks from the target. Since this is not possible for the placement of the tracker modules, it is expected that most of the photons crossing them are produced inside the target.

Figure 5.3 shows the vertices of all photons traversing the third tracker plane. The plot shows that photon vertices are distributed over the whole detector system. Photons can be produced in basically any heavy detector part and afterwards hit the tracking detector planes. Apart from the dominating target contribution, numerous photons are produced in the barrel lead shield, in the magnet, but also in the Kevlar® window.

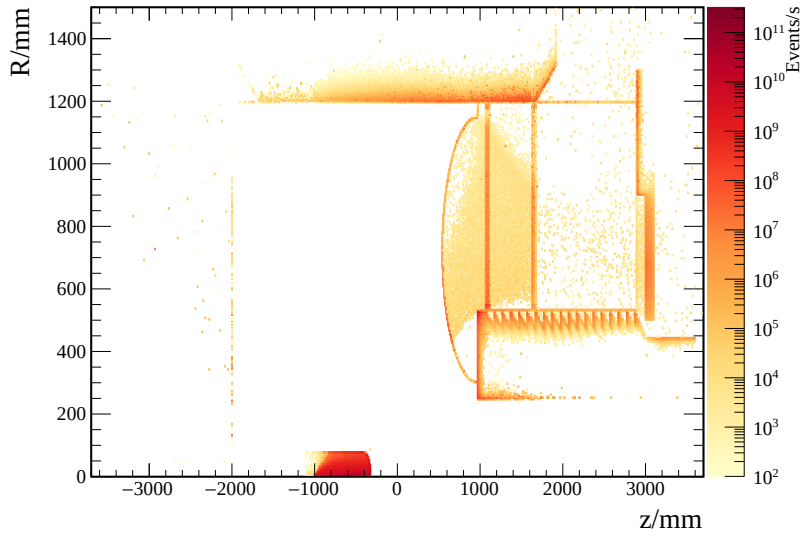

Figure 5.3.: *Vertices of photons hitting the third tracker plane, projected into the $z - R$-plane and with logarithmic color scale. The event rate is normalized for full beam current.*

It could be seen in figure 5.1c that the third tracker plane is partly shielded by the barrel shield against photons directly originating from the target. However, it was also seen that the photon rate in the shielded region at smaller radii ($R \lesssim 700\,\text{mm}$) is only reduced by around one order of magnitude. It is therefore interesting to investigate why the shielding is not more effective, in particular because it is not expected that photons can possibly traverse the lead shield. In addition, considering the photon vertices plot, the rate of photons with vertices within the target outweighs the contribution of other detector parts apparently by more than one order of magnitude. In order to explain these two seemingly contradictory observations, it is crucial to notice that the represented vertex positions represent the actual production vertex of the particle. Additional interactions in other detector parts are possible before the photon hits the tracker plane. For example, a photon produced in the target via Bremsstrahlung might be deflected in the magnet material before it hits the third tracker plane. In order to verify that this is the reason for the considerable photon

rate observed even at lower radii on the third tracker plane, the photon direction at the tracker plane is investigated further for photons that were produced inside the target.

The direction of a photon hitting the tracker plane is best described by the angle of incidence $\theta_{\text{in}}^{\gamma}$. This angle can be defined as the angle between the photon momentum $\vec{p}_{\gamma}$ and the xy-projection of the hit position vector $\vec{r}$ in global P2 detector coordinates. With this definition, the angle can be calculated using

$$\cos\left(\theta_{\text{in}}^{\gamma}\right) = \frac{\vec{p}_{\gamma} \cdot \vec{r}_{xy}}{\|\vec{p}_{\gamma}\| \, \|\vec{r}_{xy}\|}. \tag{5.1}$$

The cosine of the so-defined angle of incidence given in this equation corresponds to the projection of the normalized photon vector on the tracker plane. This projection again corresponds to the slope of a photon track projected to the $z - R$-plane and evaluated in positive z-direction. That means that photons with negative values of $\cos(\theta_{\text{in}}^{\gamma})$ probably interacted in the magnet material before hitting the tracker plane, whereas photons with positive cosine values rather interacted at last in the target or the barrel shield before hitting the tracker plane. Possible additional scatterings in the Kevlar® helium chamber opening window impose some uncertainty on this conclusion.

Figure 5.4 shows the discussed projection of photon tracks on the third tracker plane plotted against the radial coordinate R of the photon hit on this plane. The plot only considers photons which were produced within the target. The region representing direct photon tracks from the target is easily determinable by the enhanced event rate. The photon rate is suppressed for the region covered by the barrel lead shield. The remaining photon rate is rather uniformly distributed in direction and R.

The composition of the photon background can further be analyzed by projecting the distribution in figure 5.4 on the x-axis separately for $R < 700\,\text{mm}$ and for $R > 700\,\text{mm}$. This limit radius corresponds approximatively to the position of the photon rate increase observed in figure 5.1c. The resulting normalized distributions are shown in figure 5.5a. The distribution for photons hitting the third tracker plane at $R > 700\,\text{mm}$ is dominated by the peak caused by the contribution of direct photon tracks from the target. The fact that the projection of most photon momenta in the region $R < 700\,\text{mm}$ is negative indicates that these photons were additionally scattered in the magnet material or the Kevlar® window. This assumption can be further validated considering the θ-component of the initial photon momentum at its production vertex in the target. The corresponding distribution for photons being produced in the target is shown in figure 5.5b, again divided into photons hitting the third plane at $R < 700\,\text{mm}$ and $R > 700\,\text{mm}$, respectively. The distribution for the photons hitting the third tracker plane at larger radii is again dominated by the peak

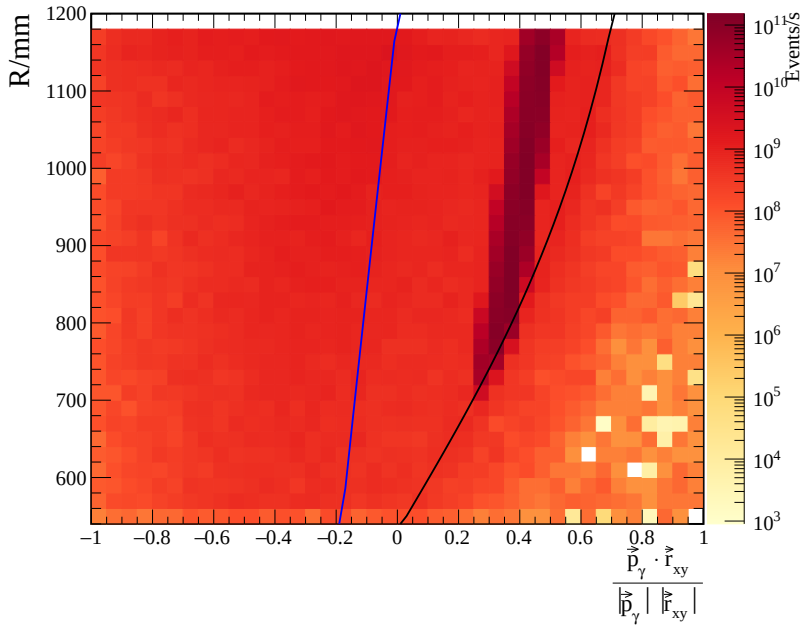

Figure 5.4.: *Projection of photon tracks to the third tracker plane, plotted against the radial coordinate of the corresponding photon hit on this plane. Considered are photons with production vertex within the target. The region on the right side from the black line is covered by the barrel shield. The region left from the blue line points to the solenoid magnet. The regions are smeared due to additional scattering in the helium chamber opening window. The event rate is normalized for full beam current, with logarithmic color scale.*

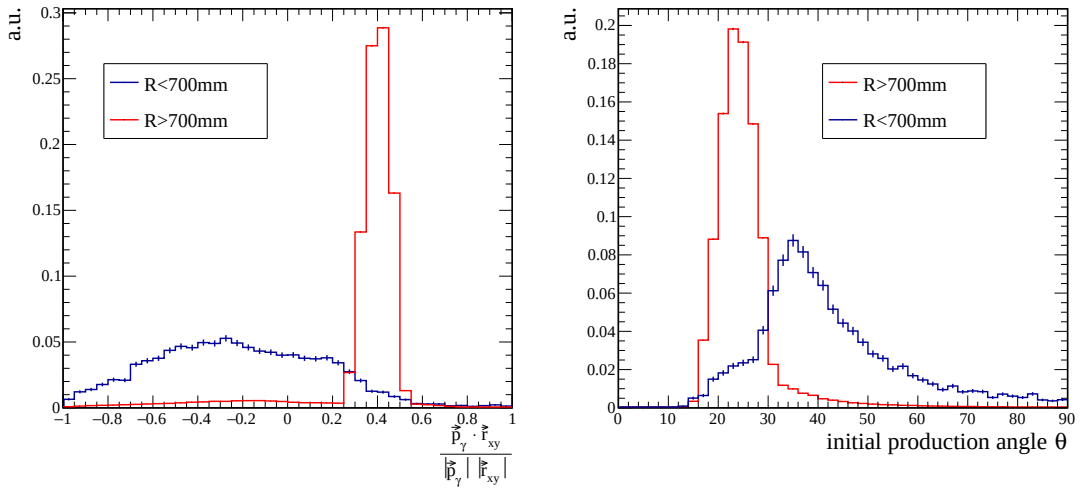

(a) *Projection of the normalized photon momentum vector on the third tracker plane*

(b) *Initial photon momentum angle θ at its production vertex within the target*

Figure 5.5.: *Photon direction for photons hitting the third tracker plane. The direction is evaluated both at the tracker plane and at the production vertex in the target. The distributions are normalized and plotted separately for photons with hits on the third plane with radial coordinate R smaller or larger than* 700 mm.

related to photons with (approximately) straight tracks from the target to that plane. The position of the peak is in agreement with the expected position based on the detector geometry. Compared to that, the photons hitting the third tracker plane at lower radii are scattered preferably at larger θ angles, which is in clear contradiction to the assumption of straight photon tracks. It is therefore shown that the barrel shield can not reduce the photon count in the shielded area by more than one order of magnitude because many photons being produced in the target hit the third plane in this area after additional scatterings in either the magnet or the helium chamber window.

The interaction probability of photons in silicon depends on the photon energy. There are several different possible interaction types which dominate in particular energy ranges. At low photon energies, photoelectric effect is the dominant interaction process. Here, the photon transfers its energy to an atomic electron and is absorbed. The electron is ejected from the atom; its kinetic energy is the difference of the initial photon energy and the electron binding energy in the atom before the photon interaction. The process is therefore only possible if the photon has enough energy to remove an electron from the atom. The lowest shell energy of pure silicon is around 99 eV, whereas the highest binding energy is 1.84 keV [135]. The energy levels might be slightly different for the doped silicon in the pixel sensors. In any case it is justified to assume that nearly all photons traversing the silicon sensors will

have enough energy to interact via photoelectric effect. The cross section for photoelectric effect interactions is highest for low energy photons above the low energy limit and then quickly drops with energy. There are additional peaks in the cross section energy curve at the material shell energies. If the liberated electron has gained enough kinetic energy from the absorbed photon, it may leave the detector material. If this is not the case, the total energy deposit in the silicon equals the initial photon energy.

Two different scattering processes can appear for photons traversing matter, namely Rayleigh scattering and Compton scattering. Rayleigh scattering usually happens at low photon energies in the keV range. The photon is scattered from an atom without ionizing or exciting it. As the only effect is the deflection of the incoming photon, this process can be neglected. In contrast to that, Compton scattering is the most important photon interaction process at intermediate photon energies. It describes the scattering of a photon with a free electron. Although the electrons in matter are bound to an atom, weakly bound electrons can be considered as essentially free if their binding energy is negligible with respect to the photon energy. In the Compton scattering process, the photon is deflected and part of its energy is transferred to the electron. If the photon is not absorbed by other processes, it can further traverse and leave the material. The same applies for the electron if the recoil is large enough.

At photon energies above 1.022 MeV, the photon can produce an electron-positron pair. This process is known as pair production. It is kinematically only possible in the vicinity of a nucleus or another electron to absorb the recoil energy. The probability of pair production increases with the photon energy and approximately with the square of the atomic number of the nearby atom. In addition to the mentioned interaction processes, photo-nuclear interactions become possible at higher photon energies, but their contribution to the total interaction cross section is negligible and therefore not further considered.

Figure 5.6 shows the simulated detection probability of photons with different energies being directed perpendicularly on a 64 µm silicon sensor plane. The plane thickness was chosen in order to enable comparing the results to experimental measurements with MuPix prototype sensors of this thickness, see chapter 6. The plot is the result of a GEANT4 based test simulation with the same physics processes enabled as used in the P2 detector simulation. For each of the 100 considered different photon energies, 2.0×10^7 incident particles were simulated. In the same way as applied in the detector simulation, the depletion zone of the pixel sensors is modeled by a 15 µm thin active layer centered inside the silicon volume. The photon is counted as detected if it produces a secondary electron that crosses the active layer. The photon interaction process is determined by evaluating the production process of the secondary electron. In general, the results of this simulation study shown in figure 5.6

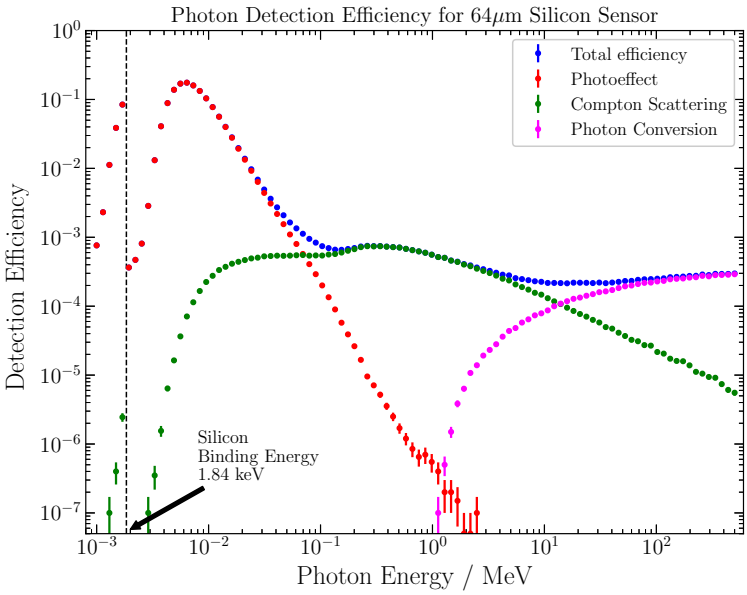

Figure 5.6.: *Photon detection probability evaluated with a test simulation for a* 64 µm *thin silicon sensor. The efficiency is divided into the relevant detection mechanisms and plotted in double logarithmic scale*

yield the expected cross section energy dependencies for each of the different photon production mechanisms.

Nevertheless, the detection efficiency curve in the photo-effect dominated low energy regime differs from the typically known cross section energy dependence, as reported e.g. in Ref. [55]. Other than expected, the detection probability sharply drops at the highest binding energy in silicon. In addition, the fraction of detected photons decreases to lower energies around 1 keV, although it would be expected to diverge to low energies. Both observations can be explained by the simulated limited thickness of the active layer inside the silicon volume. For very low energies and at the absorption K-edge, the cross section for photoelectric effect is so high that nearly all photons interact within the first few micrometers in the silicon. The probability for a secondary electron produced in this region to reach the active layer is then very low, explaining the drop in the detection probability curve. Since the actual location and thickness of the depletion zone in the actual HV-MAPS sensors can only be estimated, the sensor response to photons in this energy range is very difficult to predict.

In order to understand the photon background on the P2 tracking detector, the energy distribution of the photons arriving at the tracker planes has to be considered.

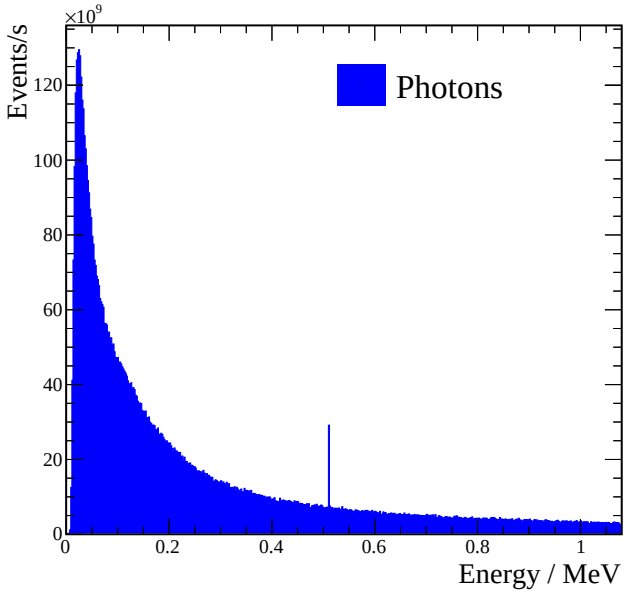

Figure 5.7.: *Energy distribution of photons traversing the first tracker plane in the P2 detector simulation*

Figure 5.7 shows the energy distribution of photons that arrive at the first detector plane. The distribution corresponds to a continuous bremsstrahlung spectrum, but very low energetic photons with $E \leq 10\,\text{keV}$ have been mostly absorbed already in the Kevlar® window between the target and the first tracker plane. The lack of very low energetic photons explains the low fraction of actually interacting photons, which is very beneficial for the operation of the tracking detector. The photon energy distribution peaks at around 25 keV. The photon detection efficiency for this energy and above however is below 1 %, as it can be read from the plot in figure 5.6. The additional peak visible in the photon energy distribution at the electron mass (511 keV) is caused by pair annihilation, where an electron-positron pair at rest annihilates to two photons.

The detection rate of photons on the tracker planes is a convolution of the photon energy distribution shown in figure 5.7 with the detection efficiency curve given by figure 5.6. As mentioned earlier, it can be estimated from the detector simulation by analyzing the number of secondary electrons that result from photon interactions within the sensor. Secondary electrons in general can also result from interactions in detector parts other than the tracker planes. For example, a photon can interact in the Kevlar window, but the resulting secondary electron might be detected on one or more tracking detector planes. In addition to that, secondary electrons can be initiated by charged particles via ionization. The energy transfer to one particular electron in the ionization process is usually very small so that most secondary

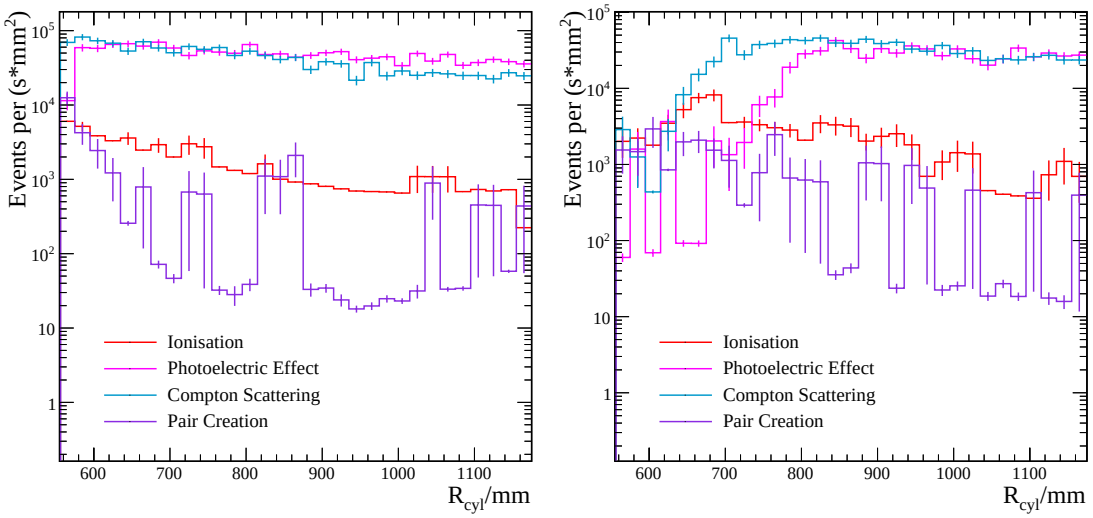

(a) *First plane* (b) *Third plane*

Figure 5.8.: *Hit rate of secondary electrons on the first and on the third tracker plane, divided into the possible production mechanisms. The bin contents are normalized according to the covered area and the rate is normalized to full beam current. No cut on the energy deposit is applied.*

electrons of that kind do not leave the initial material volume.

The contributions of the different production mechanisms to the secondary electron abundance on the first and third tracker plane are shown in figure 5.8. The accumulated rate contributions and the resulting total photon detection probability for all tracker planes are given in table 5.3. It can be seen that photoelectric effect and Compton scattering contribute to comparable amount to the abundance of secondary electrons. Pair creation does not have any considerable influence. Regarding the hit rates on the third tracker plane, it is interesting to notice that the contribution of Compton scattering electrons raises already at lower radial coordinate R compared to the contribution of photoelectric effect. In addition, the increase of photo-electrons starts about at the same coordinate R as the increase of the photon rate, see figure 5.1c. This observation indicates that the direct bremsstrahlung photons from the target are primarily detected via photoelectric effect.

The average photon detection efficiency for each plane given in table 5.3 is calculated by relating the number of secondary electrons with vertices within the plane to the total number of traversing photons. In general, it can be read from table 5.3 that the majority of secondary electrons are initiated within the tracker plane itself. The calculated average photon detection efficiency is slightly higher on the first and third plane compared to the second and fourth plane, respectively, which means that it is

Particle Type	First Plane Rate [s^{-1}]	Second Plane Rate [s^{-1}]	Third Plane Rate [s^{-1}]	Fourth Plane Rate [s^{-1}]
Secondary electrons	$5.02(7) \times 10^{10}$	$4.69(7) \times 10^{10}$	$3.00(6) \times 10^{10}$	$2.80(6) \times 10^{10}$
Ionization	$8.4(4) \times 10^{8}$	$9.9(4) \times 10^{8}$	$1.24(7) \times 10^{9}$	$1.18(6) \times 10^{9}$
Photoelectric effect	$2.64(5) \times 10^{10}$	$2.25(5) \times 10^{10}$	$1.22(4) \times 10^{10}$	$1.09(4) \times 10^{10}$
Coulomb scattering	$2.26(5) \times 10^{10}$	$2.29(5) \times 10^{10}$	$1.63(4) \times 10^{10}$	$1.55(4) \times 10^{10}$
Pair production	$4.2(6) \times 10^{8}$	$4.9(6) \times 10^{8}$	$3.7(5) \times 10^{8}$	$4.03(6) \times 10^{8}$
Vertex within plane	$3.63(6) \times 10^{10}$	$2.92(6) \times 10^{10}$	$1.81(5) \times 10^{10}$	$1.49(4) \times 10^{10}$
Photons total	$9.43(1) \times 10^{12}$	$9.17(1) \times 10^{12}$	$5.262(7) \times 10^{12}$	$5.097(7) \times 10^{12}$
Photon efficiency	0.38(1) %	0.32(1) %	0.34(1) %	0.29(1) %

Table 5.3.: *Accumulated secondary electron particle rate on the four tracker planes, divided into the possible production processes. The photon particle rate is quoted in comparison. All rates are normalized to full beam current. The given uncertainty represent the statistical uncertainty without taking into account any systematic effects.*

increased on the front plane of each plane pair. The back planes are in the shadow of the front planes, in which some of the low energetic photons with higher interaction cross section are absorbed. However, this is only a small effect because much more photons are absorbed already in the 1 mm thick Kevlar® window compared to the 50 µm thin silicon plane. In previous versions of the simulation without the Kevlar® window, the observed differences in the photon detection efficiency between the planes of each pair were much larger. It was investigated that about 98 % of all secondary electrons that reach the active silicon layer deposit more than 1 keV energy in it. Consequently, assuming that nearly all secondary electrons creating hits in the simulation also produce hit signals on the real sensor is supposed to be a valid approximation.

The contribution by ionization is only given for completeness and is not related to photons. It is important to notice that estimating the detection efficiency of charged particles by quantifying the number of ionization electrons produced in the silicon would not be adequate since the p-n-junction diode as the functional principle of the pixel sensors (see section 3.5.2) to detect charged particles is not simulated within the scope of the P2 detector simulation.

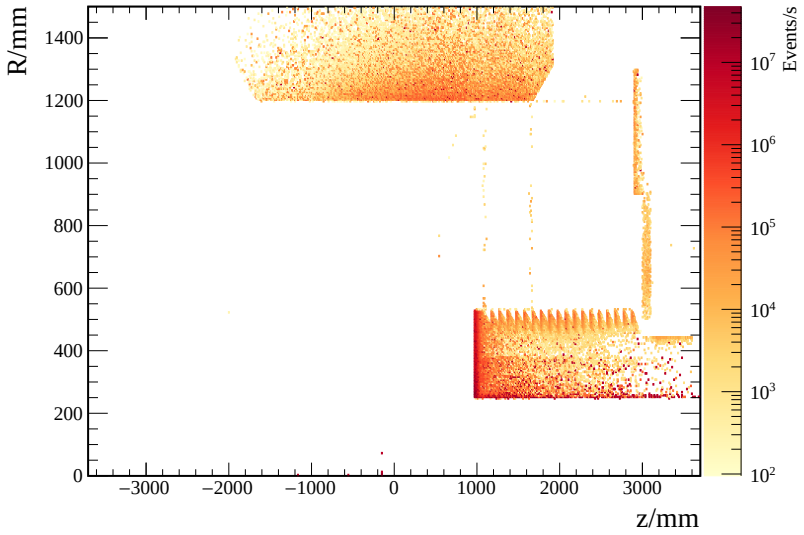

Figure 5.9.: *Vertices of neutrons hitting one or more tracker planes, projected into the $z-R$-plane and with logarithmic color scale. The event rate is normalized for full beam current.*

5.1.3. Neutrons

Neutrons can be liberated from atoms of favorably heavy materials within the P2 detector by electro-nuclear or photo-nuclear processes. Although the cross sections of these processes are rather small and the liberated neutrons can be absorbed again within the material, the tremendous amount of electrons and photons present within the detector volume during the operation of the P2 experiment will cause a considerable amount of detected neutrons.

Nevertheless, the amount of neutrons traversing the tracker planes is negligible compared to the background created by photons and the corresponding secondary electrons, as it can be seen in figure 5.1. In addition, neutrons as uncharged particles are expected to have a rather low detection probability, but even so, this probability is not further investigated here because it is not relevant for the total background rate. The neutron rate is anyway important to consider as neutrons are known to cause radiation damage in the silicon sensors or any other parts and electronics within the detector volume. While the expected radiation load for the tracking detector, which is caused by all types of particles, is discussed in section 5.3, the kinematics and vertices of neutrons in the P2 experiment are discussed in the following.

The vertices of all neutrons that traverse at least one of the tracker planes are shown in figure 5.9. Apparently, neutrons are mainly liberated from the barrel lead shield

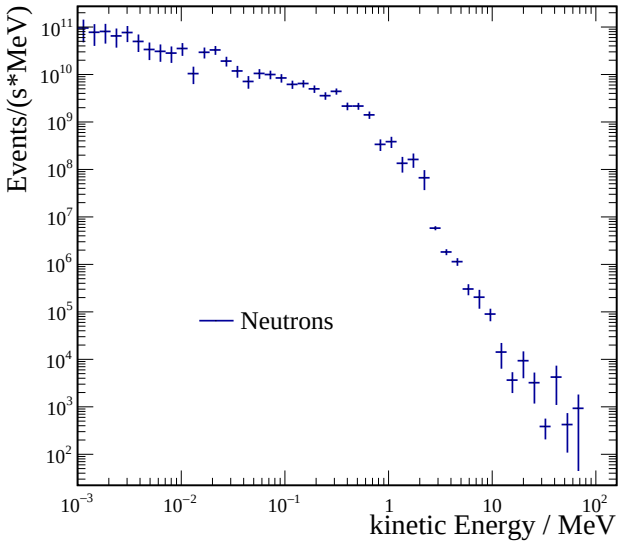

Figure 5.10.: *Kinetic energy of neutrons hitting some tracker plane, evaluated at the time of the hit, plotted with double logarithmic scale. The given uncertainties represent statistical errors. The bin contents were divided by the bin width in order to represent event rates per* MeV *neutron kinetic energy. The rates are normalized to full beam current.*

and from the magnet. The vertices are not increasingly populated near the tracker planes, but in those areas where most electrons hit the corresponding parts. In particular, most vertices can be found near the inner surface of the barrel lead shield. This volume section is exposed to many Møller electrons which left the target at low scattering angles. Neutrons produced in this region need to move almost through the complete lead shield in order to reach one of the tracker planes. However, the interaction probability of neutrons as electrically uncharged particles is much smaller compared to charged particles because of the missing ionizing energy loss. This is the main reason why there are much more neutrons hitting the tracker planes than there are protons. The kinetic energy distribution for neutrons crossing the first tracker plane can be seen in figure 5.10. The kinetic energy of the neutron is evaluated at the time it hits the tracker plane. It shows that most neutrons have quite low kinetic energies. Neutrons with a kinetic energy of a few MeV or higher are quite rare.

5.2. Readout Data Rate

The hit information recorded on the pixel chips needs to be read out, processed and then recorded for later offline analysis. For that reason, it is essential to estimate the

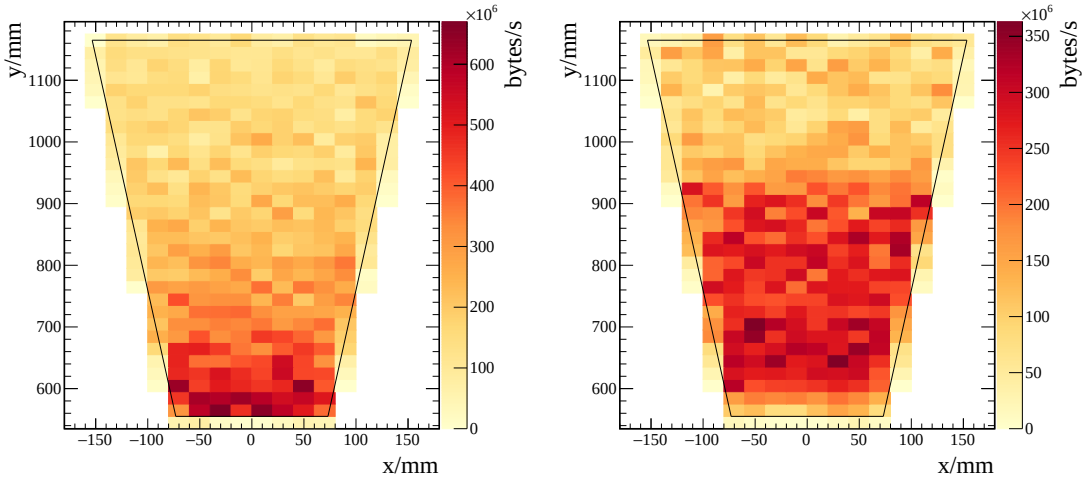

(a) *First plane* (b) *Third plane*

Figure 5.11.: *Data rate generated on the pixel sensors for the first and for the third tracker plane. Signal and background contributions are added up, accounting for all particle types apart from photons. The data rates are normalized for full beam current.*

actual amount of data that arises on the sensors. As mentioned earlier, the pixel chips will send triggerless, fully digital and zero suppressed hit data. The data amount can therefore directly be estimated from the hit rates on the tracker planes, which was shown in figure 5.1. The information on any hit consists of the column and row position of the respective pixel, both represented by 8 bit integer values. In addition, a 10 bit timestamp value is generated on the sensor and the time over threshold (TOT) is sent with 6 bit precision. In total, every hit corresponds to 4 bytes of data.

When translating the particle hit rates observed on the tracker planes in simulation to bit data rates, photon hits are omitted. As discussed previously, their contribution to the hit data collected by the sensors is represented by the amount of detected secondary electrons, so that only this contribution is considered. The data rates depending on the sensor position are shown for the first and for the third tracker plane in figure 5.11. The rates are normalized to full beam current. Note that although the area covered by each bin of the histograms plotted in this figure corresponds to the actual sensor size of 2 cm × 2 cm, the number and position of the bins do not correspond to the sensor assembly on the actual tracking detector as it will be realized in the experiment. The module shape depicted in figure 5.11 corresponds to the area covered by the tracking detector modules in the simulation. The area which will actually be covered with sensors in the technical realization of the tracker modules will differ from this simplified geometry. The technical design of the tracking detector will be discussed later in this thesis.

	First Plane [bytes/s]	Second Plane [bytes/s]	Third Plane [bytes/s]	Fourth Plane [bytes/s]
max. rate per sensor	$6.7(6) \times 10^8$	$6.1(6) \times 10^8$	$3.6(4) \times 10^8$	$3.3(5) \times 10^8$
max. rate per sensor row	$4.5(2) \times 10^9$	$4.2(2) \times 10^9$	$3.0(2) \times 10^9$	$2.9(2) \times 10^9$
total rate per segment	$8.5(8) \times 10^{10}$	$8.1(8) \times 10^{10}$	$6.4(6) \times 10^{10}$	$6.2(6) \times 10^{10}$

Table 5.4.: *Expected data rate generated on the four tracker planes for full beam current.*

The maximum data rates appear for the minimum y-coordinates on the first tracker plane. On the third tracker plane, the highest data rates are obtained at y-coordinates between 600 mm and 900 mm. This observation agrees to the distribution of the particle hit rates presented in figures 5.1a and 5.1c. It can be observed that the maximum data rate per sensor does not exceed about 7×10^8 bytes/s. As a first check, the maximum occupancy of a single pixel can be calculated, assuming a pixel dead time of 1 µs. The resulting estimate on the number of hits per pixel and dead time window is below 2.8×10^{-3}. Consequently, the observed particle rates are below the regime in which a notable amount of hits might be lost because of multiple particles hitting the same pixel within the expected dead time.

Thus, the ability of the readout system to process and record the hit data generated in the sensors is determined by the total data rate. The data rates for each plane segment are given together with the maximum data rate per sensor and per sensor row in table 5.4. The total data rate generated by the whole P2 tracking detector, which can be calculated by multiplying the sum of the last row of table 5.4 by a factor four for the number of modules in azimuthal direction, would exceed 1 Tb/s, which can not be processed by an affordable readout system.

Two possible options are envisaged to handle the excess of data rate. The first option foresees to operate the tracking detector exclusively in the single electron counting mode of the P2 experiment, which will be carried out at reduced beam rate. Reducing the beam rate by two orders of magnitude would enable the tracker readout to record all particle hits and facilitates the track finding enormously. Additional advantages when taking out the tracking detector for the main P2 measurement would be less material in the path of the electrons to the integrating Cherenkov detectors and much lower radiation tolerance requirements for the tracking detector development. However, this option would exclude the possibility to detect systematic effects possibly arising only at higher beam rates with the tracking detector. As an alternative, a

second option is to operate the pixel sensors at full beam current in a so-called gated mode. In such an operation mode, the pixel sensors would take data only within very short time slices and neglect all particle hits in between, thus reducing the data rate by basically any desired fraction. In order to profit from the advantages of both options, the current development of the tracking detector is oriented to make both of them possible. The tracking detector could then be taken out for most of the time, but measurements at full beam rate for systematic analyses would remain possible.

5.3. Radiation Dose

The discussions in this chapter so far concentrated on the instantaneous particle rate, its composition, kinematics and consequences for the readout. It is however important to additionally consider the impact of the total amount of particles accumulated over the complete measurement time. As particles interact with the sensor material and deposit energy, they might induce damage to the sensor. The type and probability of damage depends on the type of the particle and its kinetic energy. For the development of the tracking detector, it is hence imperative to ensure sufficient radiation hardness of all parts installed on the tracker modules. The particular radiation hardness requirements primarily depend on the time intervals and beam current used for measurements with the tracking detector installed. The radiation dose analyses presented in this section assume the tracking detector to be active for 10.000 h at full beam current. The radiation hardness requirements for any other measurement program are therefore easily obtainable by scaling the reported results accordingly. As the sensor performance might suffer due to damage in the whole sensor volume and not only in the depletion zone, the detector simulation was modified for this analysis such that the complete silicon volume of 50 µm is treated as active sensor volume. With this procedure, the abundance and energy deposit of particles within the complete sensor can be investigated.

Radiation damage in semiconductor devices can be classified in two categories: surface damage and displacement damage in the bulk material. Surface damage in the SiO_2 layer and in the Si-SiO_2 interface region is primarily caused by ionizing energy loss (IEL) of charged particles. Displacement damage in the crystal lattice of the bulk material is attributed to non-ionizing energy loss (NIEL). Both charged and neutral particles contribute to this type of damage, though for charged particles ionization is the primary interaction process.

5.3.1. Total Ionizing Dose

Sensor damaging effects due to the total ionizing dose (TID) are cumulative, which means that it requires persistent exposure to numerous radiation events until device degradation becomes manifest. Degradation effects particularly appear in insulating SiO_2 layers of the device due to space charge build-up. Within insulating layers, generated electron-hole pairs do not unfailingly recombine mainly because of the limited mobility of the positive charge carriers, which might get trapped at defects. Such defects are increasingly abundant at the Si-SiO_2 interface region. Possible macroscopic effects due to the space charge build-up include shifts in transistor threshold voltages and increased leakage currents. The radiation induced effects heavily depend on the chip layout, which requires to test different devices individually for their resistance against ionizing radiation.

The total ionizing dose exposure of the tracking detector is quantified by analyzing the ionizing energy deposit in the silicon by charged particles. In addition, photons contribute to the ionizing dose indirectly. The ionizing dose is usually given in units of $1\,\text{Gray} \equiv 1\,\text{Gy} = 1\,\text{J}\,\text{kg}^{-1}$ or in units of $1\,\text{rad} = 1 \times 10^{-2}\,\text{Gy}$. The ionizing energy deposit in the silicon can be extracted from the detector simulation and is related to the silicon thickness and density which are known. The contribution of different particle types to the total ionizing dose is also investigated. However, for photons interacting within the silicon material, the energy deposit is not clearly attributable to one of the interacting particles. The energy deposit in the presented analysis was assigned following the definitions used within GEANT4. For example, if a photon interacts by photoelectric effect within the silicon, the initial binding energy of the liberated electron is attributed to the photon energy deposit, while energy deposited by the secondary electron is attributed to the electron energy deposit. The total ionizing dose accumulated over all particle types is not affected by this assignment.

Figure 5.12 shows the expected total ionizing dose depending on the radial coordinate R for the first and for the third tracker plane. The overall dose is clearly dominated by the electron contribution. The dose is rather constant, at least on a logarithmic scale. It varies between 20 Mrad to 60 Mrad for most of the area on the first tracker plane and between 10 Mrad to 30 Mrad on the third plane. For comparison, the inner B-layer pixel detector of the ATLAS experiment at the Large Hadron Collider (LHC) is expected to accumulate a total ionizing dose of 100 Mrad, which will be reached at an integrated luminosity of $300\,\text{fb}^{-1}$[136]. At the end of 2018, around $150\,\text{fb}^{-1}$ integrated luminosity were collected at ATLAS [137], which means that the radiation level already reached is comparable to what is expected for the P2 tracking detector.

The radiation environment is very challenging, especially because it has to be regarded not only for the pixel sensors, but in addition for any other material or elec-

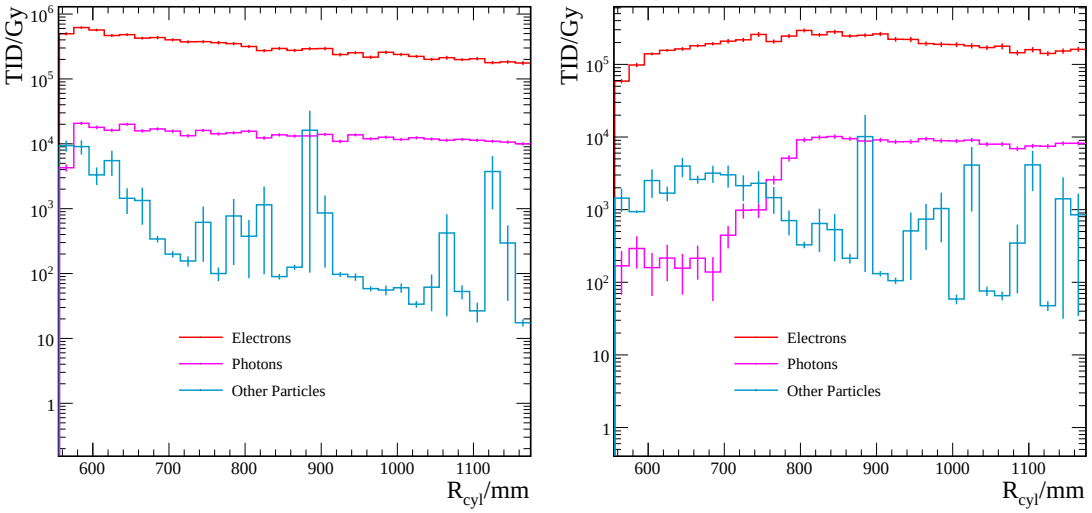

(a) *First plane* (b) *Third plane*

Figure 5.12.: *Total ionizing dose on the first and third tracker plane, evaluated with the detector simulation and normalized to* 1×10^4 h *run time at full beam current.*

tronic component placed within the detector volume. The radiation hardness ratings for commercially available electronic parts are usually below 1 Mrad, which is even true for parts being devoted specifically to space or military applications. However, much effort is currently being put into the development of components to be radiation hard up to ionizing dose levels around 1 Grad for the high luminosity upgrade of the LHC and its experiments.

5.3.2. Non-Ionizing Energy Loss

Displacement damage in the silicon bulk material can appear when a traversing particle interacts with the silicon lattice and transfers sufficient energy to remove an atom from its designated position. This effect leads to a defect in the crystal lattice and is not always reversible by annealing processes. Different types of lattice displacement defects are possible such as vacancies, interstitials and more complex cluster defects. These defects lead to a population of additional levels in the band gap of the semiconductor. Resulting macroscopic effects include an increase of leakage current, a decrease of charge collection efficiency and a change of the effective doping concentration.

Neutrons virtually only interact via the strong force so that they can dislocate lattice atoms in a single interaction with sufficient energy transfer, whereas for charged particles Coulomb interaction with the lattice is more important. Charged particles

may also interact multiple times electromagnetically with only small amounts of energy transferred in each interaction (ionizing energy loss). The minimum necessary kinetic energy of a neutron or proton to produce displacement damages in silicon is 185 eV for single defects and 35 keV for cluster defects. For electrons, the respective kinetic energies are 225 keV and 8 MeV [138].

A quantitative measure of the exposure to particles that can induce bulk damages due to non-ionizing energy loss is provided by the NIEL-scaling hypothesis. It assumes that the manifestation of bulk damage only depends on the energy transferred in collisions regardless of particle energy and type, but accounts for the different probabilities for such interactions to appear. With this ansatz, the fluence of any particle type can be related to a 1 MeV neutron equivalent fluence Φ_{eq} in units of $1\,\mathrm{MeV\,n_{eq}/cm^2}$ by applying corresponding weighting factors κ, defined as [138]

$$\kappa \equiv \frac{\Phi}{\Phi_{\mathrm{eq}}} = \frac{\int D(E)\,\Phi(E)\,\mathrm{d}E}{95\,\mathrm{MeV\,mb}\cdot\Phi} \tag{5.2}$$

with the irradiation fluence $\Phi = \int \Phi(E)\,\mathrm{d}E$. Here, $D(E)$ describes the displacement damage function for a particle with incident energy E. It can be calculated by [138]

$$D(E) = \sum_i \sigma_i(E) \int_0^{E_R,\,\mathrm{max}} f_i(E, E_R)\,P(E_R)\,\mathrm{d}E_R. \tag{5.3}$$

In this relation, the sum is over all possible interactions with cross sections σ_i. The factor $f_i(E, E_R)$ corresponds to the probability for a particular recoil energy E_R in this interaction; the Lindhard partition function $P(E_R)$ describes the fraction of the recoil energy that is deposited in displacements [139]. The value of the displacement function for a neutron with 1 MeV energy, $D_n(1\,\mathrm{MeV}) = 95\,\mathrm{MeV\,mb}$, entered the calculation of the scaling factor κ given in equation 5.2. More details on the NIEL scaling hypothesis can be found e.g. in Ref.s [138, 140, 141]. Figure 5.13 shows the displacement damage functions of relevant particles normalized to the value for 1 MeV neutrons. It shows that protons and high energy neutrons are most likely to cause displacement damage. In the P2 experiment, only very few protons are expected to reach the tracker planes. In addition, neutrons hitting the tracker planes mostly have energies below 1 MeV, see figure 5.10. The displacement damage of electrons increases with energy, but it is one to two orders of magnitude smaller than that of neutrons or protons.

The exposure to particle fluences represented as 1 MeV neutron equivalent fluences is analyzed for the P2 tracking detector based on simulation results. This procedure allows to compare the radiation level regarding non-ionizing energy loss with other particle physics experiments. The data on the displacement damages is accessible at Ref. [142] with data from Ref.s [143–146] and was used for this analysis. Each

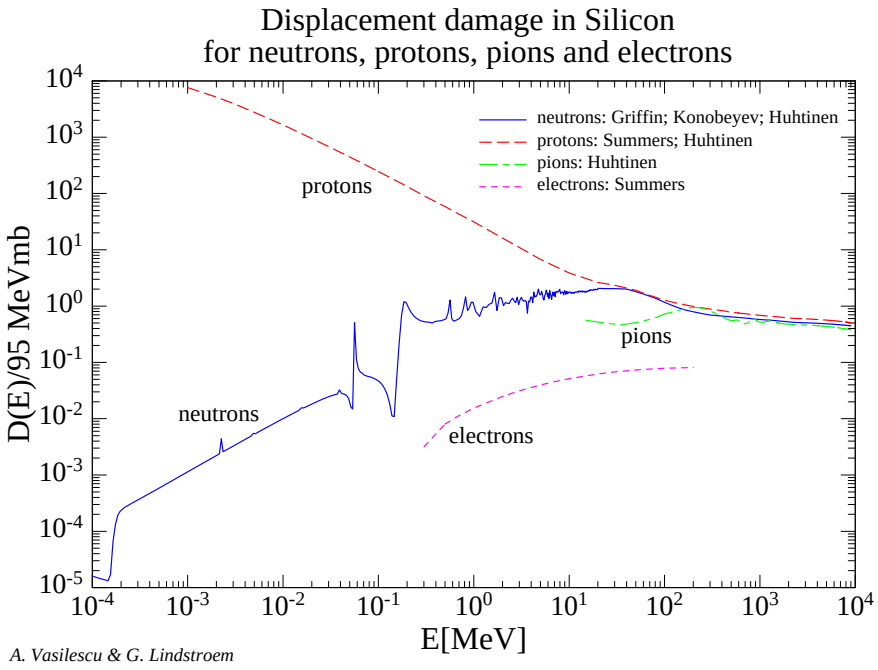

Figure 5.13.: *NIEL displacement damage functions for neutrons, protons, electrons and pions. Picture taken from Ref. [142] with data from Ref.s [143–146].*

particle traversing a tracker plane is weighted by its relative displacement damage contribution. This weight is multiplied with the normalization event weights of the P2 simulation and divided by the area covered by each bin. For electrons below 0.3 MeV kinetic energy, no data on the displacement damage was available so that this contribution was set to zero. This is justified as the energy is very close to the low energy limit below which electrons are not able to cause any lattice damages.

The analysis result is represented in figure 5.14, showing the fluence of all relevant particles in units of 1 MeV neutron equivalents per square centimeter. The dose corresponds to 10 000 h running time at full beam current. It can be observed that the contributions of neutrons and electrons are similar. Electrons are more abundant on the tracking detector planes, however, their displacement damage weighting factors are smaller compared to neutrons. The maximum level of non-ionizing radiation is obtained to be around 9×10^{13} 1 MeV n_{eq}/cm^2 on the first tracker plane and around 6×10^{13} 1 MeV n_{eq}/cm^2 on the third one. The expression of the non-ionizing radiation level in neutron equivalents allows comparisons to other experiments. Using again the inner B-layer of the ATLAS experiment as an example, one finds that this detector will accumulate more than 1×10^{15} 1 MeV n_{eq}/cm^2 until the end of LHC run 3 and a predicted accumulated luminosity of 300 fb^{-1}. The expected radiation level for the high luminosity upgrade of the LHC exceeds 1×10^{16} 1 MeV n_{eq}/cm^2 [147].

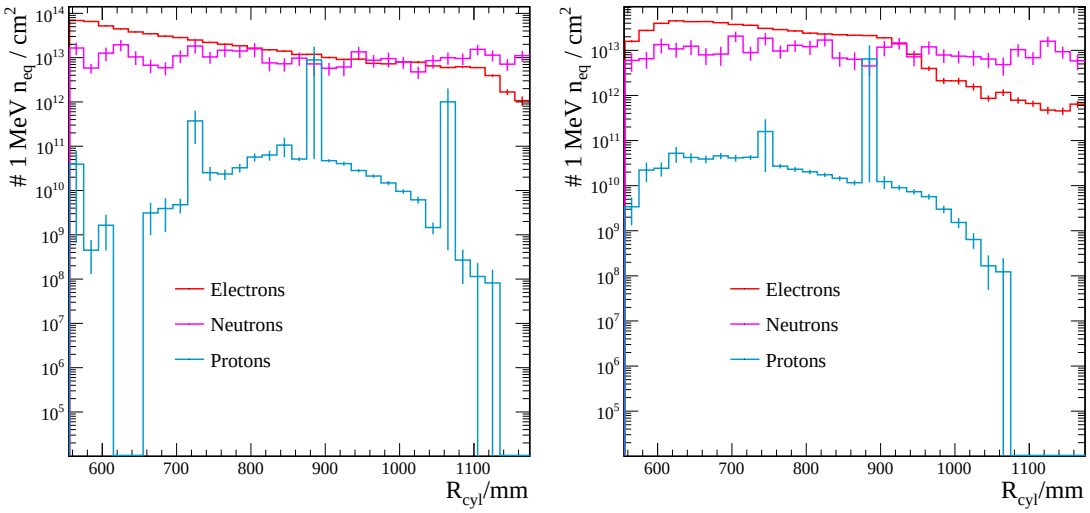

(a) *First plane* (b) *Third plane*

Figure 5.14.: *Non-ionizing radiation dose on the first and third tracker plane, evaluated in the detector simulation and given in units of* 1 MeV *neutron equivalents, normalized to* 1×10^4 h *run time at full beam current.*

Although the HV-MAPS design is not specifically optimized for radiation hardness, efficiencies above 90 % could be measured at noise rates below 40 Hz per pixel for fluences of up to 1.5×10^{15} 1 MeV n_{eq}/cm^2 with sensors cooled to 8 °C. For higher proton and neutron fluxes, a significant performance degradation was observed. All MuPix7 prototype sensors used in this test were fully functional after one year of annealing at room temperature. More details on this irradiation study and detailed results can be found in Ref. [113]. It has to be considered however that the macroscopic effects of radiation damages normally become more prominent at higher operation temperatures than for sensors cooled to low temperatures. In the P2 experiment, the pixel sensors are foreseen to be operated up to temperatures of around 70 °C.

6 Pixel Sensor Response to Photons

The large background of photons on the tracking detector planes which was observed in the simulation, dominating the electron signal partially by several orders of magnitude, requires the sensors chosen for the P2 tracking detector to have a very low detection probability for photons. In addition, solid knowledge on this photon detection probability is evidently needed for the development of the P2 tracking detector, as the amount of combinatorial background has direct implications on the reconstruction performance and on the readout. The simulation results for the suppression of the photon rate which are based on a simplified sensor model were presented in section 5.1.2, showing a suppression of the photon background by more than two orders of magnitude. The interaction processes of photons in silicon are expected to be well modeled within GEANT4, but it has to be investigated whether the simple sensor model represented by a 50 µm thin silicon volume with an active layer of 15 µm in the center models the actual sensor sufficiently well. An experimental verification of the simulation results is hence necessary so that these results can be used for the development of track finding and reconstruction algorithms.

The simulation results have shown that the detection probability highly depends on the photon energy. Consequently, experimental data needs to be collected for different photon energies. The agreement between simulation and experiment might be different depending on the photon energy since different interaction mechanisms dominate. In this chapter, results are presented for measurements with a radioactive source at low photon energy ($\sim$ 6 keV) and for a beam test measurement at the Mainzer Mikroton (MAMI) with photons in the MeV-range. The source measurements have been carried out in the scope of a Bachelor's thesis [148], so that the measurement setup and the results are only shortly summarized here. For the beam test measurement, the MuPix7 prototype sensor was placed in the photon beam behind the A2 photon tagging spectrometer at MAMI. The analysis of the collected data and the obtained results on the detection efficiency are discussed. Finally, some ideas

for possible future measurements of the photon sensor response are outlined.

6.1. Measurements with a Radioactive Photon Source

The photon detection efficiency of a MuPix7 HV-MAPS prototype was determined using an Iron-55 sample as photon source. This radioactive sample emits photons with energies of around 5.9 keV or 6.5 keV. Emitted electrons with similar energies are absorbed by the plastic enclosure of the sample. In case that a low energetic photon interacts in some material, it is usually absorbed, which makes efficiency measurements by evaluating hit coincidences with a reference detector impossible. The reference measurement therefore needs to be done separately with a detector for which the photon detection efficiency is well known. For this measurement, a cadmium zinc telluride (CZT) sensor with a thin beryllium window was used. The detection efficiency of this sensor is given by the manufacturer and has to be integrated over the photon energies present in the decay of the iron source. The uncertainty on the reference detector efficiency is a systematic uncertainty on the HV-MAPS efficiency measurement.

The active area of the MuPix7 prototype is limited to 3 mm × 3 mm, which is why an aluminum collimator with 1 mm opening diameter was used to focus the photon beam on the sensor. The hits detected on the pixel sensor can be seen on a hit map in real time which facilitates the alignment of the collimator relative to the sensor. The dimensions of the collimator were chosen such that the complete photon beam can be covered with the sensor. The collimator was also used in the reference measurement with the CZT detector to ensure comparable measurement conditions. As the dimensions of the CZT detector were about the same as for the MuPix sensor, but no photon hit position is accessible, the alignment had to be done by shifting the source in small steps in x- and y-direction in front of the sensor and determining the position with maximum detection rate. The efficiency corrected photon rate with the collimator in front of the CZT sensor was measured to be (29.8 ± 1.7) Hz [148].

The determination of the photon detection rate with the MuPix7 prototype sensor required to subtract the background count rate present without any particle source near the sensor. It was however observed that this background count rate fluctuated more than statistically expected. Because of the small rate of collimated photons, the uncertainty on the background count rate turned out to be the dominating systematic uncertainty of this efficiency measurement. It was observed that the photon detection efficiency depends on several sensor settings, but also on the particular sensor used for the measurement. Different efficiencies could be observed for sensors

which should be identical. The determined efficiencies varied between about 25 % to 35 % for settings with moderate power consumption. The largest photon efficiency of 35.6 % could be observed for a 64 µm thin MuPix7 sensor [148].

The efficiency results can be compared to the predicted detection probability evaluated with the GEANT4 simulation, which can be seen in figure 5.6. The efficiency values observed in simulation are 16.9 % for 5.6 keV photon energy and 17.5 % for 6.4 keV (closest simulated energies, with negligible statistical errors), which is about a factor two smaller than the experimental result. It has to be considered however that in this low energy region, the simulation results are very prone to systematic effects, in particular due to the uncertain actual position and width of the depletion zone in the silicon semiconductor sensor. It was discussed already that the pure photoelectric effect cross section should increase quickly to low energies and peak additionally at the largest silicon binding energy (1.84 keV). The opposite behavior was observed for the predicted photon detection probability of the silicon sensor. This effect was explained by photons interacting on the first few micrometers within the silicon material, so that secondary electrons do not reach the active silicon part. Consequently, a deviation in the position or width of the depletion zone might affect the extent of the efficiency drop observed around 2 keV and therefore even explain a discrepancy by a factor of 2 between the experimental results and the simulation. In addition, one has to consider the variance in the experimentally observed results. For some sensors, efficiencies around 25 % could be observed at 6 keV, which is not too far away from the simulation result, given the large systematic uncertainties. As a consequence, the agreement between experiment and simulation is still considered to be acceptable given the fact that both values are affected by systematic effects. More measurements at slightly higher photon energies around 20 keV would be beneficial as the efficiency curve observed in simulation at such energies is more monotonous, indicating that these values are more reliable. More over, photons of such energies are expected to be more abundant on the tracker planes in the P2 experiment.

6.2. Photon Beam Test Measurement

The sensor response to photons was measured in the energy range between 22 MeV and 419 MeV and compared to the predictions obtained with a dedicated GEANT4 Monte Carlo simulation. The measurement was performed from March 28th to April 2nd in 2016 using the MuPix7 HV-MAPS prototype.

6.2.1. Setup

The beamtest was performed at the Mainzer Mikroton (MAMI) beam facility, using the Glasgow photon tagging spectrometer (in short also referred to as "tagger") [149–151], which is otherwise used for experiments of the A2 collaboration. A schematic of the measurement setup is shown in figure 6.1a. An electron beam is directed on a thin foil radiator and thereby produces bremsstrahlung photons which are mostly oriented along the electron beam axis. Afterwards, the electron beam is directed by a dipole magnet onto the tagger detectors, while the photon beam continues in straight direction and passes a collimator with 1 mm diameter. It then traverses a vacuum window including a permanent magnet. The distance between the silicon pixel sensor and the 100 μm thick mylar foil of the vacuum window was determined to be (90 ± 1) cm. The experimental setup is completed by a 25 cm^3 lead-glass Cherenkov detector which is placed about 20 m downstream of the radiator.

The efficiency measurement principle is as follows: For photons detected on the MuPix7 sensor, coincident hits on the tagging detector are searched for. The tagger measures the electron energy based on the deflection in the magnetic field, which allows to deduce the photon energy. In this way, the number and energy of photons detected by the HV-MAPS can be related to the counting rate in the corresponding tagger channel. However, only a small fraction of all photons with tagged electrons will pass the collimator. In order to correct for this, two additional calibration runs are performed using the downstream lead glass detector.

The MAMI beam was operated at an energy of 450.17 MeV so that photons were tagged in the energy range between 22.3 MeV and 419.0 MeV. The average beam intensity was about 100 pA. Using the detector monitoring system provided by the A2 collaboration, the magnetic field of the photon spectrometer was measured and the equivalent uniform field was determined to be 0.5467 T. The magnetic field measurement allows the mapping of the 352 tagger channels to the energy of the bremsstrahlung photon.

The MuPix7 was operated at a high voltage of 85 V. Figure 6.1b shows a photograph of the MuPix7 sensor during the beamtime campaign. In this figure, a setup with the beam hitting the sensor from the back side (turned chip) is shown while most of the data was taken with the front side of the sensor pointing upstream. The sensor used in this beamtime had been thinned down to 64 μm, the PCB to which it was glued had been thinned to about 100 µm at the position of the sensitive sensor area. The MuPix data acquisition system (DAQ) at the time of this experiment allowed for the integration of eight independent signal lines as additional trigger inputs. The photon tagging spectrometer comes with a signal processing system enabling the combination of configurable subsets of the 352 tagger channels to one signal. The signal of a particle detected in the focal plane detector is then represented by a roughly 20 ns

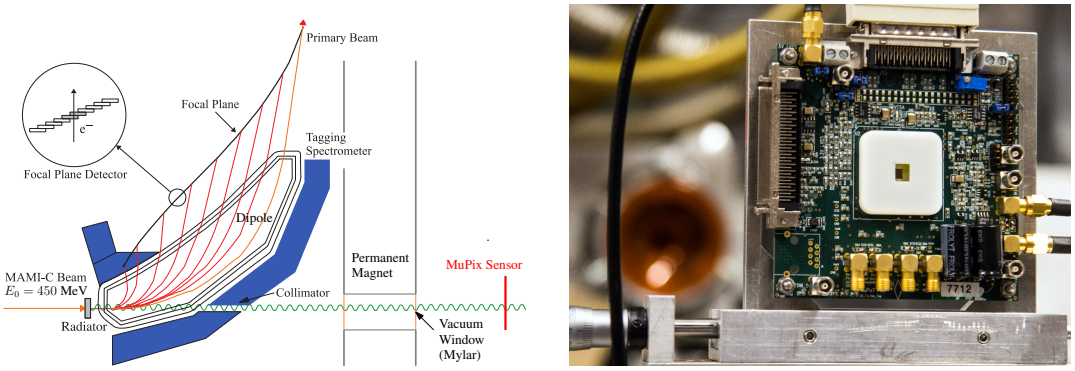

(a) *Schematic of the experimental setup (adapted from [152]). Electron trajectories are depicted by red lines, the Photon beam by the green curved line.*

(b) *MuPix7 chip and PCB with the beam line in the background.*

Figure 6.1.: *Experimental setup of the photon beamtest without power supplies, the off-chip readout system and the lead glass detector downstream of the MuPix sensor.*

wide pulse. Therefore, subsets of tagger channels were directly integrated to the MuPix readout in order to find signal time coincidences. The delay of the tagger signal with respect to particle hits on the pixel sensor was found to be about 200 ns, as shown later in section 6.2.2.

The tagger counting rate during the measurement exceeds the hit rate on the pixel sensors for several reasons. First, the photon detection efficiency of the silicon pixel sensor in the energy range of 20 MeV up to 420 MeV is at the order of $O(10^{-3})$. In addition, only a small fraction of the photons which are tagged actually hit the MuPix sensor. It has to be taken care that the trigger input rate of the connected tagger channels can be handled by the MuPix readout system, which assigns timestamps to both the trigger signals and the pixel sensor hits. As a consequence, only a small subset of tagger channels is connected as trigger inputs to the MuPix readout. The subset of tagger channels was changed from time to time such that most of the energy range covered by the photon tagging spectrometer was measured with sufficiently high statistical accuracy. The number of connected tagger channels was chosen such that the trigger input rate was observed to be between 100 kHz and 200 kHz. Since the photon energy distribution follows the Bremsstrahlung energy spectrum, this means that only single tagger channels could be connected to the MuPix DAQ for low photon energies, whereas for higher photon energies, the signals of up to ten tagger channels were merged and connected to one trigger input. The beam was configured to provide an average beam current of about 100 pA, for which an average hit rate on the silicon pixel sensor of about 500 Hz was observed. Since the tagger hit rate is used as a reference for the efficiency measurement, the numeric value of the beam

current does not enter the efficiency analysis.

6.2.2. Data Analysis

The main purpose of the beamtest experiment described here is a measurement of the response of the MuPix HV-MAPS to high energy photons. In order to evaluate this efficiency depending on the photon energy, the number of photons hitting the sensor and their corresponding energy need to be known. Since the photon energy is obtained by the tagger, hits in the tagger must be matched to hits on the MuPix sensor.

Background Suppression

The background for this efficiency analysis can be divided into two categories. On the one hand, there is a constant background level of hits distributed randomly in time. These hits can be caused by photons outside the energy range of the connected tagger channels or by noise hits which are mainly caused by electronic noise. On the other hand, there are secondary pixel hits attributed to signal particles.

Untagged photons and noise hits on the pixel sensor are rejected by analyzing time coincidences between the hits on the pixel sensor and in the photon tagging spectrometer. By considering all possible time differences below a few hundred nanoseconds between pixel hits and tagger hits, the time coincident events are expected to show up as a Gaussian peak over a flat background. Figure 6.2a shows the time difference spectrum for a reference data subset, that was recorded with one unchanged tagger configuration and a mean measuring energy of the connected tagger channels of about 317.4 MeV. The coincidence peak is clearly visible and quite well described by a Gaussian distribution. The peak position is shifted from zero mainly because of delays in the detection, processing and transmission of the tagger signal. The non-Gaussian higher tail on the signal peak is most likely caused by time walk in the pixel sensor, but was not further investigated in this analysis. More over, the background is observed to be randomly distributed in time as expected. The time coincidences can be evaluated either relative to all tagger signals without differentiating between the eight different trigger inputs, as done for figure 6.2, or for all trigger inputs individually. The latter procedure provides better resolution in energy, but less statistical accuracy.

Evaluating time coincidences between the pixel sensor and the photon tagging spectrometer does not suppress the background which is correlated in time to signal events. Such background hits occur when secondary particles of one tagged electron cause more than one hit on the pixel sensor. Those secondary hits are then

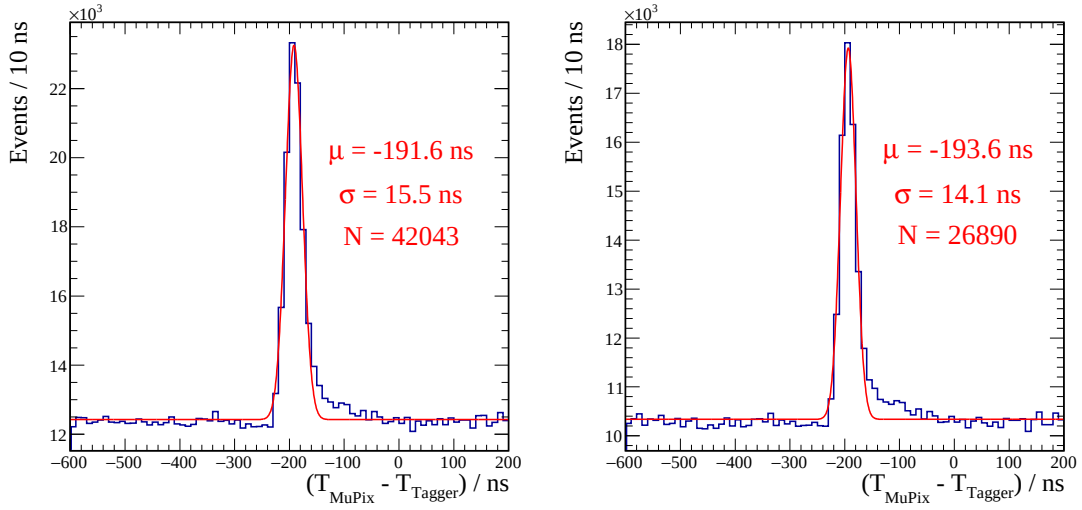

(a) *Without preselection of MuPix hits.*

(b) *Rejecting MuPix hits with* $\Delta T \leq 32\,\text{ns}$ *to previous hit in time.*

Figure 6.2.: *Spectrum of time differences between hits on the MuPix Sensor and the photon tagging spectrometer for reference subset of the data. Number of coincident signal events is extracted by fitting a Gaussian distribution.*

expected to be detected some nanoseconds after the first hit, which is considered as signal. Another possibility is cross talk on the pixel sensor electronics. For an absolute efficiency measurement, not more than one hit must be counted for any photon. At average pixel sensor hit rates of about 500 Hz while data taking, multiple hits within some nanoseconds are very unlikely to be attributable to different primary particles.

The time difference distribution for consequent pixel sensor hits is shown in figure 6.3a for the reference data subset. Assuming that all sensor hits are independent, this distribution is expected to be flat in the plotted range. The peak at low time difference values is therefore clearly identifiable as signal correlated background. Note that the time difference values for this spectrum were calculated using the MuPix chip hit timestamps, which take discrete time values of 16 ns spacing. With the histogram plotted in figure 6.3a having the same binning, the discrete time difference values are represented as the low edge of each bin. Moreover, around 81% of all time differences take higher values than the upper limit of the plotted range, but are included in the calculation of the mean time difference of $\mu = 1.935$ ms being consistent with hit rates around 500 Hz.

There are multiple possible explanations for correlated hits close in time. Figure 6.3b shows the spatial separation of consequent hits within 192 ns in the reference data subset. The excess of multiple hits for equal column indices, which is particularly

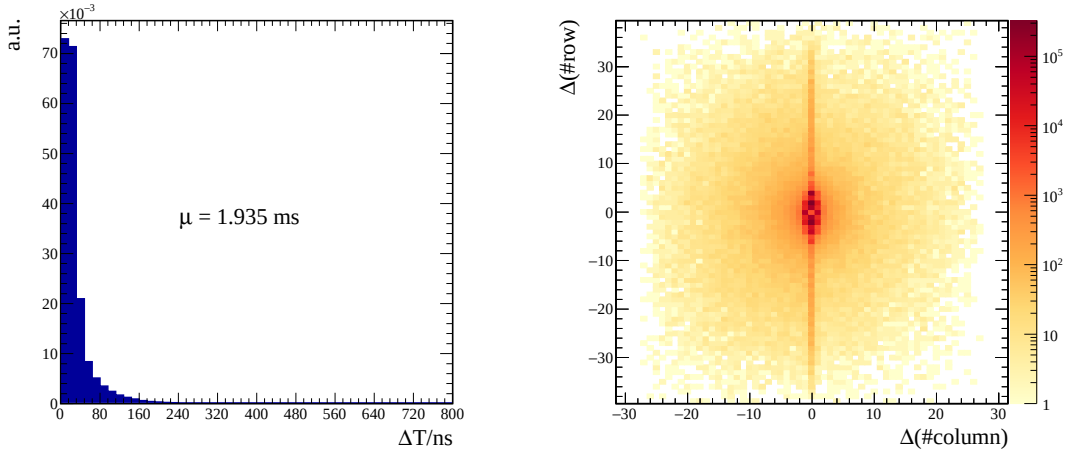

(a) *Time difference of consequent MuPix hits. The distribution is normalized including the overflow bin, which is also included in the calculation of the mean value.*

(b) *Spatial separation in row and column indices for consequent MuPix hits within* 192 ns*, with logarithmic color scale.*

Figure 6.3.: *Temporal and spatial separation of consecutive pixel sensor hits.*

enhanced for even row index differences, is attributed to effects in the chip electronics, in particular cross-talk on neighboring signal lines. However, it can be seen that most hits which are shortly separated in time are also very close to each other in space. This is a clear sign for hit clusters caused by particles depositing sufficient energy in multiple pixels. The observed hit multiplicities with higher spatial separation are either independent hits which are close in time by accident or electron-positron pairs created upstream of the pixel sensor.

In order to reject signal correlated background, the pixel sensor hits are preselected. Hits with time difference ΔT to the preceding hit below some cut value are rejected. This time difference cut value is optimized by evaluating the number of signal events in the time coincidence peak using different cut values for the preselection. The result can be seen in figure 6.4. As the number of rejected hits does not increase for cut values ΔT_{cut} above 32 ns, this cut value is chosen for the further analysis. The rejection factor of the preselection is observed to be above 35%. As it can be seen in figure 6.2b, which shows the time coincidence spectrum including the preselection, no considerable influence of the preselection on the signal or the background shape is observed. Moreover, the width of the coincidence peaks in figure 6.2 of 15 ns and 14 ns are consistent with other measurements of the MuPix 7 time resolution with similar settings.

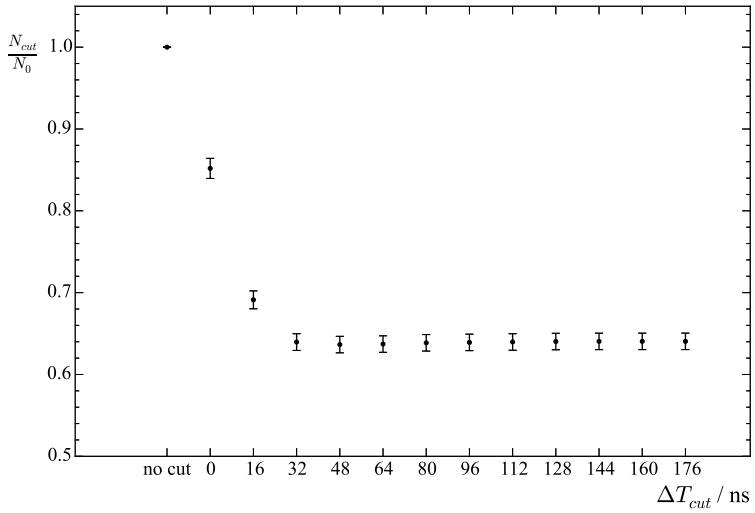

Figure 6.4.: *Number of time coincident pixel sensor hits N_{cut} after preselection with cut values ΔT_{cut} relative to the number of events N_0 without applying any preselection. Hits are rejected for $\Delta T \leq \Delta T_{cut}$.*

Tagging Efficiency

The MuPix photon detection efficiency in the MeV energy range is primarily evaluated by comparing the number of signal hits on the pixel sensor to the number of tagger signals. However, most of the photons produced by bremsstrahlung of tagged electrons are lost upstream of the pixel sensor, e.g. in the collimator of 1 mm diameter. The procedure of a tagging efficiency measurement was developed for previous measurements by the A2 collaboration and is used for this experiment. The measurement is based on the detection of photons by a 25 cm^3 lead glass detector placed about 20 m downstream from the radiator and the comparison of this measurement to the signals detected in the photon tagging spectrometer.

For this analysis, the tagging efficiency measurement was performed twice, at the beginning and the end of data taking. Both measurements lead to consistent results and were averaged, yielding the data points shown in figure 6.5. However, the measured efficiency values do not show a monotonic behavior over the whole energy range. Previously published measurements (see Ref.s [150, 151]) suggest the tagging efficiency to be rather constant and only slightly increasing with energy. In the presented measurement, this only holds for the channel range between about channels 80 and 250. The drop of the tagging efficiency for channels above 250, corresponding to photon energies below about 150 MeV, can be explained by the lead glass detector operation limit [150]. No obvious reason was found for the drop and the strongly varying data points observed at low channel numbers. This behavior was not ob-

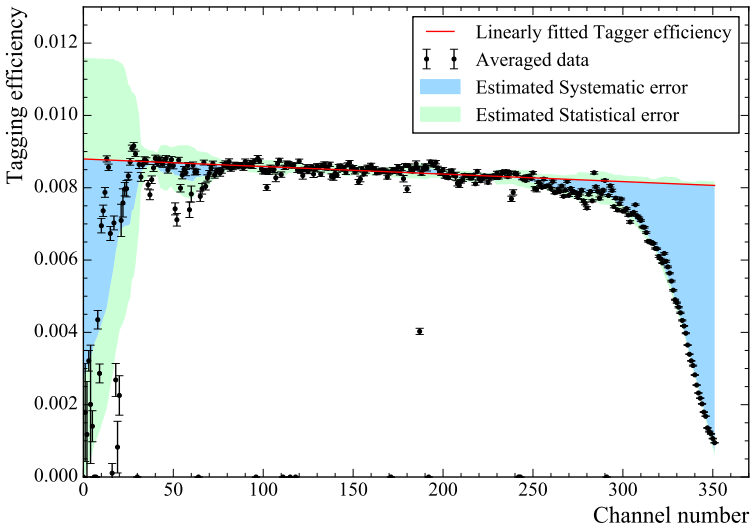

Figure 6.5.: *Tagging efficiency measured at* $E_0 = 450.17\,\mathrm{MeV}$ *beam energy for a collimator with* $d = 1\,\mathrm{mm}$. *The data points show the average of two measurements and the corresponding statistical uncertainty. The range between channels 80 and 250 was fitted linearly. The colored shaded areas represent the estimated statistical and systematic error on the corrected tagging efficiency evaluated as the extrapolation of the linear fit, see explanation in the text.*

served in the above cited measurements, which were performed at different beam energy and with larger diameters of the collimator. Consequently, it is considered to be very likely that the actual number of photons passing the collimator is in fact linearly dependent on the photon energy. For the purposes of this analysis, the linear part of the measured tagging efficiency curve is linearly fitted and extrapolated to the complete tagger energy range. The systematic uncertainty on this corrected tagging efficiency is supposed to be taken as the difference of the fitted values to the data, but at the same time should be separated from statistical fluctuations of the data points. In order to separate these statistical fluctuations, for each tagger channel, the residuals of the twenty surrounding tagger channels resulting from the linear fit were again fitted linearly. The value of this fit at the particular tagger channel is considered to be the systematic uncertainty of the corrected tagging efficiency of this channel. The standard deviation of the residuals of this second linear fit is taken as the statistical uncertainty for this channel. The result of this error estimation is represented by the shaded colored areas in figure 6.5.

At the time of data taking, it was not possible to remove all the material attributed to the Crystal Ball detector otherwise used for measurements by the A2 collaboration, which was standing between the pixel sensors and the lead glass detector. The tagging efficiency is therefore expected to underestimated in the measurement. In order

to correct for this effect, all values are additionally increased by 10%. The absolute systematic uncertainty on this correction is estimated to be 5%.

Correction for Sensor Position

It was observed that the beam halo surrounding the photon beam spot on the pixel sensor was larger than the sensitive area. Since the MuPix sensor has a quadrilateral shape of 3.3×3.2 mm, and the number of hits caused by the beam halo is supposed to decrease with the distance to the beam center, the total number of hits to be detected will depend on the relative position of the beam to the pixel sensor. The most likely reason for the wider beam halo is the presence of additional material, more precisely 100 μm of mylar and about 90 cm of air upstream of the pixel sensor. Since not all measurements at different photon energies were done with exactly the same sensor and beam position, the effect needs to be corrected in order to achieve comparable results.

The correction was evaluated by analyzing all runs of a particular sensor position as one data subset. It was found that three different positions of the beam spot on the sensor occurred during data taking. For each of those three subsets, the signal selection was repeated while varying an additional preselection cut on the hit position: all hits with larger distance R_{cut} to the center of the beam were rejected. The row and column number coordinates of the beam center were evaluated by fitting a two-dimensional error function to the hit map without any selection cuts. The function used for this fit reads:

$$N(x,y) = N_0 \cdot \left\{ \frac{1}{2} - \frac{1}{2} \cdot \mathrm{Erf}\left(\sqrt{\left(\frac{x-x_0}{a}\right)^2 + \left(\frac{y-y_0}{b}\right)^2} - R \right) \right\} + N_1 \tag{6.1}$$

with x_0, y_0 being the coordinates of the beam centre and additional parameters N_0, N_1, a, b, R parameterizing shape and normalization of the beam spot plus a constant background. By varying the cut parameter R_{cut}, it is possible to evaluate the number of signal events per area for all ranges in R which are at least partly covered by the sensor. Figure 6.6 shows both the hit map without any event selection and the evaluated beam profile of selected events for the beam position with highest statistics. In figure 6.6b, the number of events in the range $[R_{\text{cut}}^{\text{min}}, R_{\text{cut}}^{\text{max}}]$ was evaluated by selecting hits with $R \leq R_{\text{cut}}$ and then subtracting the selected events for the next smaller cut value R_{cut}. It can be seen that the statistical error on this difference increases for large values of R, which is explained by the small area available for this range and the Gaussian fit included in the event selection procedure. In order to get a corrected number of events within a circular region R_{max}, the content of each bin

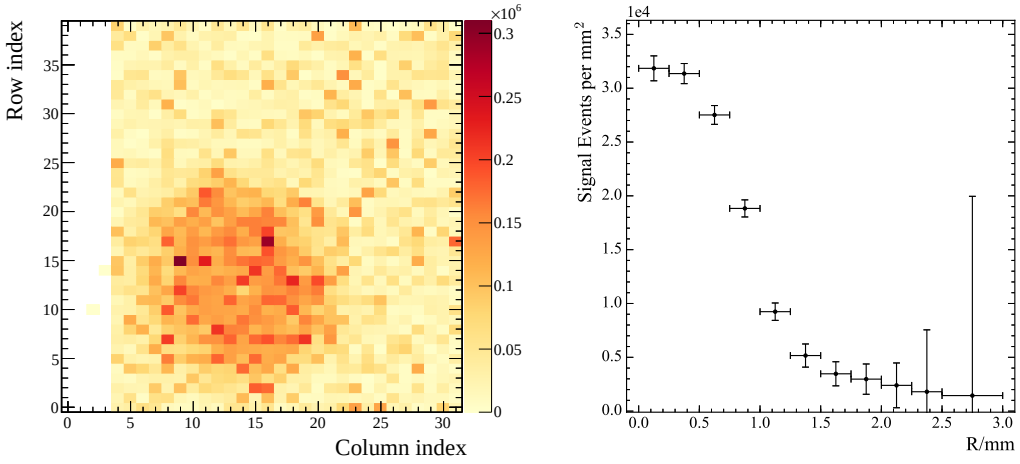

(a) *Hit map before any event selection for beam position with highest statistics. The fitted row and column number coordinates of the beam center are* $x = 14.21$ *and* $y = 12.91$.

(b) *Selected events divided by the area of the pixels inside the range* $[R_{cut}^{min}, R_{cut}^{max}]$.

Figure 6.6.: *Photon beam shape before and after event selection. Both plots represent the data set of the beam position with highest statistics.*

i in figure 6.6b, representing the number of events per area η_i, is multiplied by the area represented by the particular range in R:

$$N_{\text{corr}}(R_{\text{max}}) = \sum_i \pi \left(R_i^2 - R_{i-1}^2\right) \cdot \eta_i \text{ for bins with } R < R_{\text{max}}. \tag{6.2}$$

The correction factor γ applied to the data is then given by the ratio of N_{corr} and the selected number of events N without any cut on the spatial hit position.

For the further analysis, the correction factor was calculated for $R_{\text{max}} = 2.25\,\text{mm}$ as the statistical error on this factor increased significantly for higher maximal radii. The results for the three different beam positions are summarized in table 6.1. Since the number of data taking runs is different for the three sensor positions, the relative statistical uncertainty is very different. The number of selected signal events is corrected by the correction factors in table 6.1 corresponding to the sensor position in the particular run.

6.2.3. Simulation

The beam test experiment is modeled by a Monte Carlo (MC) simulation based on GEANT4. Only the parts of the setup (see figure 6.1) behind the permanent magnet

Position	Fitted Beam Position column	row	Corr. Hit Count N_{corr}	Raw Hit Count N	Corr. factor γ
1	22.53	14.24	$1.87 \pm 0.24 \times 10^4$	$1.42 \pm 0.04 \times 10^4$	1.32 ± 0.17
2	14.22	12.91	$1.31 \pm 0.05 \times 10^5$	$1.08 \pm 0.01 \times 10^5$	1.21 ± 0.05
3	15.04	16.22	$2.20 \pm 0.40 \times 10^4$	$1.70 \pm 0.03 \times 10^4$	1.29 ± 0.24

Table 6.1.: *Correction factors considering hits in the beam halo outside the sensitive area for three different relative sensor positions.*

are included. The photon beam is assumed to have a Gaussian beam profile with 1 mm width, equal to the collimator diameter. Photons were simulated using a uniform energy distribution, although in the experiment, the distribution is a continuous Bremsstrahlung spectrum. It was checked that using a Bremsstrahlung characteristic photon energy distribution following $1/E$ does not change the efficiency result visibly, but leads to less statistical accuracy for high photon energies. The width of the Mylar foil at the end of the vacuum window is implemented with 100 μm thickness, the distance in air between the MuPix sensor and the Mylar foil is set to 90 cm. The pixel sensor is modeled by a plane of 64 μm thick silicon. Since data was corrected to represent all hits with distance $R \leq 2.25$ mm around the beam center, the same cut is applied on the Monte Carlo hits.

The depletion zone in which the charge is collected in the HV-MAPS is again modeled as a 15 μm thick active layer centered in the silicon volume. Only particles reaching this active layer are considered for the efficiency prediction. The efficiency to detect charged particles reaching the active layer is set to 100%. A particle is considered to be produced inside the sensor if its vertex is inside the 64 μm of silicon and not necessarily inside the depletion zone. The 100 μm thick thinned PCB behind the sensor is also included in the simulation, but does not have any effect on the results.

The expected photon detection efficiency evaluated with this simulation is shown in figure 6.7. The total efficiency to detect photons increases from about 3.5×10^{-4} at 25 MeV photon energy to about 1.9×10^{-3} at 420 MeV. The contribution of different particle production processes to this total efficiency is shown as well. If multiple secondary particles (of different production processes) occur in one event, they are all counted with the weight being the inverse of the number of detected secondaries. It can be seen that the production of secondary particles inside of the sensor is dominated by the contribution of pair creation in air and the Mylar foil. This contribution also determines the increase of detected particles with energy, which became steeper after introducing the cut of $R \leq 2.25$ mm. Moreover, the contribution of secondary electrons produced by the photoelectric effect is negligible.

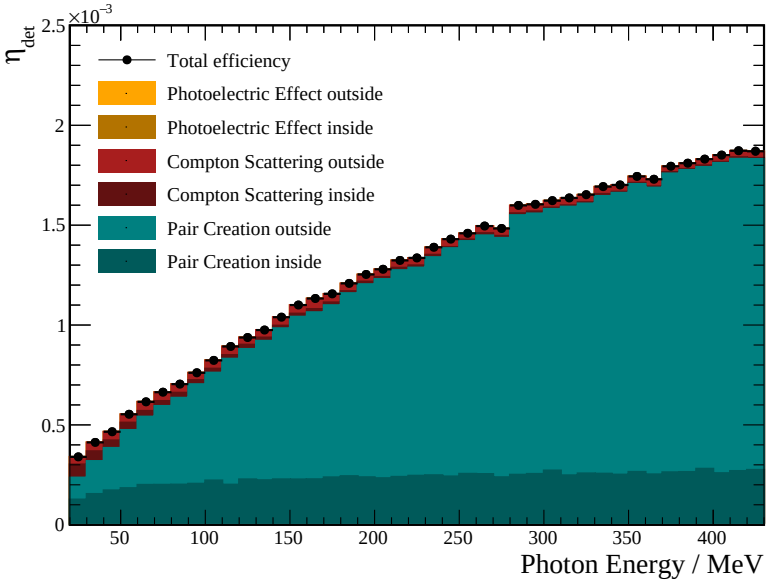

Figure 6.7.: *Ratio of detected photons η_{det} in the beamtest experiment predicted in a Monte Carlo simulation. 2×10^8 photons were simulated uniformly distributed over the tagged energy range. The contribution of all possible production processes of the detected charged particles on the sensor is also shown, divided into production inside and outside the silicon sensor. Particle production outside the* 64 µm *thick silicon sensor is possible in the* 100 µm *thick mylar foil or in* 90 cm *air in front of the sensor. Only hits with* $R \leq 2.25$ mm *are counted in consistence to the data selection.*

6.2.4. Efficiency Results

With the number of signal events N_γ, the number of tagger signals N_e, the corrected tagger efficiency α and the correction factor for the sensor position γ all being evaluated as described in the preceding sections, the detector response to photons η can be calculated by

$$\eta = \frac{N_\gamma}{N_e \cdot \alpha} \cdot \gamma \ . \tag{6.3}$$

The detector response is analyzed for each tagger channel configuration individually. For each of the different configurations, the tagger efficiency is averaged over the connected channels. The correction factor γ is taken from table 6.1 corresponding to the beam position that was present while taking the data for the particular tagger configuration. It is possible to evaluate all eight trigger inputs of the MuPix DAQ with their connected tagger channels individually or to treat them as one signal.

Figure 6.8 shows the result for both methods of analyzing the efficiency. Both strate-

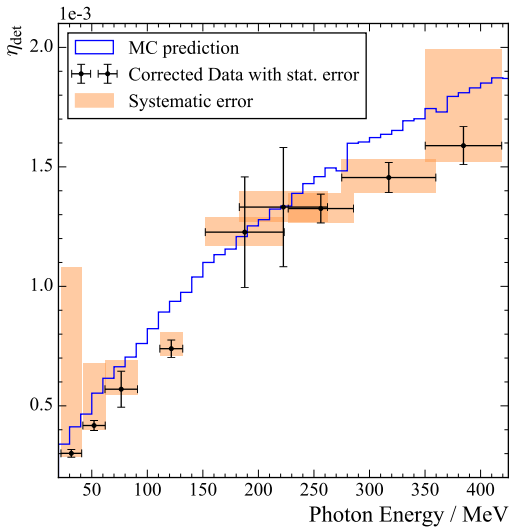

(a) *Efficiency for merging trigger inputs to one trigger signal. Each tagger channel configuration corresponds to one data point. The MC prediction shows the total response to photons as plotted in figure 6.7.*

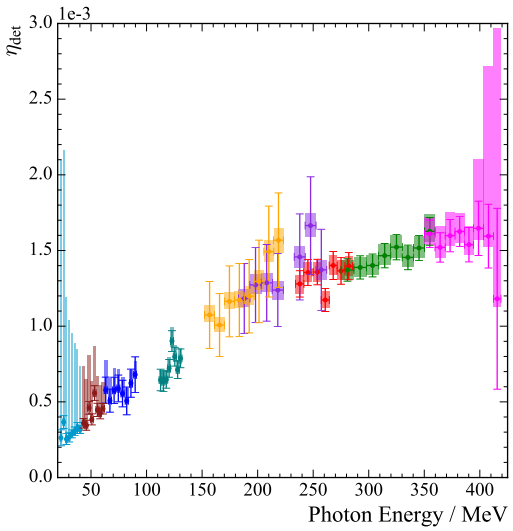

(b) *Efficiency for individual evaluation of trigger inputs. Different tagger channel configurations are grouped by color. Statistical error is represented by the error bars, systematical error by the shaded areas.*

Figure 6.8.: *Efficiency results for the HV-MAPS photon beam test experiment.*

gies yield consistent results and overlapping data points are found to be consistent with each other. When analyzing the trigger inputs individually, the case of multiple triggers firing at the same time is resolved such that one of them is chosen randomly while noisy channels are not considered. The result for merged trigger inputs in figure 6.8a is compared to the MC prediction discussed in the previous subsection. Data and MC are found to be in rather good agreement. The larger statistical errors on some of the data points are mostly attributed to the different statistical accuracy of the correction factor γ. The systematic errors shown are determined by the corrections on the tagger efficiency measurement.

Turned Sensor

The sensor response to photons was additionally tested with the sensor in the beam being turned around, meaning that the beam passes the thinned PCB before reaching the sensor. Two runs using the same tagger channel configuration as the reference subset of the data with average energy of about 317.4 MeV were performed. One measurement was done before taking data for the threshold scan explained in the next subsection and one measurement made directly afterwards in order to check the reproducibility of the results. While the detection efficiency of photons (and the

statistical error) at this energy before turning the chip was measured to be $\eta_{\text{det}} = (1.46 \pm 0.07) \times 10^{-3}$ (see the corresponding data point in figure 6.8a), the two measurements with turned chip yield $\eta_{\text{det}} = (2.36 \pm 0.18) \times 10^{-3}$ and $(2.25 \pm 0.69) \times 10^{-3}$, respectively. Both measurements with turned chip therefore show consistent results and confirm the effect of the additional PCB on the photon detection efficiency.

The difference to the previous result before turning the chip is larger than observed in another MC simulation that assumes exactly 100 μm PCB material in front of the sensor chip. The efficiency result of this simulation at $E = 317\,\text{MeV}$ is 1.96×10^{-3}. However, the results are still in agreement within two times the statistical uncertainty. In addition, the thickness of the PCB is not perfectly known, so that a deviation in this value could also explain the difference.

Threshold Scan

The threshold on the signal amplitude in the MuPix chip can be varied in order to investigate the corresponding changes in the detection efficiency. Since the amplitude in the MuPix7 is inverted, higher threshold voltage values effectively correspond to lower thresholds on the signal. The baseline is at 800 mV. The result of an efficiency and noise rate measurement in a threshold scan with multiple MuPix sensors in a 250 MeV mixed positron, muon and pion beam at the Paul Scherrer Institute (PSI) is reported in Ref. [111].

Unfortunately, in this photon beam test, problems with the DAQ occurred for smaller threshold voltages. Because of the zero-suppression of the MuPix DAQ, data is only written if a hit on the sensor was detected. However, since the trigger rates were much higher compared to the hit rates in this experiment, this lead to some buffer overflows if no hit happened for a longer time period. Consequently, this problem particularly occurred using lower threshold voltages than 0.73 V, while the measurements reported previously were all performed at a threshold voltage of 0.74 V. Since "bad" data is rejected in this threshold scan analysis, the resulting ratio of hits per trigger signals, shown in figure 6.9, will be biased for lower threshold voltages and should be interpreted only qualitatively. Nevertheless, it can be observed that the ratio of signal hits is nearly constant for threshold voltages between 0.68 V and 0.75 V. The other measurements of this beam test experiment can therefore be considered as being independent of the actual threshold voltage configuration inside this range.

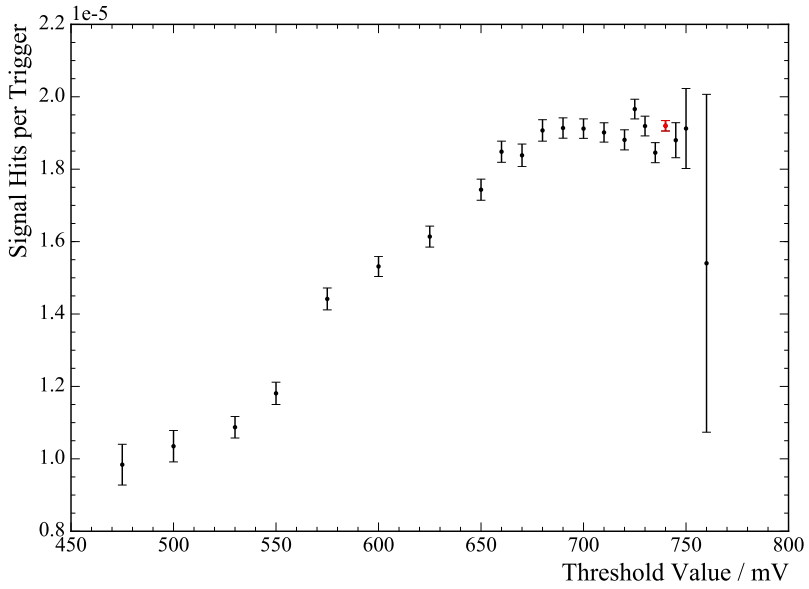

Figure 6.9.: *Signal hits per trigger signal for varied threshold voltage values. Result is biased because of problems while data taking, see the explanation in the text. The nominal threshold voltage configuration is emphasized by the red data point.*

6.2.5. Conclusions

The MuPix sensor was successfully integrated into the A2 photon tagging spectrometer setup in order to match hits on the pixel sensor to electrons detected by the spectrometer. Time coincident hits could be identified as a clear peak on top of a constant background of random time differences and were fitted using a Gaussian distribution. It was further possible to relate the number of beam particles hitting the sensor to the number of tagged electrons using two measurements with a lead glass detector positioned downstream of the pixel sensor. However, the systematic uncertainties on this tagging efficiency measurement form the largest contribution to the total uncertainty on the final efficiency measurement.

The number of hits on the pixel sensor per photon was evaluated for different photon energies and compared to the predictions based on simulation. Both results were found to be consistent. However, it was observed that most of the hits were caused by photons converting inside material upstream the pixel sensor. The presented efficiency results can therefore be interpreted as an upper limit on the actual photon detection efficiency of the HV-MAPS. In order to improve the measurement, the setup would need to be changed such that the length of air before the sensor is minimized. An additional permanent magnet could help to remove electrons and positrons created in the Mylar foil.

6.3. Possible Future Photon Response Measurements

The photon response of the HV-MAPS was measured with a radioactive source at a low photon energy of around 6 keV and for photons in the MeV range in a MAMI beamtest. As the efficiency result of the MAMI measurement was dominated by pair creation outside the sensor, it could be improved by decreasing the distance between the sensor and the vacuum window and by putting an additional magnet in between. The source measurement could be repeated with other commercially available radioactive sources that produce different photon energies. For example, measurements with Cadmium-109 at photon energies of 22 keV to 26 keV or with Americium-241 at around 60 keV would further test the predicted photon detection efficiency obtained in simulation. It would also help to use more powerful sources to increase the signal-to-background ratio of the measurement. In addition, the photon measurements carried out so far were done with the MuPix7 sensor, so that measurements with the newest MuPix8 prototype sensor would be interesting.

MuPix prototype sensors were already successfully operated in X-ray tubes normally used for student practical courses. In such an apparatus, it is possible to select any energy of the continuous Bremsstrahlung spectrum by Bragg reflection on a crystal. However, photon efficiency measurements with this setup are difficult. First, it is difficult to operate a reference detector within such a tube because of space constraints. The setup would therefore be suited mainly for relative measurements of different photon energies, while the absolute scale had to be taken from an efficiency measurement with a radioactive source. Second, the intensity of such tubes used in practical courses is quite low, which means that the counting rate would be even harder to differentiate from fluctuating background than it was already observed in the measurement with the iron-55 source [148]. Increased counting rates could be achieved only at the characteristic radiation energies of the anode material.

Part III.

Tracker Module Mechanics and Cooling

7 Technical Design

The second part of this thesis is devoted to the mechanical realization of the tracking detector for the P2 experiment. The concept and basic geometry were already presented, but need to be implemented in an actual mechanical design. As outlined previously, the P2 tracking detector consists of four tracker planes wich are arranged as two plane pairs. One pair of planes is placed at the beginning of the barrel shield and the other plane pair is located at the end of the magnet (see figure 3.10). The two tracker planes of each plane are are quite close to each other with a distance around 20 mm.

Unfortunatly, it is not affordable to build a tracking detector that covers the complete transverse plane between the barrel shield and the magnet. Each tracker plane is therefore divided into four segments covering about 15° in azimuthal direction. Consequently, the tracking detector consists of 16 plane segments. The segments of neighboring sensor planes are however built as one mechanical module, so that the detector is made up by eight identical tracker modules, as it can be seen in figures 3.6 and 3.10. The technical design of these modules is discussed in this chapter.

The development of the tracking detector mechanics from the conceptual idea of building a silicon pixel tracking detector for the P2 experiment to the technical design presented in this chapter is one of the main parts of the work done in the scope of this thesis. Autodesk® Inventor® was used as Computer Aided Desing (CAD) software tool. This chapter is structured as follows: First, the main requirements on the mechanical design are discussed, then the general concept for the tracker module implementation is presented. This general concept is then followed by the detailed design descriptions of the different module parts and the assembly of the complete tracker module. Hardware developments based on this technical design are also part of this thesis, but will be presented later in chapter 9.

7.1. Requirements

The technical design of the modules for the P2 tracking detector needs to fulfill several requirements. The reconstruction of track parameters with the P2 tracking detector will be dominated by multiple scattering. It is hence crucial to reduce the material budget wherever possible. This must be the first priority not only regarding the sensor technology choice, but also for the design of any support structures. High Voltage Monolithic Active Pixel Sensors were chosen as sensor technology not only because they are fast and granular, but also because they can be thinned to 50 µm. Considering the resolution of reconstructed track parameters, especially momentum and scattering angle, the performance is mainly determined by the amount of material within the active area of the tracker modules. Nevertheless, for the case that the tracking detector is kept within the P2 detector during the asymmetry measurement, systematic uncertainties related to any material that is traversed by electrons being detected in the Cherenkov detectors should be minimized. This includes any material for mechanical support, even if it is placed outside of the active tracker area.

The tracker modules however need to provide sufficient mechanical robustness in order to ensure safe assembly into (and possibly removal from) the P2 detector. It has to be taken into account that silicon at a thickness of 50 µm is hardly rigid and bends quite easily. The weight of the pixel sensors though is quite negligible so that the support structures mainly need to hold their own weight and some additional electronic components.

The pixel sensors need to be powered and read out; at least one fast readout link and one powering line is needed for each sensor. At this point, the detailed development of both readout and powering schemes is still ongoing, but it is clear that the design of the tracker modules must provide for sufficient space both for transmission lines and the placement of electronic components. The pixel sensors will consume power at the order of 1 W each and need to be powered at a voltage level of 1.8 V. Given these boundary conditions, it is hardly possible to transmit power for a few hundred sensors at such a low voltage level over a distance of a few meter. It is therefore either necessary to use a serial powering scheme or to use efficient power converters close to the sensors which allow to use a higher input voltage. The latter option is currently envisaged. The operation of commercial step down switching regulators is certainly not trivial because of the radiation environment and the magnetic field present in the P2 detector. The development of a power distribution design is currently ongoing for the Mu3e experiment, in which the same kind of pixel sensors will be operated in a magnetic field. An input voltage of around 20 V would be desirable, but the FEASTMP converter modules [153] developed at CERN with a maximal input voltage of 12 V are also considered as a possible option. The sensor data is transmitted from the sensors first electrically, but will be converted at some point to an optical signal. The sensors

are not able to drive the signal for several meters, which is one reason why additional components close to the sensors are necessary.

The cooling of the HV-MAPS is foreseen to be accomplished using gaseous helium. The helium cooling gas needs to be distributed close to the sensors in order to achieve the most efficient heat transfer. The technical design of the tracker module was developed in conjunction with Computational Fluid Dynamics (CFD) simulations of the cooling system, which are presented in the following chapter. The results of the cooling simulations determine the boundary conditions in terms of necessary helium gas volume flow that must be distributable. The cooling simulation in turn is always based on an input model, so that an idea on the technical design has to be worked out first. In addition, several different options in which directions to channel the helium gas were investigated, each of them requiring some adjustments in the mechanical design. These optimizations resulted in the technical design reported in this chapter. An additional requirement connected to the sensors generating heat is that temperature resistance and thermal expansion of the materials used for constructing the tracking detector modules must be considered. It has to be ensured that even fast temperature changes in the range between 0 °C to 70 °C do not cause any damage to the detector.

All parts used in the design of the tracking detector must provide sufficient radiation hardness, see the results given in section 5.3. However, the actual demands on radiation tolerance depend on the measurement program of the tracking detector over the runtime of the P2 experiment, which is still under discussion. This question also impacts the further development of a detailed powering and readout infrastructure, for which active electronic parts need to be operated. Radiation hardness is an issue not only for electronic parts, but also for the materials used in the supporting structures. In particular, it has to be considered for plastic and for composite materials.

The tracker module design itself should be as modular as possible, so that in case that some sensor chips do not work properly, it is possible to replace some submodule with only few sensors mounted. In an ideal case, the replacement procedure is easy and safely repeatable, but at the same time ensures reliable electronic connections and precise positioning of the submodules. The mechanical alignment of the silicon sensors is required to be at the order of 100 µm precision. Furthermore, the pixel sensors include some inactive part with the digital electronics on it. The actual physical sensor size is therefore rather about 23 mm × 20 mm with an active area of 20 mm × 20 mm. In order to avoid efficiency loss due to the inactive sensor area, it is necessary to develop the mechanical tracker module design such that the inactive sensor part is covered by the active area of another sensor.

7.2. Concept

The development of a detailed technical design for the tracking detector modules first requires to work out a general concept on how to cover the area between the barrel shield and the solenoid magnet in the P2 detector with sensor chips. For this task, both the detector geometry and the additional requirements discussed in the previous section need to be considered. The geometry of the area to be covered by pixel sensors on each of the tracker modules can be described approximatively by an isosceles trapezoid, as it is depicted in figure 7.1. This trapezoid covers an area of $14.93\,\mathrm{dm}^2$, which corresponds to the active area of around 373 sensor chips.

A minimized material budget is especially crucial at the active sensor area. The material of the support structure should not contribute more to the overall material budget in this region than the 50 µm thin pixel sensors. Such a low material budget can be achieved by gluing and bonding the sensor chips directly on a polyimide flexprint including aluminum traces for sensor readout and powering. Since a modular design is intended, between 8 and 14 sensor chips are patterned as a row on polyimide strips, so that each strip represents a submodule. The detailed technical design of the strip modules will be discussed in the following section.

The polyimide strips with pixel sensors mounted must be connected at both ends to some support frame, both mechanically and electrically. Since a Printed Circuit Board (PCB) is needed on this support frame for the placement of readout and powering components, it was decided to build the frame itself out of a large PCB. Such a PCB consists of a glass-reinforced epoxy laminate material, which offers an excellent strength to weight ratio. Each of the strip module ends is connected to one separate frame PCB. In the current design, 29 strip modules are patterned per tracker layer. The arrangement of the pixel chips and strip modules is depicted in figure 7.1. It can be seen that 316 chips are assembled on one sensor layer and tracker module, thus covering an area of $12.64\,\mathrm{dm}^2$. In addition, it is also shown in the sketch that the frame PCBs are connected on both ends by some additional rigid stabilizer bar. The geometry and space needed for the PCBs and additional support structures is the reason that not the complete targeted area can be covered with pixel sensors.

The strip length was chosen constant and independent of the actual number of mounted chips, which results in a rectangular frame design. An approach with a trapezoidal outer frame was considered, but found to be mechanically unfavorable. The problem in the case of a non-rectangular design is that the distance between the left and right side of the frame would differ for every strip. This would require to either have a different length for each strip or a different position on the frame for electrical connections to each strip. Any of these two options would complicate construction and operation of the tracker module. With a rectangular frame, a manageable number of different strip variants can be used so that this design was chosen.

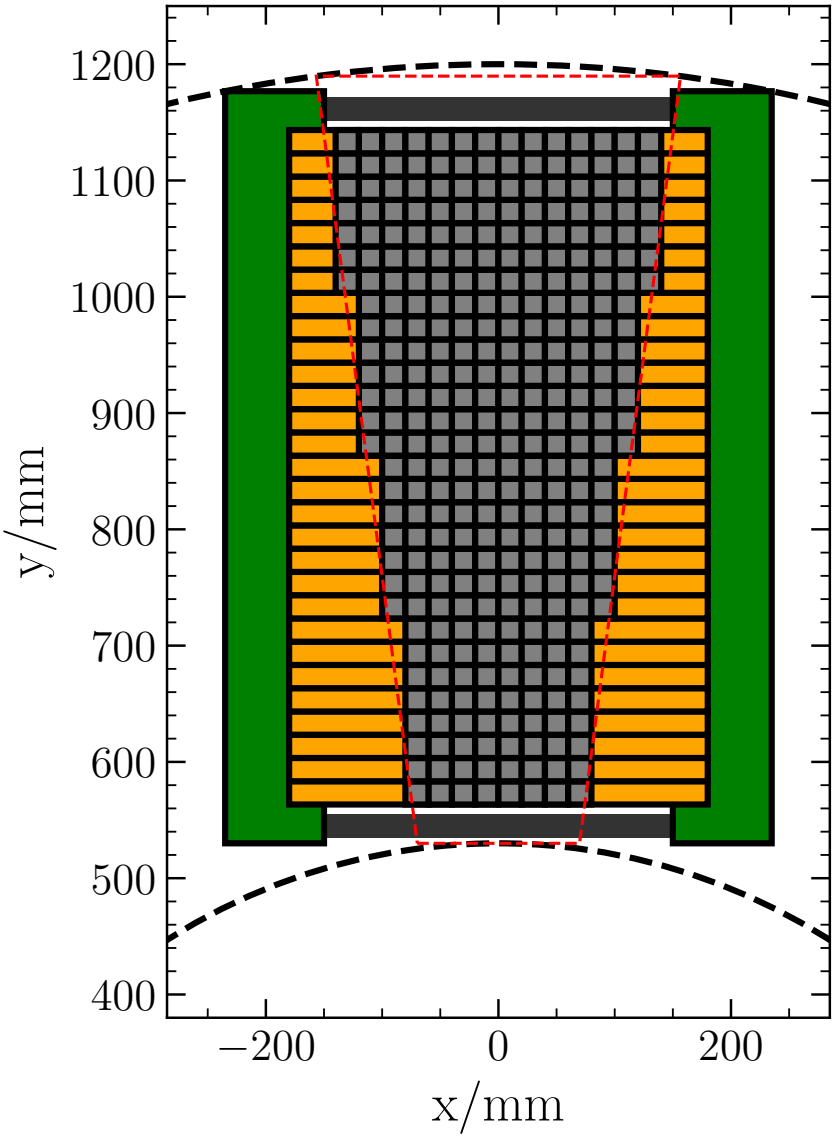

Figure 7.1.: *Sketch of the tracker module geometry and mechanical concept. Axes are defined for an upright orientation of the module. The dashed inner circular segment represents the dimensions of the barrel shield, the outer one the dimensions of the solenoid magnet. The dashed red trapezoid depicts the area that should ideally be covered with sensors for an azimuthal coverage of* 15° *and perfect radial coverage. The PCBs are sketched in green, the polyimide strips in orange, the pixel sensors in gray and the solid mechanical connectors in dark gray.*

As each tracker module comprises two tracker layers, the design concept for one layer is repeated for the second layer, which is assembled in parallel to the first one, but with opposite orientation (rotated around the vertical middle axis by 180°). The space between the frame PCBs of the two layers is used for helium gas distribution pipes. The detailed technical design of the support frame will be presented in section 7.4. In total, every tracker module includes 632 sensor chips, so that the complete P2 tracking detector consisting of eight modules contains 5056 sensor chips and covers an area of around 2 m^2.

In order to enable proper cooling of the sensors with gaseous helium, several flow directions with different helium volume flows must be implemented. The strip modules include helium channels that will guide helium gas along the sensors. In addition, a helium flow between the two sensor layers of a module will be initiated. An option to enable additional helium flow over the layers will be discussed in section 7.5.1. For each of these flow circuits, the helium must be distributed within the support frame. The helium pipes connecting the tracker modules to the outside will be placed at the inner magnet wall and therefore enter the modules from the outer side. The complete tracker module will be operated in a dry helium atmosphere, so that the helium cooling flow systems are not necessarily required to be perfectly gas tight.

The tracker modules are placed in the P2 detector at different rotation angles around the z-axis. In addition, at least the modules placed downstream at the end of the magnet must be installed such that they can be dynamically rotated around the z-axis with respect to the upstream modules. A technical design for this integration of the individual tracker modules into the P2 detector still needs to be worked out and is therefore not further discussed here.

7.3. Strip Submodules

The technical design of the strip submodules is adopted from the respective design for the Mu3e experiment [154] and adapted to the geometry of the P2 tracker module. The pixel sensors are mounted on High Density Interconnects (HDI), which consist of aluminum traces on a polyimide substrate. The HDI is also referred to as “flexprint”. Aluminum is preferred to copper traces because of its lower atomic number, leading to less multiple scattering. The flexprint includes both powering and signal lines to the sensor chips; the traces are formed by an etched conductor tape. The detailed design is currently being developed by the Mu3e collaboration, a two-layer design solution with a total thickness around 100 µm is foreseen. The envisaged signal bandwidth is 1.25 Gbit s^{-1}, which requires differential and impedance controlled electrical connections. Depending on the total bandwidth requirement, between one and three fast links can be connected to each sensor chip. In addition, power traces

must be designed for a power transmission up to 30 W in Mu3e, where a maximum number of 18 chips per flexprint is used. In the current P2 tracking detector design, the maximum number of chips is 14, so that the corresponding power transmission requirement is lower.

In order to ensure reliable electrical connections, but also to further minimize the material budget, the "Single-point Tape Automated Bonding" (SpTAB) technology [155] is applied. In this technology, the traces are connected directly through vias to the chip bonding pads or other conductor layers without any additional material or bonding wires. The connection is formed by applying heat, force and ultrasonic energy to the lead on the tape. Each sensor chip will first be glued to the HDI with precise positioning and afterwards electrically connected to 21 bonding pads of size 150 µm × 150 µm using SpTAB bonding [154]. Prototypes of a HDI design fabricated by LTU[1] have been SpTAB bonded to a test board for characterization tests, yielding promising results [156].

The base dimensions of the flexprint strip in the P2 tracker design are 360 mm × 20 mm, independent of the number of chips mounted. The chips are patterned in one row and centered on the strip, as depicted in figure 7.1. As mentioned before, there is an inactive region on the periphery of each sensor chip, so that one edge measures 23 mm instead of 20 mm. The chips are assembled on the flexprint strip such that their "long" edge extends over the strip to both sides. However, the bonding pads on the flexprint must be located under the inactive periphery region of the chips. The flexprint dimensions are hence enlarged to one side for the chip placement area, as it can be seen in figure 7.4c. This placement of the chips on the strips will allow to mount the strips on the tracker module frame in such a pattern that the chips of neighboring strips overlap (see section 7.5), thus maximizing the active tracker area.

The flexprint design is divided electrically into its two halves, so that each sensor chip is powered and read out from the closest frame PCB. Only even numbers of chips per strip are used in order to obtain a symmetric powering and readout scheme. It is planned to use only four different chip multiplicities on the strip submodules: strips with 8, 10, 12 and 14 chips. The sensor coverage could be improved by using more submodule variations, especially with uneven chip multiplicities. This would however complicate the fabrication and operation of the tracker modules. Four different chip multiplicities is considered a suitable compromise.

At both ends of the flexprint, a rigid PCB of size 35 mm × 20 mm is mounted. The rigid PCBs can be connected with the same technology as the pixel sensors by gluing and SpTAB bonding. The end PCB has both mechanical and electrical functionality, reinforcing the strip submodule at its ends. In addition, signal distribution is simpler

[1] LED technologies Ukraine, `http://www.ltu.ua/en`

on a rigid PCB compared to a flexprint, as it allows more complex layer setups and vias. On each of the two end PCBs, signal and powering traces are routed to an array of 10×10 pads. The electrical connection of the end PCBs to the frame PCBs is achieved using ZA8 Z-RAY® ultra low profile arrays by Samtec®[2], allowing high speed board-to-board connections. Two Samtec® ZSO screw connectors are placed next to the board-to-board connector ("interposer") for mechanical fixture. More details on this connection to the frame are discussed together with the frame design in the following section. The rigid PCBs mounted at the strip ends come in two variations differing in thickness: 0.8 mm and 1.55 mm. The different PCB thicknesses allow to partially overlap the covered area of sensors on neighboring strips. With this design, the inactive digital part of each sensor is covered by the active area of another sensor. The two PCB variants together with the four different chip multiplicities make for a total number of eight different strip submodules.

Each strip is additionally reinforced by a triangularly folded polyimide structure, so called "v-folds", making the strip modules self-supporting. The thickness of the additional polyimide layer is not fixed yet, 25 µm is used for the Mu3e detector [154], for which similar v-folds are envisaged. The fold geometry for P2 has to be chosen such that two nuts fit between the v-folds that can be connected to the ZSO connectors placed on the frame PCBs next to the interposers (see the renderings of the complete strip submodule in figure 7.4).

The v-folds are also used as distribution channels for helium cooling gas. This approach allows to transport the helium gas very close to the sensor chips so that the heat transfer is optimized with only very little additional material. Tests have shown that helium flow velocities up to $20\,\mathrm{m\,s^{-1}}$ are possible inside the v-fold channels, while the induced vibrations were observed to be mostly less than 10 µm in amplitude [157, 158], which is still considered to be acceptable. However, this result was observed for the geometry of the Mu3e detector and the actual implementation of the strip module fixture might have a notable impact on the vibration amplitude. Measurements with the P2 tracker module geometry are therefore needed for verification.

In order to distribute the helium gas to the v-folds and also to further fasten the polyimide strip, an end fitting made out of plastic will be mounted in addition to the rigid PCB at both ends of the strips. This end fitting can be considered as a female plug to the v-fold helium channels, as it encloses the final 5 mm of them at both strip ends. If it is necessary for a more gas tight connection, the fitting can be glued directly to the end of the v-folds. The end piece directs the helium from openings in the frame PCB (see next section) to the v-folds through internal gas channels. The helium openings to the frame PCB include notches for sealing O-rings. As the distance of the end PCB on the flexprint to the frame PCB is determined by the

[2] https://www.samtec.com/products/za8

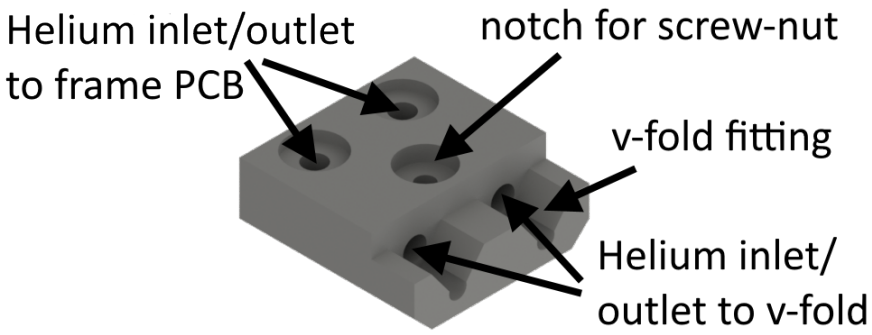

Figure 7.2.: *Strip module end fitting design.*

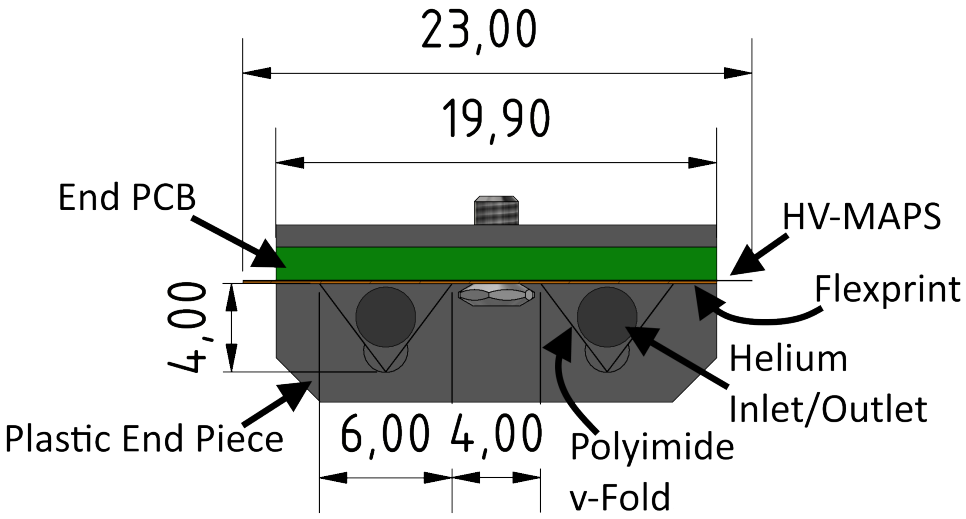

Figure 7.3.: *Cut view rendering of a strip submodule with labeled parts and important dimensions. All dimensions are in* mm.

interposer and therefore fixed, the end piece has to come in two different variants to account for the two variants of the end PCBs varying in their thickness. Each plastic end piece is fixed mechanically to the frame PCB by one screw connecting to nuts that will be mounted on the frame PCB. Together with the two Samtec® ZSO® plugs connecting to the end PCB, each strip end is fixed to the corresponding frame PCB at three points. The end fittings are designed such that they can be constructed conventionally in the sense that no 3D-printing is necessary. Since a radiation hard and temperature resistant design is targeted, polyether ether ketone (PEEK) is chosen as material for any plastic parts in the P2 tracker module design, thus including the strip module end pieces. The end piece design is shown by the labeled rendering in figure 7.2. The integration of the end piece to the strip submodule can be seen in figures 7.3 and 7.4. These two renderings also illustrate the v-fold design.

(a) *Front side of the strip submodule*

(b) *Back side of the strip submodule*

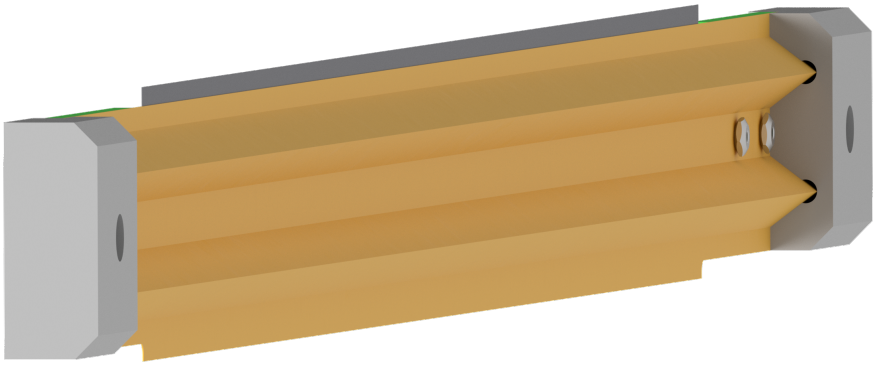

(c) *Side view on the back side of the strip submodule*

Figure 7.4.: *Renderings of the strip submodule in the version with 14 chips, shown from different perspectives.*

The design of the end pieces implies that the helium flows in both v-fold channels in the same direction. Cooling simulations were also performed for designs with counter flowing helium, but this configuration was found to cool the sensors less effectively. Aside from that, the sensor chips and the v-fold polyimide support structure are currently planned to be mounted on opposite sides on the HDI. It might however also be possible to put the HV-MAPS in between the HDI and the v-fold support structure.

Prototypes of the strip submodule design as shown in figure 7.4 have been assembled (without actual pixel sensors) and will be presented later in this thesis in section 9.2.

7.4. Support Frame

The tracker module frame includes two identical side modules which are connected to each other by solid bars. The main design concept of the side modules consists of two large PCBs which are oriented in parallel at a distance of 15 mm, which is defined by plastic profiles placed in between. The resulting channels formed by the PCBs and the plastic profiles are used as helium pipes. In particular, two cooling

channels are implemented, one for the helium flow through the v-folds and one for the helium flow between the tracker planes. The main dimensions of the frame PCB are 85 mm × 620 mm. There is some additional extension of about 40 mm × 20 mm at the top side since some space between the PCBs that is not occupied by cooling channels is needed for mechanical fixtures at this position. The PCB geometry can be seen in figure 7.5a. While one PCB of that size is not rigid, two parallel PCBs mounted at a fixed distance form a very stiff and robust structure.

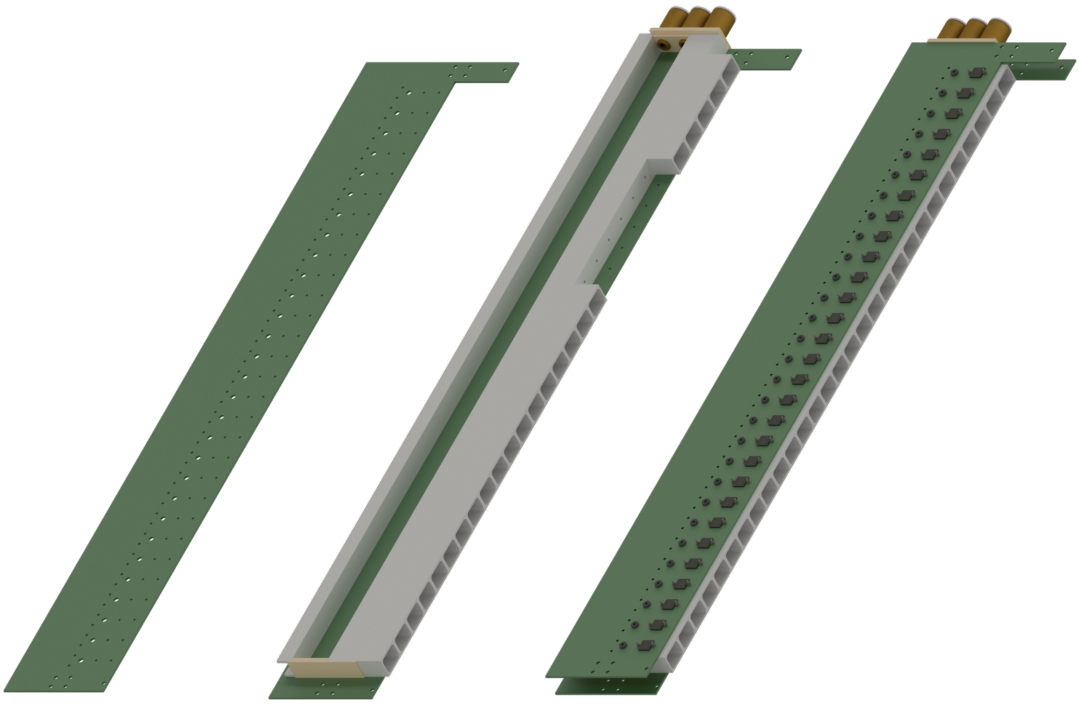

(a) (b) (c)

Figure 7.5.: *Renderings for different assembly stages of one frame side module: (a) Frame PCB without any parts, (b) Frame PCB with plastic parts and connectors for helium distribution, (c) Fully assembled frame side module with two parallel PCBs and parts for strip mounting, but without any other electrical parts.*

The cooling gas channels between the two frame PCBs can be seen in figures 7.5b and 7.6. In figure 7.6, the left channel is for the distribution of the helium gas to the strip v-folds, whereas the cooling channel on the right side distributes the helium for the gas flow between the two sensor planes of one tracker module. The cross section of the left channel is larger since more helium needs to be distributed through it, see the cooling simulations in the next chapter. The C-shaped plastic profiles forming the cooling channels and the frame PCBs will be glued to each other with Araldite® 2011 epoxy resin. A gas tight gluing connection is required for the cooling channel to

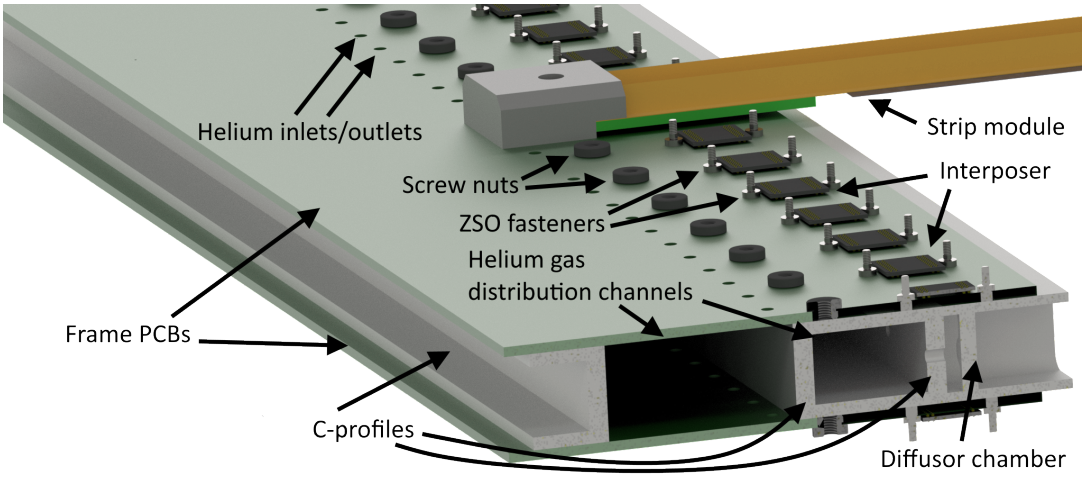

Figure 7.6.: *Cut view through frame side module with labeled components. One strip module is mounted for visualization. Only mechanically relevant parts are assembled, no electric components for readout and powering.*

the v-folds as it is confined both by the two PCBs and the backside of two C-profiles. In addition, all vias in the frame PCBs must be closed in the PCB manufacturing process so that no helium escapes through them. Note that however gas tightness is only required on a level that no relevant amount of helium gets lost for the cooling as the tracker module itself is placed in a helium atmosphere. The second cooling channel is formed by two C-profiles oriented opposite to each other.

Regarding the helium distribution to the v-folds, the gas is directed to the strip modules directly through one hole opening in the frame PCBs per v-fold. Each opening connects to its counter part at the end piece of the strip modules, see figure 7.6. The interface between the opening in the frame PCB and the strip end piece is sealed by an additional O-ring for each opening. The helium flow distribution through the v-folds is a closed system if there are no leakages. The cold helium gas enters one frame side module of a tracker module and is then distributed to the v-folds. It leaves the v-folds at the other end of the strip module to the opposing frame side module. The gas distribution system outside the tracker modules is not developed yet, so that this has to be done in the near future. More details will be given in the following chapter which is dedicated to the cooling system.

The helium in the second gas channel between the frame PCBs is distributed through openings added to the corresponding C-profile. One opening per strip guides the helium into an additional diffusor chamber. The diffusor part is added in order to achieve a steady helium gas flow between the tracker planes along the strips from the one frame side module to the other. This flow is applied in opposite direction to the flow inside the v-folds. Since the strips are mounted at different distances to the

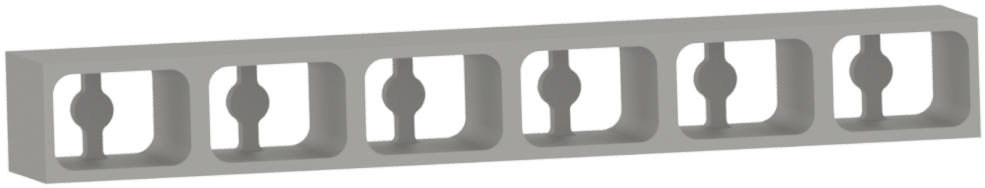

Figure 7.7.: *Rendering of diffusor part with six chambers.*

frame PCB and neighboring strips do not touch, they do not form a gas tight surface. The helium flow between the tracker planes is therefore not a closed system. Helium must be supplied to the one frame side module with overpressure and by that be blown between the tracker planes. At the opposing frame side module, the same amount of helium gas is sucked in by lower pressure. A rendering of the diffusor design can be seen in figure 7.7. It is the result of fluid dynamical simulations presented in the following chapter.

The helium flow volume between the tracker planes should be nearly constant along the whole length of the tracker module, which means that the same amount of helium should flow through each of the openings in the plastic profile to the diffusor part. A uniform helium transfer can be reached with small size openings as it was investigated in simulation (see chapter 8). The small openings however lead to large helium velocities and very localized flow. In addition, the flow is not parallel to the strip orientation as it is intended. The main task of the diffusor part is to widen the flow profile over the complete area between the tracker planes and to align it in strip direction. The main idea of the design is to place a barrier in the helium flow directly behind the opening in the plastic profile. The helium will therefore be slowed down and flow around this obstacle. The helium flow is further confined and directed by the outer chamber dimensions. The diffusor part shown in figure 7.7 features six chambers and one chamber is foreseen for every strip. Consequently, several copies of this part must be patterned and different variants are needed in order to arrive at 29 chambers, which is visualized in figure 7.5b. The full assembly with 29 chambers is built out of several parts for technical reasons in the production process. The diffusor part and the plastic parts forming the cooling channels will be made of PEEK and are designed such that no 3D printing is needed.

7.4.1. Strip mounting

The strip modules must be mounted to the frame PCBs such that reliable transmission of the fast electric signals and power is ensured. In addition, helium losses from the gas distribution to the v-folds should be avoided as much as possible. At the same time, an easy replacement procedure is desired. The cooling channel design between

the frame PCBs forbids any parts for mechanical fixture to extend through the bottom side of the PCBs.

The end piece of the strip modules is fixed to the frame PCB by a screw which connects to a screw nut mounted on the frame PCB. For that purpose, PEM® self-clinching nuts for printed circuit boards sold by KVT-Fastening GmbH[3] are used. They are fixed to the PCB through a press-fit connection.

The electrical board-to-board connection between the frame PCB and the PCBs which are mounted at the end of each strip is implemented with a dedicated high-speed connector by Samtec® ("interposer"). The envisaged single compression variant of the ZA8 ultra low-profile micro array connector combines a ball grid array (BGA) for soldering at the bottom side with gold feather compression contacts on the top side. One interposer is soldered to the frame PCB for each connected strip, see figures 7.5c and 7.6. For a readout design with one fast link per sensor chip, the interposer variant with an array of 10×10 pins is sufficient and serves as the current baseline option. In any case several other standard configurations and also customized arrays are available. The default pitch is 0.8 mm and the default stack height is 1 mm. The Samtec® interposer is specified for power transmission up to 0.9 A per pin (with ten pins in one row powered), a voltage up to 110 VAC and fast differential signal transmission up to 40 Gbit/s [159]. The interposer was tested regarding power and fast signal transmission with a dedicated test setup, the results are presented in chapter 9.

The mechanical mounting of the end PCBs of the strip modules has to ensure appropriate compression of the interposer feather contacts and is realized using Samtec® ZSO connectors which are designated for this application. One such connector is placed on each side of the interposer. The ZSO connectors are press-fit inserted to the frame PCB to be flush with its bottom side. They combine a spacer preventing over-compression of the solder balls with an alignment pin for the upper PCB placement and a thread for its fixture with the mating nut. The strip module and the frame PCB are designed such that the two ZSO pins fit two holes placed between the v-folds. The geometry of the v-folds is such that the nuts for the mounting fit in between, as visualized in figure 7.4c.

The PCBs mounted at the two ends of each strip extend over the frame PCB by around 5 mm, see figure 7.6. This configuration allows to place some small parts directly at the end of the strips, which can be exploited in particular for the placement of noise reducing fast capacitors close to the sensor chips.

[3] `https://www.kvt-fastening.de`

7.4.2. Side module connection

The two frame side modules must be connected by a rigid cross bar placed outside of the active sensor area. Consequently, the rigid connectors are placed at both ends of the frame PCBs, as depicted in figure 7.1. As an easy solution, one could fix two rigid bars with some screws. This implementation however does not account for the thermal expansion of the strip modules. The cooling system for the tracker modules will be designed to keep the operation temperature between 0° to 70°. The thermal expansion of polyimide in this temperature range is at $\mathcal{O}(20\,\mathrm{ppm/K})$, so a 360 mm long polyimide strip expands by around 0.5 mm for a temperature difference of 70 K. The precise actual value will depend on the particular polyimide variant that is used. With a completely rigid connection of the frame side modules, the strips would need to deform in order to accommodate for their thermal expansion. It is questionable whether the characteristic of this deformation is predictable and reproducible, which implies larger and temperature dependent sensor alignment uncertainties. The actual impact of this effect on the reconstruction performance still needs to be investigated. Thus, a connection mechanism for the frame side modules is developed that adjusts the distance to the thermal expansion of the strip modules.

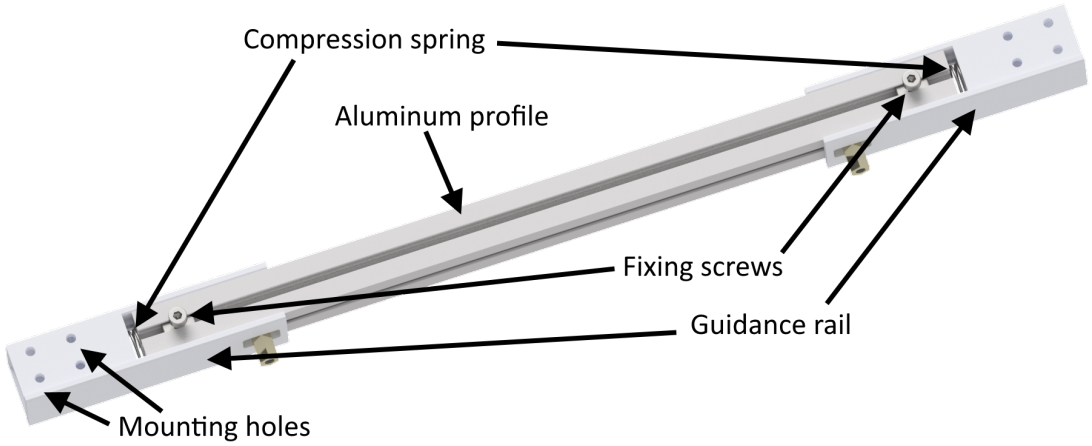

Figure 7.8.: *Rendering of the connection mechanism for the frame side modules with labeled components.*

The connection between the frame side modules features a 15 mm×15 mm aluminum profile (MakerBeamXL®[4]) which is mounted on compression springs. A rendering of this setup is shown in figure 7.8. At both ends, the aluminum profile is attached to guiding rails which are fixed to the frame PCBs. The guidance rail restricts movement of the aluminum profile to shifts of a few millimeter perpendicular to the frame side module. The compression springs push the two frame side modules away from

[4] www.makerbeam.com/makerbeamxl/

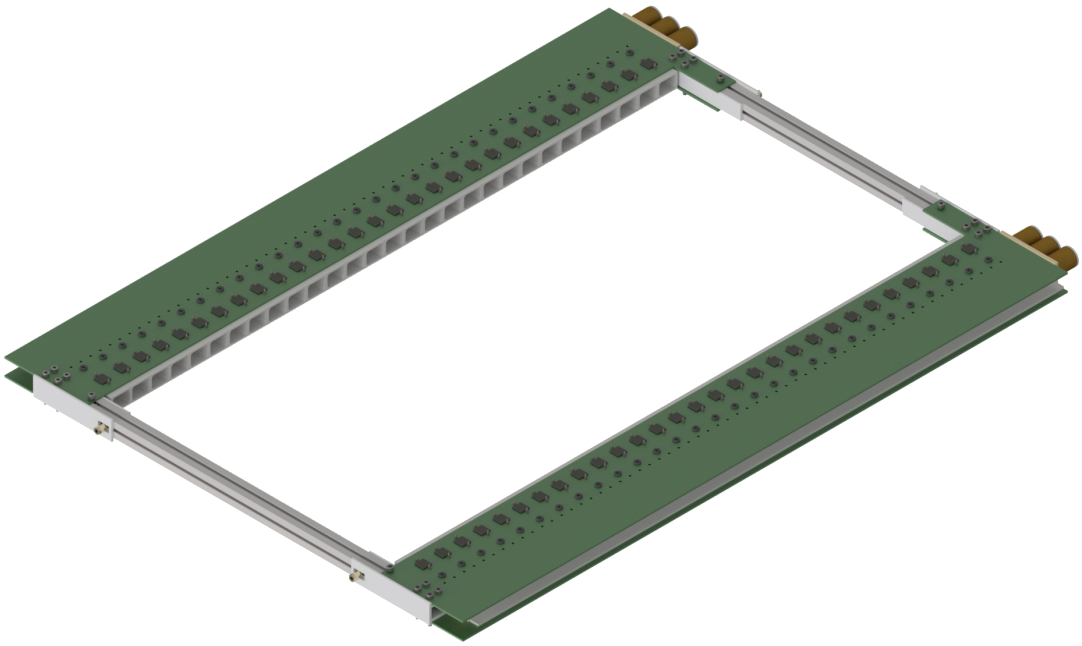

Figure 7.9.: *Rendering of the complete tracker module frame including the two side modules and the connecting aluminum profiles.*

each other, which slightly pulls the strips and therefore enables their expansion with temperature. Any movement can however be prevented with additionally mounted fixing screws, which is needed especially for the assembly of the strip modules.

Figure 7.9 shows the complete frame consisting of two frame side modules and the connecting aluminum profiles. As mentioned earlier, the integration of the tracker modules to the P2 detector still needs to be worked out. The MakerBeamXL aluminum profiles indeed are a likely starting point for connecting the tracker modules to any outer support structure.

7.5. Tracker Module Assembly

The assembly of the tracker module is completed by mounting all 2×29 strips on the module frame. Due to the two different variants of the strip module end PCBs, which vary in their thickness, the mounted sensors are located at different distances to the frame PCB. In order to arrive at a partial overlap between the sensors of neighboring strips, strips with thick end PCBs and strips with thin ones are mounted alternatingly. Figure 7.10 shows a cut view through 2×4 neighboring assembled strips, visualizing the partial overlap between the sensor areas. It also shows that for the replacement

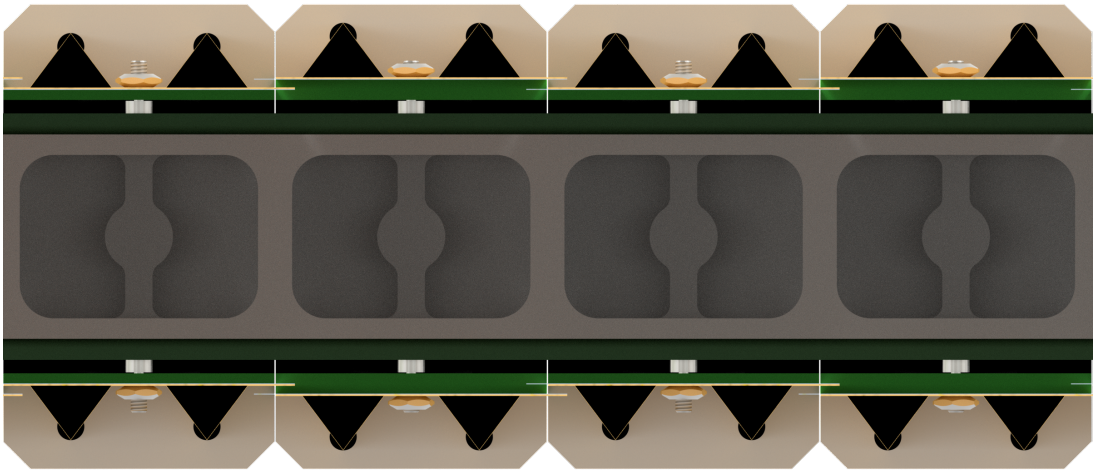

Figure 7.10.: *Cut view through several neighboring and opposing strips mounted on a tracker module, visualizing the sensor offset and partial overlap.*

of a strip module with the thin end PCB, the two neighboring strips need to be removed first. The strips with the thick end PCB can be removed without touching any other strip. After releasing the fixation screws, the strip modules can be moved out perpendicular to the frame PCB. The overlapping strip configuration implies that the sensor planes of the P2 tracking detector are not completely flat, but the z-position of each strip is known and has to be taken into account. With the configuration as shown in figure 7.10, the distances of opposing sensors are 21.6 mm and 23 mm for every second strip. The sensors are oriented to the inner side of the tracker module and the polyimide v-folds to the outer side.

The strip variants with different chip multiplicities are assembled in the configuration that is depicted in figure 7.1. Starting from the outer module side, 7 strips with 14 chips are assembled, followed by 7 strips with 12 chips and then again by 7 strips with 10 chips; 8 strips with 8 chips complete a plane to a total of 29 strips. As discussed earlier, this chip configuration approximates the targeted trapezoidal shape for the coverage area of the tracking detector. Figure 7.11 shows renderings of the assembled tracker module both with only one tracker plane assembled and with all strips mounted. The actually covered area can be seen only for the rendering with one plane assembled, as it is hidden by the second plane because of the sensor orientation to the inner module side.

The free space on the top side of the frame PCBs (see the rendering of the full module in figure 7.11b) will be used for the electronic parts needed for powering and readout. It has to be investigated whether the available space is sufficient. In the presented technical design, the frame PCBs have a width of 85 mm, of which 45 mm are occu-

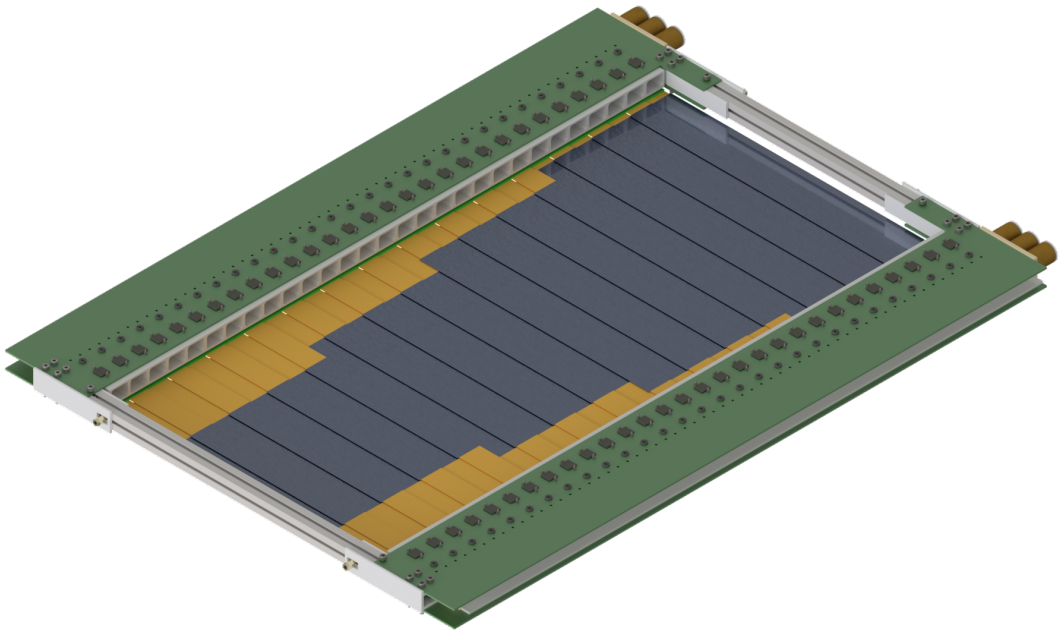

(a) *Strips of one tracker plane mounted*

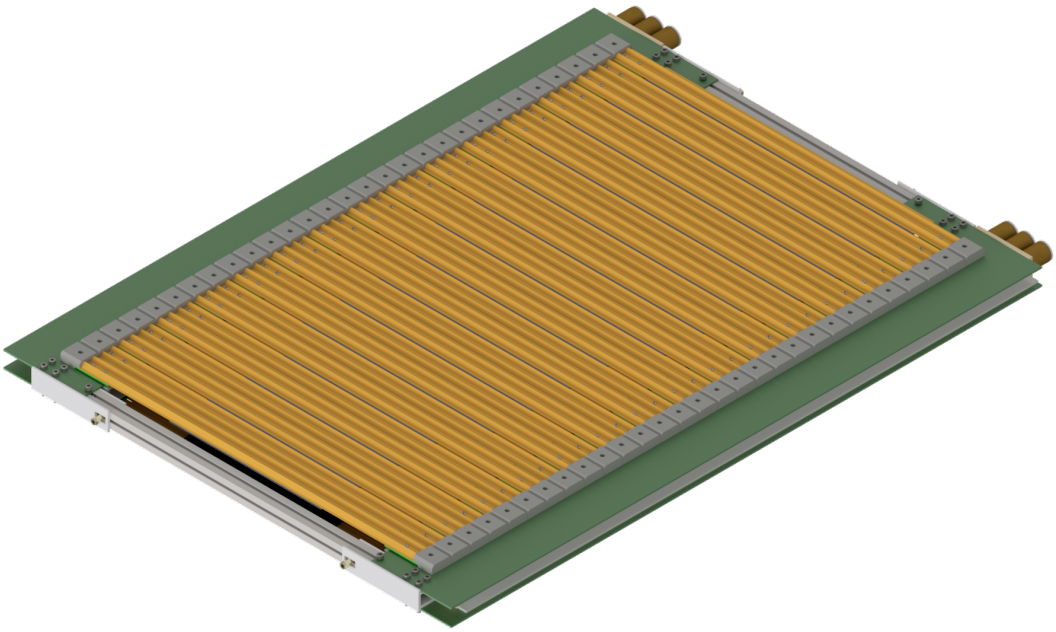

(b) *All strips mounted*

Figure 7.11.: *Renderings of the assembled tracker module.*

pied with the mounted strip modules. On the bottom side of each frame PCB, the only available space of about 5 mm is at the side because of the cooling channels, see figure 7.6. In addition, it was already mentioned that some small parts can be mounted on the end PCBs of each strip module. More space can be occupied by assembling parts on dedicated submodules with right-angled connectors. In particular, the FEASTMP converter modules mentioned as a base line option for power conversion come with such a connector and could therefore be mounted on the frame PCB in such a space saving manner. Otherwise, it is of course possible to extend the dimensions of the frame PCBs further, but that would increase the transverse section of rigid parts being placed into the electron trajectories to the integrating Cherenkov detectors in the P2 experiment.

The presented technical design of the tracker modules has just been realized in a thermo-mechanical prototype with 2×18 heatable strip modules, but without actual pixel sensors. The construction of the prototype demonstrates the practicability of the presented technical design. In addition, cooling tests in the laboratory have already started with smaller prototypes and will be continued with the larger detector model. The prototype developments are reported in chapter 9.

7.5.1. Additional Cover Option

The technical design of the tracker module presented so far, visualized in figure 7.11, offers the possibility to cool the sensors with helium flows through the v-folds and between the tracker planes. It was observed in cooling simulations that will be presented in the following chapter that for a high power consumption of the sensors around 400 mW cm^{-2}, it is hard to keep the temperatures below 70° with this cooling configuration. The flow velocities cannot be increased unlimitedly because laminar flow is required. As a consequence, an option for the implementation of an additional helium flow over the back side of the strip modules is developed. Nevertheless, considerable effort should be taken regarding the sensor design and operation to keep the power consumption at a level that makes this additional cooling omissible. The additional cooling flow would increase both the total helium flow rate and the material budget of the tracker module.

In order to enable an additional helium flow over the back side of the tracker planes, an additional cover is developed that could be mounted on each side of the tracker module. Similar to the baseline tracker module design, this additional cover consists of a frame that is used for distributing the helium gas. A slightly modified copy of the diffusor part developed for the helium flow between the tracker plane is used to achieve a steady and aligned helium flow along the strip back sides. The cover setup is completed by an additional thin foil that is fixed to both frame sides and spanned over the complete tracker module area. The foil is placed at a distance around 15 mm

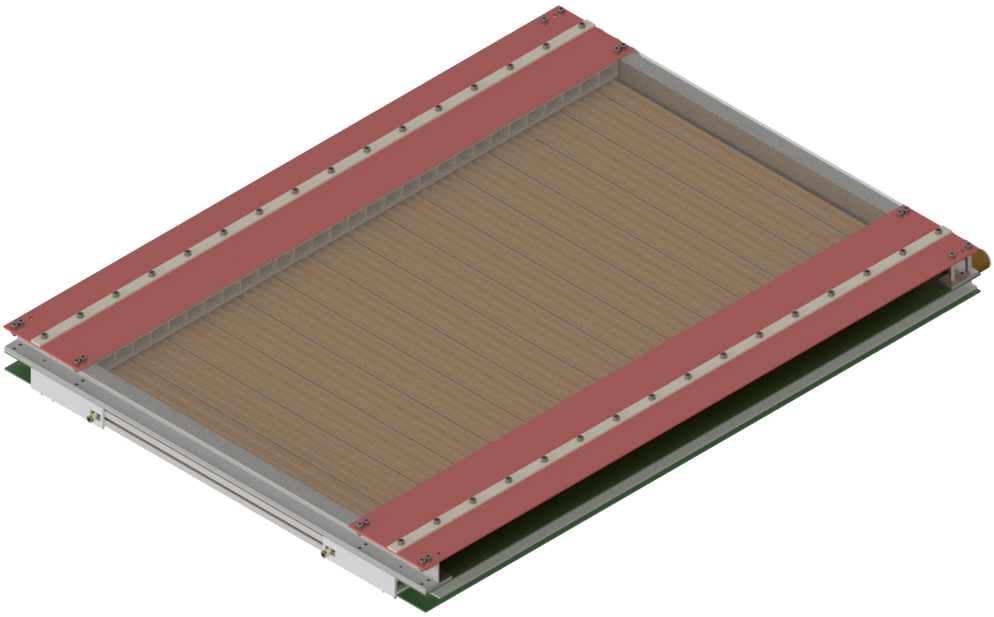

Figure 7.12.: *Rendering of tracker module with additional cover.*

to the strips and by that confines the helium flow to be close to the strips. Figure 7.12 shows a rendering of the tracker module with the additional cover.

The additional cover is not developed to great mechanical detail yet, but rather at a conceptual design level that allows to test the principle in cooling simulations. For example, the cross bars for the cover are not implemented to be mounted on springs at this design status. In addition, no materials are assigned. Most of the parts needed could certainly be built out of plastic, including the two rectangular plates which are depicted in red in figure 7.12. The cooling channels are hidden in this figure because they are mounted to the bottom side of these two plates. Note that the installation of such an additional cover would require to remove it temporarily every time a strip module needs to be exchanged.

8 Cooling Studies

Cooling the silicon pixel sensors is one of the biggest challenges in the development of the P2 tracking detector. The power dissipation of the silicon pixel sensors is expected to be between 100 mW cm^{-2} and 400 mW cm^{-2}. Studies on the performance of the MuPix7 and MuPix8 prototype sensors at different settings and power dissipation are presented in Ref. [160]. It was shown that that the MuPix7 has an optimal working point at a power dissipation of 300 mW cm^{-2}, whereas this value is reduced for the MuPix8 to approximately 200 mW cm^{-2}.

The demand for material reduction requires to use a cooling medium of lowest possible density, which leads to gaseous helium as an obvious choice. Hydrogen gas is the only material with lower density, but is discarded because of the related safety hazards. The low density of gaseous helium however comes with a low volumetric heat capacity[1] compared to any liquid coolant and therefore requires higher volume flow rates.

Even though helium was chosen as cooling gas primarily for to its low density, it turns out to have also good cooling capabilities compared to other gases. Table 8.1 shows the thermo-physical properties of helium and air for comparison. Helium features a higher specific heat capacity than air, and even a comparable volumetric heat capacity despite its lower density. In addition, the heat conductivity of helium is better, which is the most important property for the cooling performance. The increased speed of sound allows to preserve laminar flow of helium at much higher flow velocities compared to air.

In the proposed cooling system of the P2 detector, the helium is piped through a closed loop that includes the P2 tracking detector and a heat exchanger. The technical implementation of the global cooling loop still needs to be worked out. This first

[1] heat capacity per unit volume, not to be confused with the specific heat capacity at constant volume

	Helium	Air
density ρ [kg m^{-3}]	0.1625	1.177
specific heat capacity c_p [J kg^{-1} K^{-1}]	5193	1007
volumetric heat capacity [J m^{-3} K^{-1}]	844	1185
heat conductivity k [W m^{-1} K^{-1}]	0.156	0.02623
kinematic viscosity ν [cm^2 s^{-1}]	1.23	0.158
Prandtl number Pr	0.664	0.713
speed of sound c_s [m s^{-1}]	1019	347

Table 8.1.: *Some thermophysical properties of helium and air at* $T = 300\,\mathrm{K}$ *and normal pressure* $p = 101\,325\,\mathrm{Pa}$ *[161].*

requires to investigate the helium flow rates needed in order to achieve sufficient cooling of a tracker module. The development of the local cooling gas distribution within the tracker modules and the quantifying the associated flow rates was done as part of this thesis. The local cooling concept for each tracker module was outlined in the previous chapter because of its direct implications on the mechanical design. The focus of this chapter is to describe the fluid dynamics simulations that were performed in order to evaluate the cooling flow requirements, which served as an input to the mechanical design.

An initial assessment of the necessary helium flow rate is made based only on the specific heat capacity c_p of gaseous helium. For this estimation, the minimum helium flow rate $\dot{V}$ needed in order to arrive at a steady state energy equilibrium is evaluated assuming perfect heat transfer (the full helium volume is heated up to the maximum allowed temperature) and a heat flux ϕ_q of the silicon pixel sensors:

$$\dot{V}_{\mathrm{min}} = \frac{N_{\mathrm{sensor}} \cdot A_{\mathrm{sensor}} \cdot \phi_q}{c_p \cdot \rho \cdot \Delta T_{\mathrm{max}}} \tag{8.1}$$

Here, N_{sensor} is the total number of sensors to be cooled, A_{sensor} is the sensor surface area, ρ is the density of the coolant and ΔT_{max} is the maximum temperature difference between incoming and outgoing cooling gas that is allowed during operation. For the P2 tracking detector, 8 modules with 632 sensors each will be constructed and operated. The sensor area is $20\,\mathrm{mm} \times 23\,\mathrm{mm}$. The maximum operating temperature is estimated to be 70 °C and also taken as an estimate on the maximum temperature difference, implying an initial helium temperature of 0°. Table 8.2 shows calculation results on the minimum helium flow rate for different assumptions on the sensor power dissipation. These values can only be interpreted as a lower limit and are expected to be exceeded considerably by any predictions based on dedicated heat transfer simulations.

Sensor	Tracker Module		Full Tracker	
ϕ_q [mW cm^{-2}]	$\dot{Q}$ [W]	$\dot{V}$ [L s^{-1}]	$\dot{Q}$ [kW]	$\dot{V}$ [L s^{-1}]
100	290.7	4.48	2.33	35.84
200	581.4	8.96	4.65	71.69
300	872.2	13.4	6.98	107.5
400	1162.8	17.9	9.30	143.4

Table 8.2.: *Total heat production $\dot{Q}$ and lower limit on the helium flow $\dot{V}$ needed for an energy equilibrium, calculated for different assumptions on the sensor power dissipation ϕ_q. The calculation is based on the simplified assumption that the full helium flow is heated up by $\Delta T = 70°$. The volume flow is evaluated at the helium density at the inlet temperature $T = 0°$, $\rho = 0.1785\,\mathrm{kg\,m^{-3}}$. Results are given both for a single tracker module and the full tracking system consisting of eight modules.*

For more realistic predictions on the volume flow rates, the temperature and velocity profiles of the helium flow need to be considered. Fluid flow and heat transfer are governed by partial differential equations, in particular the continuity equation, the Navier-Stokes equation, and the energy equation. The continuity equation for incompressible flow and the velocity field $\vec{v}$ reads

$$\vec{\nabla} \cdot \vec{v} = 0. \tag{8.2}$$

The equation of motion for incompressible flow is given by the Navier-Stokes equation:

$$\rho \left(\frac{\partial \vec{v}}{\partial t} + (\vec{v} \cdot \vec{\nabla})\, \vec{v} \right) = -\vec{\nabla} p + \mu \Delta \vec{v} + \vec{g} \tag{8.3}$$

with density ρ, the dynamical viscosity μ and external body forces $\vec{g}$ like gravity or Coriolis force. The gravitational force needs to be considered only for flow applications where natural convection has a notable impact. The Coriolis force can be neglected for all applications reported in this thesis. In addition, only steady state solutions are considered, which leads to $\frac{\partial \vec{v}}{\partial t} = 0$.

Incompressible flow implies that density changes can be neglected for a fluid parcel that moves with the flow velocity. A fluid parcel is an infinitesimal volume that is chosen large enough to neglect the molecular composition. Density changes can be caused by large pressure or temperature variations. For cooling setups with moderate flow velocities and with forced convection as the dominant cooling mechanism, incompressible flow is a valid assumption. However, in case that natural convection has a considerable impact, buoyancy forces due to temperature induced density vari-

ations in conjunction with gravity are crucial. Having said this, it is important to notice that incompressible flow is in some cases[2] defined less restrictive to be low Mach number flow (or pseudo-incompressibility), then requiring solely a flow velocity below 0.3 times the speed of sound. Using only this requirement for incompressible flow then explicitly allows for large perturbations in density due to temperature changes and is almost always fulfilled regarding cooling simulations for the P2 tracking detector.

The Navier-Stokes equation is non-linear so turbulence can occur. An indicator whether such phenomena must be taken into account is represented by the so-called Reynolds number, defined as

$$\mathrm{Re} = \frac{v\,L}{\nu}. \tag{8.4}$$

Here, L is a characteristic length dimension of the flow geometry and ν is the kinematic viscosity. Laminar flow (no turbulence) can be assumed for values below a critical value of the Reynolds number R_{crit}, which also depends on the actual geometry.

The energy equation for incompressible flow and neglecting viscous heating can be written in terms of the static temperature T:

$$\rho\, c_p \left(\frac{\partial T}{\partial t} + \vec{v} \cdot (\vec{\nabla}\, T) \right) = \vec{\nabla} \cdot \left(k \vec{\nabla}\, T \right) + q_V \tag{8.5}$$

with the heat conductivity k and any volumetric heat source q_V. The partial time derivative of the temperature vanishes for steady state solutions. The energy equation is completely decoupled from the continuity equation and the Navier-Stokes equations for incompressible flow unless the viscosity depends on the temperature. In conclusion, there are five equations (continuity equation, three momentum equations given by the Navier-Stokes equation and the energy equation) for five unknown variables: three components of the velocity vector $\vec{v}$, the pressure p and the temperature T.

For simple flow applications, several further approximations allow to greatly simplify the relevant equations and thus enable to deduce analytical results. An interesting case of such a simple configuration is a laminar gas flow over a flat heated surface. It is considered in more detail e.g. in Ref.s [161, 162]. For this configuration, one can derive that both the velocity and the temperature profile are described by a boundary layer as depicted in figure 8.1. The layer thicknesses δ_v for the flow boundary layer

[2] for example within the Autodesk® CFD software

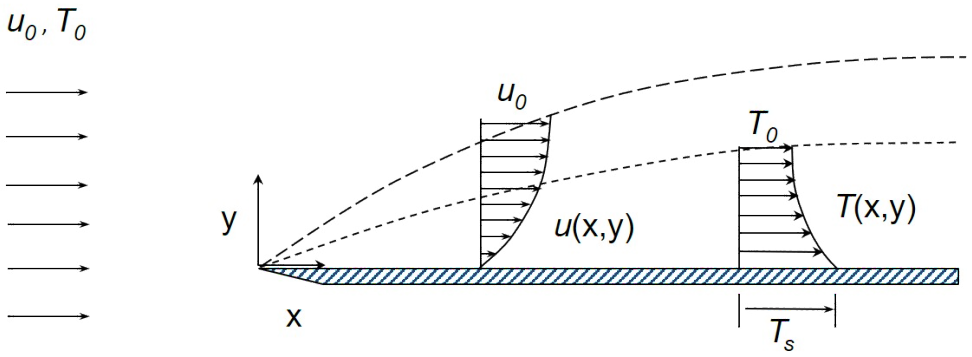

Figure 8.1.: *Schematic drawing depicting fluid flow over a flat plate; taken from Ref. [163].*

and δ_t for the temperature boundary layer are related by the Prandtl number

$$\frac{\delta_t}{\delta_v} = \mathrm{Pr}^{-\frac{1}{3}}. \tag{8.6}$$

The Prandtl number for hard-sphere mono-atomic gases is $\frac{2}{3}$; it can be seen from table 8.1 that the value for helium is very close to this prediction. The layer thicknesses are defined as the distances to the boundary where temperature (velocity) have reached 99 % of the free stream temperature T_0 (velocity u_0). The Reynolds number at length x along the surface is given by

$$\mathrm{Re}_x = \frac{u_0\, x}{\nu}. \tag{8.7}$$

The critical Reynolds number is here around 3.5×10^5. For a constant heat flux q_w across the boundary, it can further be derived that [161, 162]

$$\frac{q_w\, x}{k\,(T_w - T_0)} = 0.453 \cdot \mathrm{Re}_x^{\frac{1}{2}} \cdot \mathrm{Pr}^{\frac{1}{3}}\ . \tag{8.8}$$

This relation shows that the wall temperature T_w along the surface is proportional to $\sqrt{x}$.

For more complex fluid dynamical problems such as helium flow and heat transfer in the P2 tracker modules, analytical calculations by hand become impossible. The behavior of liquids and gases is hence commonly analyzed with Computational Fluid Dynamics (CFD) tools. The analyses presented here were done with Autodesk® CFD, which is based on the finite element method (FEM) and thus has good flexibility in modeling any geometric shape. The partial differential equations are reduced to a set of algebraic equations at discrete points and nodes on every element (discretization

method).

The work flow for any CFD simulation starts with an input model describing the geometry. For flow simulations without any heat transfer involved, it is sufficient to know the material and the geometry of the flow volume. The integration of heat transfer requires to define the material and the geometry of any solid parts surrounding the gas flow. The input model should be simplified as much as possible so that it only includes features that are relevant for the CFD simulation. After importing the geometry model and applying the correct materials to all the parts, the boundary conditions for the CFD simulation must be defined. The boundary conditions include constraints on temperature, heat transfer, inlet flow velocities and pressure. The geometry model is then converted to a simulation model in the meshing procedure. After that, the physical processes to be simulated must be defined, including settings for using (in)compressible flow, inclusion of heat radiation or gravity. The simulation is then performed iteratively until sufficient convergence of velocity, pressure and temperature is achieved.

The prediction of helium volume flows for the P2 tracking detector in the scope of CFD simulations involves many simplifications, in particular the representation of the geometry in a discretized simulation model. Only a limited number of finite elements can be simulated with affordable computational infrastructure. The results of CFD simulations hence come with large uncertainties that are difficult to quantify. It is therefore crucial to validate these results with experimental cooling tests wherever possible. First cooling tests in the laboratory were already made with test setups including single strips. In addition, a prototype of the P2 tracker modules has been constructed that will allow to perform extended cooling studies. Details on this prototype are discussed in chapter 9.

Several cooling tests and simulations have already been performed for the Mu3e experiment, that will use a similar cooling concept with gaseous helium for a very different geometry. These investigations are reported in Ref.s [157, 158, 162, 164–167]. They include both experimental tests and numerical simulations. In addition, a more detailed discussion on the validity of finite element simulations can be found in Ref. [166].

8.1. Helium Distribution in the Tracker Module

The cooling of the silicon pixel sensors on the tracker modules for the P2 experiment is implemented by forced convection of a gaseous helium stream. The minimum flow rates considered in 8.2 showed that forced convection is necessary since natural convection is not sufficient to dissipate the heat produced by the sensors. Cooling

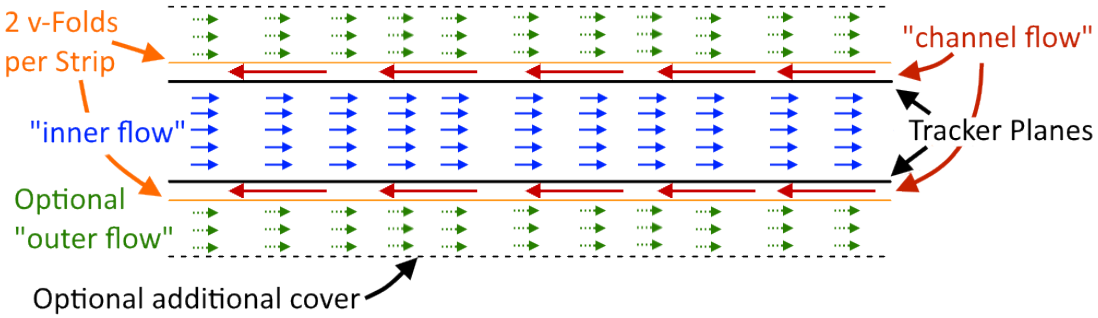

Figure 8.2.: *Schematic cut view through a tracker module visualizing the different helium cooling flows. The schematic is not to scale.*

the sensors by forced convection requires to establish a continuous helium stream along the sensor surface. Therefore, the gaseous helium must be distributed through a channel system implemented in each tracker module.

The base design of the tracker module without additional cover integrates two helium flow circuits. The first helium distribution system channels the helium through the two v-folds mounted on each strip ("channel flow"). The channel system is designed such that about the same helium flow rate is achieved in the v-folds of all strips. The second helium distribution system is responsible for the helium flow between the two tracker planes ("inner flow"). Again, the same amount of helium should flow along each strip. In addition, the piping must ensure that a steady laminar flow along the strips without turbulences is established. The additional cover option would include a third helium distribution system ("outer flow") of helium streaming above the tracker planes. Figure 8.2 sketches a cut view through the tracker module and visualizes the different flow directions.

The main task in the development of the helium distribution system for the channel flow is to provide equal flow rates to all v-folds. The same challenge arises for the inner flow. Even though there are no separated flow channels in this case, the free streaming velocity along the strips should be rather uniformly distributed among the strips. The helium distribution system for each of the two flow circuits basically consists of one helium pipe along the frame, with one hole opening for each v-fold and for each diffusor chamber, respectively. One diffusor chamber is implemented for each strip, see figures 7.5b, 7.7 and 7.11a. The outlet openings to the individual v-folds and diffusor chambers must be small enough to prevent that more helium than designated is passed through the first few openings behind the main gas inlets. For a constant diameter and spacing of the hole openings, the uniformity of the helium distribution to the individual openings is determined by the accumulated cross section of all openings compared to the cross section of the distributing pipe. Figure 8.3 shows this effect observed in the CFD simulation. In this case, helium flow through

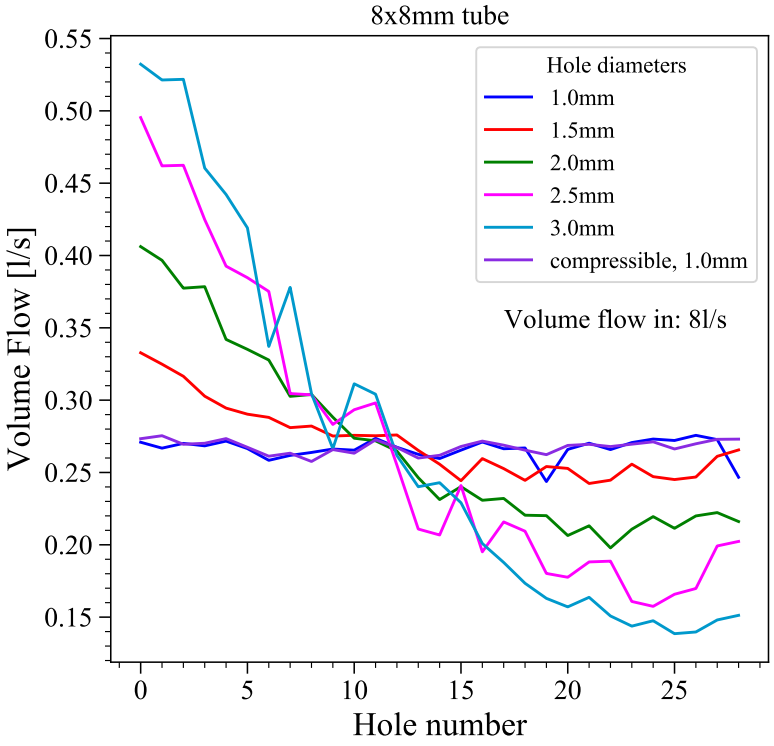

Figure 8.3.: *Helium flow through openings in a gas channel depending on the hole diameter.*

a pipe with a rectangular cross section of 8 mm × 8 mm was simulated; 29 holes of equal diameter and with 20 mm spacing were implemented as outlet openings. The openings were placed centered on one of the lateral surfaces of the pipe. The simulation was repeated for several different values of the opening diameter and each time the flow through the individual openings was investigated. It can be seen that a sufficiently uniform helium distribution is achieved for a diameter of 1.5 mm or smaller. This corresponds to a ratio of the accumulated cross section of all openings to the pipe cross section of about 0.8. For 1 mm opening diameter, the expected average helium velocity in the opening is around 350 m s^{-1}, so that the influence of simulating compressible flow was considered. No notable difference in the simulation outcome could be observed compared to incompressible flow.

In the considered technical design of the tracker modules, the cross sections of the two helium distribution channels within the frame side modules are larger than 8 mm × 8 mm. The channel for the v-fold flow circuit measures 30 mm × 15 mm and the channel for the inner flow 18 mm × 11 mm. However, there are 116 v-folds and

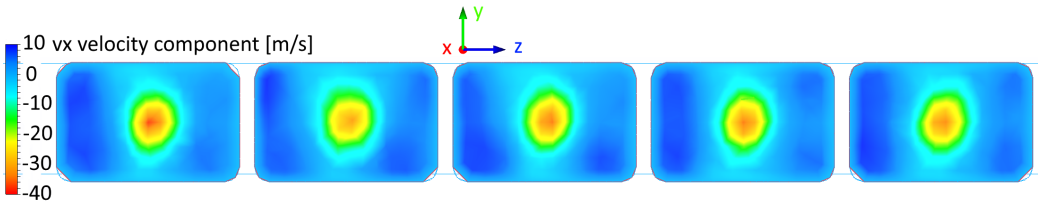

(a) *Simulation without the additional bridge installed in the diffusor part*

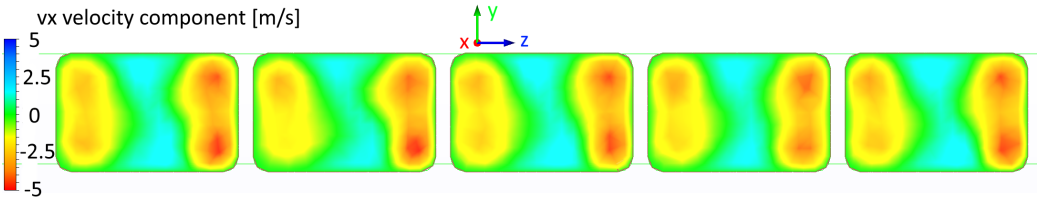

(b) *Simulation with complete diffusor part*

Figure 8.4.: *Simulation of the helium outlets for the inner flow. The total helium flow is* $6\,\mathrm{L\,s^{-1}}$ *in both simulations. The flow through the diffusor part is simulated once without the bridge as an obstacle behind the opening and once with the full design. The plot shows the velocity perpendicular to the opening surface at the outlet of the first six out of 29 diffusor chambers. Negative velocities indicate gas flow out of the diffusor part. The helium flow in the distributing channel is in positive z-direction.*

therefore the same amount of openings in the corresponding helium channel. A hole diameter of 2 mm is chosen which then again corresponds to a cross section ratio of around 0.8. The same opening size is used for the inner flow channel, the ratio in this case is about 0.5. The openings are not chosen smaller in order to prevent very high helium flow velocities at the openings. If slightly more helium is distributed to the first few strips, it might be even beneficial because these are the strips with the highest multiplicity of mounted sensors.

In an initial design of the tracker modules, the diffusor part was not implemented and the inner flow was distributed to the volume between the two tracker planes directly through the hole openings in the corresponding helium distribution channel. It was then observed in a flow simulation that this leads to chaotic helium flow between the tracker planes. The diffusor part was hence installed in order to arrive at a steady helium flow aligned along the strip modules. This design is shown in figure 7.7. It consists of one chamber per strip and an additional bridge directly behind the outlet opening as an additional obstacle for the helium flow. The effect of this additional bridge is shown in figure 8.4. In these two simulations, the helium flow is simulated once with the additional bridge and once without. The total flow volume is $6\,\mathrm{L\,s^{-1}}$ in both simulations. It can be observed that the maximum velocity at the outlet of the chambers is much lower (about $5\,\mathrm{m\,s^{-1}}$ instead of $37\,\mathrm{m\,s^{-1}}$) with the additional

bridge installed since the flow is distributed over a larger area. However, even with the full diffusor part installed the helium flow is not uniformly distributed over the chamber opening. Without the additional bridge, the maximum outgoing helium velocities are observed localized directly behind the outlet openings. The additional bridge however redirects the helium flow to the sides of the diffusor chamber. Recirculating flow occurs for both configurations. Nevertheless, in flow simulations of the complete tracker module, it can be observed that with the full diffusor part put in place, the velocity differences at the outlet compensate in the helium volume between the tracker planes so that a homogeneous flow profile is achieved (see the following section). The helium velocity profiles obtained in simulations involving the complete tracker module are additionally influenced by the simulation of heat transfer.

The flow simulation of the diffusor part additionally allows to analyze the total rate of helium flowing through each of the diffusor chambers. As mentioned before, one chamber is installed for each strip. The magnitude of the helium flow volume should be the same for each of the diffusor chambers. Figure 8.5 shows that the helium flow is indeed distributed quite uniformly through all chambers which confirms that the opening diameter of 2 mm at the pipe outlet is sufficiently small. The volume flow per diffusor chamber even slightly increases with the distance to the main gas inlet, which is surprising and probably attributable to the specific flow geometry. This effect is not observable in the simulation without the bridge installed in the diffusor part. In any case the differences in the volume flow per chamber are very small and therefore not considered to be relevant for the cooling performance.

8.2. CFD Simulations of the Complete Tracker Module

The simulation of the complete tracker module including heat transfer requires to define several further boundary conditions and physical constraints. First of all, the heat production of the silicon sensors must be set. The cooling of the P2 tracking detector is simulated for two scenarios regarding the heat dissipation of the HV-MAPS: a moderate heat dissipation scenario of $200\,\mathrm{mW\,cm^{-2}}$ and a scenario with an increased power consumption of $400\,\mathrm{mW\,cm^{-2}}$. For the moderate power consumption scenario, the base design of the tracker module without additional cover and outer flow is simulated. For the high power scenario however, the additional cover and outer flow are added. The sensor dimensions in the CFD simulation are $22\,\mathrm{mm} \times 20\,\mathrm{mm}$ and the heat dissipation is distributed uniformly over the complete area. Sensor tests have shown that most heat is actually dissipated in the inactive

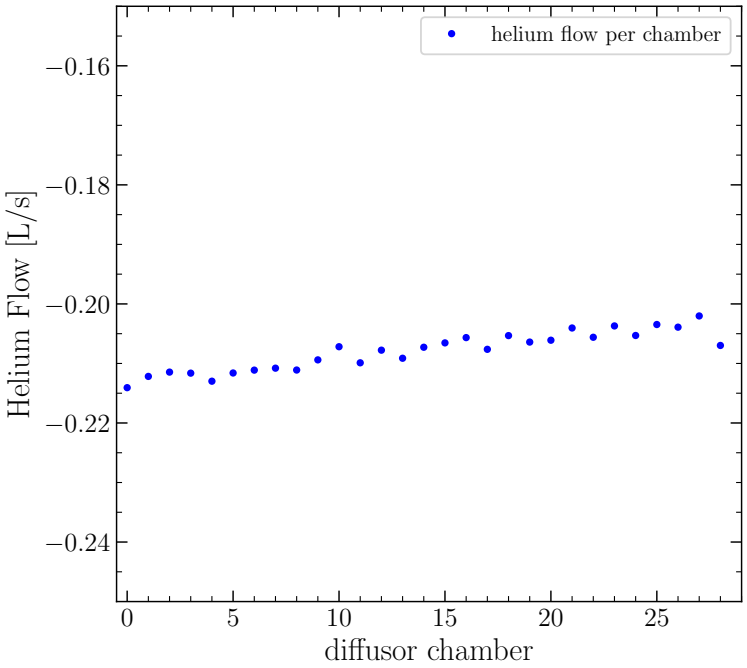

Figure 8.5.: *Helium volume flow through each of the diffusor chambers.*

periphery region. The effect of locally increased heat load hence must be considered in future investigations.

The cooling of the pixel sensors with gaseous helium will predominantly be realized by forced convection. In addition, cooling is improved by natural convection and thermal radiation. Regarding CFD simulations, these two additional cooling mechanisms impose significant additional computational costs. When simulating only forced convection, it is possible to simulate the helium flow and the heat transfer separately since the equations of motion and energy are independent from each other. This is no longer the case if helium density variations are taken into account, so that flow and heat transfer are coupled and must be simulated simultaneously. An efficient approach is to obtain a rough estimate on the cooling performance by simulating solely forced convection first and then achieve more precise results by enabling natural convection and thermal radiation consecutively. For that, the results based on forced convection can be used as an input such that convergence is then usually obtained with less than 100 additional iterations. The Autodesk® CFD software defines incompressible flow as low Mach number flow and so heat induced density variations are controlled as a separate setting. Incompressible flow in that sense is therefore assumed in all simulation scenarios while allowing temperature induced density variations controls the presence of natural convection. Thermal radiation can be enabled with an additional switch in the CFD software.

The mechanical input model of the tracker module is simplified in such a way that irrelevant features like screws or connectors are omitted or replaced by simpler shapes. The simulations presented here make use of the automatic mesh sizing with only small adjustments. The geometry of the P2 tracker modules is rather inconvenient for CFD simulations with finite mesh size since it includes several very thin parts that result in a very large number of elements. The automatic mesh sizing adjusts the element size to the modeled geometry. It allows for variable element sizes in order to arrive at an efficiently solvable simulation model.

For the tracker module base design without additional cover, an external enveloping helium volume is added to the simulation model. This external gas volume is necessary in order to consider the effect of natural convection. Its size is chosen such that a further extension had only negligible influence on the temperature simulation results. An extension of about 5 cm measured from each of the two tracker planes was found to be sufficient. All exterior surfaces of the simulation models are treated as adiabatic surfaces with zero velocity. For the design with additional cover, no external gas volume is added since in this case the flow volume is already enclosed by the foil mounted on the cover frame. The foil itself is omitted in the simulation model as it is sufficient to limit the helium volume. Due to the adiabatic boundary condition at exterior surfaces, the heat transfer through the foil to the helium gas chamber is in this scenario neglected, so that the cooling performance is slightly underestimated. Figure 8.6 shows the geometry that is used for the two simulation scenarios. The directions of the coordinate axes are the same for both scenarios and also shown in this figure. The coordinate origin is defined in the center of the tracking module, so that the yz-plane is the midplane between the frame side modules and the xz-plane is the midplane between the two tracker planes. The coordinate directions are therefore the same as used in the CFD simulation of the diffusor design, see figure 8.4. Note that this coordinate system definition in the CFD simulation however differs from the one chosen for the P2 detector simulation which is also the one used for the technical design of the tracker modules.

8.2.1. Flow Velocity Results

The efficient cooling of the pixel sensors requires to distribute the helium cooling gas evenly across the tracker module. Laminar helium flow must be ensured near the sensors in order to limit any vibrations caused by the helium flow. It is therefore important to check the velocity profiles near the pixel sensors in the simulation of the complete tracker module. Figure 8.7 shows the velocity profile for the inner flow between the tracker planes which was evaluated in the moderate heat load scenario (without additional cover). The important input parameters for this scenario are given in table 8.3. It can be seen that the velocity is oriented in x-direction and

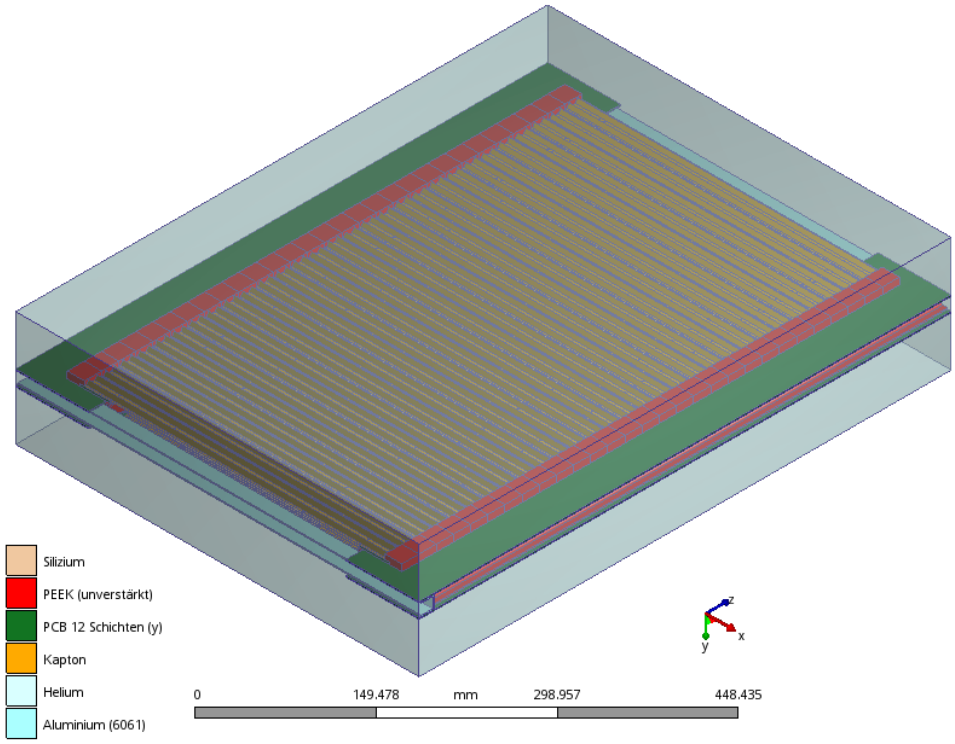

(a) *Base design of the tracker module with extended helium volume.*

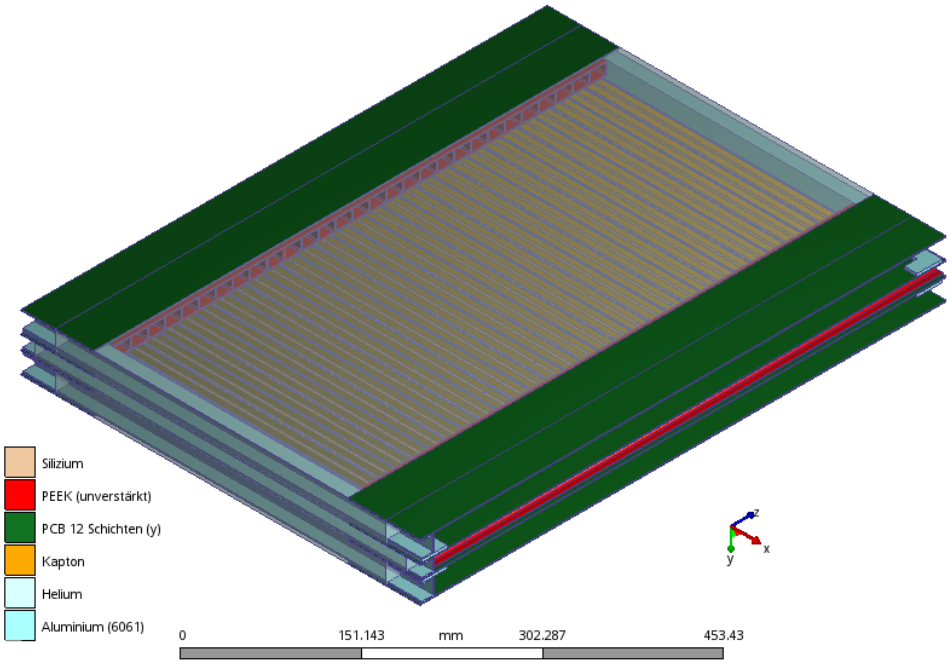

(b) *Tracker module with additional cover*

Figure 8.6.: *Rendered CFD simulation geometries for the two scenarios considered, more details are given in the text.*

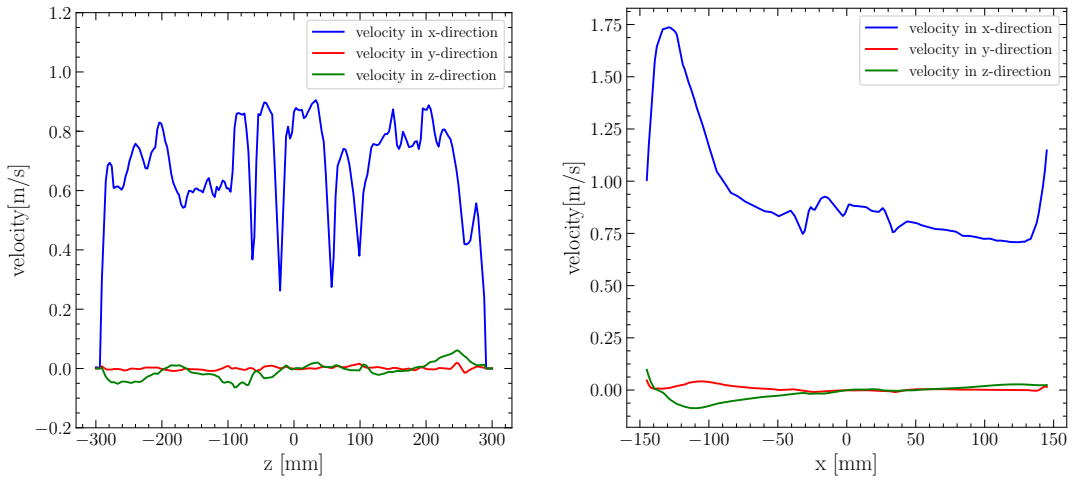

(a) *Inner flow velocities along the z-axis ($x = y = 0$)*

(b) *Inner flow velocities along the x-axis ($y = z = 0$)*

Figure 8.7.: *Flow velocities of the inner flow between the tracker planes evaluated in the CFD simulation. Both plots are evaluated on the midplane between the tracker planes, $y \equiv 0$.*

hence along the strips, which is the desired behavior. The other velocity components are much smaller. Looking at the velocities along the z-axis (perpendicular to the orientation of the strip modules, in the middle between the two frames) in figure 8.7a, it can be seen that the velocity in x-direction however fluctuates considerably. Nevertheless, the fluctuations are random without any visible pattern or tendency. As a consequence, they are rather attributable to the finite mesh size than to any actual physical effect.

The velocity profile between the tracker planes along the x-axis (along the strip orientation) plotted in figure 8.7b shows an increase directly behind the gas outlet of the diffusor ($x = -145\,\text{mm}$). The x-axis is defined to be at the center of the module and thus located at the center of a diffusor chamber. The analysis of the diffusor design (see figure 8.4b) has shown that the flow is not distributed uniformly over the outlet, but is minimal at the center. The increase of flow velocity seen in figure 8.7b is therefore attributable to the balancing of the flow velocities directly behind the diffusor outlet. This is confirmed by figure 8.8, which shows the profile of the velocity in x-direction on the midplane between the two tracker planes (xz-plane) at the diffusor outlet. It can be seen that at a few centimeter distance to the diffusor outlet, the maximum velocity can be observed at the center and no longer at the sides of the diffusor. In addition, by simulating the complete gas volume between the tracker planes, the recirculating flow at the diffusor outlet (negative velocity in x -direction) disappeared. In general, figure 8.7b shows a velocity drop of the inner flow along the

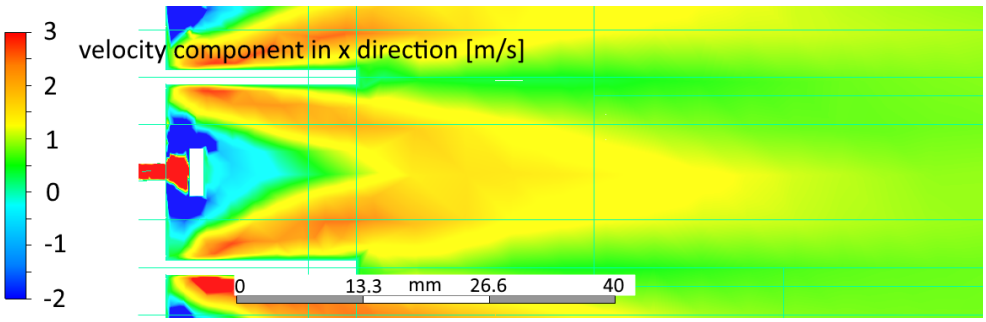

Figure 8.8.: *Profile of the velocity in x-direction in the midplane between the tracker planes at the diffusor outlet. The range of the color scale is chosen to cover the velocities appearing outside the diffusor chamber; the velocities inside partially extend over the range covered by the color scale.*

strips. The volume between the tracker planes is not perfectly enclosed by the strips so that helium gas is escaping between the strips. In addition, the helium volume is open at the first and the last strip of each plane. The same amount of helium that is blown on the one side is sucked in again at the frame side module on the other side, which explains the clear flow velocity increase observed in front of this outlet.

For the channel flow, the helium flow through the v-folds is analyzed. The v-folds are shaped as isosceles triangles with base side length $a = 6\,\text{mm}$ and height $h = 4\,\text{mm}$, see the geometry shown in figure 7.3. The cross section thus is $A_c = 12\,\text{mm}^2$. The Reynolds number for the flow through the v-folds can be calculated according to equation 8.4. For non-circular tubes, the length scale L has to be replaced by the so-called hydraulic diameter [168]

$$D_h = \frac{4A_c}{P} \tag{8.9}$$

where P is the wetted perimeter. For the v-folds, it is given by the sum of the triangle's side lengths, thus $P = a + 2b = 16\,\text{mm}$ with $b = \sqrt{(\frac{a}{2})^2 + h^2} = 5\,\text{mm}$. Finally, one gets $D_h = 3\,\text{mm}$. The maximum Reynolds number for which laminar flow in a pipe will always be stable is 2100 [161]. For the volume flows considered in the cooling simulations of the P2 tracking detector, the Reynolds number in the v-folds is always far below this critical value, see table 8.3.

The calculations of the Reynolds numbers assume that the helium flow is equally distributed to all v-folds. Figure 8.9 shows the distribution of the helium flow volumes through each individual v-fold for both cooling scenarios. Apart from the different total volume flow in the two scenarios, the distributions are very similar. The helium flow through most of the v-folds is slightly above the average, but a reduced helium flow is observed for some v-folds. No pattern can be observed where these v-folds

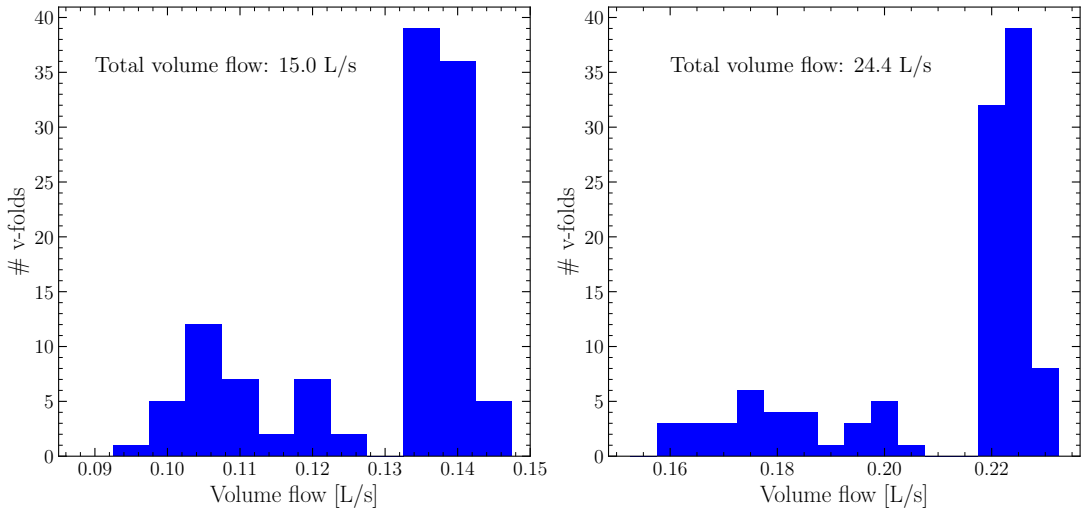

(a) *Moderate power scenario (*200 mW cm^{-2}*)* (b) *High power scenario (*400 mW cm^{-2}*)*

Figure 8.9.: *Distribution of the helium volume flow to the v-folds in the two simulated cooling scenarios.*

are located. In any case, the differences are not too large so that the evenness of the helium distribution is considered to be acceptable. The total volume flow of 24.4 L s^{-1} obtained in the high power scenario exceeds the incoming helium flow of 24 L s^{-1} (see table 8.3). Helium expands with temperature so that the volume flow is not a conserved quantity. It was checked for both cooling scenarios that sufficient mass flow balance at the global gas inlets and outlets of the simulation model is obtained. Although the helium volume flow through the v-folds was evaluated at the beginning of the v-folds where the gas enters, for the high power scenario the helium was apparently slightly heated up before by the environment.

8.2.2. Thermal Results

The results discussed so far have shown that the helium distribution system within the tracker module works as expected and that only laminar helium flow should occur around the pixel sensors. In order to investigate the cooling performance, the thermal simulation results need to be considered. The simulations were conducted with 0 °C initial helium temperature. In the experiment, it is a good idea to use a slightly higher input temperature in order to prevent any ice forming on detector parts. The temperatures observed in the CFD simulation should be interpreted as temperature differences to the input temperature, which means that a higher input temperature would need to be added to the observed temperatures.

	moderate power scenario	high power scenario
sensor heat load	200 mW cm^{-2}	400 mW cm^{-2}
total heat	556.16 W	1112.3 W
channel flow	15 L s^{-1}	24 L s^{-1}
inner flow	6 L s^{-1}	6 L s^{-1}
outer flow	-	2 × 6 L s^{-1}
total helium flow per module	21 L s^{-1}	42 L s^{-1}
flow per v-fold	0.13 L s^{-1}	0.21 L s^{-1}
average v-fold velocity	10.7 m s^{-1}	17.2 m s^{-1}
v-fold Reynolds number	306	493
fluid elements	5 945 291	7 101 593
fluid nodes	1 987 532	2 523 844
solid elements	2 782 555	3 573 141
solid nodes	273 951	372 081
inlet helium temperature	0 °C	0 °C
maximum sensor temperature		
- no heat radiation	60.3 °C	75.6 °C
- with heat radiation	60.0 °C	74.5 °C

Table 8.3.: *Summary table of important parameters for the two cooling scenarios. The v-fold volume flow, velocity and Reynolds number are calculated for* 0 °C *helium temperature.*

Figure 8.10 shows the temperatures observed on the sensors in the two simulated cooling scenarios. The boundary conditions are given in table 8.3. The qualitative temperature profiles are quite similar for both scenarios. The maximum temperatures are visible on the first few strips counted from the top. In general, the sensors on the left side (low x-value) are hotter. It can be concluded that more heat is transported away from the sensors by the channel flow which is oriented in negative x-direction (from right to left). The helium in the v-fold channels heats up so that the cooling becomes less efficient to the left side. The inner flow (and the outer flow in the high power scenario) is (are) oriented in the opposite direction to compensate for that (see figure 8.2), but the cooling capability is lower. The cooling performance of the different flow circuits can be further investigated by considering the average temperature and helium mass flow at the global gas outlets:

$$\dot{Q} = \dot{m}\, c_p\, \langle \Delta T \rangle. \tag{8.10}$$

The temperature difference ΔT is the difference between the helium temperatures at

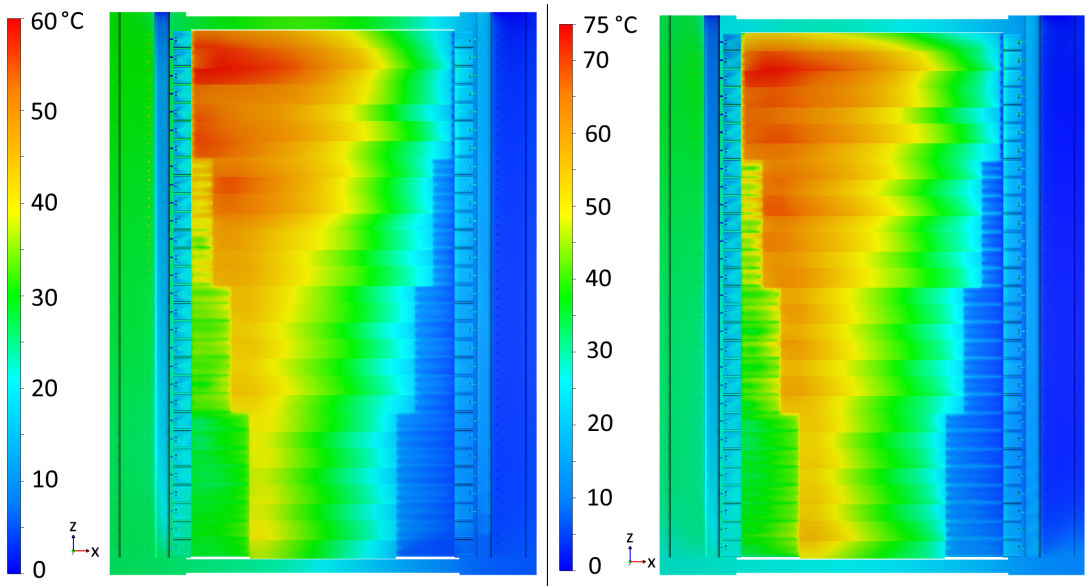

(a) *Moderate power scenario (*200 mW cm^{-2}*)* (b) *High power scenario (*400 mW cm^{-2}*)*

Figure 8.10.: *Temperature results for the two simulated cooling scenarios. For visibility, the tracker module is cut in the xz-plane, showing the sensors of one tracker plane. The channel flow was oriented in negative x-direction (from the right to the left), the inner flow (and outer flow) in positive x-direction.*

inlet and outlet. Table 8.4 summarizes the heat dissipated at the outlets of all cooling circuits. These numbers represent only an estimate on the actual cooling performance of the flow circuits because of heat transfer through the pipes to the environment. The results given in this table are evaluated before activating heat radiation because radiation additionally complicates the quantification of cooling attributed to a particular flow channel. An energy imbalance of a few percent is observed for both scenarios. The average temperature at the outlet is calculated based on nodal data and therefore only an approximation. Autodesk® CFD minimizes the energy equation residual at the nodes, as opposed to forcing fluxes to balance. This helps to

flow circuit	moderate power scenario	high power scenario
total heat production	556 W	1112 W
channel flow	446 W	822 W
inner flow	89 W	83 W
outer flow	-	174 W
energy imbalance	21 W	33 W

Table 8.4.: *Heat dissipated via the various flow circuits in the two simulation scenarios.*

flow circuit	moderate power scenario	high power scenario
channel flow	29.8 $\mathrm{W\,L^{-1}}$	34.2 $\mathrm{W\,L^{-1}}$
inner flow	14.8 $\mathrm{W\,L^{-1}}$	13.9 $\mathrm{W\,L^{-1}}$
outer flow	-	14.5 $\mathrm{W\,L^{-1}}$

Table 8.5.: *Heat dissipated through the various flow circuits in the two simulation scenarios, evaluated per liter of incoming helium at* 0 °C.

ensure an accurate prediction of component temperatures. This often means that the temperature on the object is independent of whether an energy balance is achieved. An energy imbalance in the few percent range is considered to be very good according to the Autodesk® CFD software documentation [169].

The heat dissipation values listed in table 8.4 confirm that the channel flow is in fact the cooling circuit with the best cooling performance regarding the absolute heat transfer. In addition, the dissipated heat is related to the corresponding volume flow and reported in table 8.5. These results show that the channel flow is also the most efficient cooling circuit. The outer flow and the inner flow show comparable cooling efficiency in the high power scenario. More heat per liter helium is dissipated through the channel flow in the high power scenario compared to the moderate power scenario. The temperatures observed in the high power scenario are in general higher so that larger temperature gradients appear and result in more heat transferred per helium volume unit. However, this increase of the cooling efficiency does not occur for the inner flow circuit.

Safe and reliable operation of the pixel sensors was tested up to 70 °C. The temperature results for the two cooling scenarios in figure 8.10 show that the maximum temperature is well below this value for 200 $\mathrm{mW\,cm^{-2}}$ heat production of the sensors. However, for 400 $\mathrm{mW\,cm^{-2}}$ heat production, increasing the volume flow for the channel flow and adding the outer flow, in total resulting in a doubled volume flow rate (see table 8.3), was not enough to keep the sensor temperatures below the desired maximum value. The maximum temperature of 70 °C is however exceeded by less than 5 °C, so that sufficient cooling might be achievable by optimizing the cooling system efficiency without further increasing the flow rate.

In order to further quantify the temperatures of the hottest sensors observed in the CFD simulations, the temperature profile of the strips with 14 sensor chips mounted is analyzed and plotted in figure 8.11. The figure confirms that the sensors on the left side of the strips (low x-coordinate values) have the highest temperatures. The temperature decreases almost monotonously in x-direction along the strips, apart from an increase for very small x-coordinates in the high power scenario. Here, the lower temperatures that can be observed for the first two sensors on most strips can

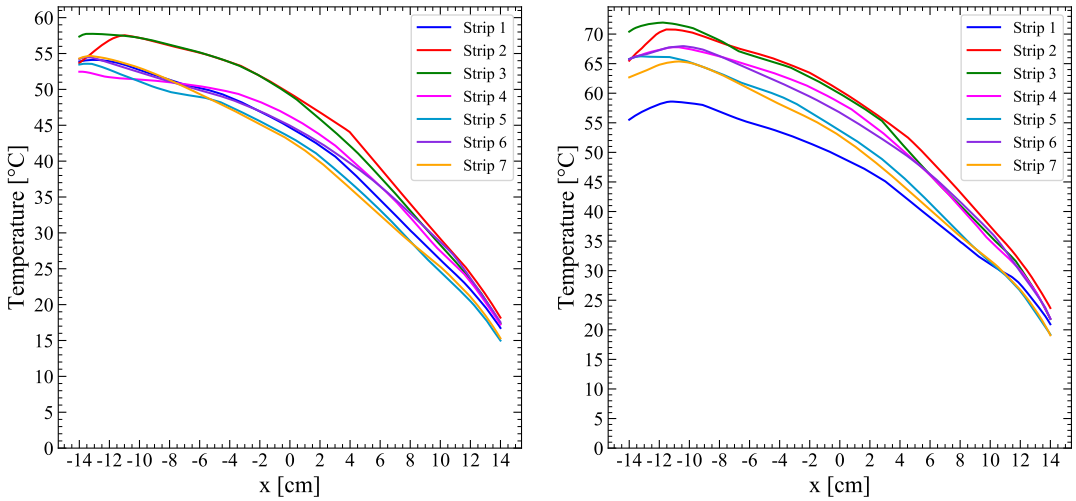

(a) *Moderate power scenario (*200 mW cm^{-2}*)* (b) *High power scenario (*400 mW cm^{-2}*)*

Figure 8.11.: *Temperatures on the strips with 14 sensors for the two simulated cooling scenarios. The temperature is evaluated in x-direction along the center of each strip.*

be attributed to the cooling effect of the inner flow and the outer flow. The sensors on the right side of the strips, where the channel flow arrives first, are cooled to about room temperature. The temperature trend is very similar for most of the strips, while in both scenarios the second and the third strip show the highest temperatures. The maximum temperatures visible in figure 8.11 are slightly lower compared to figure 8.10 since the temperatures are evaluated along the center of the strips and the highest temperatures in the simulation appear at sensor edges.

8.3. Conclusions

The cooling analysis presented here represents a proof of principle that cooling the P2 tracker modules with gaseous helium is possible. The cooling simulations also contributed to the development of the technical design of the tracker modules. The helium volume flow that is needed to achieve sufficient cooling of the pixel sensors for a given power consumption was quantified. For 200 mW cm^{-2} heat dissipation on the sensors, a maximum sensor temperature of around 60 °C is obtained for a cooling configuration with 21 L s^{-1} helium volume flow. In the scenario with doubled heat dissipation and flow rate, the maximum temperature is about 75 °C, which is 5 K above the tested maximum operation temperature of a MuPix prototype sensor. In testbeam measurements, the newest MuPix8 prototype could however be operated efficiently with a power consumption well below 400 mW cm^{-2}. The simulations

presented here assume a heat dissipation that is uniformly distributed over the sensor area. They need to be followed by investigations taking into account that more heat is dissipated at the inactive sensor periphery area.

In order to achieve further improvement of the cooling performance, several optimizations are possible. The range of sensor temperatures in the steady state simulation results is quite large; depending on the configuration temperature differences of 40 °C to 50 °C are observed. The sensor performance in terms of efficiency and background rate is expected to be influenced by these temperature differences only to an extent that can be compensated by tuning the sensor settings. However, an obvious approach to improve the cooling efficiency is to aim for more homogeneous sensor temperatures. The temperature increase along the strips is mainly in the flow direction of the channel flow in the two v-folds. It was therefore tested whether a configuration with helium flowing in reverse directions in the two v-folds of each strip helps to reduce the temperature differences. This flow configuration helped to move the maximum temperatures towards the middle of the strips, but the overall cooling efficiency was reduced so that in general no improvement was achieved.

Another promising way to reduce the maximum temperature is the adjustment of the flow volume rates in the various flow circuits relative to each other. The maximum flow velocity in the v-folds though should be kept below $20\,\mathrm{m\,s^{-1}}$ to limit possible vibrations and is thereby almost reached in the presented high power scenario. In general, the flow volumes in the presented scenarios were motivated by the considered flow velocities and cooling studies conducted for the Mu3e experiment. In particular, the volume flow of the inner flow (and outer flow) was chosen such that the flow velocity is mostly below $1\,\mathrm{m\,s^{-1}}$, see figure 8.7. For more insights on which flow velocities can be realized without disturbing the sensor operation, dedicated experiments with prototypes reflecting the geometry of the P2 tracker module need to be conducted. Developments on a thermo-mechanical prototype of the P2 tracker module are presented in the following chapter.

The technical design regarding the helium distribution within the tracker module was implemented with the premise to provide the same helium volume flow to all the strip modules. As the cooling simulation results show higher temperatures on strips with many sensors mounted, an improvement of the cooling efficiency could be expected by increasing the helium flow only for those strips and reducing it for other strips. For such an optimization, the cross section of the outlet openings from the main gas distributing channel could be further optimized.

Since the cooling investigations presented here are limited to the helium cooling inside the tracker modules, the development of a global closed helium distribution system including a heat exchanger has to follow. The results presented here allow to dimension the helium supply system. In addition to cooling the pixel sensors, the heat dissipation of other electronic parts needs to be investigated. In particular,

power converters will have limited efficiency and might increase the total heat production by another 10 % to 20 %. As the additional electronic components are placed outside the active detector area of the tracking detector, an additional liquid coolant based cooling system for these components is an option.

9 Hardware Development

The technical design of the tracking detector modules represents a pathway to the realization of a tracking detector that fits to the requirements and to geometry of the P2 experiment. In order to actually build such a detector, the practicability of the design idea needs to be tested. Since the sensor and flexprint development is done by other groups mainly for the Mu3e experiment, the tests for the P2 experiment concentrate on all parts that are necessary to mount and operate the sensors attached to the flexprint strips. In addition to the tests of the detector mechanics, the cooling system must be tested experimentally. For both reasons, a thermo-mechanical prototype of the P2 tracker module is developed. This prototype does not include the actual pixel sensor chips, but heatable polyimide strips will allow to reproduce the expected heat dissipation of the sensors. Apart from the pixel sensors and the related electronics, the prototype detector includes all relevant features of the final detector.

This chapter describes the hardware developments which were done in the scope of this thesis. The construction of the final prototype was preceded by investigations on several sub-components and fabrication methods that will be discussed in the following.

9.1. Interposer Test

The first detector component that was tested experimentally is the connection of the strip modules to the detector frame. In particular, two Printed Circuit Boards (PCBs) were designed in order to check the board-to-board connection implemented with the Samtec® Z-Ray® interposer. The main purpose of this investigation is to find out whether reliable transmission of fast signals and power can be achieved. In addition,

the PCB design and device footprints developed for this test can serve as templates for further designs with this interposer device.

As mentioned previously, the communication with the pixel sensors will be implemented in the Low Voltage Differential Signal (LVDS) standard with a bit rate of 1.25 Gbit s^{-1}. At maximum three fast links can be connected to each sensor. The flexprint strips with the pixel sensors will be connected to the detector frame at both ends and therefore half of the sensors is read out from each side. With at maximum 14 sensor chips mounted on one strip, the communication with 7 sensors must be possible via one interposer. Consequently, at maximum 21 differential pairs and thus 42 connection pins are necessary. By using only one fast link per sensor, this number is reduced to 14 connection pins. The considered Samtec® interposer is rated for the transmission of differential signals up to a bit rate of 40 Gbit s^{-1} [159].

In addition to the fast signals, power for the pixel sensors must be transmitted through the interposer. The maximum power consumption per sensor is estimated to 1.6 W at a supply voltage of 1.8 V. Therefore, the maximum current through one interposer (for 7 sensors) is about 6.2 A. The power rating for the interposer is 0.9 A per pin with 10 pins in one row powered [159]. At least 7 power pins and the same number of ground (GND) pins are hence necessary, but a higher pin count for power transmission is certainly advisable.

The Samtec® Z-ray® interposer version considered in this hardware test features an array of 10×10 pins with a pitch of 0.8 mm. It has a thickness of 1 mm and comes in the single compression variant, which means that it is soldered on a Ball Grid Array (BGA) on the bottom board and uses compression springs as contacts to the top board. This interposer variant is also implemented in the current technical design of the P2 tracker modules. The pin count is sufficient for one fast link per sensor while using three links would require to use a larger interposer.

9.1.1. Printed Circuit Board Design

The two PCBs for the interposer test are designed such that the transmission of fast signals and power between them can be tested. The remaining pins of the interposer are connected to Light Emitting Diodes (LEDs) on the upper PCB in order to quickly test the connection reliability of many pins in several plugging and unplugging cycles. In addition, the bottom board for the interposer test can be connected directly to an Altera® Field Programmable Gate Array (FPGA) evaluation board via a High Speed Mezzanine Card (HSMC) connector. This configuration allows to generate test signal patterns on the FPGA and transfer them through the interposer. Seven differential signal pairs are connected to the FPGA of which six pairs are routed on the test board to the interposer. On the top board, the signals are first routed away from the

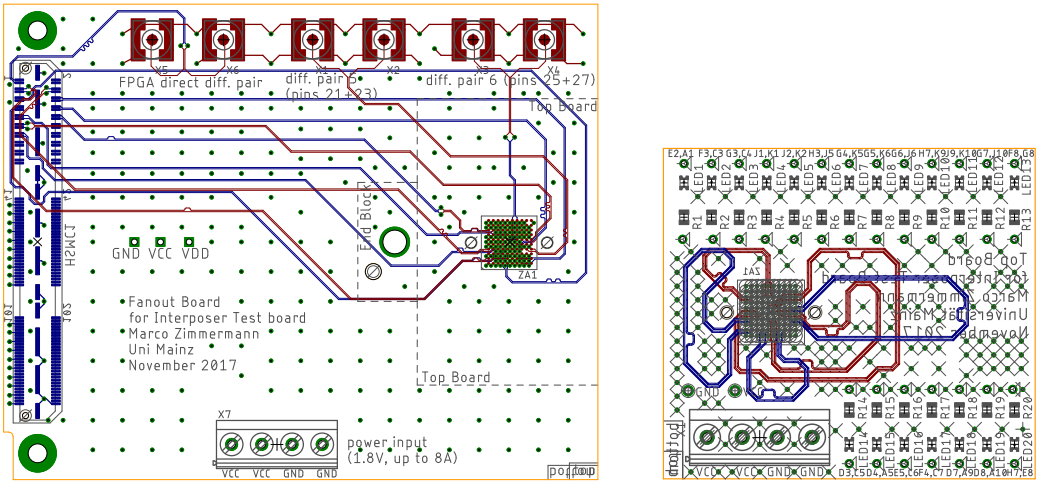

(a) *Bottom PCB* (100 mm × 80 mm)

(b) *Top PCB* (54 mm × 48 mm)

Figure 9.1.: *Selected layers of the PCB designs for the interposer test. Shown are layers on which the differential signal pairs are routed. The scale is different for the two plots. The full PCB designs of the two boards with all layers are shown in the appendix.*

interposer, but then in a loop back to it. The signals are hence transferred through the interposer for a second time back to the bottom board. Four of these differential signal pairs are routed back to the HSMC connector; the remaining two pairs are connected to SubMiniature version A (SMA) connectors. These signals can be investigated with an oscilloscope. One additional differential pair is routed directly from the HSMC connector to an SMA plug as a reference signal. Figure 9.1 shows the layouts of the PCB layers with the differential signals. The full PCB layouts and the schematics are shown in the appendix, see figures A.1 and A.2.

The transmission of fast signals up to 1.25 Gbit s^{-1} requires to take care of the differential impedances of the signal traces. The two boards were designed for 100 Ω differential impedance. The differential impedance of a pair mainly depends on the trace width, the trace distance, the distance to the reference planes and the relative permittivity of the substrate. The bottom board is a six layer design with the differential signals routed on the top and bottom plane. Both planes are flanked by a reference ground layer. The two inner layers are used for power planes. The top board is an eight layer design, but only slow signals and no copper planes are routed on the top and bottom plane. The additional two layers were necessary because no traces could be routed between the pads for the interposer spring contacts on the bottom plane, see figure 9.2. The differential pairs are thus routed on the 2nd and on the 7th layer, each of them again has a ground reference plane on the next inner layer.

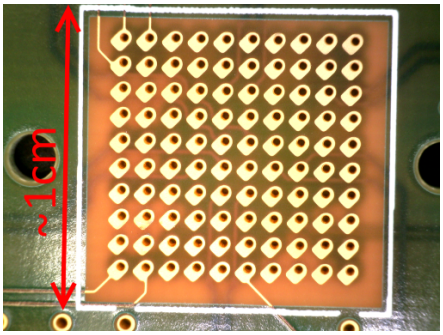

Figure 9.2.: *Contact pins on top board for interposer compression springs. The connecting vias could be placed within the pads without being filled since the pads are not soldered.*

The pin-out of the 10×10 pin array on the interposer was chosen such that various configurations of the differential pairs are tested. The pins of the differential pairs are colored in orange in the illustration in figure 9.3. Different distances between neighboring differential pairs were tested. In addition, several pairs are placed at the edge pins of the array while others are located inside. The pins illustrated with purple color (labeled with VCC) represent the pins used for power transmission. These pins and the GND pins colored in light gray are located in the periphery of the array in order to connect them with sufficiently wide copper traces. The remaining pins are used to connect each LED individually. All the LEDs are connected to the same power and ground signal on the bottom board, but on the top board the signals are routed individually in order to test the connection of each interposer pin separately. For powering the LEDs, the 3.3 V pins defined on the HSMC connector are used.

Multiple copies of the interposer test PCBs were ordered and assembled. The top PCB and the bottom PCB were connected several times in different combinations of the board copies. In any of these configurations, all LEDs were working, proving that each of the 40 individual pins powering the LEDs was connected properly.

9.1.2. Fast Signal Transmission Measurements

The transmission of fast signals through the interposer is tested in several ways: First, a Bit Error Rate Test (BERT) is conducted for several months with the four differential pairs that start and end at the HSMC connector. Figure 9.4 shows the corresponding test setup with the bottom test board connected to an FPGA evaluation board. Second, the signal of the two differential pairs going through the interposer to an SMA plug is analyzed with an oscilloscope and compared with the reference signal being transmitted directly from the FPGA to an SMA connector on the bottom board. In addition, a time domain reflectometry analysis was done in order to investigate the differential impedances of the boards and the connectors.

	A	B	C	D	E	F	G	H	J	K
1	G1	DP1_in	GND	DP1_out	VCC	VCC	VCC	DP4_out	VDD4	G4
2	GND	DP1_in	GND	DP1_out	VDD1	VCC	VCC	DP4_out	VDD5	G5
3	GND	GND	G2	VDD14	DP6_in	VDD2	VDD3	VDD6	VCC	VCC
4	GND	DP2_in	G3	VDD15	DP6_in	VDD17	VDD7	VCC	VCC	VCC
5	G15	DP2_in	G14	DP3_in	VDD16	DP6_out_sma	VDD8	DP4_in	G6	G7
6	VCC	VCC	G16	DP3_in	DP3_out	DP6_out_sma	VDD9	DP4_in	G9	G8
7	VCC	DP2_out	G17	VDD18	DP3_out	VDD20	VDD12	VDD10	VCC	VCC
8	VCC	DP2_out	GND	VDD19	G20	VDD13	G13	GND	VCC	VCC
9	G18	GND	GND	DP5_out_sma	GND	DP5_in	GND	GND	VDD11	G10
10	G19	GND	GND	DP5_out_sma	GND	DP5_in	GND	GND	G12	G11

Figure 9.3.: *Interposer array pin-out in the test setup. VCC, GND = pins for power tests, DP1 ... DP6 = differential pairs, VDD1 ... VDD20, G1 ... G20 = pins for LEDs. More information about the pin functionalities is given in the text.*

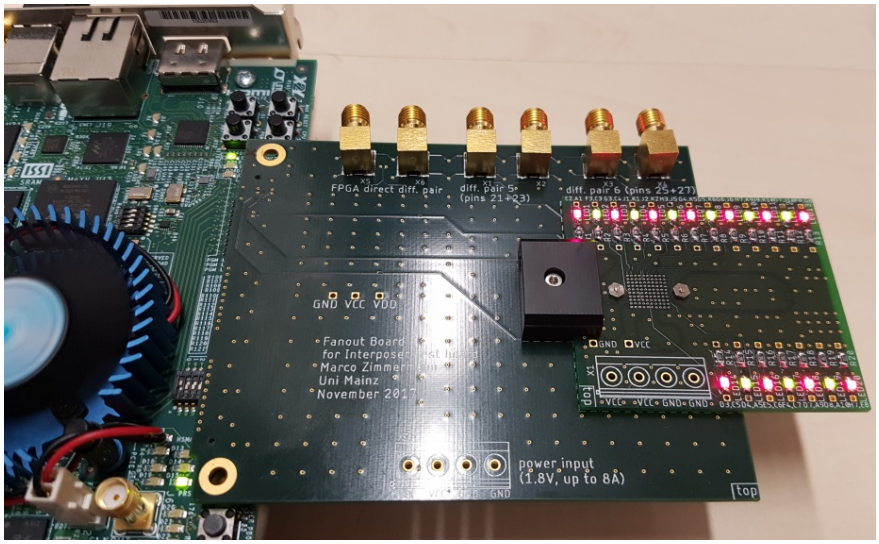

Figure 9.4.: *Test setup for bit error rate tests with the interposer. The black plastic block was mounted as a part of mechanical tests.*

The bit error rate test was conducted by transmitting the pseudo-random binary sequence PRBS31 [170]. Four differential signal channels were tested in parallel. For each of the four channels, 3.16×10^{16} bits were transferred at a bit rate of 2.5 Gbit s^{-1}. No bit error was observed. Consequently, the interposer in conjunction with the board design is proven to be very reliable in the transmission of signals being even faster than the required speed of 1.25 Gbit s^{-1}. In addition, no dependence on the position of the transmitting pin pair on the interposer array could be identified.

As an additional test, the differential signal was analyzed with an oscilloscope at a sampling rate of 25 GS s^{-1}. The signal quality can be assessed by investigating the eye diagram of the signal. This diagram is obtained by superimposing several measurements of the signal at different times. A digital oscilloscope with a storage unit was used to automatize this recording. Figure 9.5 shows an eye diagram for one of the two differential pairs that are routed to an SMA plug after traversing the bottom board, the top board and twice the interposer. In addition, the channel connecting the SMA connector on the bottom board directly to the FPGA output is considered as a reference signal. The eye diagrams show that the average width and height of the signal being transmitted to both boards and the interposer are slightly reduced compared to the direct transmission through the bottom board. In addition, both rise and fall time are increased on average. Nevertheless, the signal quality is definitely adequate for a transmission rate up to 1.25 Gbit s^{-1}. In any case, it has to be taken into account that this test includes the signal transmission through the test boards. The differences in the eye diagrams can thus have other reasons than the interposer. The fact that the observed signal quality is sufficient however shows that the interposer

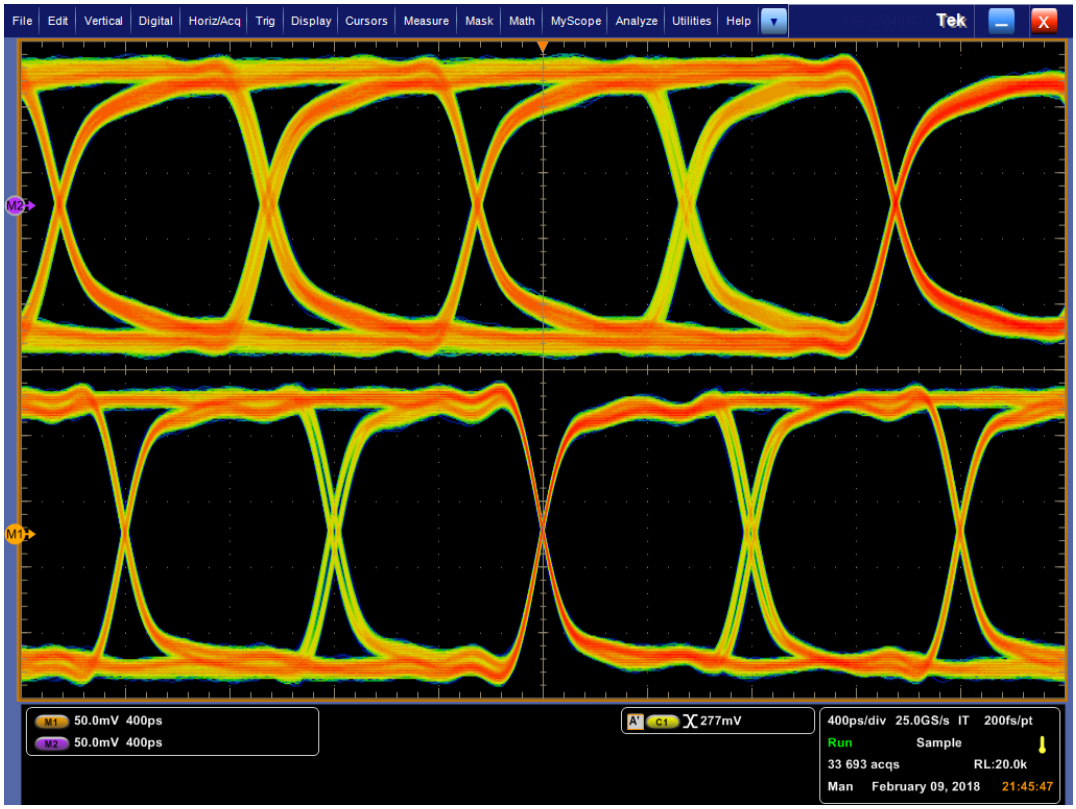

Figure 9.5.: *Eye diagrams for signals transmitted through the interposer test boards. The signal at the bottom is the reference signal routed on the bottom test board directly from the FPGA to the oscilloscope, the signal at the top shows one of the channels directed through the interposer twice.*

is suitable for the transmission of fast signals and can be used in the experiment.

For further insights on the signal transmission through the test board setup, a Time Domain Reflectometry (TDR) measurement was done in Heidelberg. In this measurement, an incident signal is sent from one end of the channel, the other end is left open. The change of impedance in the conductor causes reflections of the signal which are then analyzed. This procedure allows to analyze the impedance depending on the signal propagation delay. Figure 9.6 shows the result of this TDR analysis. The open end shows up as an infinite impedance. The reflections caused by impedance changes allow to allocate the different parts of the signal transmission setup. In particular, the SMA plug causes the largest reflection amplitude. There are also reflections visible for the two passages through the interposer. However, the differential pairs need to be divided for short distances on both boards to be routed between the interposer pads, so that the impedance cannot be controlled in this area. Therefore, the impedance changes are expected.

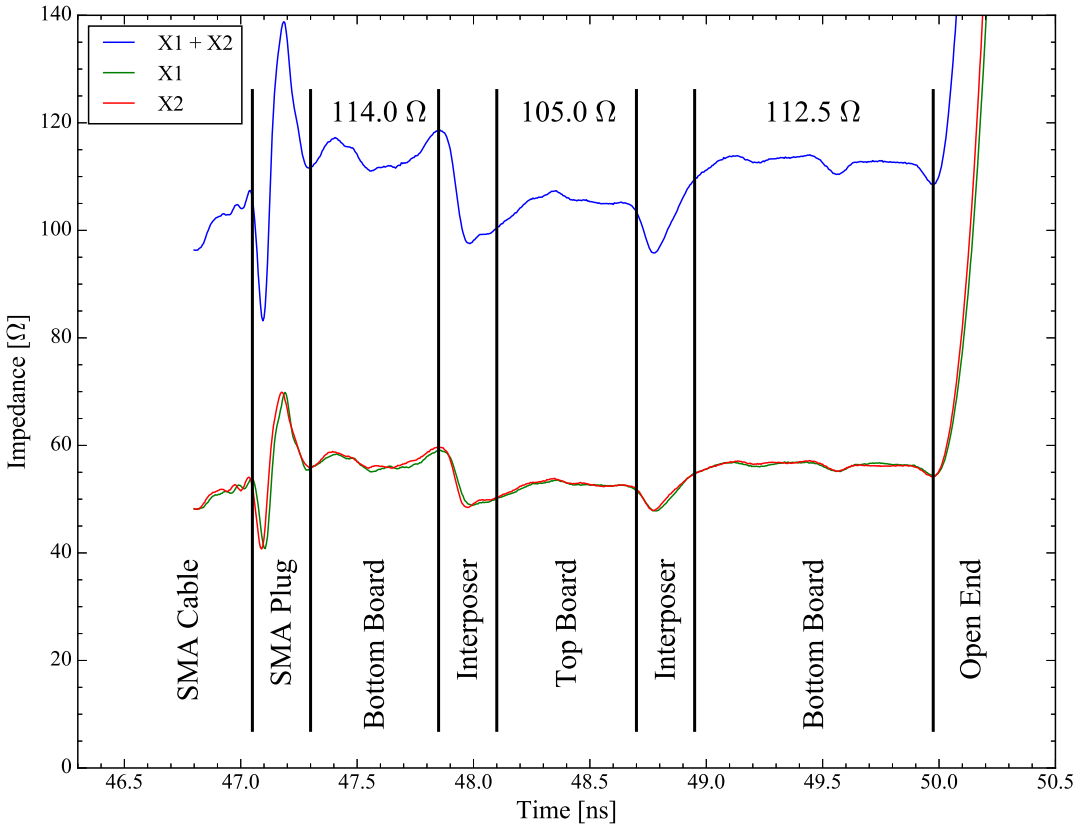

Figure 9.6.: *Time Domain Reflectometry measurement of the interposer test setup. The impedance of the individual traces is shown in green and red, the differential impedance in blue. The ranges of the labeled parts are estimated based on the impedance curve.*

The average impedance is evaluated for the signal transmission on the test boards. The targeted differential impedance of 100 Ω is met on both boards within 15 % precision. On the top board, the impedance was met even better. This result is satisfying as no special layer setup for the test boards was ordered, but the trace widths and distances were adjusted to the given default layer setup provided by the chosen PCB vendor. The impedance calculations for the PCB layout were done with free software from Saturn PCB Design[1]. In further board designs using the same layer setup, the differential pair layout can be adjusted to account for the increased differential impedance observed on the bottom test PCB.

9.1.3. Power Transmission Test

The test boards include another separated electric circuit for power transmission tests. For this test, a CMOS temperature sensor was glued to both the bottom and to the top test PCB on the opposite sides to the interposer. The power test setup is shown in figure 9.7. An active electric load was connected to the top PCB which allows to control the current. The bottom PCB was connected to a voltage source. The nominal voltage was chosen to be 1.8 V, which corresponds to the voltage level at which the HV-MAPS will be powered. A LabJack® device connected to a PC is used to power and readout the temperature sensors and to control the current drawn by the load. In addition, it is used as an ADC to measure the voltage at different points of the circuit so that increasing voltage drops for higher current values can be detected and located immediately.

The power rating of the interposer is tested in two approaches. As a first test, the current is increased iteratively about every 120 s by around 0.5 A up to a maximum value of 14 A. No unexpected behavior was observed in this test, in particular neither the test boards nor any parts assembled on it failed. The voltage drop on the interposer and the two test boards was recorded and is plotted against the current in figure 9.8a. It increases linearly, which proves that everything behaves as an ohmic resistance. After this test, the test setup was operated for about an hour at high current to investigate the temperature behavior. Figure 9.8b shows the result of such tests with 10 A and 14 A current. It can be seen that the test PCBs are heated up and then reach a plateau of constant temperature below 40 °C. No active cooling is applied, but both boards feature several ground and power planes connected to the interposer that transfer the heat away effectively. The slightly oscillating temperature curve is attributable to varying ambient cooling since the setup is not placed in an isolated system.

[1]Saturn PCB Design Toolkit Version 7.03, `http://www.saturnpcb.com/pcb_toolkit/`.

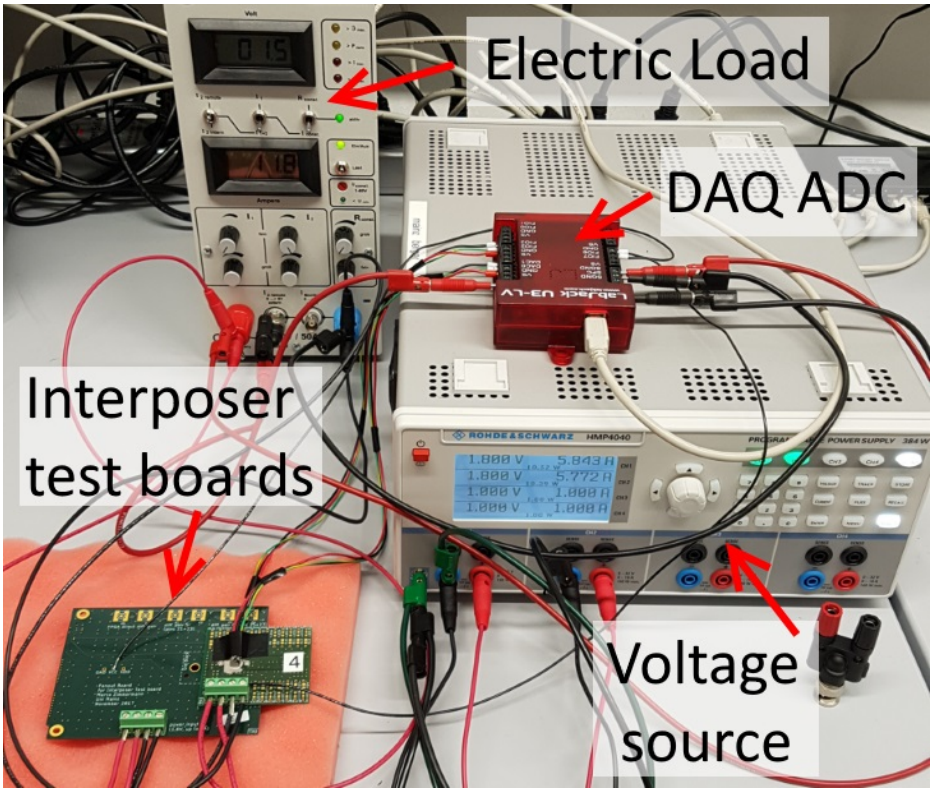

Figure 9.7.: *Power Transmission Test Setup.*

The maximum current of 14 A corresponds to a power transmission of about 0.8 A per pin, which is only slightly below the power rating of 0.9 A per pin given by the manufacturer. However, the Samtec® power rating was limited to 10 pins in one row. The power tests shown here prove that connecting more pins to increase the absolute power transmission is possible. The tested current of 14 A is well above the maximum current estimated for the tracking detector modules in the P2 experiment of about 8 A.

As a conclusion of both the power transmission and the fast signal transmission tests presented in this section, the interposer is shown to fulfill all requirements of the P2 tracking detector. The test setup has also shown that the mechanical fixture of the top PCB to the bottom PCB with two of the Samtec® ZSO® connectors placed next to the interposer is satisfying and allows comparably easy and reliable assembly and disassembly. The same holds true for the mounting of the plastic end block foreseen for the strip modules (see the technical design presented in chapter 7) via a press fit nut assembled on the bottom PCB, which was tested additionally as a part of this interposer test setup, see figure 9.4.

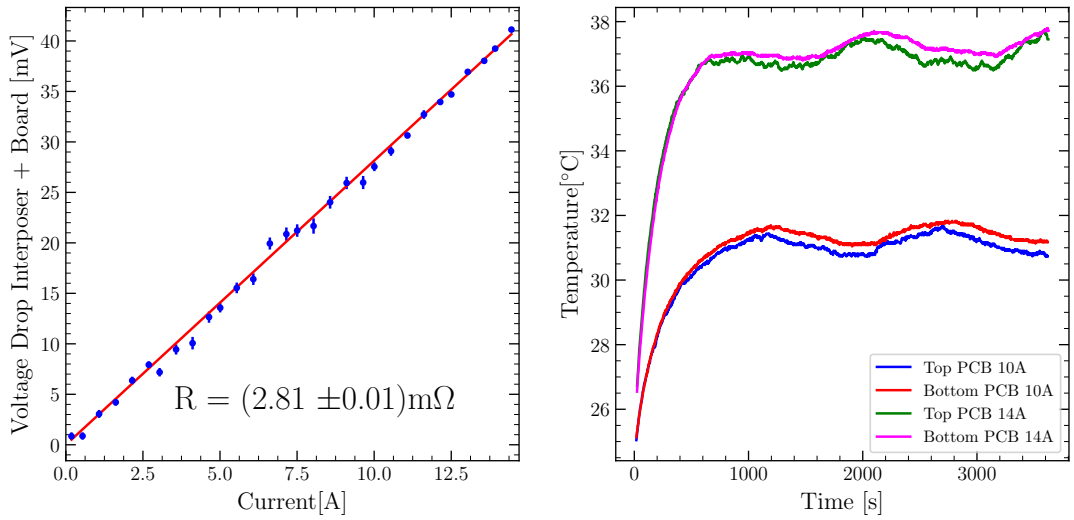

(a) *Voltage drop against applied current.*

(b) *Temperature curves of long-term power tests.*

Figure 9.8.: *Interposer power transmission tests*

9.2. Design and Fabrication of Heatable Strip Modules

Heatable strip modules are developed in order to simulate the power dissipation and cooling of the pixel sensors in a thermo-mechanical prototype detector model which does not contain actual HV-MAPS. The design of all components for this prototype detector is intended to be as close as possible to the aspired detector design for the final experiment. For the experiment, the pixel sensors will be glued and bonded to the polyimide flexprints as described in section 7.3.

For the prototype detector, the sensors must be replaced by a different heating device. The easiest way to heat a polyimide strip is to cover it with one long trace of a thin conducting wire and to transmit current through it. There are several commercial heating foils sold which are based on this technology. However, a given geometry of the heatable strips is required for the tracker prototype project. It is thus necessary to either develop a technology to produce such kind of heatable strips by oneself or to use a technology that allows to order a tailored strip geometry for an affordable price. For cooling studies of the Mu3e pixel detector, heatable strips based on polyimide foil metallized with aluminum were developed. The conductor traces can be defined with a laser which allows to implement basically any trace layout. However, it is very difficult to solder or to use electrically conducting glue on aluminum as it is always covered by an oxide layer. Attaching and connecting an end PCB electri-

(a) *Flex-PCB design*

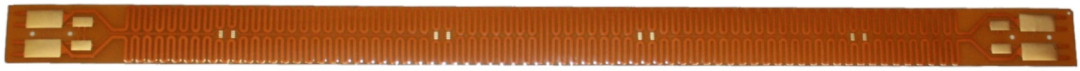

(b) *Picture of a flexprint copy*

Figure 9.9.: *Flexprint heatable strip. The dimensions are* 360 mm × 19.90 mm.

cally to these kind of strips is therefore rather difficult. In order to construct strip modules close to the technical design of the P2 tracking detector, it was decided to use a different technology that facilitates attaching the end PCBs to the strips. Flexprint PCBs in any custom layout with copper as conductor and solderable contact pads can be ordered at various PCB vendors. This commercial technology allows fully customizable designs for a comparably low price. In addition, it enables the possibility to attach temperature sensors on the heated strips for quantitative cooling studies. Otherwise, the temperature can also be determined with heat cameras or by evaluating the change in resistivity of the copper traces for an estimate on the average temperature.

Figure 9.9 shows the electrical flexprint layout, which is a single layer design, and a picture of one manufactured copy. The electrical design of the flexprint is divided in the middle of the strip. The connecting pads for powering the strip halves and for the temperature readout are implemented at the strip ends. This layout is motivated by the layout in the final detector where also half of the chips are powered and read out from the corresponding strip end and the connected frame PCB. The width of the copper power trace is chosen to be 1 mm. A lower width would make it possible to cover more area of the flexprint with copper and by that also increases the resistance. However, it would also increase the chance of damage when operating the flexprint with current values of a few ampere. The copper layer has a thickness of 18 µm. The resistance of the fabricated strips was measured to be $(1.6 \pm 0.1)\,\Omega$ at room temperature.

Four temperature sensors are mounted on each heatable flexprint. The chosen Maxim® DS18B20 temperature sensors can be operated with only two traces connected. They are powered and read out through one data line and need a second trace for the reference ground. This "parasitic" operation mode requires to wait for some time between two temperature readouts. The maximum achievable readout rate depends on the requested precision. For 12 bit precision, about 800 ms must be observed, for 10 bit this delay time can be reduced to about 200 ms. As the measured temperatures in the prototype detector setup are dominated by other systematic effects, a readout precision

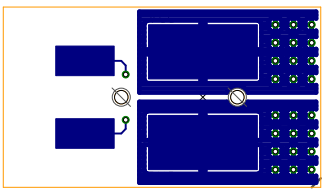

(a) *PCB layout top layer*

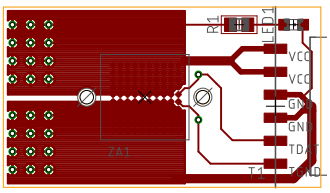

(b) *PCB layout bottom layer*

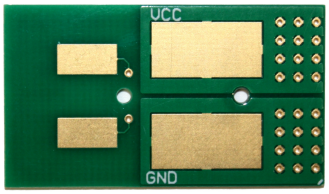

(c) *Picture an end PCB copy, top side*

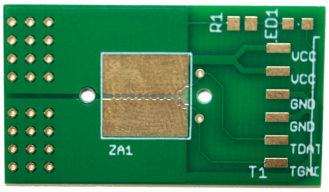

(d) *Picture an end PCB copy, bottom side*

Figure 9.10.: *End PCB for the heatable strip prototypes. The dimensions are* 35 mm × 19.90 mm.

of 0.25 K is sufficient. The final design of the heatable flexprints was decided after testing with a temporary wiring on a breadboard that 36 temperature sensors can be powered and read out through one data line.

Four pads are implemented at each end of the strips. Two larger pads are for power and ground of the heating circuit, the two smaller pads are for the two traces to the temperature sensors. Rigid end PCBs are attached to the strips in order to establish the connection to the samtec interposer. The design is shown in figure 9.10.

The end PCBs come in two variants differing solely in their thickness of 0.8 mm and 1.55 mm, respectively. In the technical design of the P2 tracker modules, the two thickness variants of the end PCBs are implemented for a partial overlap of the pixel sensors that eliminates inactive sensor areas. Although no sensors are mounted on the strip prototypes discussed here, the two different thicknesses are implemented to imitate the final design. The end PCBs are fixed to the flexprint strips with electrically conducting glue applied to the four mating contact pads. As there are only four signals, the pads are dimensioned such that each pad dimension is at least a few millimeter so that gluing is sufficiently reliable. Consequently, no sophisticated bonding technology is needed for the prototypes. As another alternative, one could also order the complete module of flexible heat strip and rigid end PCB as one flex-rigid PCB, but this option would increase the costs significantly, especially because of the two thickness variants of the rigid PCBs.

The end PCBs are designed to be connected to the 10×10 single compression variant of the Samtec® interposer as it was discussed in the previous section. 49 contacts are

Figure 9.11.: *Heatable flexprint with rigid PCBs and temperature sensors attached to it.*

used both for power and ground, one contact pin is used for the temperature data line and one for the corresponding digital ground. On the bottom side, additional pads are foreseen for an LED with pre-resistor that turns on if the heat strip is operated at a voltage above 2 V. It is also possible to solder a plug strip as a Surface Mount Device (SMD) on the end PCB for initial tests without the interposer.

The temperature sensors are soldered to the flexprints manually and some thermal grease is added to improve the thermal connection. The readout of the sensors is controlled with an Arduino® microcontroller. Each of the temperature sensors has a unique 64 bit address for communication. The addresses of all four temperature sensors are detected once with a dedicated Arduino® firmware. Each fabricated strip copy is numbered and the strip designator is logged to a file together with the addresses of the corresponding temperature sensors. Figure 9.11 shows a picture of the heatable flex with mounted end PCBs and temperature sensors.

9.2.1. Calibration Measurements

The digital temperature sensors Maxim® DS18B20 measure temperatures from −55 °C to 125 °C; in the range −10 °C to 85 °C the accuracy is 0.5 K [171]. A calibration measurement of the temperature sensors is done in order to test for possible systematic deviations. However, the temperature sensors in the chosen µSOP package are not water proof so that a calibration in a liquid with controlled temperature is not possible. The calibration measurement is thus conducted inside a climate chamber that represents a closed system with controlled ambient temperature. It is also possible to control the humidity but this feature is not required for this measurement. For this calibration measurement, two heatable flexprints with end PCBs attached were mounted on some first small prototype detector model that will be presented in section 9.3.1. This detector model with two strips and thus eight temperature sensors was placed on a grid at half height within the climate chamber.

The temperature in the climate chamber is varied between 5 °C to 80 °C in steps of 5 K. The climate chamber would allow to test for a wider range and also negative temperatures, but the measurement was restricted to the temperatures expected in upcoming cooling studies. After applying a new temperature setting to the climate chamber, it takes a few minutes until a constant temperature is achieved in the complete chamber volume. There are temperature sensors installed at different places in the climate

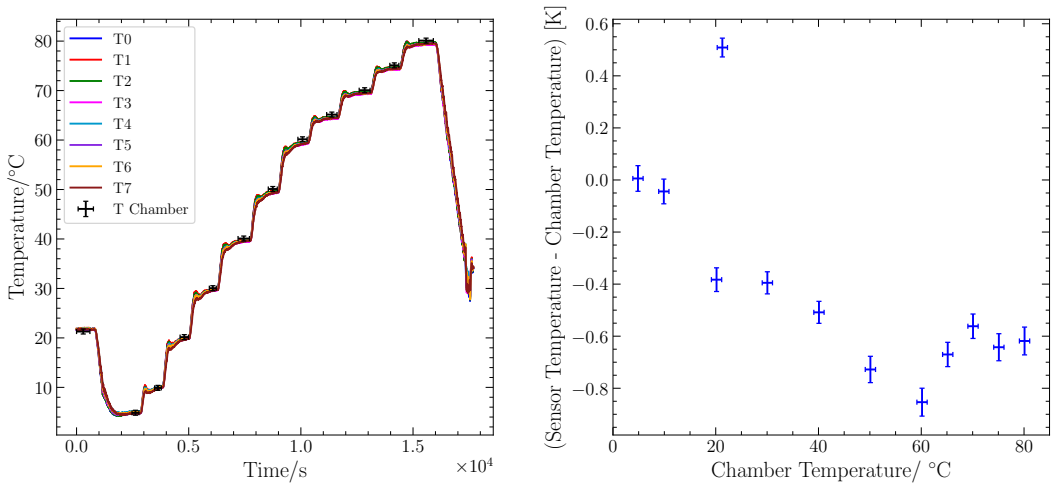

(a) *Sensor temperatures evaluated for the complete measuring time*

(b) *Difference between chamber temperature and the average temperature of the tested temperature sensors on the flexprint*

Figure 9.12.: *Climate chamber measurement for the calibration of the temperature sensors.*

chamber for monitoring. In addition, the air within the chamber is circulated. The error on the measured chamber temperatures is thus estimated to be 1 K.

The temperatures recorded in the calibration measurement are plotted in figure 9.12a against the measurement time. The black data points represent the temperatures measured with the climate chamber sensors. The horizontal errors on these data points represent the time slots in which the temperature was constant. The measurement was started at room temperature, then the temperature was decreased to the lowest measurement temperature of 5 °C and afterwards increased for each new measurement point. It can be seen that the temperature sensors on the flexprint reflect the chamber temperatures quite precisely. The temperature comparison is further advanced in figure 9.12b. In this plot, the temperatures of the sensors on the flexprint are first averaged in time and then the average of the eight temperature sensors is evaluated. These averaged temperatures are then compared to the measured chamber temperature. The vertical error bars give the statistical error on the mean value; the uncertainty on the chamber temperature is only represented in the horizontal error bars. The differences between the temperatures measured by the climate chamber and the tested temperature sensors on the flexprint are below 1 K for all measurement points. The deviations are therefore covered by the discussed systematic effects of the measurement. Consequently, the temperature values obtained by the Maxim® DS18B20 temperature sensors do not need to be corrected.

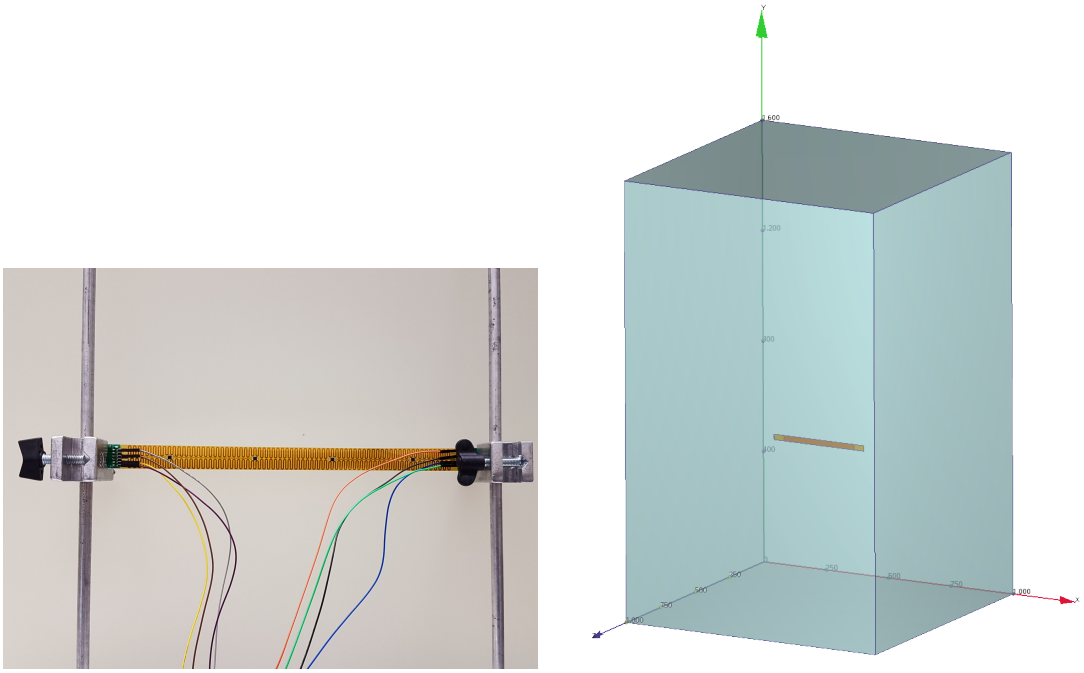

(a) *Heatable flexprint test setup in the laboratory* (b) *CFD simulation setup*

Figure 9.13.: *Experimental test and CFD simulation of single heatable polyimide strip*

As an initial cooling test, the temperature of one single heated flexprint strip being cooled by the ambient air is considered. A CFD simulation of this setup is conducted for comparison. Figure 9.13 shows both the experimental setup and the model used for the CFD simulation. In the laboratory experiment, the heat strip is fixed on two support rods and by that hanging horizontally in the surrounding air. The interposer is not used for this test. The connections for heating and for the temperature readout are realized with cables plugged to the end PCBs. In the CFD simulation model, the heat strip is enclosed in an air volume with dimensions 1 m × 1 m × 1.6 m, where gravity points along the long edge. The heating copper trace is replaced by a continuous copper foil of 18 µm thickness and 28 cm × 2 cm area. The dimensions of the polyimide strip in the CFD simulation are 36 cm × 2 cm and hence correspond to the geometry of the actual flexprints. The average copper temperature is evaluated in the CFD simulation for heat production values between 2 W to 12 W in steps of 2 W.

In the laboratory setup, the heating power is controlled by the applied voltage. Voltages up to 3.3 V are tested. The corresponding heat production is calculated by multiplying the voltage with the current evaluated by the power supply, so that no assumption on the resistance is made. The observed resistance can be used to analyze

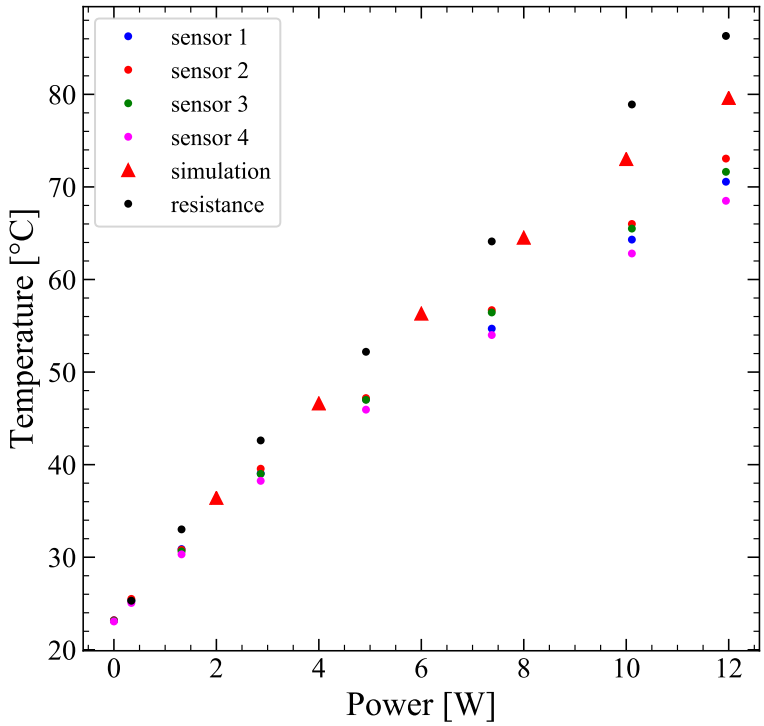

Figure 9.14.: *Temperature results for test of heatable flexprint*

the average temperature of the strip halves because the copper resistivity changes with temperature. A reference resistivity is measured at room temperature with a low applied voltage of 50 mV. The temperatures observed with different methods in the experiment and in the CFD simulation are compared in figure 9.14. The temperature sensors on the heatable flexprint are numbered from the left to the right.

The comparison of temperatures shows that considerable differences occur for large heat production values. First of all, there are differences between the four sensors on the flexprint of a few °C. In particular, the inner sensors usually show higher temperatures than the outer ones. This difference can be explained by the fact that the flexprint is fixed at its ends to support rods so that heat might be transferred away there. Much larger differences can be observed in the comparison of the sensor temperatures to the simulation results and also to the temperatures evaluated with the copper resistivity. Two effects might explain that the sensor temperatures are lower. First, the flexprint design (see figure 9.9a) is such that the heated copper trace is routed around the temperature sensors. The heat thus needs to be transferred to the sensors through the polyimide which features a low heat conductivity. As a consequence, the actual copper temperature might be higher than the measured tem-

perature. The second effect that has to be considered are possible air circulations in the laboratory. In the simulation, the air volume is perfectly separated from the environment, which is not the case for the experimental setup. In order to account for this effect, the sensor temperatures in figure 9.14 are the maximum values observed in time. However, this effect can not explain the discrepancy between the temperatures measured by the sensors and the temperature based on the copper resistivity. In addition, no good explanation is found why these temperatures even exceed the simulation results. In any case, the CFD simulation comes with a systematic uncertainty that might explain discrepancies up to a few degrees.

In order to further examine the temperature measured by the sensors attached to the flexprint, the heated flexprint is further analyzed with an infrared camera system. The flexprint was examined from the back side because no parts are mounted there, so that the emissivity is expected constant over the complete area. The polyimide emissivity has to be set in order to define an absolute temperature scale. It was estimated to $\epsilon = 0.9$ by forcing the heat camera temperature at the center position of one temperature sensor to match the temperature measured by this sensor. The emissivity value however primarily influences the absolute temperature scale while this measurement focuses on the evaluation of temperature differences along the heatable flexprint. Figure 9.15 shows the temperature distribution on the heated flexprint around a temperature sensor for two different voltages.

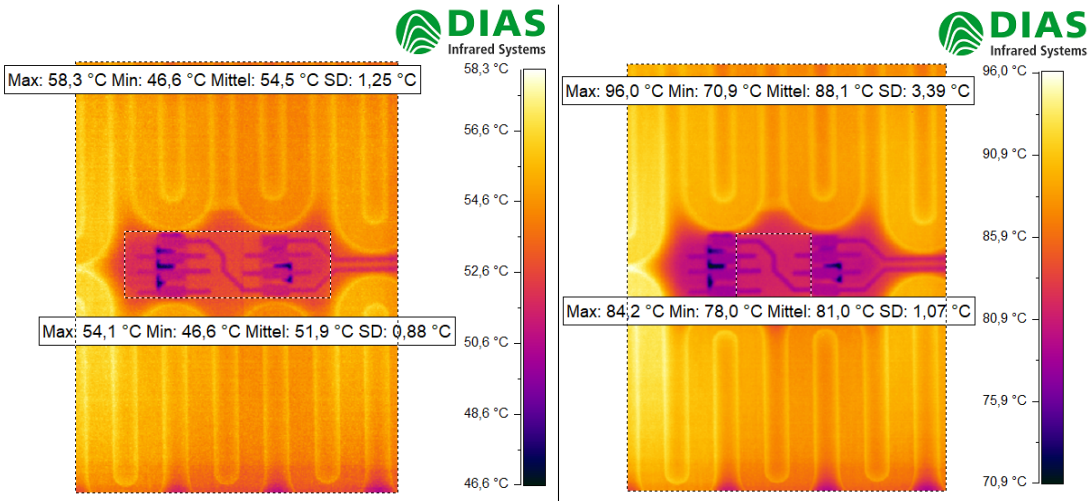

(a) 2.5 V *voltage applied* (b) 3.5 V *voltage applied*

Figure 9.15.: *Infrared camera measurement of the heated flexprint around a temperature sensor. Two pictures taken with different voltage applied to the flexprint are shown.*

The temperature at the position of the temperature sensors is considerably reduced compared to the temperature of the copper trace used for heating. The pads and the

traces connected to the temperature sensor are clearly visible. The labels in the pictures show the maximum, average and minimum temperatures within the rectangles drawn. As a consequence, this effect needs to be taken account of when interpreting the temperature results of future cooling studies. However, the systematic underestimation of the copper temperature by the temperature sensors can be estimated and corrected. For more precise results, it will be beneficial to again examine temperature gradients on the flexprints with an infrared camera.

9.2.2. Fabrication of Polyimide v-Folds

In order to use the heatable strip modules in a prototype detector that can be used for cooling studies, the v-folds as cooling gas channels need to be implemented. Tools for fabricating many pieces of such v-folds with high precision for the final production of the Mu3e detector have been developed in Heidelberg and Oxford. It is planned to use 25 µm thin polyimide foil. However, the fabrication procedure is still being optimized and improved, so that it might be adopted for the P2 experiment once the final solution is established. In addition, the cross section of the v-folds produced for the Mu3e experiment does not match the current layout in the P2 technical design. For the prototype detector, the precision of the v-folds anyhow does not need to be very good. It was therefore decided that they can be produced manually for this purpose.

The manual fabrication procedure for the v-folds is realized in the following way. First, the polyimide foil is cut to strips of the appropriate dimensions and the later kink positions are scratched with a scalpel. It was tested that 75 µm thick polyimide foil is suited best for this procedure. The polyimide strip is then manually folded at the marked positions along the strip. For fixing the v-folds to the heatable flexprints, the adhesive transfer tape 3M® 467MP is used which consists of a 50 µm thick adhesive. It is covered by transport foil on both sides, but after application only the adhesive layer is left. The adhesive is first cut to 2 mm and 4 mm thick strips and then applied to the contact surfaces between the v-folds and the flexprints. The v-folds are placed on the opposite side to the temperature sensors and the end PCBs. A picture of a completely assembled prototype strip module can be seen in figure 9.16. Due to the manual fabrication, the cross section and shape of the v-folds is not perfectly uniform along the strip. However, the most important criteria are to ensure that gaseous helium or air can pass the cooling channels and that no considerable amount of cooling gas is lost.

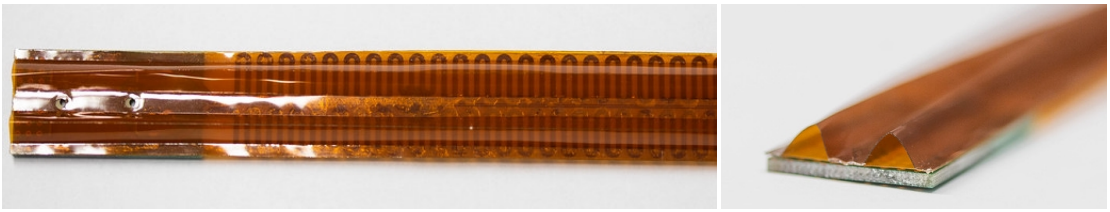

Figure 9.16.: *Heatable strip prototype with v-folds.*

9.3. Thermo-Mechanical Tracker Module Prototype

The realization of the thermo-mechanical tracker module prototype follows the technical design of the tracker modules planned for the experiment. The strips with HV-MAPS are replaced with the prototype strips discussed. The missing HV-MAPS facilitate the design of the electronics since any parts for the sensor readout are omitted. The challenges for powering the strips are similar for the prototype and in the experiment because in both cases considerable power is needed at low voltages. The prototype detector however does not require radiation hardness or operation in a magnetic field. The development of the prototype can be divided into the realization of mechanics based on the detector technical design on the one hand and of the electric design which is specially developed for the prototype on the other hand. The mechanical design is first tested with a small prototype that includes two strips mounted on PCBs and is further described.

9.3.1. First Prototype with Two Strips

First experience regarding the mechanical strip-frame connection was already gained during the investigation of the Samtec® interposer. As another step towards a prototype of the full tracker module, a small prototype is built that makes it possible to fix two strip module prototypes to PCBs at both ends. This prototype allows to test the transmission of cooling gas to the v-folds and enables first cooling tests with forced convection. In addition, the prototype includes the connection mechanism that was developed to account for the thermal expansion of the polyimide strips. The connecting MakerBeamXL® aluminum profiles are loaded on springs so that the polyimide strips are mounted under slight stretching tension. A rendering of this mechanism is visualized in figure 7.8.

The four PCBs installed on this prototype are identical copies. The interposer and some terminal blocks are the only mounted parts. The electric functionality of these PCBs is limited to the transmission of signals. The PCB layout and the schematic are

shown in the appendix (see figure A.3). Pictures of the prototype are shown in figure 9.17. The pull-up circuitry which is needed for the temperature sensor control is wired externally on a breadboard. The two strips are powered directly by an external voltage source.

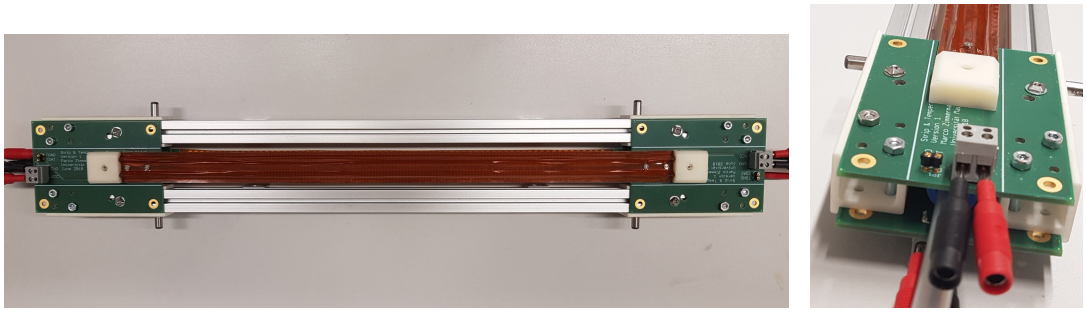

(a) *Top view* (b) *Side view*

Figure 9.17.: *Prototype with two heatable strips with v-folds. One strip is hidden in the pictures as it is mounted from the bottom side.*

An adapter part is placed between the two PCBs on one side of the prototype in order to connect a gas pipe. This pipe is connected to a rotameter with a valve in order to control and measure the gas flow. For first cooling tests, the gas pipe is connected to the pressurized air outlet in the laboratory. The cooling studies with this prototype were conducted as part of a bachelor thesis and are presented in detail in Ref. [172]. The total air flow provided to the prototype detector was varied up to $0.27\,\mathrm{L\,s^{-1}}$ within these studies and compared to CFD simulations. The agreement between simulation and experiment was found to be acceptable. Figure 9.18 shows an exemplary result for $0.17\,\mathrm{L\,s^{-1}}$ air volume flow and 8 W heating power per strip. The data points represent the temperatures measured with the four temperature sensors mounted on each of the two strips. In an additional measurement presented in Ref. [172], the expansion of the polyimide strips with temperature was investigated. The measured thermal expansion coefficient is in agreement with the expected literature value for polyimide. The setup is therefore shown to allow for thermal expansion of the polyimide strips and at the same time provides the necessary mechanical support.

9.3.2. Electrical design for the Frame PCBs

In order to scale the small prototype to a larger model, a more sophisticated PCB design is necessary. The tracker module prototype is dimensioned such that each plane contains 18 strips. This size is considerably smaller than the tracker modules foreseen

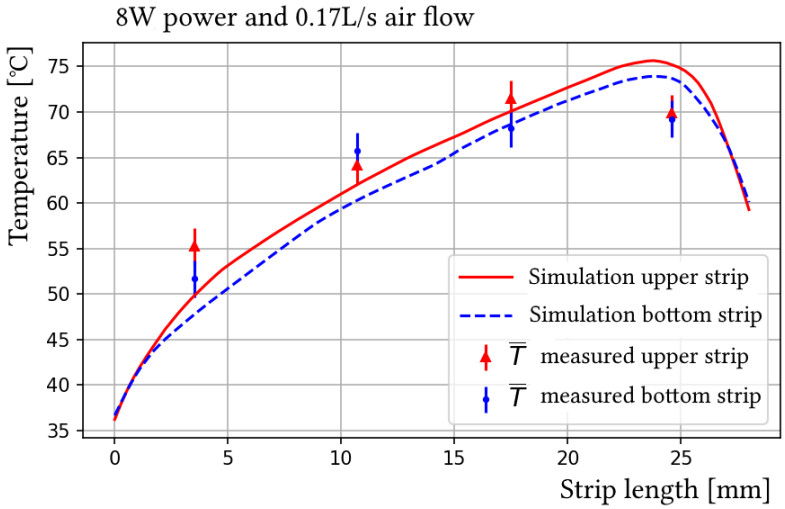

Figure 9.18.: *Result for cooling test with two heated strips. The plot shows the measured and simulated temperature on the polyimide strip depending on the position along the strip. Figure modified from Ref. [172].*

for the experiment with 29 strips per sensor plane, but it is sufficient for meaningful tests of the tracker mechanics and the cooling concept. A heating power of 14 W per strip is required to enable tests of realistic heating scenarios. As mentioned before, the strips are electrically divided into their two halves, each half features a heating circuit with about 1.6 Ω resistance. Consequently, the desired heating power per strip corresponds to a current of about 4 A. The total current necessary to heat all strips with maximum power is therefore roughly 150 A. Providing such a current is difficult even with multiple power supplies connected.

As mentioned previously, the same problem occurs for the final experiment. One solution avoiding the transmission of such high currents is using power converters. In this case, an input voltage up to 20 V is applied and then converted to a lower voltage at each strip. This approach is also chosen for the prototype detector. Here, no special care needs to be taken of any magnetic field or radiation. It is therefore possible to chose a switching power module with integrated coil. A switching power module is needed that provides a high efficiency for an input voltage of up to 20 V, an output voltage of up to 4 V and a current of up to 3 A. In addition, a small package size and a low count of external components is desired. The LMZ22005 SIMPLE SWITCHER® power module from Texas Instruments® was found as a suitable choice. It provides efficiencies well above 80 % for most power configurations that are relevant for the developed prototype. Detailed efficiency and power dissipation curves can be found in the datasheet [173]. There are no particular voltage stability requirements for heating the prototype strips as long as the switching converters are operational

and the applied heating power is known to about 5 %. The amount of voltage stabilizing capacities is therefore minimized to one capacity of 22 µF on the input side and two on the output side with 220 µF and 47 nF, respectively.

The further electric design of the frame PCBs is developed based on the recommendations and requirements defined in the application notes of the power converter module. The output voltage is regulated via two voltage dividing resistors placed in a feedback loop. However, replacing solder mounted resistors in order to change the output voltage is not practical for the tracker prototype. Instead, digital potentiometers that can be controlled by a microcontroller are used. The chosen Microchip® MCP42010 dual digital potentiometer [174] provides two resistor networks, each with a variable resistance of up to 10 kΩ and 8 bit resolution. The output voltage of two strip halves is therefore controlled with one digital potentiometer device. The potentiometers support the industry standard Serial Peripheral Interface (SPI) and allow daisy-chaining of multiple devices which makes an individual chip select line to each device redundant.

The power converter modules include an enable pin which turns the device on in case that the applied voltage exceeds a threshold value around 1.4 V. A usual approach is to connect this pin to a voltage divider between the input voltage and the ground line so that each power module is turned on as soon as the input voltage exceeds a fixed threshold. For the prototype detector, the heating of individual strips should be controllable with the same microcontroller that controls the potentiometers and manages the temperature sensor readout. This functionality is achieved by inserting a digital switch between the enable pin and the ground line in parallel to the second resistor of the voltage divider. By turning on the switch, the enable pin is pulled to ground and thus the power converter is switched off. If the switch is turned off, the power converter is turned on in case that the input voltage is high enough. The Maxim® DS2413 1-Wire® dual channel addressable switch device [175] is used as it supports the same data protocol as the temperature sensors and so again multiple devices can be controlled via the same data line. In order to exclude any interference, separate data lines are connected to the switches and to the temperature sensors on the strips. Since each switch device includes two channels, one switch device is needed for two power converter modules.

Both the potentiometers and the switches are powered with 5 V. The PCB schematic is designed such that this voltage can be either supplied through the Arduino® microcontroller or by an external voltage source. The design includes a separate digital and analog ground which can be connected at one point with a jumper. It is also possible to mount a small resistance in between instead. The detailed schematic of the circuitry for two strips is shown in the appendix. The design is then basically repeated nine times for all 18 strips, with the constraint that the switches and temperature sensors must be connected in parallel, while the potentiometers must be

daisy-chained. The PCB layout can also be seen in the appendix, see figure A.4. The schematic for the right frame board is identical to the left one, but the PCB design is mirrored. The frame design of the tracker modules requires a flat surface for gluing on the bottom side of the frame PCBs. All parts apart from connectors at the board periphery are consequently surface mount packages. The boards additionally need to be gas tight due to the cooling gas transmission within the frame so that all vias were filled with hardening non-conductive paste and plated over as part of the manufacturing process.

9.3.3. Prototype Assembling

The assembly of the thermo-mechanical tracker module prototype needs to be done in a defined order of several work steps and starts with the fabrication of the various components. The fabrication of the strip modules was already discussed in section 9.2. The frame PCBs were manufactured and assembled at external companies according to the design discussed in the previous section. A picture of an assembled left frame PCB is shown in figure 9.19. In addition, the custom plastic parts included in the technical design are scaled to the size of the prototype and manufactured at the mechanics workshop. Instead of Polyether ether ketone (PEEK), Acrylnitril-Butadien-Styrol (ABS) plastic is used for the prototype. PEEK is preferred for the final detector because of its excellent radiation hardness, but this is not a requirement for the prototype. Here, ABS provides suitable mechanical properties up to at least 80 °C and is much cheaper compared to PEEK. The only part which can not be produced conventionally is the connecting part between the MakerbeamXL® aluminum profiles and the frames. This part is therefore 3D-printed out of Polyamide 12. Figure 9.20 shows pictures of the most important fabricated plastic parts.

The picture of the frame board in figure 9.19 already includes the mounted press fit connectors needed for the fixation of the strip modules. The insertion of these connectors to the boards is done with a knuckle joint press and a custom stamper mounted to it. For this assembling step, a flat bottom surface of the board is required. As a consequence, only surface mount parts could be assembled to the PCB beforehand. The connectors with through hole mounting at the board periphery are therefore soldered manually after the insertion of the press fit connectors. Three press fit connectors are implemented on the frame board for each strip: two Samtec® ZSO® connectors for the interposer and one nut for the fixation of the plastic end block of the strip module. These three connectors are inserted in one stroke and then the board is moved to the position of the next strip. A photo taken during the press fit insertion process is shown in figure 9.21.

After insertion of the press fit connectors and soldering of the through hole components, the assembled frame PCBs are tested for their electric functionality. In partic-

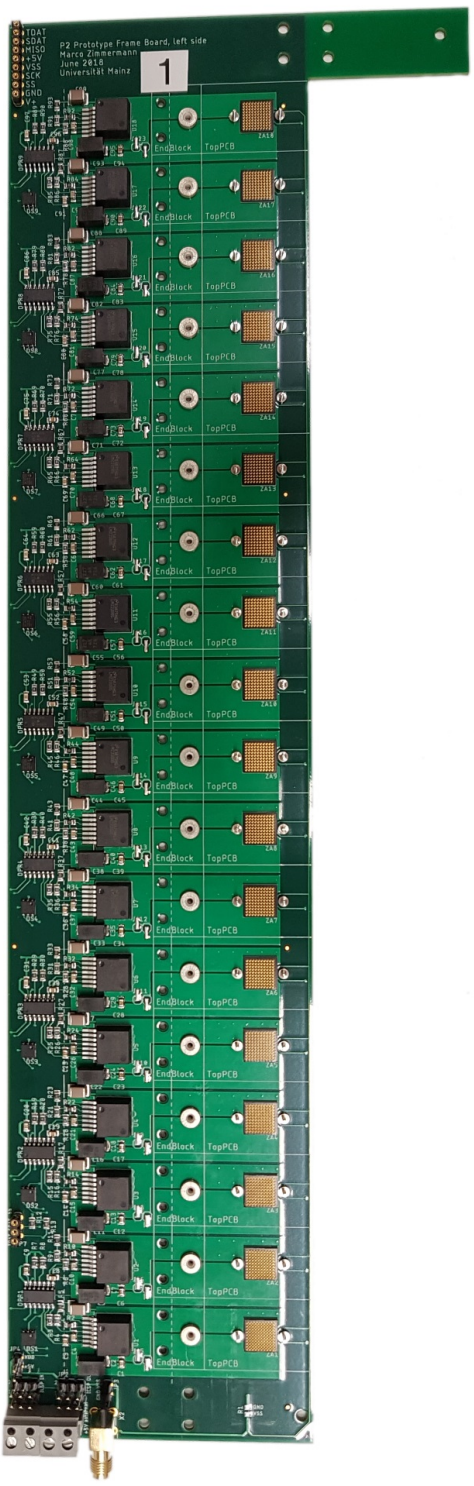

Figure 9.19.: *Assembled frame PCB for the left side of the large prototype with the possibility to mount 18 strip modules. The basic PCB dimensions are* 85 mm×400 mm *with an additional* 50 mm *extension at the top.*

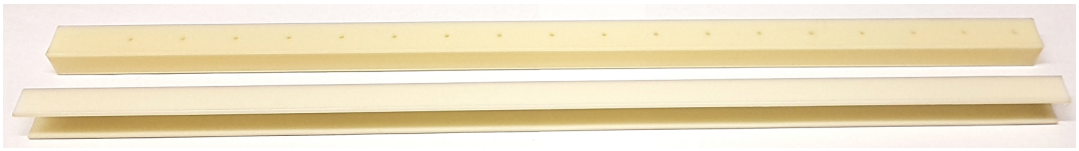

(a) *Gas channel plastic profiles. The profiles are* 380 mm *long, the height is* 15 mm *and the width* 12 mm.

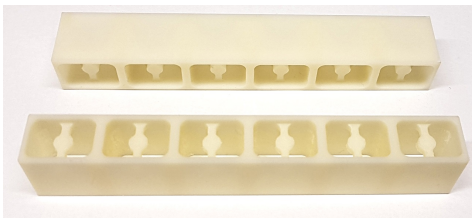

(b) *Diffusor components. Basic dimensions of each part are* 120 mm × 15 mm × 20 mm.

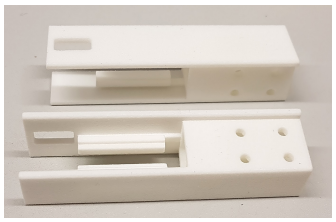

(c) *Connection part for the aluminum profiles (each* 80 mm × 20 mm × 20 mm*)*

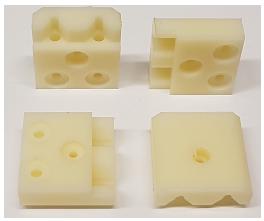

(d) *End block part copies for the strip modules (each* 20 mm × 20 mm × 8 mm*)*

Figure 9.20.: *Plastic parts manufactured for the tracker prototype.*

ular, the interposers are tested to connect the correct signals without any shortcuts. In addition, the communication with the potentiometers and the switches is checked. Several strips are mounted to the completed frame PCBs in order to test the heating and the readout of the temperature sensors. All assembled frame PCBs were found to be operational.

The completed and tested frame PCBs are glued with the plastic profiles to form frame modules. The gluing process was tested beforehand with purely mechanical prototypes. The plastic profiles must be glued to the correct positions and the resulting cooling channels must be sufficiently gas tight. Alignment pins and blocks are used for the positioning. A good control on the glue layer thickness helps to obtain a precise and reproducible connection. The glue is therefore evenly applied to a 200 µm deep notch that was implemented on the surface of the plastic profiles. The electric parts mounted on the PCBs prevent the boards from being put on a table to that side, which is necessary to glue anything on the back side. An adequately shaped aluminum plate was manufactured to circumvent this problem.

The gluing of the frame modules is followed by assembling the necessary parts to connect the two frame modules to a complete tracker module frame. Finally, 18 strips are mounted to both sides of the frame modules. As a result, the construction of the large thermo-mechanical tracker module prototype with 36 heatable strips is ultimately finished and commissioning can start. Figure 9.22 shows the completely assembled prototype.

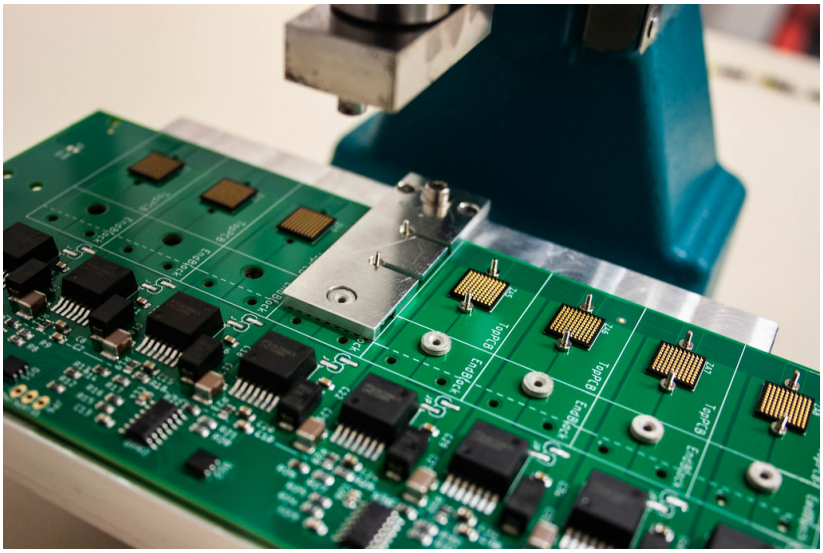

Figure 9.21.: *Insertion of press fit connectors with a knuckle joint press.*

The construction of the prototype detector demonstrates the implementability of the technical design presented in chapter 7. For several assembly steps, the development of dedicated tooling was necessary. Some minor issues were observed during the assembly of the prototype that need to be taken care of. It would be helpful to adjust the setup for the press fit connector insertion such that also through hole mounted parts on the PCB can be assembled beforehand together with the surface mount parts. The design of the strip module end blocks should be slightly adjusted in order to facilitate their removal for the replacement of particular strips. In addition, it was observed that adhering to the specified torque of 4 ozf in for the Samtec® ZSO® connectors is crucial as they shear if higher torque is applied. It is impossible to replace damaged press-fit connectors as they cannot be removed from the PCB.

9.3.4. Temperature Readout and Control of the Heating

The heating and the temperature readout for the prototype module are controlled with one Arduino® Mega microcontroller. The microcontroller is connected to a PC via USB for serial communication on the one side and to the four frame PCBs at the other end. One separate cable connection from the Arduino to each of the four frame PCBs is needed for the following connections: one chip select line for the SPI connection to the potentiometers, one data line to the switches and one data line to the temperature sensors. In addition to these three separate signals to each PCB, the same signal is distributed to all four boards for the Master Out Slave In (MOSI) SPI signal, the SPI clock signal (SCK), the digital ground (VSS) and optionally the 5 V

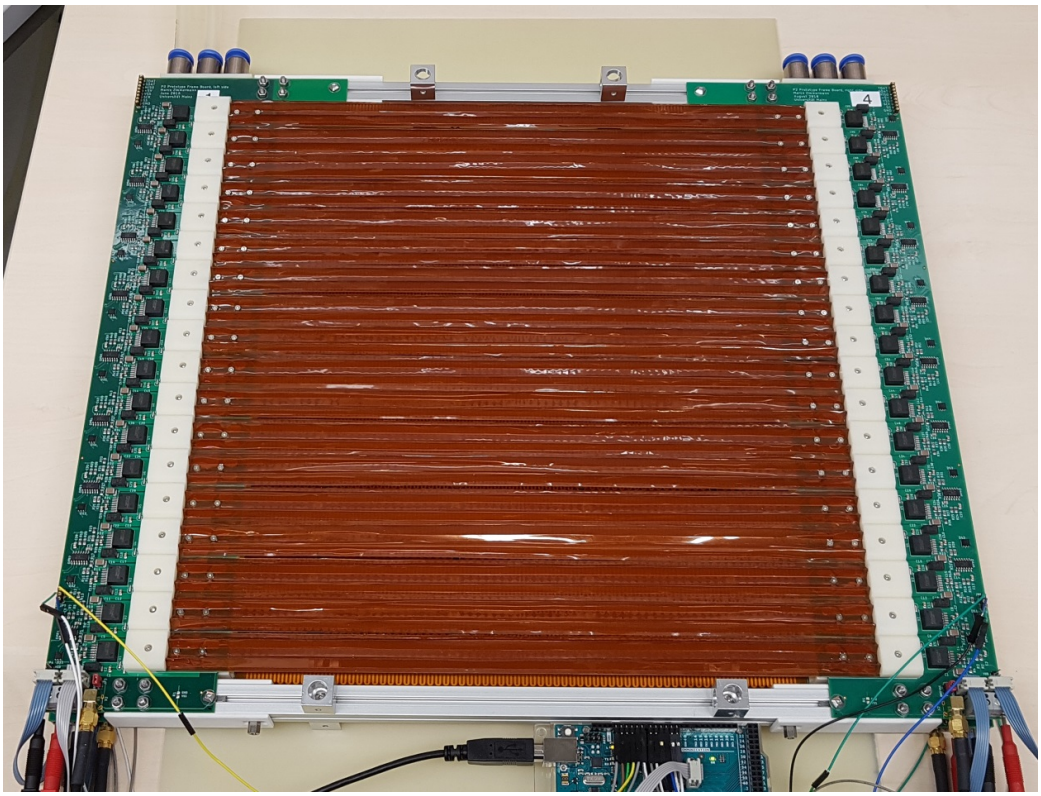

Figure 9.22.: *Assembled large frame prototype, with 36 strips including v-folds mounted. Each strip can be heated individually with adjustable power. The prototype implements the presented technical design and allows to test the discussed cooling concept experimentally. The total dimensions are about* 470 mm × 420 mm × 40*mm.*

supply voltage. Finally, 144 temperature sensors and 72 power converters (through 36 dual channel switches and 36 potentiometers) are controlled by one Arduino with in total only 16 connected signal lines.

An Arduino firmware is written that allows to change settings of the switches and potentiometers and to read the measured temperatures from the sensors. The temperatures can be measured at time intervals ≥ 3 s. One of the limiting factors is the parasitic powering mode of the temperature sensors which requires to wait for a conversion time of 200 ms at the chosen 10 bit precision after sending the temperature conversion request to all the sensors. Afterwards, the temperatures of the sensors are read out consecutively, which takes about 1 s to 2 s. The readout time could be decreased by reading the sensors connected to different PCBs in parallel, but that would require using multiple microcontrollers.

The change of particular switch or potentiometer settings and the temperature readout are initiated by sending correspondingly defined commands from the PC to the Arduino microcontroller. A graphical user interface (GUI) is programmed in Python in order to simplify the communication with the Arduino and the control over the prototype. The measured temperatures are displayed on the GUI and recorded to a text file. The GUI offers the possibility to easily change the state (on or off) and the output voltage of any particular strip half or for all strips at once.

9.3.5. Commissioning

After completion of the tracking detector prototype, the proper operation of the heating and the temperature readout was tested. It was found that all components are working as expected, so that future cooling measurements can be controlled with the implemented data acquisition system. All hole openings for the cooling gas distribution were inspected to ensure that they were not unintentionally covered with glue during the assembling process.

Accomplishing cooling studies will require to install the tracker prototype into a cooling gas supply system. The prototype already includes plugs for cooling pipes. The cooling studies with the small prototype were done directly with the pressurized air supply in the laboratory and a rotameter measuring flows up to $2400\,\mathrm{L\,h^{-1}}$. A larger rotameter for gas flows between $2500\,\mathrm{L\,h^{-1}}$ to $25\,000\,\mathrm{L\,h^{-1}}$ air flow was already purchased, but needs to be integrated into the gas supply system. In addition, it has to be tested whether such large flow volume rates can be provided by the pressurized air supply.

Part IV.

Conclusion

10 Summary and Outlook

This work presents feasibility studies on the silicon pixel tracking detector for the P2 experiment. The first part of the thesis covers background rate studies and radiation load estimates based on Monte Carlo simulations of the experiment. In the second part, the technical implementation of the tracking detector is addressed. These investigations include a technical design layout, simulations of the cooling system and the development of detector prototypes.

The P2 experiment aims to test the Standard Model of particle physics at the low energy intensity frontier by measuring the parity violating asymmetry in elastic electron-proton scattering with very high precision. This precision test of the Standard Model becomes possible at the Mainz Energy-Recovering Superconducting Accelerator which is currently under construction. With an estimated run time of 11 000 h and a projected instantaneous luminosity of about $2.38 \times 10^{39}\,\mathrm{cm^{-2}\,s^{-1}}$, the parity violating asymmetry $A_{\mathrm{PV}} = -39.94 \times 10^{-9}$ can be measured with an absolute accuracy of of 0.57×10^{-9}. The asymmetry determination allows for an extraction of the weak mixing angle $\sin^2\theta_w$ at low momentum transfer $Q^2 = 4.5 \times 10^{-3}\,\mathrm{GeV^2}$ to a relative precision of 0.15 % [13].

A tracking detector is integrated into the P2 detector in order to reconstruct individual electron tracks and to determine the electron momentum transfer Q^2 in the target. The novel technology of High Voltage Monolithic Active Pixel Sensors (HV-MAPS) reduces the material budget to a minimum by integrating the readout chip on the sensor substrate. These sensors feature both very high spatial resolution and good timing resolution. Both features make these sensors a perfect choice for high rate tracking of electrons with momenta at which multiple scattering dominates the resolution of reconstructed track parameters. The assembly of more than 5000 of these silicon sensors without introducing too much material to the detector is a challenging task that was tackled as a part of this work. The area to cover by the tracking

detector has a disc-like geometry with an outer diameter of about 2.4 m. Four tracker planes will be mounted, arranged as two pairs of planes being close to each other at around 20 mm distance and with a wide drift region of around 600 mm in between. The large area however requires to limit the covered area to four slices in azimuthal direction, each with around 15° angular coverage. The azimuthal slices of the tracker plane pairs are arranged as detector modules with identical technical design.

The contributions of background particles complicate the reliable reconstruction of track parameter distributions of electrons collected for the asymmetry measurement. Investigating the feasibility of the track reconstruction thus has to start with an estimation of the major background sources. The analyses presented here are based on Monte Carlo simulations and have shown that bremsstrahlung photons being produced in the target are the most abundant type of background. The geometry of the P2 detector does not allow for a geometric shielding of the tracker modules against these particles. Photoelectric effect and Compton scattering were found to be the most probable photon detection mechanisms for thin silicon sensors. The rate of photons traversing the pixel sensors partially exceeds the signal electron track rate by more than two orders of magnitude. However, the photon detection probability is found to be less than 0.4 %. The sensor technology and in addition the envisaged arrangement of the pixel sensors as plane pairs are therefore very efficient in suppressing the photon background.

The rate of detected photons and thus the photon detection probability are crucial for any track finding or reconstruction studies. The simulation studies were therefore complemented by experimental tests of the pixel sensor response to photons. The photon detection efficiency results obtained in measurements with an iron photon source ($E_{\mathrm{ph}} \approx 6\,\mathrm{keV}$) were compared to the predictions based on simulation and found to be compatible, but both methods are subject to considerable systematic uncertainties. An additional test with photons in the MeV energy range was successfully conducted with the A2 facility at the MAMI accelerator. Although the rate observed on the pixel sensors is dominated by pair creation electrons, an upper limit on the photon detection efficiency has been obtained that is in agreement with the corresponding simulation results.

The presented background rate studies are followed by the ongoing development of sophisticated analyses of track finding and reconstruction. The development of an unbiased momentum transfer reconstruction algorithm is a very difficult task since it is influenced by various phenomena such as multiple scattering in the target, the asymmetric Landau probability density function for the energy loss in the target or track reconstruction inefficiencies that might depend on particular track parameters.

Furthermore, the high signal and background particle rates are one of the main challenges for the tracking system. Due to the electron scattering rate in the target of around 0.1 THz, the total data rate collected on the pixel sensors reaches around

1 Tbit/s and is thus beyond an affordable data acquisition infrastructure. The tracking detector hence needs to be operated at lower beam current or the data taking needs to be restricted to short time slices already on the sensor. The high rates additionally lead to a challenging radiation load. The presented radiation analysis shows that operating the tracking detector during the complete run time with nominal beam current amounts to a radiation load of up to 60 Mrad and 9×10^{13} 1 MeV n_{eq}/cm^2 to the sensors and to any other electronics and materials installed on the tracker modules.

The technical design of the tracker modules presented here fulfills all requirements imposed by the HV-MAPS technology and the P2 experiment. In particular, the material budget is reduced by utilizing Printed Circuit Boards not only for sensor powering and readout, but also as mechanical support. A mechanically robust frame is obtained by mounting two boards in parallel and integrating gas channels in between. The gas channels are formed by plastic profiles and are necessary for the distribution of gaseous helium in order to provide cooling to the pixel sensors. With this design, electronic and mechanical functionality as well as distribution of the cooling gas are achieved with a minimal amount of components. The active detector area is maximized using an overlapping sensor configuration that allows to overcome the inactive digital part of each sensor. The mounting of the pixel sensors on polyimide strips is adopted from the design of the Mu3e experiment, which will also allow to profit from further design developments regarding the electric strip design and the fabrication technology. The presented design of a P2 tracker module additionally takes into account possible thermal expansions of the strips during operation.

After completing the design of the individual tracker modules, their integration to the P2 detector system now has to be worked out. This includes mechanical fixation, piping for the cooling gas distribution and the distribution of cables for readout and powering. In addition, the ongoing progress on the pixel sensor design has to lead on to the implementation of a final sensor which can be operated in the experiment.

The P2 tracking detector modules will be cooled with gaseous helium, which keeps the material budget low and has good cooling properties compared to other gases. The presented cooling studies based on CFD simulations have shown that sufficient cooling of the pixel sensors is possible, but requires considerable helium flow rates of at least 21 L s^{-1} for each module. The cooling studies were further used to optimize the discussed technical design with regard to an efficient distribution of the cooling gas to the pixel sensors. It is crucial to proceed the work on the cooling system with the development of a full design for the global cooling gas loop including all necessary components for the heat exchange.

An important step on the way to an operational detector system are experimental tests of the various detector components. The assembly of a thermo-mechanical prototype has just been completed, demonstrating the practicability of the developed

technical design. In addition, this prototype can be further used for extensive experimental cooling studies which are needed to confirm the results of the presented CFD simulations.

The estimation of relevant background particle rates and the total radiation load, the development of a technical design and the implementation of a prototype detector as well as the proof of concept for the detector cooling are all important cornerstones on the path to an operational tracking detector for the P2 experiment. The achievements presented in this thesis show that the development of the P2 tracking detector is making great progress. The reconstruction of individual electron tracks with the tracking detector to be installed in the P2 detector will allow for a precise momentum transfer determination and so add valuable physics information needed for a successful running of the P2 experiment.

Appendix

A Printed Circuit Board Designs

The PCB designs which were created in the scope of the projects pursued within this thesis are given in the following. The flex PCB for the heatable strips is a 1-layer design which was already presented within the thesis main matter and is therefore omitted here. The same holds for the design of the end PCBs that are mounted twice on each strip; they feature a 2-layer design that was already presented.

A.1. Interposer Test Boards

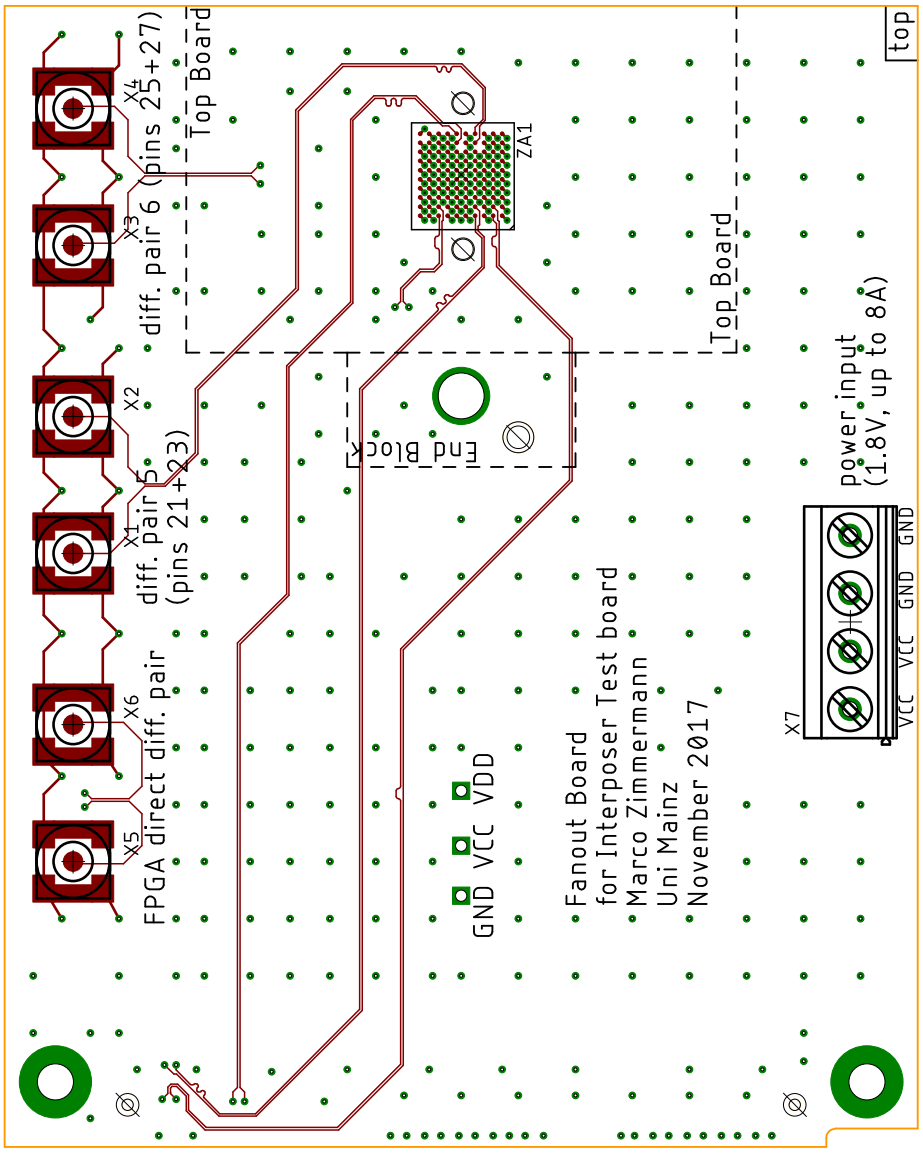

(a) *Layer 1 (top layer), scale 1.5*

Figure A.1.: *Bottom board for Interposer test, PCB design of all layers and schematic.*

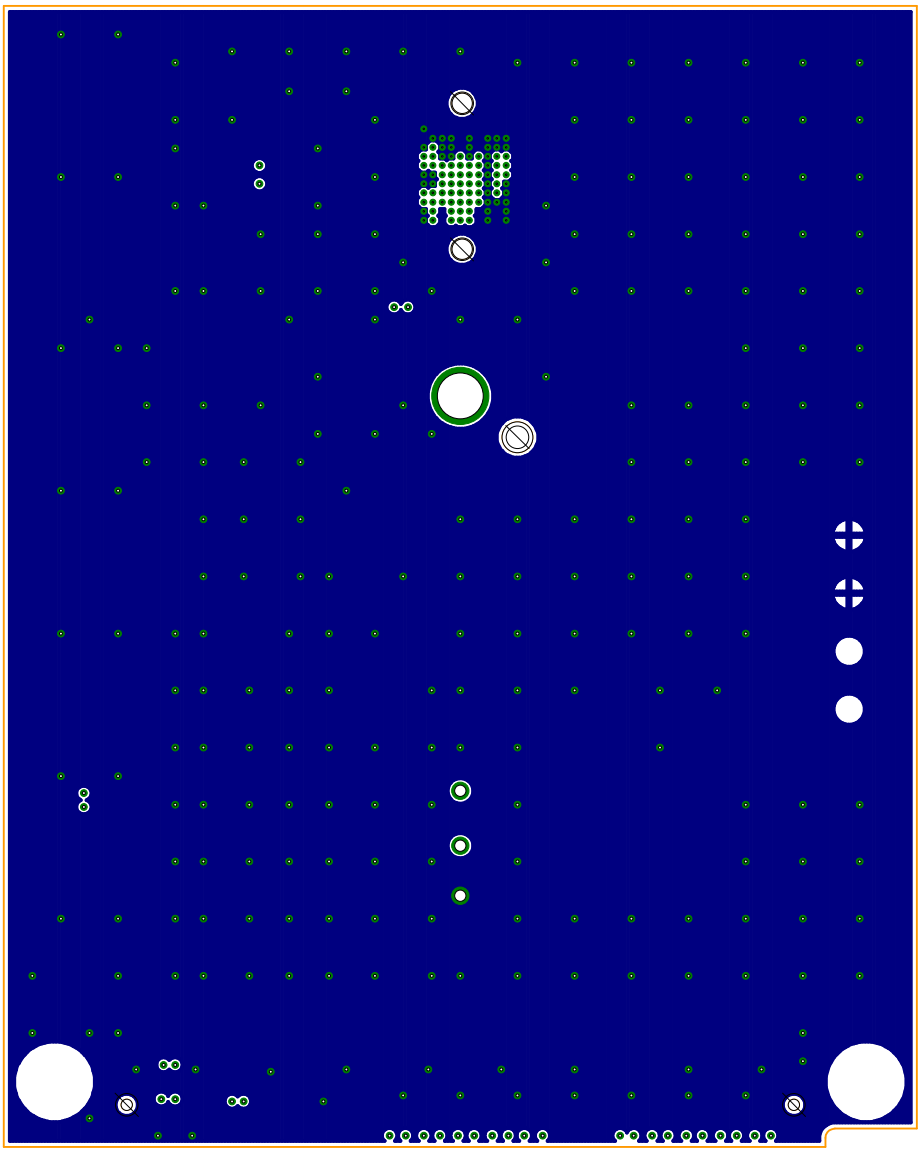

(b) *Layer 2 (GND plane), scale 1.5*

Figure A.1.: *Bottom board for Interposer test, PCB design of all layers and schematic.*

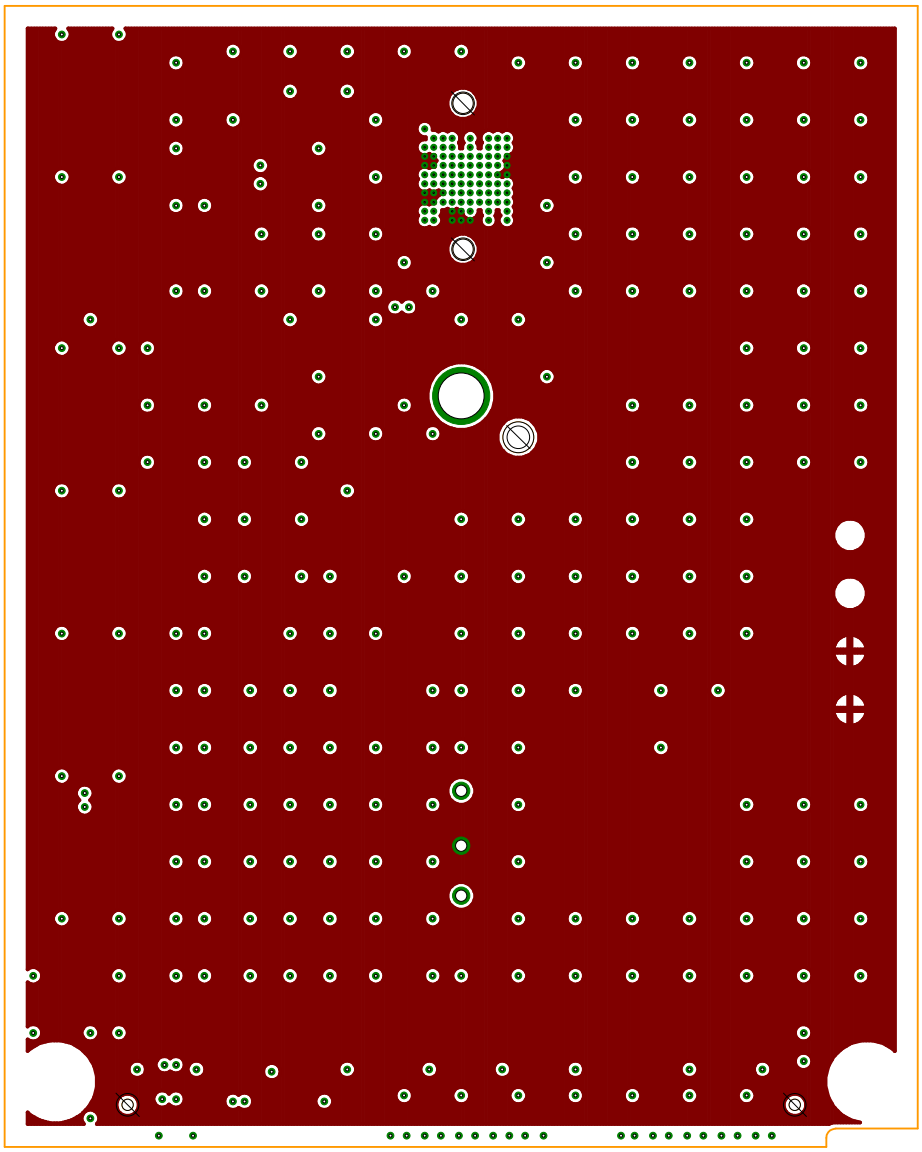

(c) *Layer 3 (VCC plane), scale 1.5*

Figure A.1.: *Bottom board for Interposer test, PCB design of all layers and schematic.*

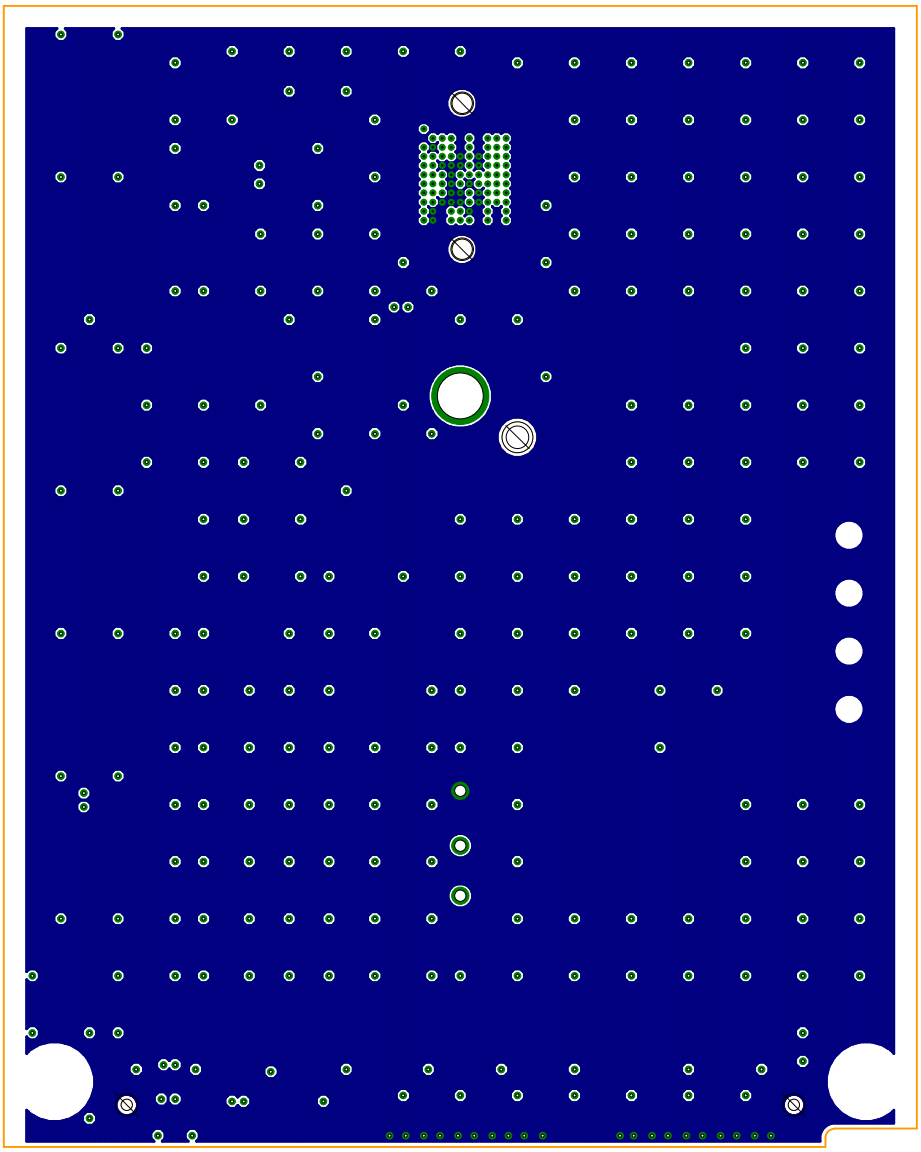

(d) *Layer 4 (VDD plane), scale 1.5*

Figure A.1.: *Bottom board for Interposer test, PCB design of all layers and schematic.*

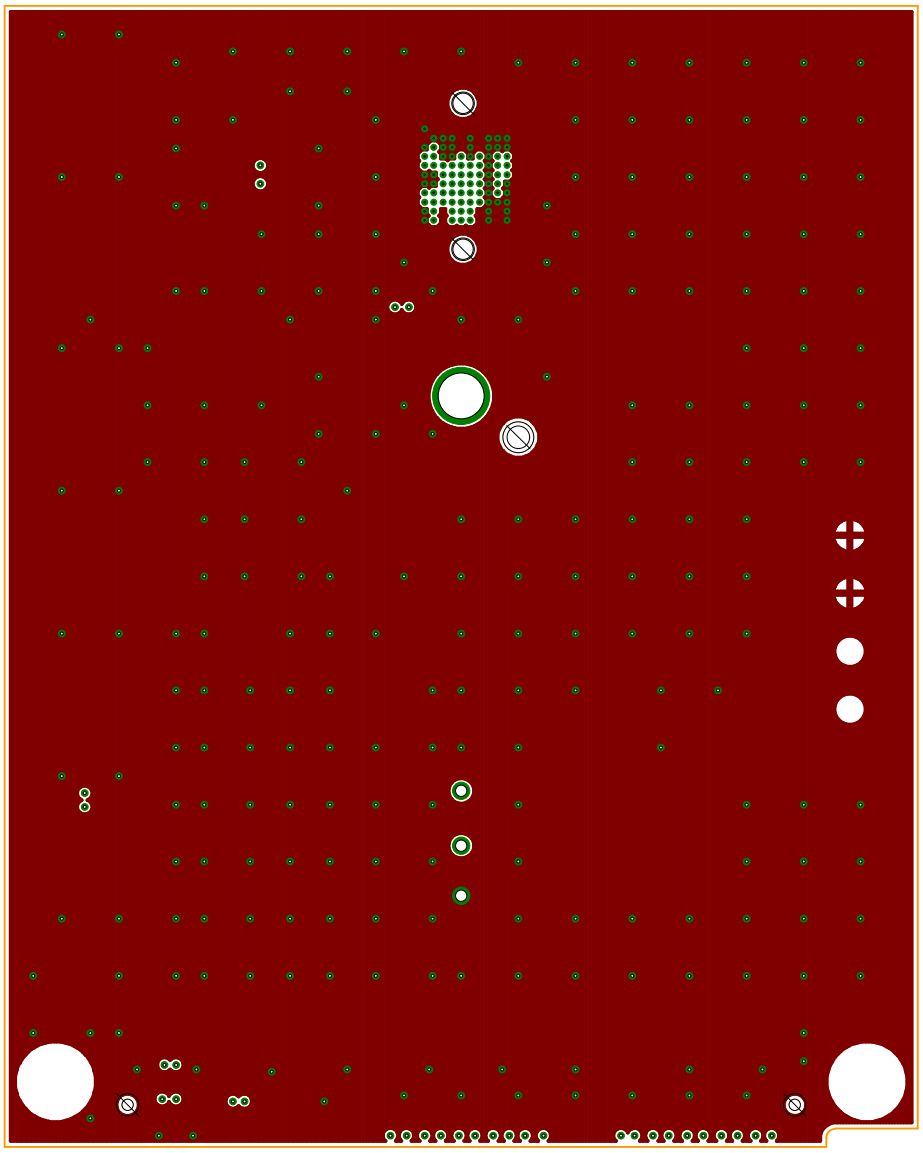

(e) *Layer 5 (GND plane), scale 1.5*

Figure A.1.: *Bottom board for Interposer test, PCB design of all layers and schematic.*

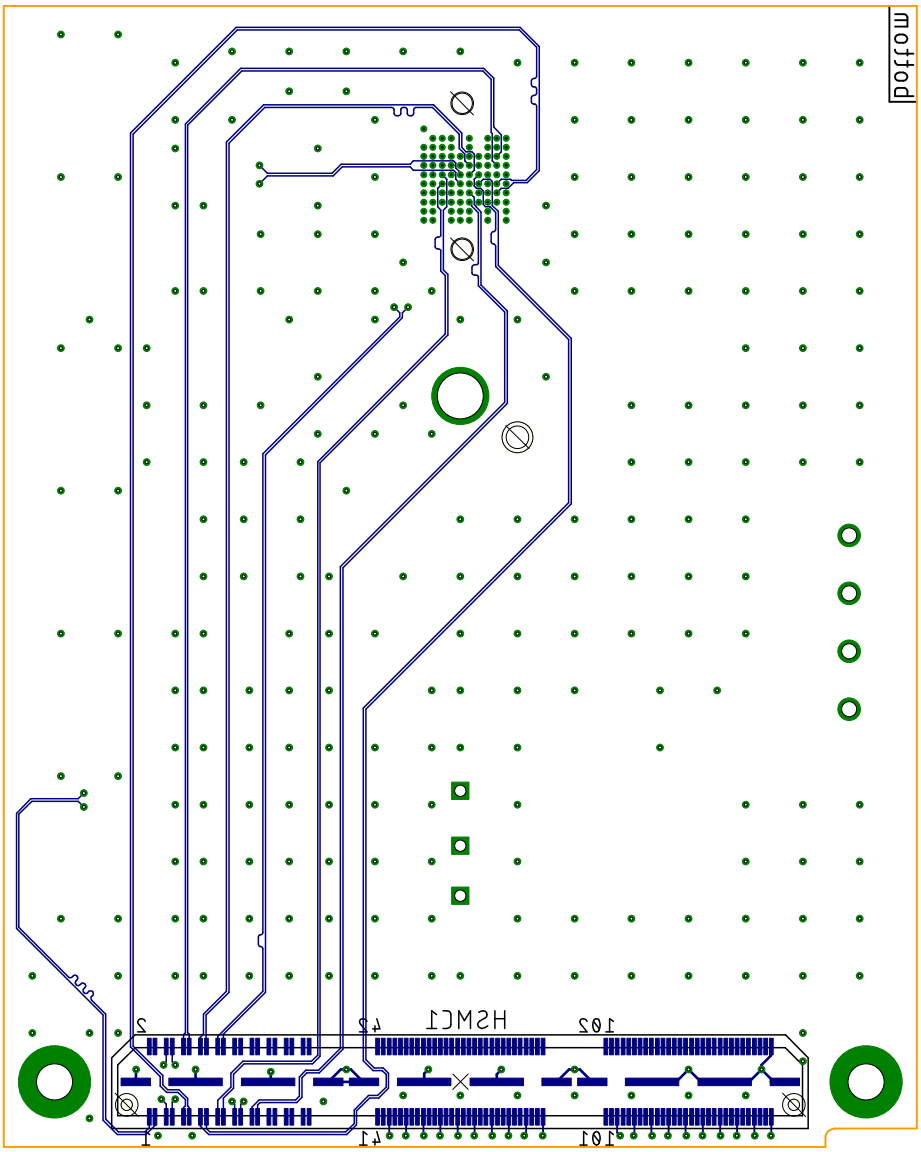

(f) *Layer 6 (bottom layer), scale 1.5*

Figure A.1.: *Bottom board for Interposer test, PCB design of all layers and schematic.*

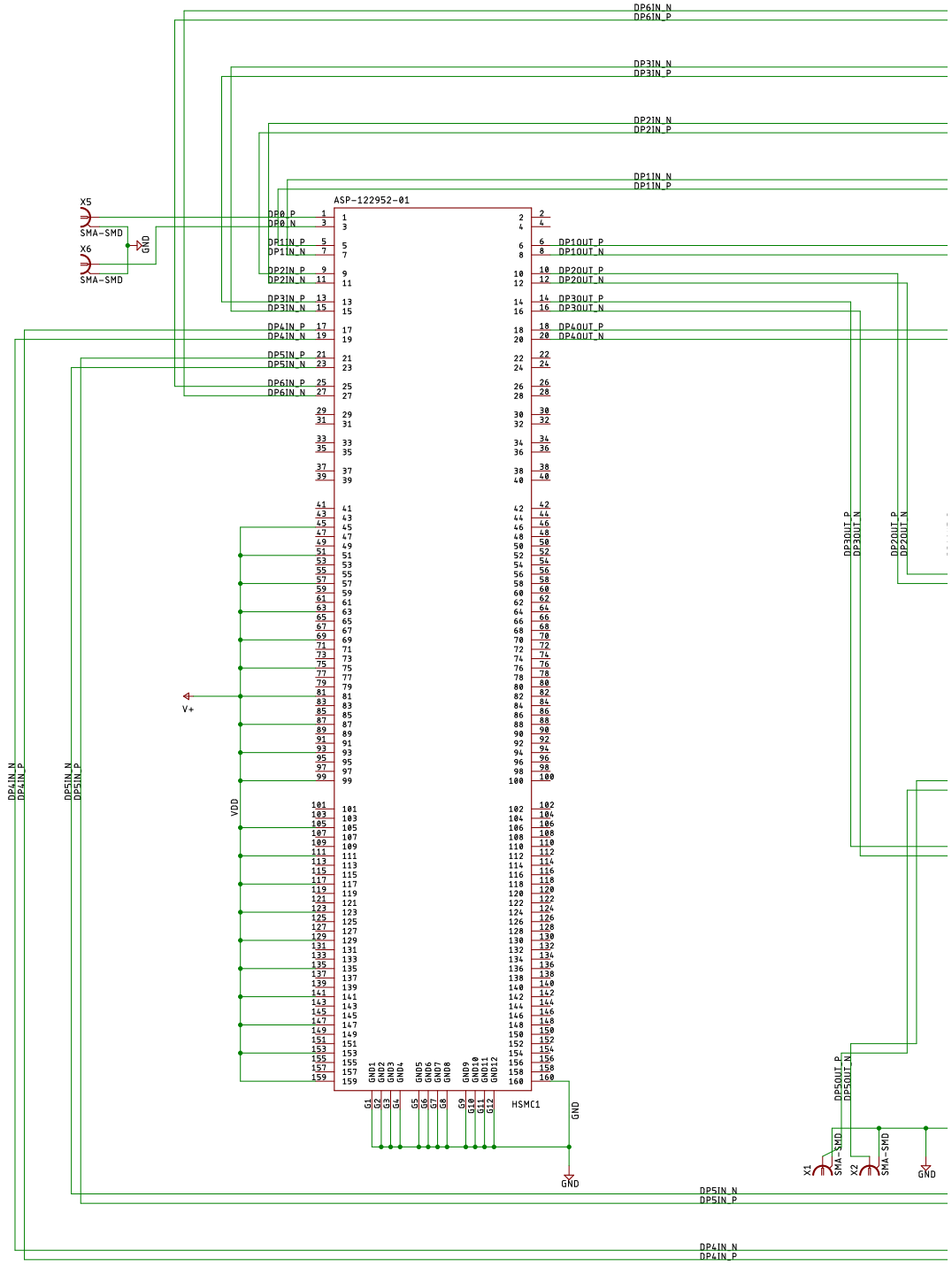

(g) *Schematic (continues on next page)*

Figure A.1.: *Bottom board for Interposer test, PCB design of all layers and schematic.*

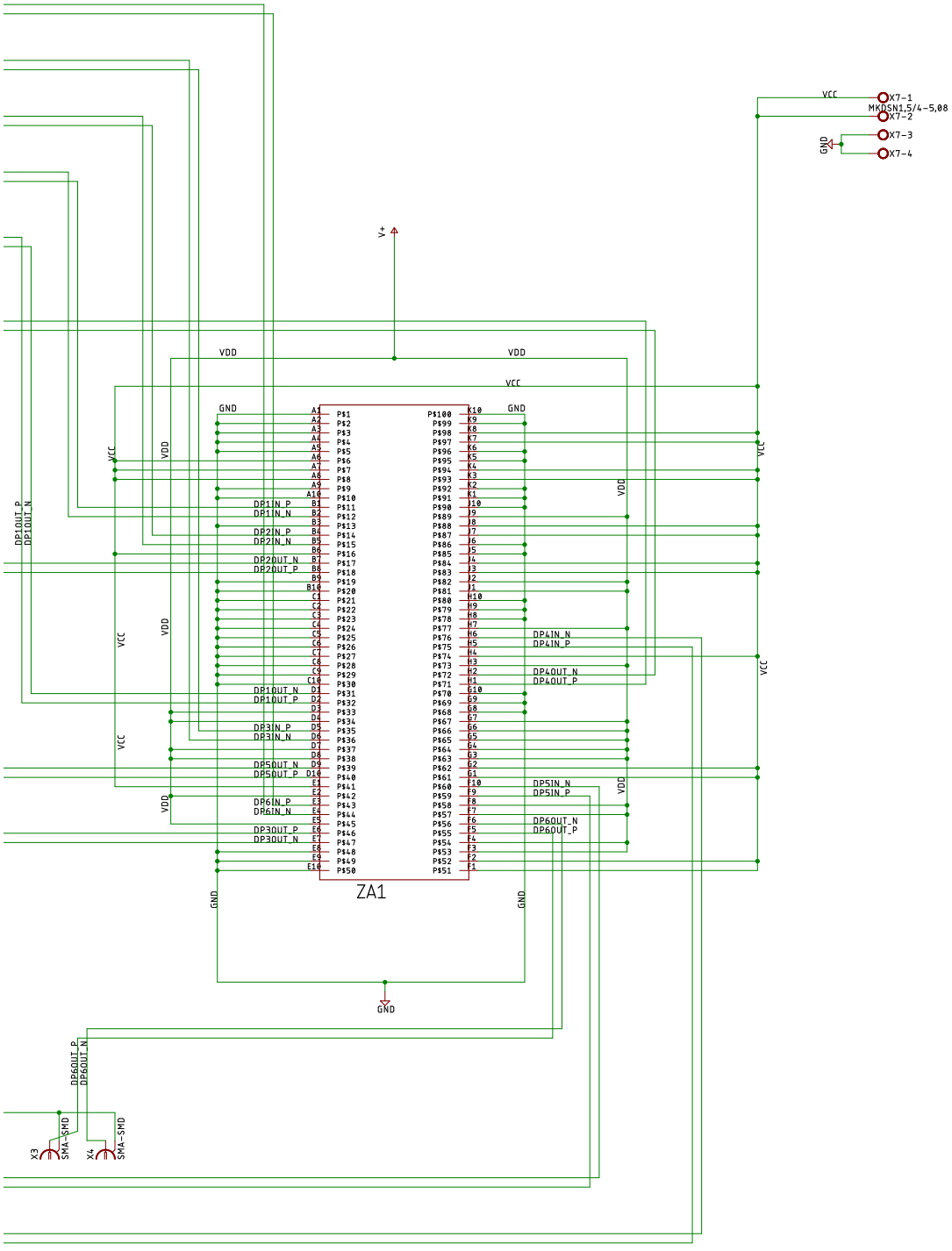

(h) *Schematic (continued)*

Figure A.1.: *Bottom board for Interposer test, PCB design of all layers and schematic.*

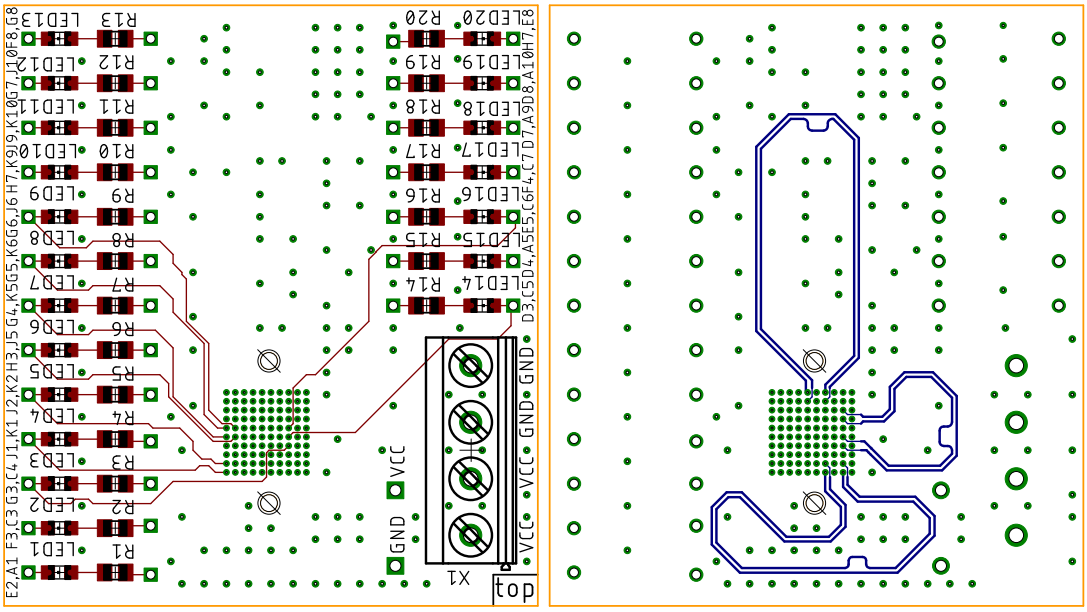

(a) *Layer 1 (top layer), scale 1.5*

(b) *Layer 2, scale 1.5*

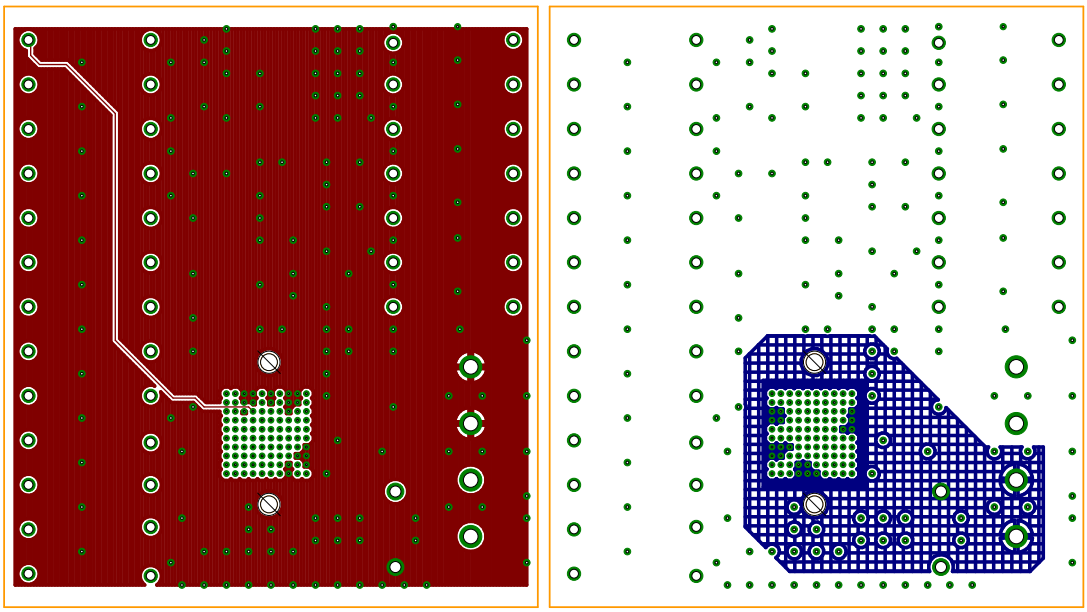

(c) *Layer 3 (GND plane), scale 1.5*

(d) *Layer 4 (parially VCC plane), scale 1.5*

Figure A.2.: *Top board for Interposer test, PCB design of all layers and schematic.*

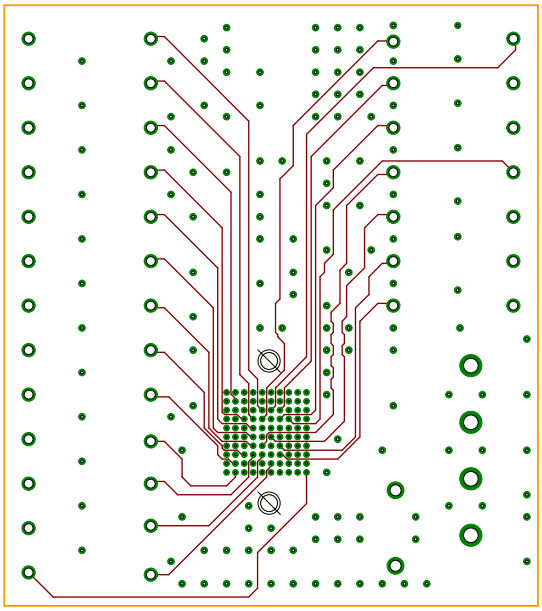

(e) *Layer 5, scale 1.5*

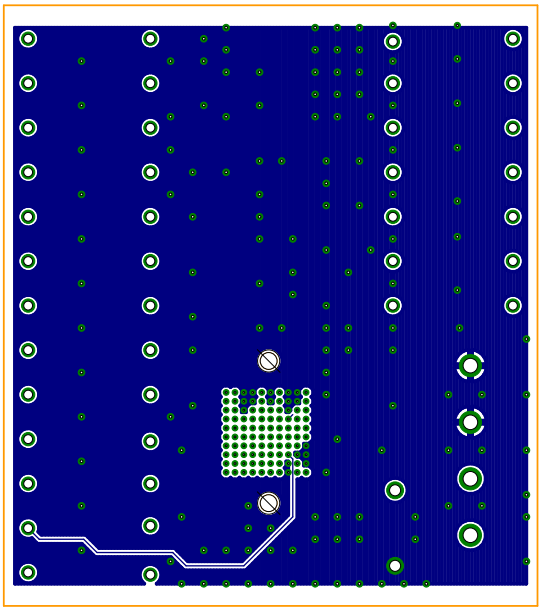

(f) *Layer 6 (GND plane), scale 1.5*

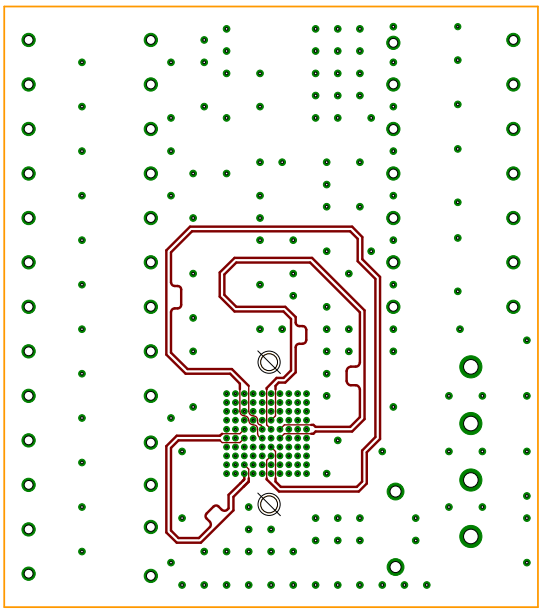

(g) *Layer 7, scale 1.5*

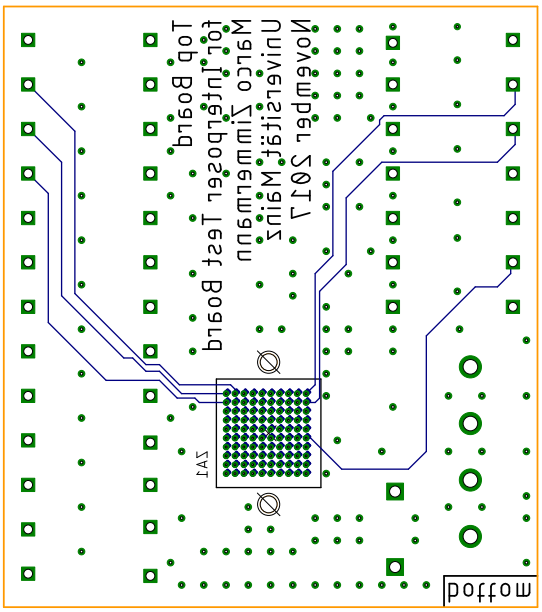

(h) *Layer 8 (bottom layer), scale 1.5*

Figure A.2.: *Top board for Interposer test, PCB design of all layers and schematic.*

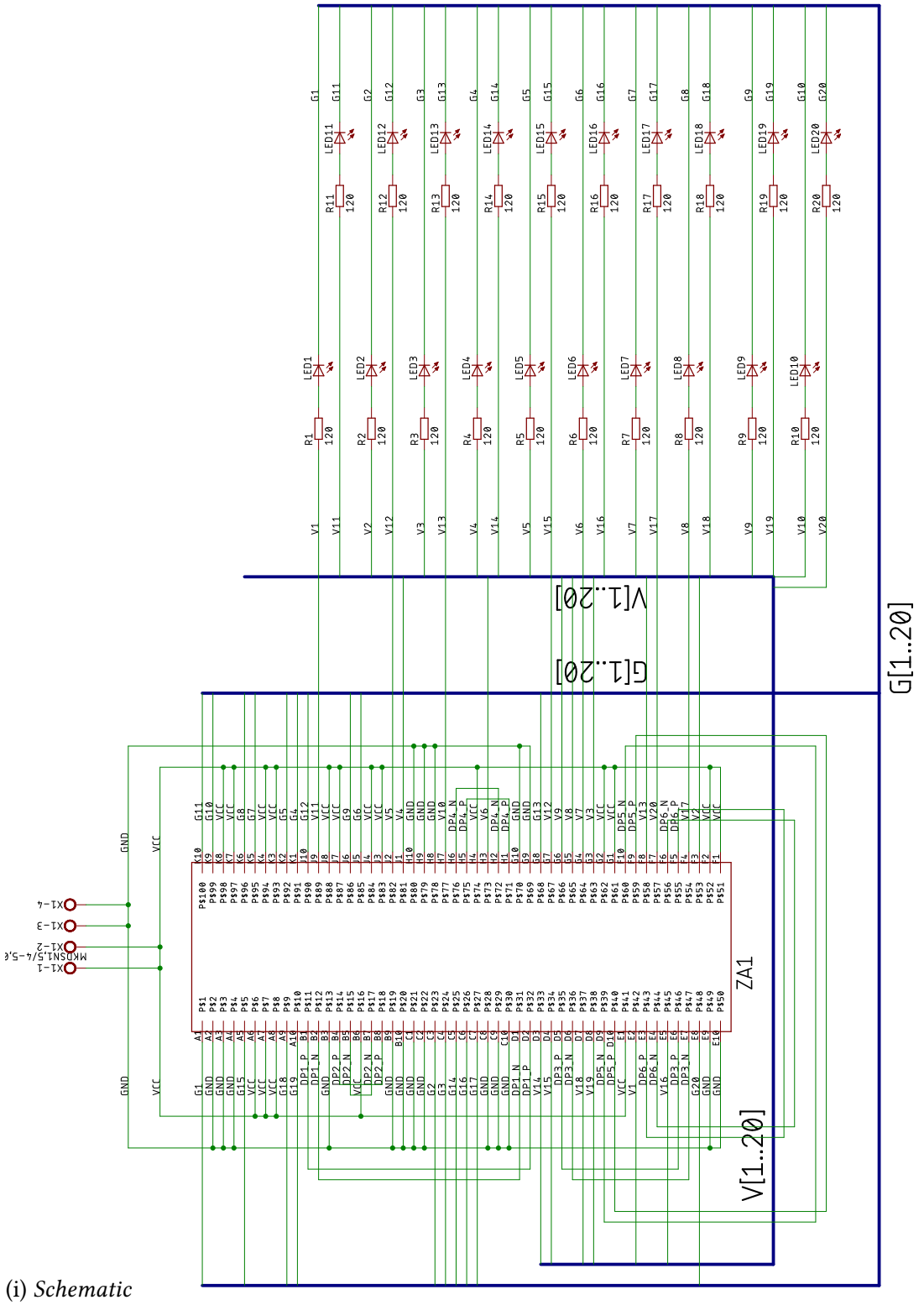

(i) *Schematic*

Figure A.2.: *Top board for Interposer test, PCB design of all layers and schematic.*

A.2. Board for Prototype with Two Strips

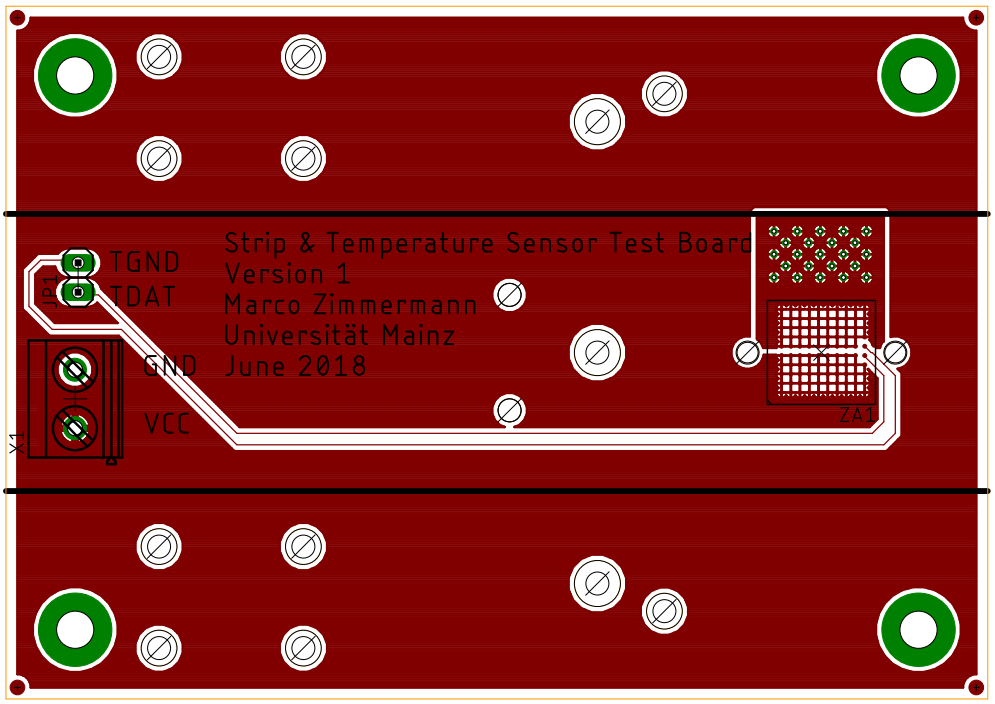

(a) *Layer 1 (top layer, mainly VCC plane), scale 1.5*

Figure A.3.: *Board for Prototype with Two Strips, PCB design of all layers and schematic.*

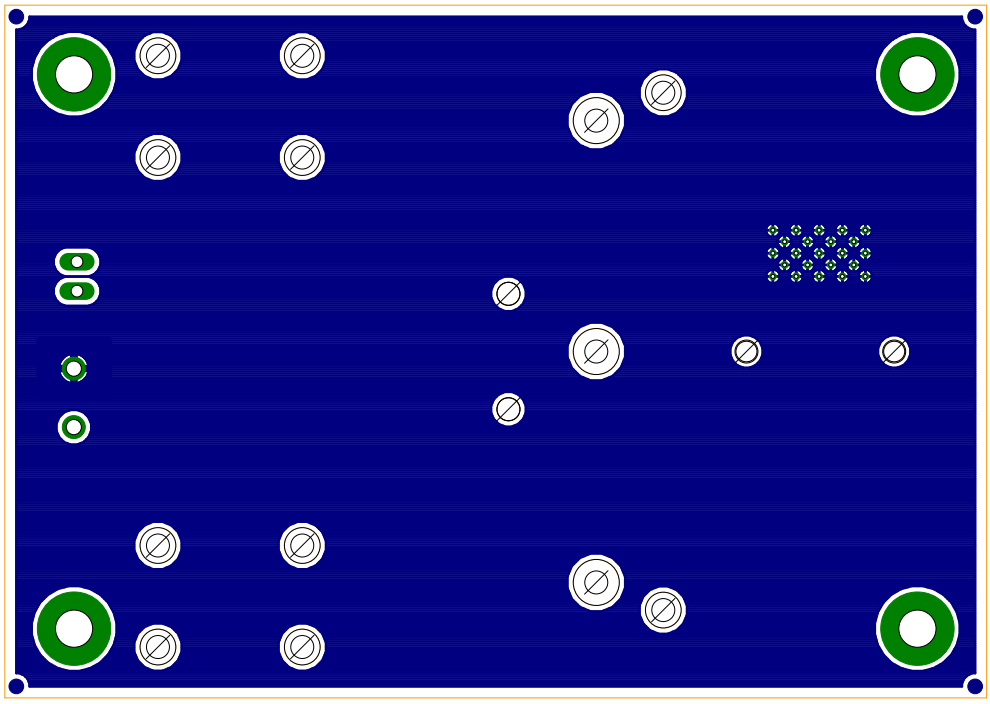

(b) *Layer 2 (bottom layer, GND plane), scale 1.5*

Figure A.3.: *Board for Prototype with Two Strips, PCB design of all layers and schematic.*

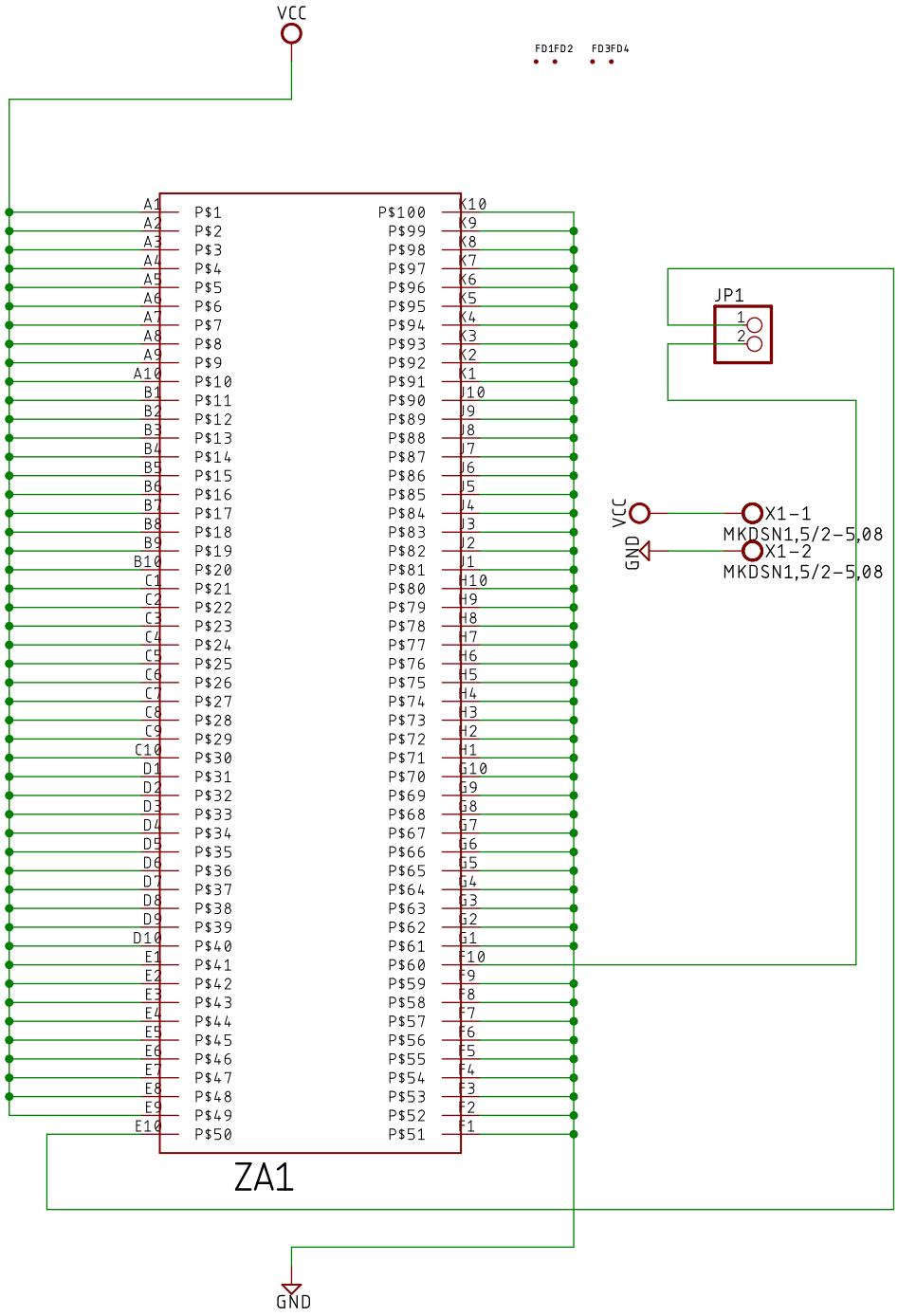

(c) *Schematic*

Figure A.3.: *Board for Prototype with Two Strips, PCB design of all layers and schematic.*

A.3. Frame Boards for the Tracker Module Prototype

The tracker module prototype includes four PCBs with two different designs. The two different designs are however very similar, they include the exact same parts and the same electronic functionality, so that the schematic is identical. The only difference is that the two designs are "mirrored" with respect to each other along the vertical axis. As one can not mirror electric components, they are rotated by 180°, which then requires adapting the connecting traces. However, as there are no functional differences between the two PCB designs, only the design for the "left" frame PCB is shown in the following.

The frame PCBs for the prototype allow to connect 18 strips. The PCB layout and the schematic mainly consist of a pattern with nine copies of identical design blocks, each of them connects a pair of strips. For reasons of clarity and comprehensibility, the plotted schematic is limited to one such design block. In addition, part of the PCB design that consists exclusively of repetitions is omitted in the plots.

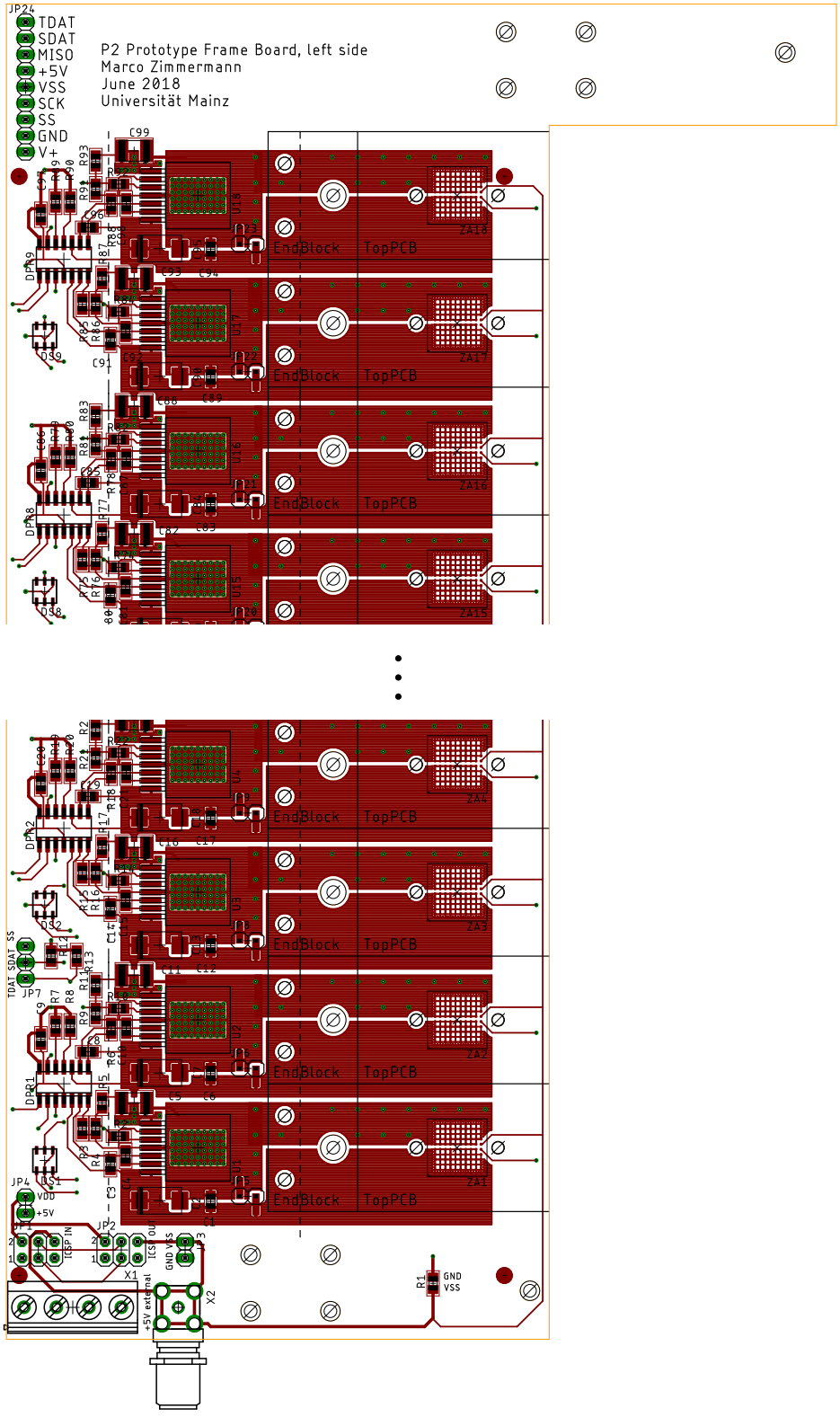

(a) *Layer 1 (top layer), scale 1.0. The middle part of the design for 10 strips is hidden.*

Figure A.4.: *Left Frame Board for the Tracker Module Prototype, PCB design of all layers and schematic.*

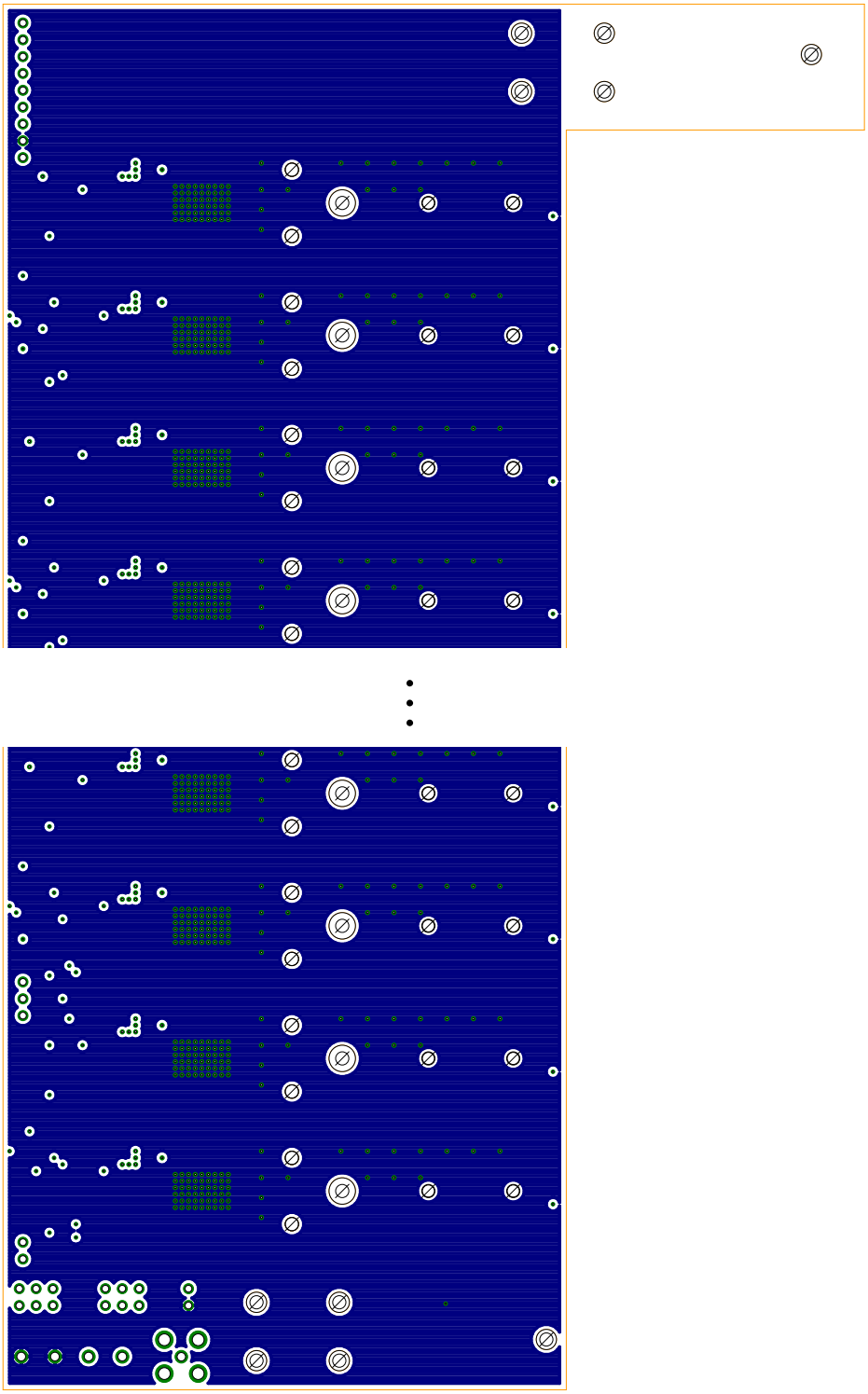

(b) *Layer 2 (GND plane), scale 1.0. The middle part of the design for 10 strips is hidden.*

Figure A.4.: *Left Frame Board for the Tracker Module Prototype, PCB design of all layers and schematic.*

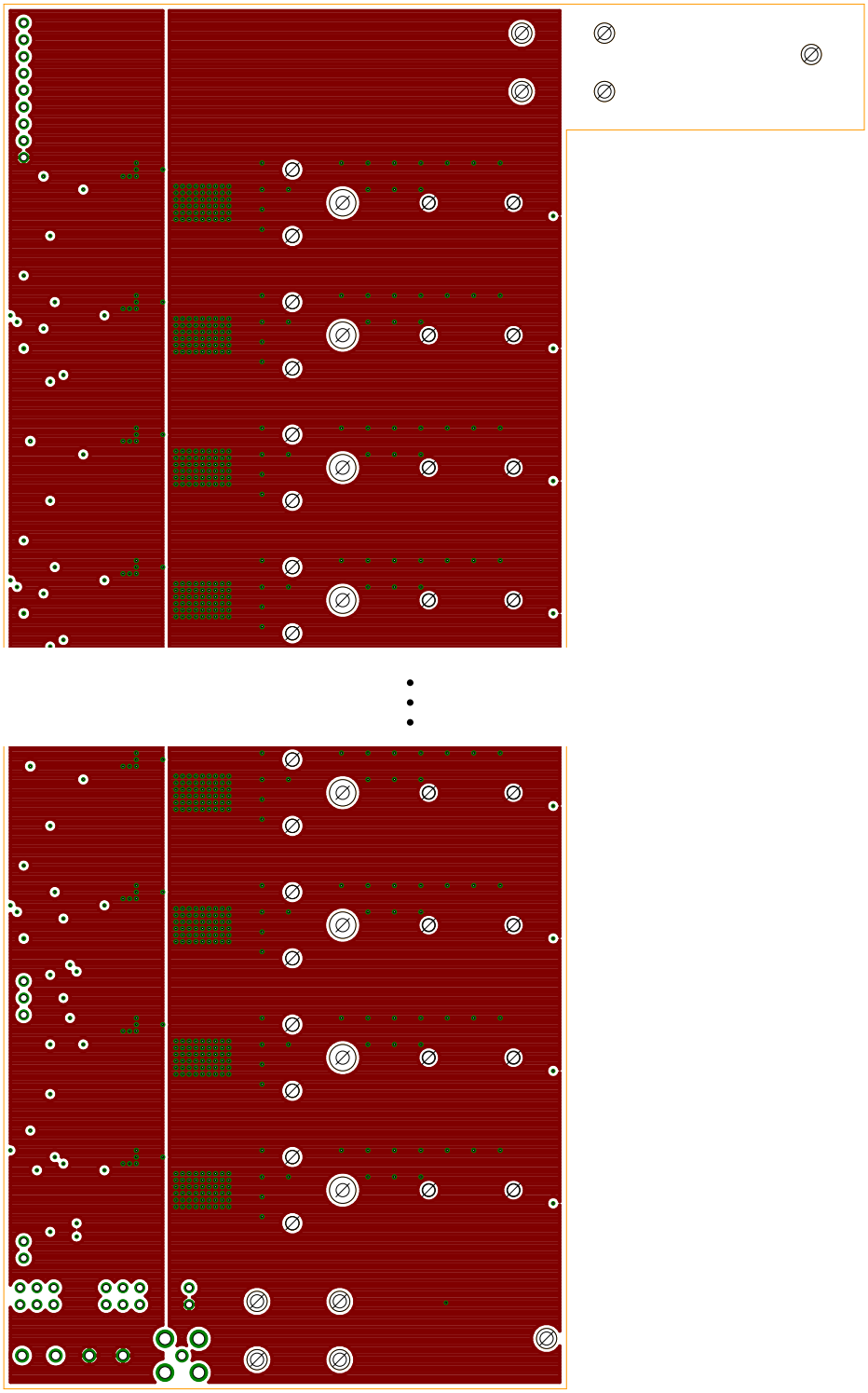

(c) *Layer 3 (VCC and GND plane), scale 1.0. The middle part of the design for 10 strips is hidden.*

Figure A.4.: *Left Frame Board for the Tracker Module Prototype, PCB design of all layers and schematic.*

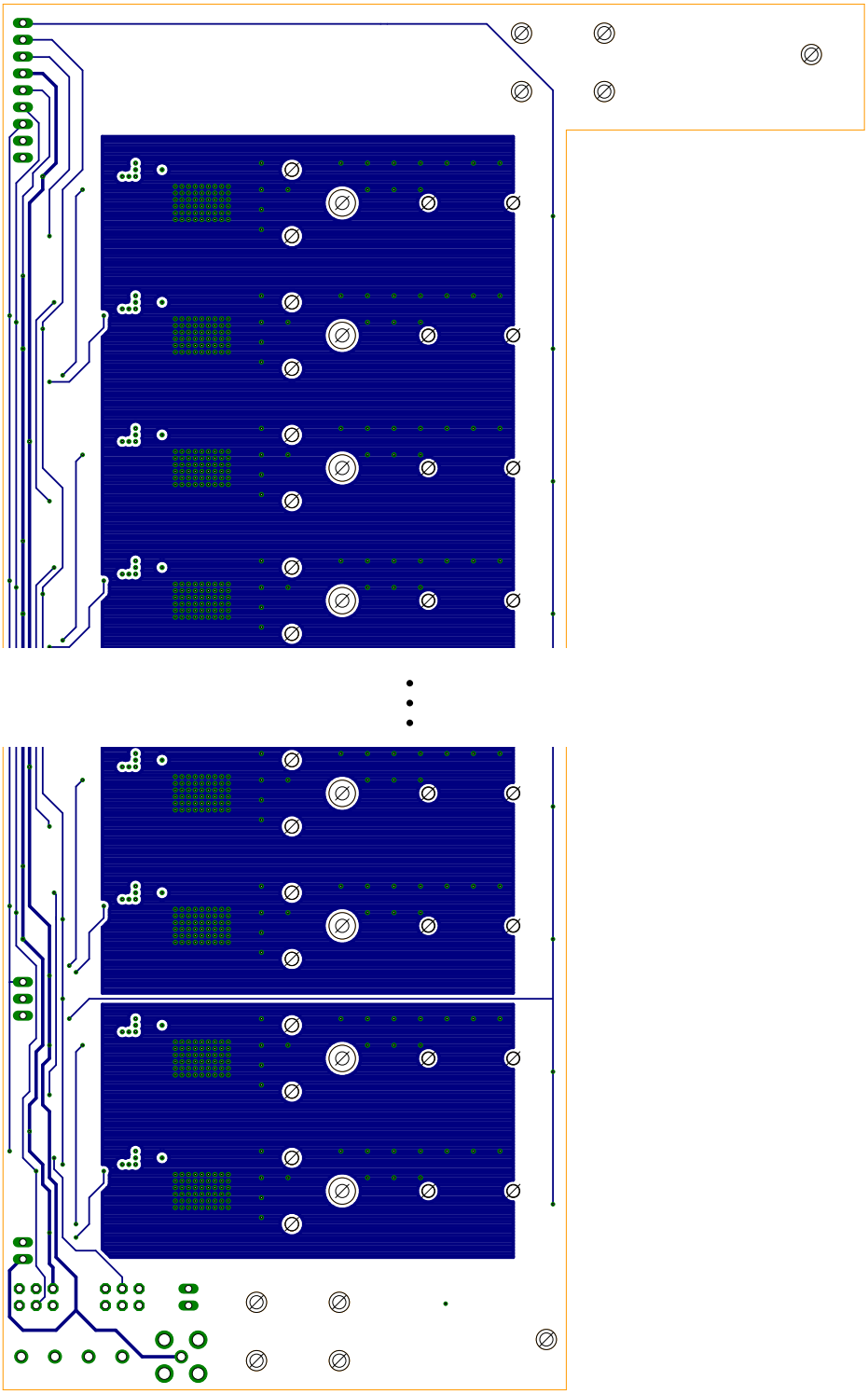

(d) *Layer 4 (bottom layer), scale 1.0. The middle part of the design for 10 strips is hidden.*

Figure A.4.: *Left Frame Board for the Tracker Module Prototype, PCB design of all layers and schematic.*

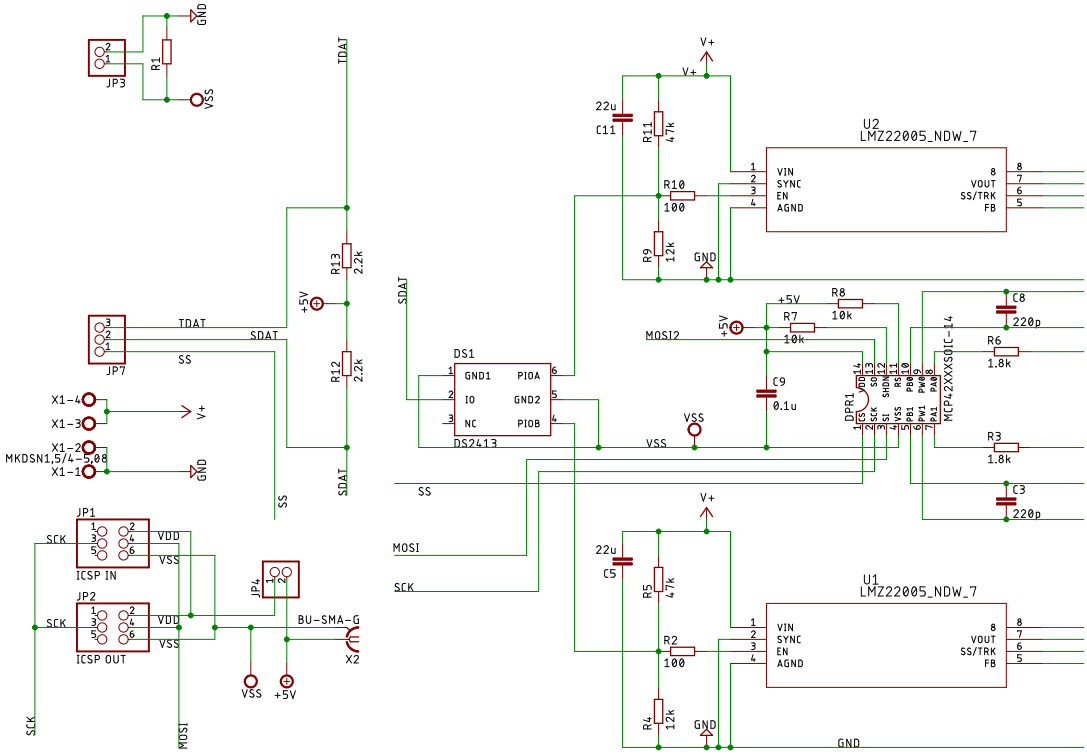

(e) *Schematic, limited to the first two strips (continues on next page). The schematic is repeated for the remaining strip pairs.*

Figure A.4.: *Left Frame Board for the Tracker Module Prototype, PCB design of all layers and schematic.*

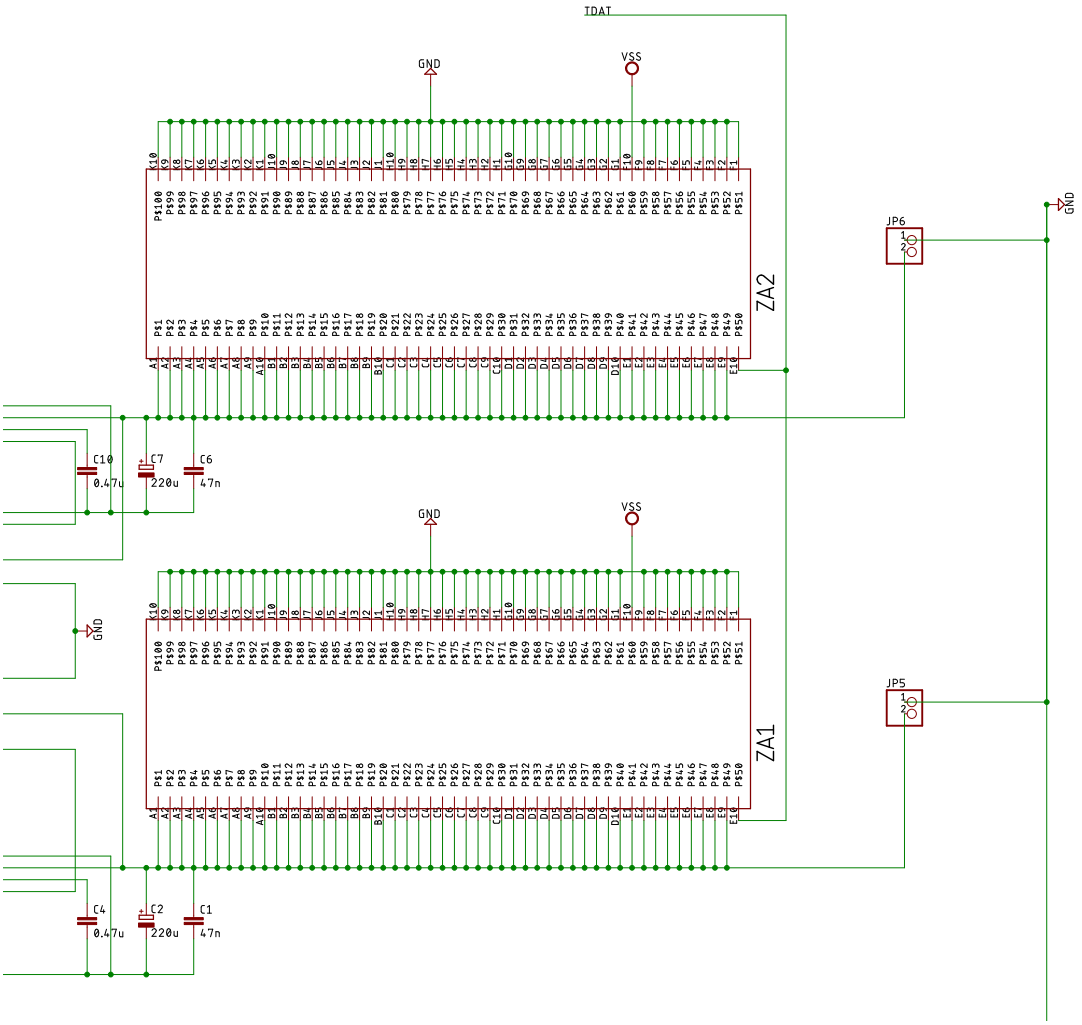

(f) *Schematic, limited to the first two strips (continued). The schematic is repeated for the remaining strip pairs.*

Figure A.4.: *Left Frame Board for the Tracker Module Prototype, PCB design of all layers and schematic.*

Back Matter

List of Figures

List of Tables

Bibliography

[1] G. Aad et al. (ATLAS Collaboration). "Observation of a new particle in the search for the Standard Model Higgs boson with the ATLAS detector at the LHC." *Phys.Lett.* B716 (2012), 1–29. DOI: 10.1016/j.physletb.2012.08.020. arXiv: 1207.7214 [hep-ex].

[2] S. Chatrchyan et al. (CMS Collaboration). "Observation of a new boson at a mass of 125 GeV with the CMS experiment at the LHC." *Phys.Lett.* B716 (2012), 30–61. DOI: 10.1016/j.physletb.2012.08.021. arXiv: 1207.7235 [hep-ex].

[3] R. Adam et al. (Planck Collaboration). "Planck 2015 results - I. Overview of products and scientific results." *A&A* 594 (2016), A1. DOI: 10.1051/0004-6361/201527101.

[4] Y. Fukuda et al. (Super-Kamiokande Collaboration). "Evidence for oscillation of atmospheric neutrinos." *Phys.Rev.Lett.* 81 (1998), 1562–1567. DOI: 10.1103/PhysRevLett.81.1562. arXiv: hep-ex/9807003 [hep-ex].

[5] Q. Ahmad et al. (SNO Collaboration). "Measurement of the rate of $\nu_e + d \rightarrow p+p+e^-$ interactions produced by ^8B solar neutrinos at the Sudbury Neutrino Observatory." *Phys.Rev.Lett.* 87 (2001), 071301. DOI: 10.1103/PhysRevLett.87.071301. arXiv: nucl-ex/0106015 [nucl-ex].

[6] K. Eguchi et al. (KamLAND Collaboration). "First results from KamLAND: Evidence for reactor anti-neutrino disappearance." *Phys.Rev.Lett.* 90 (2003), 021802. DOI: 10.1103/PhysRevLett.90.021802. arXiv: hep-ex/0212021 [hep-ex].

[7] K. Aulenbacher. "The MESA accelerator." *AIP Conf. Proc.* 1563 (2013), 5–12. DOI: 10.1063/1.4829369.

[8] R. Heine. "Current Status of the MESA Project." *Proceedings, 6th ICFA Advanced Beam Dynamics Workshop on Energy Recovery Linacs (ERL 2015): Stony Brook, NY, USA, June 7-12.* 2015. DOI: 10.18429/JACoW-ERL2015-WEIBLH1049.

[9] F. Hug et al. "MESA - an ERL Project for Particle Physics Experiments." *Proceedings, 28th International Linear Accelerator Conference (LINAC16): East Lansing, Michigan, September 25-30.* 2016. DOI: 10.18429/JACoW-LINAC2016-MOP106012.

[10] S. Aulenbacher. "Design and Simulation of the Internal Gas-Target for MAGIX." Diploma thesis. JGU Mainz, 2014.

[11] H. Merkel. "Internal Target Experiments at the MESA accelerator." *PoS* BORMIO (2016), 037. DOI: 10.22323/1.272.0037.

[12] N. Berger et al. "Measuring the weak mixing angle with the P2 experiment at MESA." *J. Univ. Sci. Tech. China* 46.6 (2016), 481–487. DOI: 10.3969/j.issn.0253-2778.2016.06.006. arXiv: 1511.03934 [physics.ins-det].

[13] D. Becker et al. "The P2 Experiment - A future high-precision measurement of the electroweak mixing angle at low momentum transfer." *Eur. Phys. J. A* 54 (2018), 208. DOI: 10.1140/epja/i2018-12611-6. arXiv: 1802.04759 [nucl-ex].

[14] D. Becker. "Voruntersuchungen zur Messung der schwachen Ladung des Protons im Rahmen des P2-Experiments." PhD thesis. Universität Mainz, 2018.

[15] M. Thiel et al. "Neutron skin studies of medium and heavy nuclei." *EPJ Web Conf.* 73 (2014), 07007. DOI: 10.1051/epjconf/20147307007.

[16] H. Hertz. "Ueber einen Einfluss des ultravioletten Lichtes auf die electrische Entladung." *Ann. Phys.* 267.8 (1887), 983–1000. DOI: 10.1002/andp.18872670827.

[17] A. Einstein. "Über einen die Erzeugung und Verwandlung des Lichtes betreffenden heuristischen Gesichtspunkt [AdP 17, 132 (1905)]." *Ann. Phys.* 14.S1 (2005), 164–181. DOI: 10.1002/andp.200590004.

[18] C. S. Wu et al. "Experimental Test of Parity Conservation in Beta Decay." *Phys. Rev.* 105 (1957), 1413–1414. DOI: 10.1103/PhysRev.105.1413.

[19] J. H. Christenson et al. "Evidence for the 2π Decay of the K_2^0 Meson." *Phys. Rev. Lett.* 13 (1964), 138–140. DOI: 10.1103/PhysRevLett.13.138.

[20] Wikipedia. *Standard Model.* 2017. URL: https://en.wikipedia.org/wiki/Standard_Model.

[21] P. W. Higgs. "Broken Symmetries and the Masses of Gauge Bosons." *Phys. Rev. Lett.* 13 (16 Oct. 1964), 508–509. DOI: 10.1103/PhysRevLett.13.508.

[22] P. W. Higgs. "Spontaneous Symmetry Breakdown without Massless Bosons." *Phys. Rev.* 145 (4 May 1966), 1156–1163. DOI: 10.1103/PhysRev.145.1156.

[23] F. Englert and R. Brout. "Broken Symmetry and the Mass of Gauge Vector Mesons." *Phys. Rev. Lett.* 13 (9 Aug. 1964), 321–323. DOI: 10.1103/PhysRevLett.13.321.

[24] P. W. Anderson. "Plasmons, Gauge Invariance, and Mass." *Phys. Rev.* 130 (1 Apr. 1963), 439–442. DOI: 10.1103/PhysRev.130.439.

[25] G. S. Guralnik, C. R. Hagen, and T. W. B. Kibble. "Global Conservation Laws and Massless Particles." *Phys. Rev. Lett.* 13 (20 Nov. 1964), 585–587. DOI: 10.1103/PhysRevLett.13.585.

[26] T. W. B. Kibble. "Symmetry Breaking in Non-Abelian Gauge Theories." *Phys. Rev.* 155 (5 Mar. 1967), 1554–1561. DOI: 10.1103/PhysRev.155.1554.

[27] O. Eberhardt et al. "Impact of a Higgs boson at a mass of 126 GeV on the standard model with three and four fermion generations." *Phys. Rev. Lett.* 109 (2012), 241802. DOI: 10.1103/PhysRevLett.109.241802. arXiv: 1209.1101 [hep-ph].

[28] E. Noether. "Invarianten beliebiger Differentialausdrücke." ger. *Nachrichten von der Gesellschaft der Wissenschaften zu Göttingen, Mathematisch-Physikalische Klasse* 1918 (1918), 37–44. URL: http://eudml.org/doc/59011.

[29] N. Cabibbo. "Unitary Symmetry and Leptonic Decays." *Phys. Rev. Lett.* 10 (1963), 531–533. DOI: 10.1103/PhysRevLett.10.531.

[30] M. Kobayashi and T. Maskawa. "CP Violation in the Renormalizable Theory of Weak Interaction." *Prog. Theor. Phys.* 49 (1973), 652–657. DOI: 10.1143/PTP.49.652.

[31] M. Peskin and D. Schroeder. *An Introduction to Quantum Field Theory*. Advanced book classics. Addison-Wesley Publishing Company, 1995. ISBN: 9780201503975.

[32] P. Schmüser. *Feynman - Graphen und Eichtheorien Für Experimentalphysiker*. Lecture notes in physics. Springer Berlin Heidelberg, 1995. ISBN: 9783540584865.

[33] D. Griffiths. *Introduction to Elementary Particles*. Physics Textbook. Wiley, 2008. ISBN: 9783527406012.

[34] M. Thomson. *Modern Particle Physics*. Modern Particle Physics. Cambridge University Press, 2013. ISBN: 9781107034266.

[35] S. Glashow. "Partial Symmetries of Weak Interactions." *Nucl.Phys.* 22 (1961), 579–588. DOI: 10.1016/0029-5582(61)90469-2.

[36] A. Salam. "Weak and Electromagnetic Interactions." *Conf.Proc.* C680519 (1968), 367–377.

[37] S. Weinberg. "A Model of Leptons." *Phys.Rev.Lett.* 19 (1967), 1264–1266. DOI: 10.1103/PhysRevLett.19.1264.

[38] P. J. Mohr, D. B. Newell, and B. N. Taylor. "CODATA Recommended Values of the Fundamental Physical Constants: 2014." *Rev. Mod. Phys.* 88.3 (2016), 035009. DOI: 10.1103/RevModPhys.88.035009. arXiv: 1507.07956 [physics.atom-ph].

[39] W. Hollik. "Renormalization of the Standard Model." *Adv. Ser. Direct. High Energy Phys.* 14 (1995), 37–116. DOI: 10.1142/9789814503662_0003.

[40] M. J. G. Veltman. "Perturbation theory of massive Yang-Mills fields." *Nucl. Phys.* B7 (1968), 637–650. DOI: 10.1016/0550-3213(68)90197-1.

[41] G. 't Hooft. "Renormalizable Lagrangians for Massive Yang-Mills Fields." *Nucl. Phys.* B35 (1971), 167–188. DOI: 10.1016/0550-3213(71)90139-8.

[42] G. 't Hooft and M. J. G. Veltman. "Regularization and Renormalization of Gauge Fields." *Nucl. Phys.* B44 (1972), 189–213. DOI: 10.1016/0550-3213(72)90279-9.

[43] G. 't Hooft and M. J. G. Veltman. "Combinatorics of gauge fields." *Nucl. Phys.* B50 (1972), 318–353. DOI: 10.1016/S0550-3213(72)80021-X.

[44] K. S. Kumar et al. "Low Energy Measurements of the Weak Mixing Angle." *Ann. Rev. Nucl. Part. Sci.* 63 (2013), 237–267. DOI: 10.1146/annurev-nucl-102212-170556. arXiv: 1302.6263 [hep-ex].

[45] W. J. Marciano. "Radiative corrections to neutral current processes." *Adv. Ser. Direct. High Energy Phys.* 14 (1995), 170–200. DOI: 10.1142/9789814503662_0005.

[46] G. Alexander et al. (LEP, DELPHI, OPAL, ALEPH, L3 Collaborations). "Electroweak parameters of the Z^0 resonance and the Standard Model: the LEP Collaborations." *Phys. Lett.* B276 (1992), 247–253. DOI: 10.1016/0370-2693(92)90572-L.

[47] G. Passarino and M. J. G. Veltman. "On the Definition of the Weak Mixing Angle." *Phys. Lett.* B237 (1990), 537–544. DOI: 10.1016/0370-2693(90)91221-V.

[48] W. J. Marciano and A. Sirlin. "Precise SU(5) Predictions for $\sin^2(\theta_W)^{\exp}$, m_W and m_Z." *Phys. Rev. Lett.* 46 (1981), 163. DOI: 10.1103/PhysRevLett.46.163.

[49] A. Sirlin. "Role of $\sin^2\theta_W(m_Z)$ at the Z^0 Peak." *Phys. Lett.* B232 (1989), 123–126. DOI: 10.1016/0370-2693(89)90568-6.

[50] G. Degrassi, S. Fanchiotti, and A. Sirlin. "Relations Between the On-shell and $\overline{\text{MS}}$ Frameworks and the $m_W - m_Z$ Interdependence." *Nucl. Phys.* B351 (1991), 49–69. DOI: 10.1016/0550-3213(91)90081-8.

[51] G. Degrassi and A. Sirlin. "Comparative analysis of electroweak corrections to $e^+e^- \to f + \bar{f}$ in on-shell and (MS) frameworks." *Nucl. Phys.* B352 (1991), 342–366. DOI: 10.1016/0550-3213(91)90446-5.

[52] P. Gambino and A. Sirlin. "Relation between $sin^2\hat{\theta}_W(m_Z)$ and $\sin^2\theta^{\text{lept}}_{\text{eff}}$." *Phys. Rev.* D49 (1994), 1160–1162. DOI: 10.1103/PhysRevD.49.R1160. arXiv: hep-ph/9309326 [hep-ph].

[53] S. Schael et al. (SLD Electroweak Group, DELPHI, ALEPH, SLD, SLD Heavy Flavour Group, OPAL, LEP Electroweak Working Group, L3 Collaborations). "Precision electroweak measurements on the Z resonance." *Phys. Rept.* 427 (2006), 257–454. DOI: 10.1016/j.physrep.2005.12.006. arXiv: hep-ex/0509008 [hep-ex].

[54] J. Erler and M. J. Ramsey-Musolf. "The Weak mixing angle at low energies." *Phys. Rev.* D72 (2005), 073003. DOI: 10.1103/PhysRevD.72.073003. arXiv: hep-ph/0409169 [hep-ph].

[55] C. Patrignani et al. (Particle Data Group). "Review of Particle Physics." *Chin. Phys.* C40.10 (2016), 100001. DOI: 10.1088/1674-1137/40/10/100001.

[56] A. Czarnecki and W. J. Marciano. "Polarized Moller scattering asymmetries." *Int. J. Mod. Phys.* A15 (2000), 2365–2376. DOI: 10.1142/S0217751X00002433. arXiv: hep-ph/0003049 [hep-ph].

[57] J. Arrington, C. D. Roberts, and J. M. Zanotti. "Nucleon electromagnetic form-factors." *J. Phys.* G34 (2007), S23–S52. DOI: 10.1088/0954-3899/34/7/S03. arXiv: nucl-th/0611050 [nucl-th].

[58] D. S. Armstrong and R. D. McKeown. "Parity-Violating Electron Scattering and the Electric and Magnetic Strange Form Factors of the Nucleon." *Ann. Rev. Nucl. Part. Sci.* 62 (2012), 337–359. DOI: 10.1146/annurev-nucl-102010-130419. arXiv: 1207.5238 [nucl-ex].

[59] J. Erler and M. J. Ramsey-Musolf. "Low energy tests of the weak interaction." *Prog. Part. Nucl. Phys.* 54 (2005), 351–442. DOI: 10.1016/j.ppnp.2004.08.001. arXiv: hep-ph/0404291 [hep-ph].

[60] J. Erler, A. Kurylov, and M. J. Ramsey-Musolf. "The Weak charge of the proton and new physics." *Phys. Rev.* D68 (2003), 016006. DOI: 10.1103/PhysRevD.68.016006. arXiv: hep-ph/0302149 [hep-ph].

[61] C. Y. Prescott et al. "Parity Nonconservation in Inelastic Electron Scattering." *Phys. Lett.* B77 (1978). [,6.31(1978)], 347–352. DOI: 10.1016/0370-2693(78)90722-0.

[62] W. Heil et al. "Improved Limits on the Weak, Neutral, Hadronic Axial Vector Coupling Constants From Quasielastic Scattering of Polarized Electrons." *Nucl. Phys.* B327 (1989), 1–31. DOI: 10.1016/0550-3213(89)90284-8.

[63] P. A. Souder et al. "Measurement of parity violation in the elastic scattering of polarized electrons from C-12." *Phys. Rev. Lett.* 65 (1990), 694–697. DOI: 10.1103/PhysRevLett.65.694.

[64] D. Androić et al. (Qweak Collaboration). "Precision measurement of the weak charge of the proton." *Nature* 557.7704 (2018), 207–211. DOI: 10.1038/s41586-018-0096-0.

[65] J. Benesch et al. (MOLLER Collaboration). "The MOLLER Experiment: An Ultra-Precise Measurement of the Weak Mixing Angle Using Møller Scattering" (2014). arXiv: 1411.4088 [nucl-ex].

[66] P. L. Anthony et al. (SLAC E158 Collaboration). "Observation of parity nonconservation in Moller scattering." *Phys. Rev. Lett.* 92 (2004), 181602. DOI: 10.1103/PhysRevLett.92.181602. arXiv: hep-ex/0312035 [hep-ex].

[67] J. P. Chen et al. (SoLID Collaboration). "A White Paper on SoLID (Solenoidal Large Intensity Device)" (2014). arXiv: 1409.7741 [nucl-ex].

[68] J. Erler et al. "Weak Polarized Electron Scattering." *Ann. Rev. Nucl. Part. Sci.* 64 (2014), 269–298. DOI: 10.1146/annurev-nucl-102313-025520. arXiv: 1401.6199 [hep-ph].

[69] H. Davoudiasl, H.-S. Lee, and W. J. Marciano. "'Dark' Z implications for Parity Violation, Rare Meson Decays, and Higgs Physics." *Phys. Rev.* D85 (2012), 115019. DOI: 10.1103/PhysRevD.85.115019. arXiv: 1203.2947 [hep-ph].

[70] H. Davoudiasl, H.-S. Lee, and W. J. Marciano. "Muon Anomaly and Dark Parity Violation." *Phys. Rev. Lett.* 109 (2012), 031802. DOI: 10.1103/PhysRevLett.109.031802. arXiv: 1205.2709 [hep-ph].

[71] H. Davoudiasl, H.-S. Lee, and W. J. Marciano. "Dark Side of Higgs Diphoton Decays and Muon g-2." *Phys. Rev.* D86 (2012), 095009. DOI: 10.1103/PhysRevD.86.095009. arXiv: 1208.2973 [hep-ph].

[72] H. Davoudiasl, H.-S. Lee, and W. J. Marciano. "Muon $g-2$, rare kaon decays, and parity violation from dark bosons." *Phys. Rev.* D89.9 (2014), 095006. DOI: 10.1103/PhysRevD.89.095006. arXiv: 1402.3620 [hep-ph].

[73] M. J. Ramsey-Musolf and S. Su. "Low Energy Precision Test of Supersymmetry." *Phys. Rept.* 456 (2008), 1–88. DOI: 10.1016/j.physrep.2007.10.001. arXiv: hep-ph/0612057 [hep-ph].

[74] H. Herminghaus et al. "The Design of a Cascaded 800-MeV Normal Conducting CW Racetrack Microtron." *Nucl. Instrum. Meth.* 138 (1976), 1–12. DOI: 10.1016/0029-554X(76)90145-2.

[75] K. H. Kaiser et al. "The 1.5-GeV harmonic double-sided microtron at Mainz University." *Nucl. Instrum. Meth.* A593 (2008), 159–170. DOI: 10.1016/j.nima.2008.05.018.

[76] M. Dehn et al. "The MAMI-C Accelerator: 25 Years of Operation and Strategies for the Next Decade." *Proceedings, 8th International Particle Accelerator Conference (IPAC 2017): Copenhagen, Denmark, May 14-19.* 2017. DOI: 10.18429/JACoW-IPAC2017-TUPIK054.

[77] K. Aulenbacher et al. "The MAMI source of polarized electrons." *Nucl. Instrum. Meth.* A391 (1997), 498–506. DOI: 10.1016/S0168-9002(97)00528-7.

[78] K. Aulenbacher. "Polarized beams for electron accelerators." *Eur. Phys. J. ST* 198 (2011), 361–380. DOI: 10.1140/epjst/e2011-01499-6.

[79] R. Heine et al. "Current Status of the Milliampere Booster for the Mainz Energy-recovering Superconducting Accelerator." *Proceedings, 7th International Particle Accelerator Conference (IPAC 2016): Busan, Korea, May 8-13.* 2016. DOI: 10.18429/JACoW-IPAC2016-TUPOW002.

[80] F. Hug and R. Heine. "Injector linac stability requirements for high precision experiments at MESA." *J. Phys. Conf. Ser.* 874.1 (2017). [MOPVA014(2017)], 012012. DOI: 10.1088/1742-6596/874/1/012012.

[81] T. Stengler et al. "Modified ELBE Type Cryomodules for the Mainz Energy-Recovering Superconducting Accelerator MESA." *Proceedings, 17th International Conference on RF Superconductivity (SRF2015): Whistler, Canada, September 13-18.* 2015. DOI: 10.18429/JACoW-SRF2015-THPB116.

[82] K. Aulenbacher, I. Alexander, and V. Tioukine. "The polarimetry chain for the P2 experiment." *Nuovo Cim.* C035N04 (2012), 186–191. DOI: 10.1393/ncc/i2012-11301-y.

[83] A. Gellrich, K. Jost, and J. Kessler. "Elimination of instrumental asymmetries in electron polarization analysis." *Review of Scientific Instruments* 61.11 (1990), 3399–3404. DOI: 10.1063/1.1141591.

[84] M. Molitor. "Double scattering polarimeter for the P2 experiment at MESA." *PoS* PSTP2015 (2016), 030. DOI: 10.22323/1.243.0030.

[85] V. Tioukine, K. Aulenbacher, and E. Riehn. "A Mott polarimeter operating at MeV electron beam energies." *Review of Scientific Instruments* 82.3 (2011), 033303. DOI: 10.1063/1.3556593.

[86] E. Chudakov and V. Luppov. "Moeller polarimetry with atomic hydrogen targets." *IEEE Trans. Nucl. Sci.* 51 (2004). [Eur. Phys. J.A24S2,123(2005)], 1533–1540. DOI: 10.1140/epjad/s2005-04-028-8, 10.1109/TNS.2004.832575.

[87] P. A. Bartolomé, K. Aulenbacher, and V. Tyukin. "Møller polarimetry with polarized atomic hydrogen at MESA." *AIP Conference Proceedings* 1563.1 (2013), 243–246. DOI: 10.1063/1.4829420.

[88] S. D. Covrig et al. "The Cryogenic target for the G0 experiment at Jefferson Lab." *Nucl. Instrum. Meth.* A551 (2005), 218–235. DOI: 10.1016/j.nima.2005.05.074. arXiv: nucl-ex/0502019 [nucl-ex].

[89] D. Androic et al. (G0 Collaboration). "The G0 Experiment: Apparatus for Parity-Violating Electron Scattering Measurements at Forward and Backward Angles." *Nucl. Instrum. Meth.* A646 (2011), 59–86. DOI: 10.1016/j.nima.2011.04.031. arXiv: 1103.0761 [nucl-ex].

[90] J. Ritman (FOPI Collaboration). "The FOPI detector at SIS/GSI." *Nucl. Phys. Proc. Suppl.* 44 (1995), 708–715. DOI: 10.1016/0920-5632(95)00606-0.

[91] V. Fanti et al. (NA48 Collaboration). "The Beam and detector for the NA48 neutral kaon CP violations experiment at CERN." *Nucl. Instrum. Meth.* A574 (2007), 433–471. DOI: 10.1016/j.nima.2007.01.178.

[92] S. Agostinelli et al. (GEANT4 Collaboration). "GEANT4: A Simulation toolkit." *Nucl. Instrum. Meth.* A506 (2003), 250–303. DOI: 10.1016/S0168-9002(03)01368-8.

[93] J. Allison et al. "Geant4 developments and applications." *IEEE Trans. Nucl. Sci.* 53 (2006), 270. DOI: 10.1109/TNS.2006.869826.

[94] J. Allison et al. "Recent developments in Geant4." *Nucl. Instrum. Meth.* A835 (2016), 186–225. DOI: 10.1016/j.nima.2016.06.125.

[95] V. L. Highland. "Some Practical Remarks on Multiple Scattering." *Nucl. Instrum. Meth.* 129 (1975), 497. DOI: 10.1016/0029-554X(75)90743-0.

[96] G. R. Lynch and O. I. Dahl. "Approximations to multiple Coulomb scattering." *Nucl. Instrum. Meth.* B58 (1991), 6–10. DOI: 10.1016/0168-583X(91)95671-Y.

[97] A. Magnon et al. "Tracking with 40x40-cm**2 MICROMEGAS detectors in the high energy, high luminosity COMPASS experiment." *Nucl. Instrum. Meth.* A478 (2002), 210–214. DOI: 10.1016/S0168-9002(01)01759-4.

[98] J. Bortfeldt et al. "High-Rate Capable Floating Strip Micromegas." *Nucl. Part. Phys. Proc.* 273-275 (2016), 1173–1179. DOI: 10.1016/j.nuclphysbps.2015.09.184. arXiv: 1508.00802 [physics.ins-det].

[99] I. Peric. "A novel monolithic pixelated particle detector implemented in high-voltage CMOS technology." *Nucl. Instrum. Meth.* A582 (2007), 876–885. DOI: 10.1016/j.nima.2007.07.115.

[100] I. Peric and C. Takacs. "Large monolithic particle pixel-detector in high-voltage CMOS technology." *Nucl. Instrum. Meth.* 624.2 (2010), 504–508. ISSN: 0168-9002. DOI: https://doi.org/10.1016/j.nima.2010.03.161.

[101] I. Peric, C. Kreidl, and P. Fischer. "Particle pixel detectors in high-voltage CMOS technology - New achievements." *Nucl. Instrum. Meth* 650.1 (2011), 158–162. ISSN: 0168-9002. DOI: https://doi.org/10.1016/j.nima.2010.11.090.

[102] I. Peric. "Active pixel sensors in high-voltage CMOS technologies for ATLAS." *JINST* 7 (2012), C08002. DOI: 10.1088/1748-0221/7/08/C08002.

[103] I. Perić et al. "High-voltage pixel detectors in commercial CMOS technologies for ATLAS, CLIC and Mu3e experiments." *Nucl. Instrum. Meth.* A731 (2013), 131–136. DOI: 10.1016/j.nima.2013.05.006.

[104] A.-K. Perrevoort. "Sensitivity Studies on New Physics in the Mu3e Experiment and Development of Firmware for the Front-End of the Mu3e Pixel Detector." PhD thesis. Universität Heidelberg, 2018. DOI: 10.11588/heidok.00024585.

[105] Wikipedia. *p-n-Übergang*. 2018. URL: https://de.wikipedia.org/wiki/P-n-%C3%9Cbergang.

[106] N. Wermes. "Pixel Detectors for Charged Particles." *Nucl. Instrum. Meth.* A604 (2009), 370–379. DOI: 10.1016/j.nima.2009.01.098. arXiv: 0811.4577 [physics.ins-det].

[107] A. Blondel et al. "Research Proposal for an Experiment to Search for the Decay $\mu \to eee$" (2013). arXiv: 1301.6113 [physics.ins-det].

[108] S. Shrestha (Mu3e Collaboration). "The High-Voltage Monolithic Active Pixel Sensor for the Mu3e Experiment." *PoS* TIPP2014 (2014), 047. DOI: 10.22323/1.213.0047.

[109] H. Augustin et al. "The MuPix high voltage monolithic active pixel sensor for the Mu3e experiment." *JINST* 10.03 (2015), C03044. DOI: 10.1088/1748-0221/10/03/C03044.

[110] H. Augustin et al. "MuPix8 - Large area monolithic HVCMOS pixel detector for the Mu3e experiment." *Nucl. Instrum. Meth.* (2018). DOI: https://doi.org/10.1016/j.nima.2018.09.095.

[111] H. Augustin et al. "The MuPix System-on-Chip for the Mu3e Experiment." *Nucl. Instrum. Meth.* A845 (2017), 194–198. DOI: 10.1016/j.nima.2016.06.095. arXiv: 1603.08751 [physics.ins-det].

[112] H. Augustin et al. "MuPix7—A fast monolithic HV-CMOS pixel chip for Mu3e." *JINST* 11.11 (2016), C11029. DOI: 10.1088/1748-0221/11/11/C11029. arXiv: 1610.02210 [physics.ins-det].

[113] H. Augustin et al. "Irradiation study of a fully monolithic HV-CMOS pixel sensor design in AMS 180 nm." *Nucl. Instrum. Meth.* A905 (2018), 53–60. DOI: 10.1016/j.nima.2018.07.044. arXiv: 1712.03921 [physics.ins-det].

[114] I. Sorokin. "Parameterization-based tracking for the P2 experiment." *EPJ Web Conf.* 150 (2017), 00012. DOI: 10.1051/epjconf/201715000012.

[115] A. Tyukin. "to be published." PhD thesis. Universität Mainz.

[116] C. Kleinwort. "General Broken Lines as advanced track fitting method." *Nucl. Instrum. Meth.* A673 (2012), 107–110. DOI: 10.1016/j.nima.2012.01.024. arXiv: 1201.4320 [physics.ins-det].

[117] L. Bugge and J. Myrheim. "Tracking and Track Fitting." *Nucl. Instrum. Meth.* 179 (1981), 365–381. DOI: 10.1016/0029-554X(81)90063-X.

[118] A. Strandlie and W. Wittek. "Derivation of Jacobians for the propagation of covariance matrices of track parameters in homogeneous magnetic fields." *Nucl. Instrum. Meth.* 566 (2006), 687–698. DOI: https://doi.org/10.1016/j.nima.2006.07.032.

[119] E. Lund et al. "Track parameter propagation through the application of a new adaptive Runge-Kutta-Nystroem method in the ATLAS experiment." *JINST* 4 (2009), P04001. DOI: 10.1088/1748-0221/4/04/P04001.

[120] E. Lund et al. "Transport of covariance matrices in the inhomogeneous magnetic field of the ATLAS experiment by the application of a semi-analytical method." *JINST* 4 (2009), P04016. DOI: 10.1088/1748-0221/4/04/P04016.

[121] U. Hartenstein. "Track Based Alignment for the Mu3e Pixel Detector." PhD thesis. Universität Mainz, 2018.

[122] V. Blobel. "Software alignment for tracking detectors." *Nucl. Instrum. Meth.* A566 (2006), 5–13. DOI: 10.1016/j.nima.2006.05.157.

[123] V. Blobel, C. Kleinwort, and F. Meier. "Fast alignment of a complex tracking detector using advanced track models." *Comput. Phys. Commun.* 182 (2011), 1760–1763. DOI: 10.1016/j.cpc.2011.03.017. arXiv: 1103.3909 [physics.ins-det].

[124] G. Folger, V. N. Ivanchenko, and J. P. Wellisch. "The Binary Cascade." *Eur. Phys. J. A* 21.3 (Sept. 2004), 407–417. DOI: 10.1140/epja/i2003-10219-7.

[125] D. Wright. *A Short Guide to Choosing a Physics List.* 2012. URL: http://geant4.slac.stanford.edu/MSFC2012/ChoosePhys.pdf.

[126] V. N. Ivanchenko et al. "Geant4 models for simulation of multiple scattering." *Journal of Physics: Conference Series* 219.3 (2010), 032045. DOI: 10.1088/1742-6596/219/3/032045.

[127] N. Berger et al. "Multiple Coulomb Scattering in Thin Silicon." *JINST* 9 (2014), P07007. DOI: 10.1088/1748-0221/9/07/P07007. arXiv: 1405.2759 [physics.ins-det].

[128] A. Bagulya et al. "Recent progress of GEANT4 electromagnetic physics for LHC and other applications." *J. Phys. Conf. Ser.* 898.4 (2017), 042032. DOI: 10.1088/1742-6596/898/4/042032.

[129] S. Goudsmit and J. L. Saunderson. "Multiple Scattering of Electrons." *Phys. Rev.* 57 (1940), 24–29. DOI: 10.1103/PhysRev.57.24.

[130] J.M.Fernández-Varea et al. "On the theory and simulation of multiple elastic scattering of electrons." *Nucl. Instrum. Meth.* B 73 (1993), 447–473. ISSN: 0168-583X. DOI: 10.1016/0168-583X(93)95827-R.

[131] M. H. Mendenhall and R. A. Weller. "An algorithm for computing screened Coulomb scattering in Geant4." *Nucl. Instrum. Meth.* B 227 (2005), 420–430. ISSN: 0168-583X. DOI: 10.1016/j.nimb.2004.08.014.

[132] L. Urbán (GEANT4 Collaboration). *A model for multiple scattering in GEANT4.* Tech. rep. CERN-OPEN-2006-077. CERN, Dec. 2006. URL: http://cds.cern.ch/record/1004190.

[133] G. Wentzel. "Zwei Bemerkungen über die Zerstreuung korpuskularer Strahlen als Beugungserscheinung." *Zeitschrift für Physik* 40.8 (Aug. 1926), 590–593. ISSN: 0044-3328. DOI: 10.1007/BF01390457.

[134] R. Brun and F. Rademakers. "ROOT: An object oriented data analysis framework." *Nucl. Instrum. Meth.* A389 (1997), 81–86. DOI: 10.1016/S0168-9002(97)00048-X.

[135] J. A. Bearden and A. F. Burr. "Reevaluation of X-Ray Atomic Energy Levels." *Rev. Mod. Phys.* 39.1 (1967), 125–142. DOI: 10.1103/RevModPhys.39.125.

[136] ATLAS Collaboration. *Radiation induced effects in the ATLAS Insertable B-Layer readout chip.* Tech. rep. ATL-INDET-PUB-2017-001. CERN, Nov. 2017. URL: https://cds.cern.ch/record/2291800.

[137] ATLAS Collaboration. *ATLAS experiment public results. LuminosityPublicResultsRun2.* 2018. URL: https://twiki.cern.ch/twiki/bin/view/AtlasPublic/LuminosityPublicResultsRun2#Multiple_Year_Collision_Plots.

[138] F. Hartmann. *Evolution of Silicon Sensor Technology in Particle Physics.* 2017, 135–166. DOI: 10.1007/978-3-319-64436-3.

[139] J. Lindhard and V. Nielsen. "Nuclear collisions and ionisation fluctuations in charged particle detectors." *Phys. Lett.* 2.5 (1962), 209–211. DOI: 10.1016/0031-9163(62)90229-9.

[140] T. Angelescu and A. Vasilescu. "Comparative radiation hardness results obtained from various neutron sources and the Niel problem." *Nucl. Instrum. Meth.* A374 (1996), 85–90. DOI: 10.1016/0168-9002(96)00087-3.

[141] A. Vasilescu and G. Lindstroem. *Notes on the fluence normalisation based on the NIEL scaling hypothesis.* Tech. rep. ROSE/TN/2000–02. June 2000.

[142] A. Vasilescu and G. Lindstroem. *Displacement damage in silicon, on-line compilation.* Aug. 2000. URL: https://rd50.web.cern.ch/rd50/NIEL/default.html.

[143] P. Griffin et al. *SNL RML recommended dosimetry cross section compendium.* Tech. rep. SAND-92-0094. Nov. 1993. DOI: 10.2172/10115441.

[144] A. Konobeyev, Y. Korovin, and V. Sosnin. "Neutron displacement cross-sections for structural materials below 800 MeV." *J. Nucl. Mater.* 186 (1992), 117–130. DOI: 10.1016/0022-3115(92)90328-I.

[145] G. P. Summers et al. "Damage correlations in semiconductors exposed to gamma, electron and proton radiations." *IEEE Trans. Nucl. Sci.* 40 (Dec. 1993), 1372–1379. DOI: 10.1109/23.273529.

[146] M. Huhtinen and P. Aarnio. "Pion induced displacement damage in silicon devices." *Nucl. Instrum. Meth.* A335 (1993), 580–582. DOI: 10.1016/0168-9002(93)91246-J.

[147] B. Nachman (ATLAS collaboration). "Modeling Radiation Damage to Pixel Sensors in the ATLAS Detector." *Proceedings, Meeting of the APS Division of Particles and Fields (DPF 2017)*. 2017. arXiv: 1710.03916 [physics.ins-det].

[148] M. Müller. "Effizienz eines HV-MAP Sensors auf niederenergetische Photonen." Bachelor's Thesis. Universität Mainz, 2017. URL: www.psi.ch/mu3e/ThesesEN/BachelorMueller.pdf.

[149] I. Anthony et al. "Design of a tagged photon spectrometer for use with the Mainz 840-MeV microtron." *Nucl. Instrum. Meth.* A301 (1991), 230–240. DOI: 10.1016/0168-9002(91)90464-2.

[150] S. J. Hall et al. "A focal plane system for the 855-MeV tagged photon spectrometer at MAMI-B." *Nucl. Instrum. Meth.* A368 (1996), 698–708. DOI: 10.1016/0168-9002(95)00661-3.

[151] J. C. McGeorge et al. "Upgrade of the Glasgow photon tagging spectrometer for Mainz MAMI-C." *Eur. Phys. J.* A37 (2008), 129–137. DOI: 10.1140/epja/i2007-10606-0. arXiv: 0711.3443 [nucl-ex].

[152] M. Unverzagt (Crystal Ball at MAMI). "eta and eta-prime Physics at MAMI." *Nucl. Phys. Proc. Suppl.* 198 (2010), 174–181. DOI: 10.1016/j.nuclphysbps.2009.12.034. arXiv: 0910.1331 [hep-ex].

[153] *Development of DCDC converters at CERN*. Version rev. 2.1. CERN. URL: https://project-dcdc.web.cern.ch (visited on 02/2019).

[154] Mu3e Collaboration. *Technical design of the Phase I Mu3e experiment*. Tech. rep. internal note, publication scheduled. 2019.

[155] M. Oinonen et al. "ALICE Silicon Strip Detector module assembly with single-point TAB interconnections." *Proceedings, eleventh Workshop on Electronics for LHC and Future Experiments, Heidelberg, Germany, 12-16 September*. 2005. URL: https://cds.cern.ch/record/920152.

[156] L. Noethe. "Flexprint design and characterization for the Mu3e experiment." Bachelor's Thesis. Universität Heidelberg, 2016. URL: https://www.psi.ch/mu3e/ThesesEN/BachelorNoehte.pdf.

[157] R. P. Austermuhl. "Analyse von Michelson-Interferometriedaten von Vibrationsmessungen eines dünnen gasgekühlten Pixeldetektors." Bachelor's Thesis. Universität Heidelberg, 2015. URL: https://www.psi.ch/mu3e/ThesesEN/BachelorAustermuehl.pdf.

[158] L. Henkelmann. "Optical Measurements of Vibration and Deformation of the Mu3e Silicon Pixel Tracker." Bachelor's Thesis. Universität Heidelberg, 2015. URL: https://www.psi.ch/mu3e/ThesesEN/BachelorHenkelmann.pdf.

[159] Samtec inc. *ZA8 0.8mm Ultra Low Profile Micro Array Product Specification*. Jan. 2016. URL: http://suddendocs.samtec.com/productspecs/za8.pdf.

[160] L. Huth. "A High Rate Testbeam Data Acquisition System and Characterization of High Voltage Monolithic Active Pixel Sensors." PhD thesis. Universität Heidelberg, 2019. DOI: 10.11588/heidok.00025785.

[161] J. Lienhard IV and J. Lienhard V. *A Heat Transfer Textbook*. 4th. Version 2.12. Phlogiston Press, 2018. URL: http://ahtt.mit.edu.

[162] M. Zimmermann. "Cooling with Gaseous Helium for the Mu3e Experiment." Bachelor's Thesis. Universität Heidelberg, 2012. URL: https://www.psi.ch/mu3e/ThesesEN/BachelorZimmermann.pdf.

[163] D. Weyburne. "New thickness and shape parameters for describing the thermal boundary layer" (2017). arXiv: 1704.01120v3 [flu-dyn].

[164] L. Huxold. "Cooling of the Mu3e Pixel Detector." Bachelor's Thesis. Universität Heidelberg, 2014. URL: https://www.psi.ch/mu3e/ThesesEN/BachelorHuxold.pdf.

[165] A. Herkert. "Gaseous Helium Cooling of a Thin Silicon Pixel Detector for the Mu3e Experiment." Master's Thesis. Universität Heidelberg, 2015. URL: https://www.psi.ch/mu3e/ThesesEN/MasterHerkert.pdf.

[166] Y. Ng. "Finite Element Analysis of the Cooling System for the Mu3e Experiment." Master's Thesis. Universität Heidelberg and Hochschule Jena, 2015. URL: https://www.psi.ch/mu3e/ThesesEN/MasterNg.pdf.

[167] C. Tormann. "Thermal Analysis of the Silicon Pixel Detector for the Mu3e Experiment." Bachelor's Thesis. Universität Heidelberg, 2018. URL: https://www.psi.ch/mu3e/ThesesEN/BachelorTormann.pdf.

[168] T. Bergman et al. *Fundamentals of Heat and Mass Transfer*. Wiley, 2011.

[169] Autodesk Inc. *Autodesk CFD online documentation*. URL: https://knowledge.autodesk.com/support/cfd.

[170] I. Landau and G. Zito. *Digital Control Systems: Design, Identification and Implementation*. Communications and Control Engineering. Springer, 2007.

[171] Maxim Integrated. *DS18B20 - Programmable Resolution 1-Wire Digital Thermometer. Datasheet.* 2018. URL: https://www.maximintegrated.com/en/products/sensors/DS18B20.html.

[172] F. J. Stieler. "Tests der Mechanik und Kühlung des Spurdetektors für das P2-Experiment." Bachelor's Thesis. Universität Mainz, 2018.

[173] Texas Instruments. *LMZ22005 5-A SIMPLE SWITCHER Power Module With 20-V Maximum Input Voltage (Rev. J). Datasheet.* 2015. URL: http://www.ti.com/product/LMZ22005.

[174] Microchip Technology Inc. *MCP 42010 Dual Digital Potentiometer with SPI Interface. Datasheet.* 2003. URL: https://www.microchip.com/wwwproducts/en/MCP42010.

[175] Maxim Integrated. *DS2413 1-Wire Dual Channel Addressable Switch. Datasheet.* 2015. URL: https://www.maximintegrated.com/en/products/interface/controllers-expanders/DS2413.html.